

A high precision measurement of the neutron magnetic form  
factor using the CLAS detector.

by

Jeffrey Douglas Lachniet

A preliminary version of the dissertation. A dissertation  
submitted in partial fulfillment of the requirements for  
the degree of

Doctor of Philosophy

in the Department of Physics

Carnegie Mellon University

June 2005

## Abstract

The neutron magnetic form factor  $G_M^n$  has been extracted from the ratio of quasi-elastic e-n to e-p scattering from a deuterium target using the CLAS detector. The measurement covers the range 0.5 to 4.5 (GeV/c)<sup>2</sup> in four-momentum transfer squared. High precision was achieved by use of the ratio technique, with which many uncertainties cancel. A dual-cell target was used, featuring a deuterium cell and a hydrogen cell, which allowed a simultaneous *in-situ* calibration of the neutron detection efficiency. Neutrons were detected using the CLAS Time-of-Flight system and the Forward Electromagnetic Calorimeter. Data was taken at two different electron beam energies, allowing up to four semi-independent measurements of  $G_M^n$  to be made at each value of  $Q^2$ . The data is compared to previous measurements, and with several theoretical and phenomenological models. It is found that for  $Q^2 > 1$  (GeV/c)<sup>2</sup> the standard dipole parametrization gives a good representation of the data over a wide range of  $Q^2$ .

# Contents

<b>1</b>	<b>Introduction</b>	<b>1</b>
1.1	Electromagnetic Form Factors . . . . .	1
1.1.1	Electron-Nucleon scattering in the Single Photon Exchange Approximation . . . . .	1
1.1.2	Interpretation of Elastic Form Factors . . . . .	4
1.1.3	Models and Theoretical Predictions . . . . .	5
1.2	Previous $G_M^n$ measurements . . . . .	13
1.3	Experimental technique . . . . .	13
<b>2</b>	<b>Experimental Setup</b>	<b>16</b>
2.1	The CEBAF Accelerator . . . . .	16
2.2	The CLAS spectrometer . . . . .	16
2.2.1	Toroidal Magnet . . . . .	16
2.2.2	Drift Chambers . . . . .	19
2.2.3	Time of Flight System . . . . .	20
2.2.4	Cherenkov Counters . . . . .	22
2.2.5	Forward Electromagnetic Calorimeter . . . . .	24
2.2.6	E5 Target . . . . .	27
2.2.7	Trigger and Data Acquisition . . . . .	27
<b>3</b>	<b>Experiment Analysis</b>	<b>32</b>
3.1	Event Reconstruction . . . . .	32
3.2	Run Selection . . . . .	32
3.3	Neutron Detection Efficiency Measurement . . . . .	34
3.3.1	Electron Identification . . . . .	34
3.3.2	$\pi^+$ Identification . . . . .	36
3.3.3	Neutron selection . . . . .	37
3.3.4	Efficiency Measurement in the Forward Calorimeter . . . . .	38
3.3.5	Efficiency Measurement in the Time of Flight system . . . . .	46
3.4	Proton Detection Efficiency Measurement . . . . .	53
3.4.1	Electron Identification . . . . .	53
3.4.2	Proton Identification . . . . .	54
3.4.3	Efficiency calculation . . . . .	55

3.5	Momentum Corrections . . . . .	55
3.6	Quasi-elastic ratio measurement . . . . .	61
3.6.1	Quasi-elastic electron selection . . . . .	61
3.6.2	Quasi-elastic $D(e, e'p)$ selection . . . . .	61
3.6.3	Quasi-elastic $D(e, e'n)$ selection . . . . .	62
3.6.4	Rejection of unreconstructed proton tracks . . . . .	62
3.6.5	Acceptance matching and fiducial cuts . . . . .	65
3.6.6	Efficiency corrections and Ratio calculation . . . . .	70
3.7	Corrections to Quasi-elastic ratio . . . . .	73
3.7.1	Uncalibrated SC paddles . . . . .	73
3.7.2	Losses due to Fermi motion of the target . . . . .	73
3.7.3	Quasi-elastic event generator . . . . .	77
3.7.4	Fermi Loss Corrections . . . . .	82
3.7.5	Radiative Corrections . . . . .	86
3.7.6	Nuclear Corrections . . . . .	91
<b>4</b>	<b>Experiment Results</b>	<b>101</b>
4.1	$G_M^n$ extraction from ratio . . . . .	101
4.2	Systematic Errors . . . . .	104
4.2.1	Systematic error due to uncertainty in Proton cross-section . .	104
4.2.2	Systematic error due to uncertainty in $G_E^n$ . . . . .	105
4.2.3	Other sources of systematic error . . . . .	109
4.2.4	Combined systematic error . . . . .	134
<b>5</b>	<b>Conclusions</b>	<b>139</b>
5.1	Comparison to previous measurements . . . . .	139
5.1.1	Comparison to theoretical predictions and fits . . . . .	140
	<b>Bibliography</b>	<b>144</b>
<b>A</b>	<b>Measured <math>G_M^n</math> values and errors</b>	<b>147</b>
<b>B</b>	<b>EC neutron detection efficiency fits</b>	<b>152</b>
B.1	2.5 GeV beam energy . . . . .	152
B.2	4.2 GeV beam energy . . . . .	159
<b>C</b>	<b>SC neutron detection efficiency fits</b>	<b>166</b>
C.1	2.5 GeV beam energy . . . . .	166
C.2	4.2 GeV beam energy . . . . .	177
<b>D</b>	<b>Kinematics of quasi-elastic scattering</b>	<b>188</b>

# Chapter 1

## Introduction

### 1.1 Electromagnetic Form Factors

Neutrons and protons are fundamental building blocks of the visible matter in the universe. If the proton and neutron were simple, structureless Dirac particles like the electron, they would have a magnetic moment given by:

$$\mu_N = \frac{q}{m} |\vec{s}| \quad (1.1)$$

where  $q, m,$  and  $\vec{s}$  are the nucleon's charge, mass and spin respectively (using natural units  $\hbar = c = 1$ ). In particular, the proton magnetic moment should be equal in magnitude to  $\mu_N$ , where  $\mu_N = \frac{e}{2M_p}$ , and the neutron magnetic moment should vanish. Otto Stern's measurement of the proton magnetic moment in 1933, which showed that the proton magnetic moment was  $\mu_p = 2.79\mu_N$ , indicated that the proton was not a structureless Dirac particle. Subsequent measurement of the neutron magnetic moment ( $\mu_n = -1.91\mu_N$ ) confirmed the non-Dirac nature of the neutron. Beginning in the 1950s, electron scattering experiments by Hofstadter and others showed evidence of charge and magnetization distributions inside the proton. Form factors, called  $G_E^p$  and  $G_M^p$  were introduced to parametrize the proton internal structure revealed in the electron scattering experiments.

#### 1.1.1 Electron-Nucleon scattering in the Single Photon Exchange Approximation

From the Feynman rules for quantum electrodynamics (QED), the amplitude for electron-nucleon scattering in the single-photon exchange approximation is given by:

$$-iM = j^\mu \frac{-ig_{\mu\nu}}{q^2} J^\nu \quad (1.2)$$

In this expression,  $j^\mu$  is the electron transition current,  $J^\nu$  is the proton transition current and  $g_{\mu\nu}$  is the metric tensor. This is illustrated in Fig 1.1 for an electron of

initial(final) momentum  $k(k')$  and a nucleon of initial(final) momentum  $p(p')$ . The four-momentum transferred in the reaction is  $q = k - k'$ .

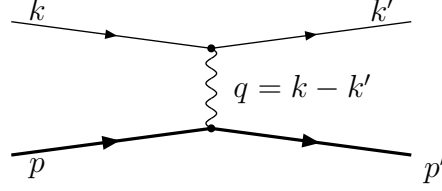


Figure 1.1: Elastic electron-nucleon scattering in the single-photon exchange approximation

The electron is an elementary spin- $\frac{1}{2}$  particle. The form of its transition current is known:

$$j^\mu = -e\bar{u}_e(k')\gamma^\mu u_e(k)e^{iq\cdot x} \quad (1.3)$$

In this expression,  $u_e(k)$  and  $\bar{u}_e(k')$  are Dirac spinors representing the incident and scattered electron, and the  $\gamma^\mu$  are the usual Dirac matrices.

The nucleon is a composite particle, with non-trivial internal structure, so the simple form of Eqn 1.3 must be replaced with a more complicated form:

$$J^\mu = -e\bar{u}(p')\Gamma^\mu u(p)e^{iq\cdot x} \quad (1.4)$$

$\Gamma^\mu$  must be constructed such that  $J^\mu$  transforms like a 4-vector. The ingredients available to construct such an expression for  $\Gamma^\mu$  are functions of  $p, p', q$  and combinations of Dirac gamma matrices. It can be shown that the most general nucleon current, subject to the requirements of current conservation, parity conservation and Lorentz invariance, can be written as:

$$J^\mu = e\bar{u}(p') \left[ F_1(Q^2)\gamma^\mu + \frac{\kappa}{2M}F_2(Q^2)i\sigma^{\mu\nu}q_\nu \right] u(p)e^{iq\cdot x} \quad (1.5)$$

where  $\kappa$  is the nucleon anomalous magnetic moment,  $M$  is the nucleon mass and  $F_1$  and  $F_2$  are scalar functions of  $Q^2$  (with  $Q^2 = -q^2$ ) called the Dirac and Pauli form factors respectively. The form factors parametrize our ignorance of the details of the internal structure of the nucleon.

Long wavelength photons ( $Q^2 \rightarrow 0$ ) do not resolve the interior structure of the nucleon, so in that limit, the nucleon current must reduce to that of a point particle of appropriate charge and magnetic moment. This requirement fixes the values of the form factors at  $Q^2 = 0$ :

$$F_1^p(0) = 1, \quad F_2^p(0) = 1 \quad (1.6)$$

$$F_1^n(0) = 0, \quad F_2^n(0) = 1. \quad (1.7)$$

The superscripts label the isospin state of the nucleon.

With this expression for the nucleon electromagnetic current, the cross section for elastic electron-nucleon scattering can be calculated (in the lab frame, where the nucleon is initially at rest):

$$\frac{d\sigma}{d\Omega} = \sigma_{Mott} \left[ \left( F_1^2 + \frac{\kappa^2 Q^2}{4M^2} F_2^2 \right) + \frac{Q^2}{2M^2} (F_1 + \kappa F_2)^2 \tan^2\left(\frac{\theta}{2}\right) \right], \quad (1.8)$$

where  $\theta$  is the electron scattering angle, and  $\sigma_{Mott}$  is the Mott cross section (using natural units,  $\hbar = c = 1$ ):

$$\sigma_{Mott} = \frac{\alpha^2 E' \cos^2(\frac{\theta}{2})}{4E^3 \sin^4(\frac{\theta}{2})} \quad (1.9)$$

Eqn 1.8 is inconvenient due to the  $F_1 F_2$  term. If the so-called Sachs' form factors are defined as:

$$G_E \equiv F_1 - \frac{\kappa Q^2}{4M^2} F_2 \quad (1.10)$$

$$G_M \equiv F_1 + \kappa F_2, \quad (1.11)$$

then Eqn 1.8 can be rewritten as:

$$\frac{d\sigma}{d\Omega} = \sigma_{Mott} \left( G_E^2 + \frac{\tau}{\epsilon} G_M^2 \right) \left( \frac{1}{1 + \tau} \right) \quad (1.12)$$

In this equation,  $\tau = \frac{Q^2}{4M^2}$  and  $\epsilon = (1 + 2(1 + \tau) \tan^2(\frac{\theta}{2}))^{-1}$ . The Sachs' form factors  $G_E$  and  $G_M$  are known as the *electric* and *magnetic* form factors, respectively. The  $Q^2 = 0$  limit of these form factors can be found by combining Eqn 1.11, Eqn 1.6 and Eqn 1.7, giving:

$$G_E^p(0) = 1, \quad G_M^p(0) = \mu_p \quad (1.13)$$

$$G_E^n(0) = 0, \quad G_M^n(0) = \mu_n, \quad (1.14)$$

where  $\mu_p$  and  $\mu_n$  are the proton and neutron magnetic moment ( $\mu_p = 1 + \kappa_p$ ,  $\mu_n = \kappa_n$ ), respectively.

Early measurements of the elastic form factors showed that  $G_E^p$  could be parameterized using the so-called dipole form:

$$G_D(Q^2) = \frac{1}{(1 + Q^2/\Delta)^2} \quad (1.15)$$

where  $\Delta = 0.71$  (GeV/c)<sup>2</sup>. Furthermore the other elastic form factors, with the exception of  $G_E^n$ , were found to be well approximated by scaling  $G_E^p$ :

$$G_E^p(Q^2) \approx G_D(Q^2) \quad (1.16)$$

$$G_M^p(Q^2) \approx \mu_p G_D(Q^2) \quad (1.17)$$

$$G_M^n(Q^2) \approx \mu_n G_D(Q^2) \quad (1.18)$$

It is a standard practice when showing form factor data to scale the data points to the dipole. The dipole does not describe  $G_E^n$ , which is frequently parametrized using the Galster fit:

$$G_E^n(Q^2) = \frac{\mu_n \tau G_D}{1 + \eta \tau} \quad (1.19)$$

where  $\tau = Q^2/4M_n^2$  and  $\eta = 5.6$ .

### 1.1.2 Interpretation of Elastic Form Factors

The introduction of the Sachs' form factors removed the interference term from the cross section, simplifying experimental analysis. The Sachs' form factors also have a somewhat more direct physical interpretation. In the non-relativistic region  $Q^2 \ll M_N^2$ , the Sachs' form factors can be interpreted as Fourier transforms of the charge and magnetization distributions:

$$G_E(Q^2) = \int \rho(r) e^{i\vec{q}\cdot\vec{r}} d^3r \quad (1.20)$$

The dipole form  $G_D(Q^2)$  discussed in the previous section corresponds to an exponential fall-off in the spatial charge and magnetization distributions.

The integrand in the equation can be expanded in powers of  $q$  to obtain the RMS charge radius of the nucleon:

$$G_E = \int \rho(r) \left\{ 1 - \frac{1}{2}(qr)^2 \cos^2 \theta + \dots \right\} r^2 \sin \theta dr d\theta d\phi \quad (1.21)$$

Differentiating with respect to  $q^2$  and taking the limit  $q^2 \rightarrow 0$  gives:

$$\langle r^2 \rangle = -6 \left. \frac{dG_E(q)}{dq^2} \right|_{q^2=0} \quad (1.22)$$

At higher  $Q^2$ , this simple interpretation is complicated by relativistic effects. However, a simple connection between the form factors and the electromagnetic structure of the nucleon still exists in a special reference frame, called the Breit, or "Brick Wall" frame. In this frame, defined by the condition  $\mathbf{p} = -\mathbf{p}'$ , where no energy is transferred to the nucleon, it can be shown that the form factors are related to the charge and magnetic moment distributions in the nucleon in momentum-space [1].

In this frame,

$$J^0(Q^2) = \rho(Q^2) = 2MeG_e(Q^2) \quad (1.23)$$

$$J^1(Q^2) \pm iJ^2(Q^2) = \mp 2|\mathbf{q}| eG_M(Q^2). \quad (1.24)$$

so that there is a connection between the components of the nucleon current 4-vector and the elastic form factors.

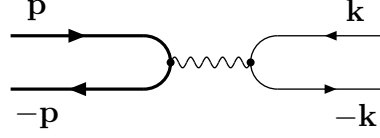


Figure 1.2: Elastic electron-nucleon scattering in the Breit frame

The measurement of the elastic form factors of the nucleon is topic of great interest. The elastic form factors encode fundamental information about hadron structure, and the nucleon is the only hadron for which precise form factor measurements are possible. Hence, the elastic form factors provide the most stringent test for models of hadron structure.

### 1.1.3 Models and Theoretical Predictions

#### 1.1.3.1 IJL model

The model of Iachello, Jackson and Lande [2] uses isospin symmetry to relate the proton and neutron form factors, which are decomposed into linear combinations of isoscalar and isovector terms [3]:

$$G_M^p(Q^2) = (F_1^{is} + F_1^{iv}) + (F_2^{is} + F_2^{iv}) \quad (1.25)$$

$$G_E^p(Q^2) = (F_1^{is} + F_1^{iv}) + \frac{Q^2}{4M^2}(F_2^{is} + F_2^{iv}) \quad (1.26)$$

$$G_M^n(Q^2) = (F_1^{is} - F_1^{iv}) + (F_2^{is} - F_2^{iv}) \quad (1.27)$$

$$G_E^n(Q^2) = (F_1^{is} - F_1^{iv}) + \frac{Q^2}{4M^2}(F_2^{is} - F_2^{iv}) \quad (1.28)$$

The virtual-photon/nucleon interaction is modeled as a combination of a direct photon-nucleon coupling, described by a dipole form factor of the form  $g(Q^2) = (1 + \gamma Q^2)^{-2}$ , and VMD pole terms for isoscalar ( $\omega$  and  $\phi$ ) and isovector ( $\rho$ ) meson couplings. The model interactions are illustrated if Fig 1.3.

The meson-nucleon coupling parameters and the direct coupling parameters were obtained by fitting to the form factor data available at the time. The model was found to give an adequate description of the proton form factors, and successfully predicted the fall-off of the ratio  $\frac{\mu_p G_E^p}{G_M^p}$  recently observed in polarization-transfer measurements at Jefferson Lab [4, 5].

The prediction of the IJL model for  $G_M^n$  is shown (scaled to the dipole) in Fig 1.5.

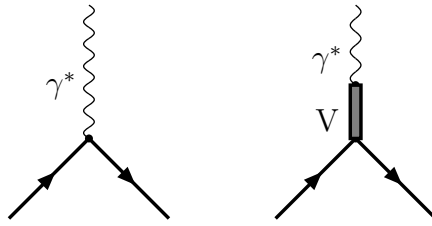


Figure 1.3: Photon-Nucleon interactions in the IJL model

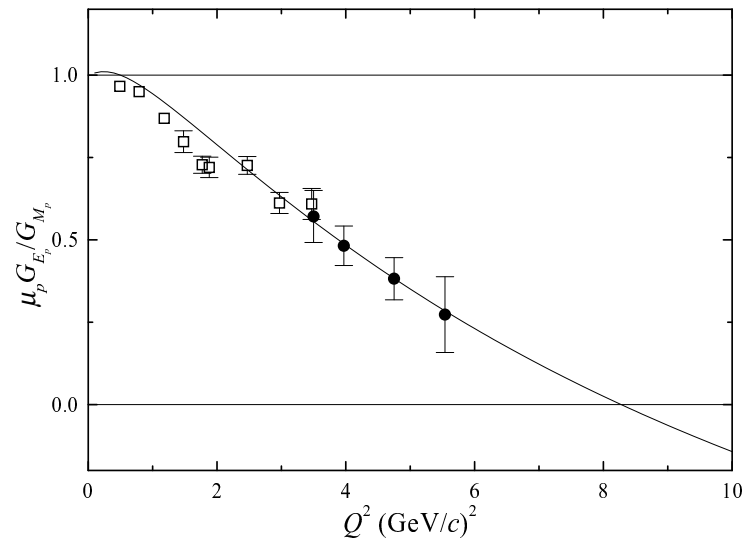


Figure 1.4: The prediction of the IJL model for  $\frac{\mu_p G_{E_p}^p}{G_{M_p}^p}$ , compared to recent data from JLab. The open squares are from [4], the filled circles from [5]

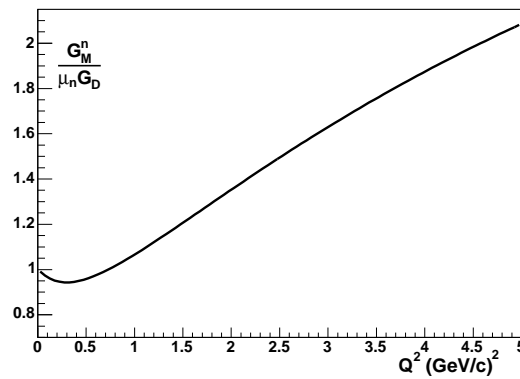


Figure 1.5: The prediction of the IJL model for  $G_M^n$ , scaled to the dipole

### 1.1.3.2 Lomon/GK fit

The Gari-Krümpelmann model [6] attempts to model the nucleon form factors in a manner which incorporates the VMD model at low  $Q^2$  and perturbative QCD at high  $Q^2$ . The Dirac and Pauli form factors are decomposed into isoscalar and isovector parts, as described in Section 1.1.3.1. As in the IJL model, the isoscalar and isovector form factors are modeled as being due to a photon/vector-meson/nucleon interaction and a direct photon-nucleon coupling (see Fig 1.3):

$$F_1^{iv}(Q^2) = \left[ \frac{m_\rho}{m_\rho + Q^2} \frac{g_\rho}{f_\rho} + \left( 1 - \frac{g_\rho}{f_\rho} \right) \right] F_1(Q^2) \quad (1.29)$$

$$\kappa_V F_2^{iv}(Q^2) = \left[ \frac{m_\rho}{m_\rho + Q^2} \frac{\kappa_\rho g_\rho}{f_\rho} + \left( \kappa_V - \frac{\kappa_\rho g_\rho}{f_\rho} \right) \right] F_2(Q^2) \quad (1.30)$$

$$F_1^{is}(Q^2) = \left[ \frac{m_\omega}{m_\omega + Q^2} \frac{g_\omega}{f_\omega} + \left( 1 - \frac{g_\omega}{f_\omega} \right) \right] F_1(Q^2) \quad (1.31)$$

$$\kappa_S F_2^{is}(Q^2) = \left[ \frac{m_\omega}{m_\omega + Q^2} \frac{\kappa_\omega g_\omega}{f_\omega} + \left( \kappa_S - \frac{\kappa_\omega g_\omega}{f_\omega} \right) \right] F_2(Q^2) \quad (1.32)$$

The  $\phi$  meson is taken to be completely decoupled from the nucleon, in accord with the Zweig rule. The  $F_1$  and  $F_2$  terms are chosen to satisfy the meson-dynamics prediction [7] of a monopole type dependence at low  $Q^2$ :

$$F_1 \sim F_2 \sim \frac{\Lambda_1^2}{\Lambda_1^2 + Q^2} \quad (1.33)$$

with  $\Lambda_1 \sim 0.8 \text{ GeV}$ . At large  $Q^2$ , perturbative QCD makes predictions for the  $Q^2$  dependence of the form factors [8]:

$$F_1 \sim \left[ \frac{1}{Q^2 \log(Q^2/\Lambda_{QCD}^2)} \right]^2 \quad (1.34)$$

$$F_2 \sim \frac{F_1}{Q^2} \quad (1.35)$$

To interpolate between these two limiting  $Q^2$  regimes, Gari and Krümpelmann use intrinsic form factors of the form:

$$F_1(Q^2) = \frac{\Lambda_1^2}{\Lambda_1^2 + \tilde{Q}^2} \frac{\Lambda_2^2}{\Lambda_2^2 + \tilde{Q}^2} \quad (1.36)$$

$$F_2(Q^2) = \frac{\Lambda_1^2}{\Lambda_1^2 + \tilde{Q}^2} \left[ \frac{\Lambda_2^2}{\Lambda_2^2 + \tilde{Q}^2} \right]^2 \quad (1.37)$$

where

$$\tilde{Q}^2 = Q^2 \frac{\log(\frac{\Lambda_2^2 + Q^2}{\Lambda_{QCD}^2})}{\log(\frac{\Lambda_2^2}{\Lambda_{QCD}^2})} \quad (1.38)$$

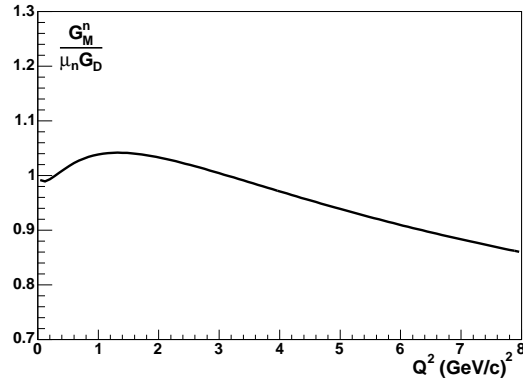


Figure 1.6: The  $G_M^n$  prediction of the Lomon's extended GK model, scaled to the dipole

Lomon [9, 10] extended the GK model by including  $\phi$  coupling to the nucleon, adding the  $\rho'(1450)$  and replacing the  $\rho$  pole term with a dispersion relation term [11]. The meson-nucleon coupling constants and cut-off scale factors ( $\Lambda_1, \Lambda_2, \Lambda_{QCD}$ ) were determined by fitting to the world data on  $G_M^p, G_E^p, G_M^n, G_E^n$  and the recent JLab results for  $\frac{\mu_p G_M^p}{G_E^p}$ . The  $G_M^n$  values generated by the best-fit parameters [10] are shown in Fig 1.6.

### 1.1.3.3 Miller model

The model of Miller [12] treats the nucleon as a relativistic bound state of three constituent quarks surrounded by a pion cloud. Poincaré invariance is imposed using light-front dynamics, in which fields are quantized at a fixed light-cone time  $\tau = x^0 + x^3 \equiv x^+$ . The advantage of using the light-cone for form-factor calculations is that light-cone boost operators are independent of interactions (the initial and final state nucleons in elastic scattering are connected by a boost operator). The model uses a relativistic quark model first proposed by [13] and [14]. Quark effects are dominant at large  $Q^2$ . Pion cloud effects, important at low  $Q^2$ , are implemented using a cloudy-bag approach. The results of Miller's Light Front Cloudy Bag model (LFCBM) for  $G_M^n$  are shown in Fig 1.7.

### 1.1.3.4 Wagenbrunn model

The model of Wagenbrunn *et al.* [15] uses a constituent quark model in which the interaction between two quarks is modeled by single Goldstone boson exchange [16]. Poincaré invariance is obtained by using the “point-form”, a third variety of relativistic dynamics, in which the fields are quantized on the surface of a hyperboloid  $t^2 - \vec{x}^2 = \kappa^2$ . The results of the point-form CQM are shown in Fig. 1.8.

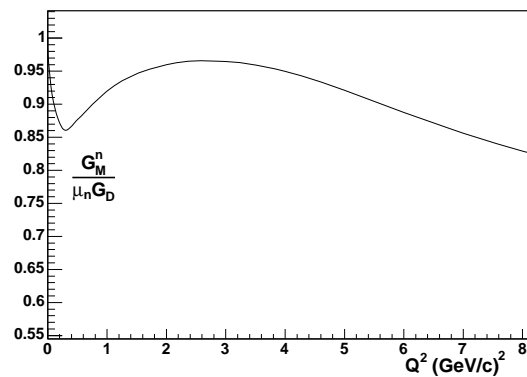


Figure 1.7: The  $G_M^n$  prediction of the Miller model, scaled to the dipole

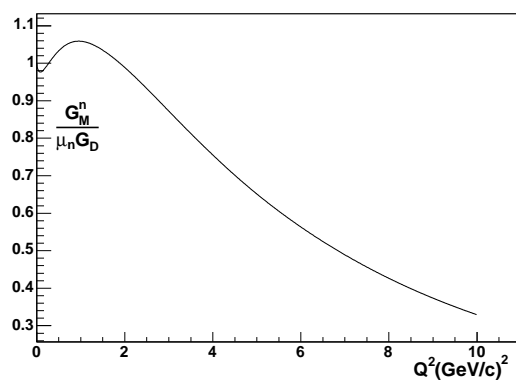


Figure 1.8: The  $G_M^n$  prediction of the Wagenbrunn model, scaled to the dipole

### 1.1.3.5 Lattice-based calculation

Isvector and isoscalar form factors can be defined as linear combinations of the standard form factors:

$$G^v = G_p - G_n \quad (1.39)$$

$$G^s = G_p + G_n \quad (1.40)$$

The QCDSF collaboration [17] have made quenched lattice calculations of the isovector and isoscalar form factors. Present computer power does not allow the calculations to be performed at realistic quark masses, so the calculations were performed with quark masses 5-10 times higher than the physical value. Three different values of the lattice spacing were used. Ashley *et al.* [18] use results obtained from chiral perturbation theory to perform the extrapolation down to physical values of the quark masses. All of the electromagnetic form factors are assumed to have a dipole form:

$$G(Q^2) = \frac{G(0)}{(1 + Q^2/\Lambda)^2} \quad (1.41)$$

At each value of the pion mass and lattice spacing, the QCDSF form factor result was fitted with a dipole form. The dipole mass ( $\Lambda$  in Eqn 1.41) is fitted as a function of the pion mass, using a functional form determined from chiral perturbation theory, as shown in Fig 1.9. The value of the isovector and isoscalar dipole mass determined from this extrapolation are used to calculate  $G_M^n$ , with the results shown in Fig 1.10. A range of values is shown.

### 1.1.3.6 Kelly Fit

Kelly [19] fit a selection of world data with a function of the form:

$$G_M^n(Q^2) = \frac{\sum_{k=0}^n a_k \tau^k}{1 + \sum_{k=1}^{n+2} b_k \tau^k} \quad (1.42)$$

where  $\tau = Q^2/4M_p^2$  and the  $a_k, b_k$  are coefficients of the fit. This form contains only even powers of  $Q$  in the denominator, ensuring that  $\langle r^2 \rangle$  is finite, and the degree of the polynomial in the denominator is higher than the numerator, ensuring the  $Q^{-4}$  behavior predicted by pQCD at large  $Q^2$ . The results of the fit are shown in Fig 1.11.

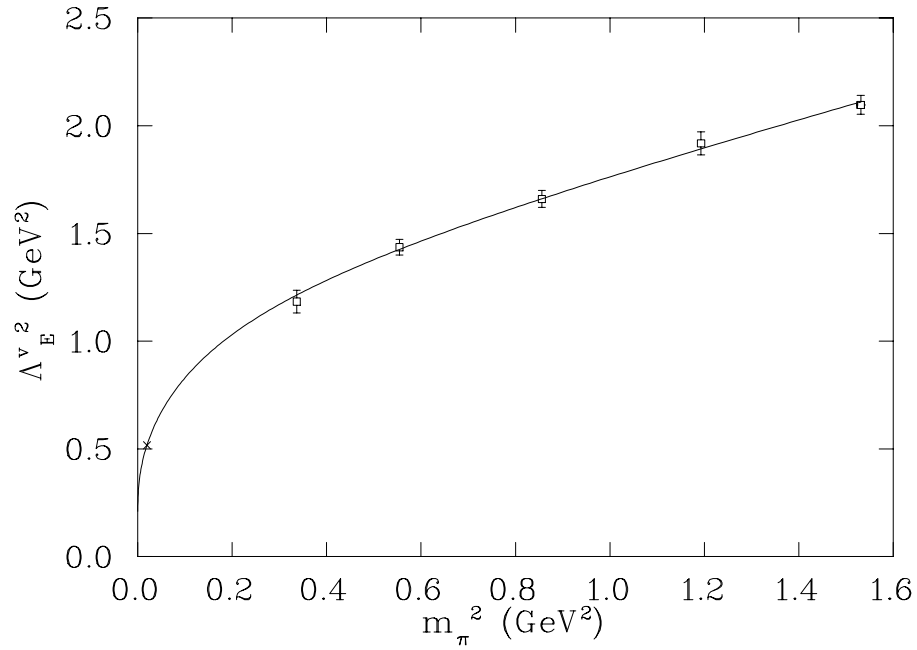


Figure 1.9: Fits to values of the isovector dipole mass, as a function of  $m_\pi^2$ . The lattice calculations are indicated by the open box, and the extrapolated value at the physical pion mass is shown with the x.

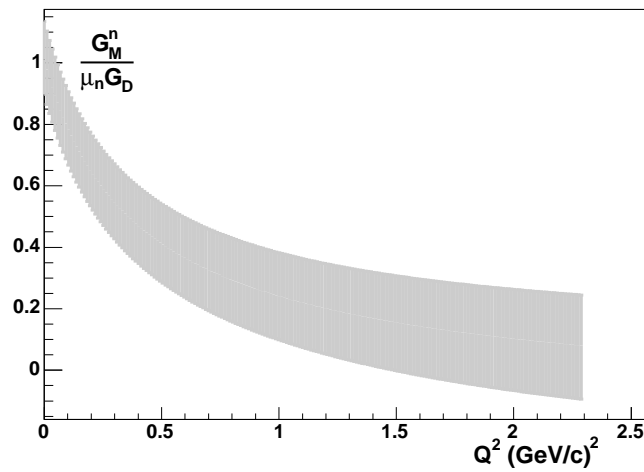


Figure 1.10: The range of  $G_M^n$  values (scaled to the dipole) predicted from the lattice calculations of Ashley et al [18].

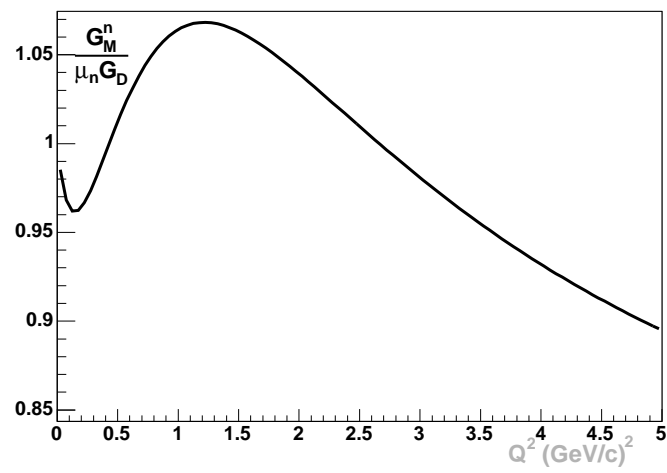


Figure 1.11: Results of the fit by Kelly to world  $G_M^n$  data.

## 1.2 Previous $G_M^n$ measurements

The lack of free neutron target complicates measurements of the neutron form factors. The deuteron is the simplest target nucleus, and most previous  $G_M^n$  measurements have used deuteron targets. For inclusive e-d scattering, used in Ref [20–24], a longitudinal-transverse separation of the scattering cross section must be made, followed by a subtraction of the proton contribution. This subtraction introduces significant model dependence due to the choice of deuteron model and treatment of final state interactions. The proton-subtraction error is avoided in exclusive quasi-elastic measurements where the neutron in  $D(e, e'n)p$  is also observed [25–27]. The price that is paid for removing the proton subtraction uncertainty is that this method requires knowledge of the neutron detection efficiency. Anti-coincidence measurements of  $d(e, e'NOT - p)$  where the *absence* of a scattered proton is required have also been performed [28].

Most recent unpolarized measurements of  $G_M^n$  measure the ratio of the cross section ratio for  $D(e, e'n)p$  to  $D(e, e'p)n$  scattering [29–31]. Taking this ratio reduces the sensitivity to the nucleon structure and radiative corrections. This is the same technique used in the present e5 analysis. As with the  $D(e, e'n)p$  exclusive measurements, this technique requires accurate determination of the neutron detection efficiency. Fig 1.12 shows the world data on  $G_M^n$  from unpolarized electron-deuteron experiments.

Neutron form factor information, typically at lower values of  $Q^2$ , can also be extracted from measurements on polarized targets. Recent  $G_M^n$  results from measurements using polarized targets are shown in Fig 1.13. Typically, a polarized  $^3\text{He}$  target is used. The  $^3\text{He}$  nucleus is dominated by a spatially symmetric S-wave state in which the two proton spins cancel, so that the  $^3\text{He}$  spin is carried by the neutron. Spin-dependent response functions can be extracted from the  $^3\text{He}(e, e')$  cross section, which under the right kinematic configuration contains terms proportional to  $G_M^n$ .

## 1.3 Experimental technique

The value of  $G_M^n$  was extracted from a measurement of the ratio of quasi-elastic e-n to e-p scattering from a deuterium target:

$$R = \frac{\frac{d\sigma}{d\Omega}(D(e, e'n))}{\frac{d\sigma}{d\Omega}(D(e, e'p))} \quad (1.43)$$

This ratio is nearly equal to the ratio of the *free nucleon* e-n to e-p cross sections:

$$R = a(Q^2) \frac{\frac{G_{En}^2 + \tau G_{Mn}^2}{1 + \tau} + 2\tau G_{Mn}^2 \tan^2(\frac{\Theta}{2})}{\frac{G_{Ep}^2 + \tau G_{Mp}^2}{1 + \tau} + 2\tau G_{Mp}^2 \tan^2(\frac{\Theta}{2})} \quad (1.44)$$

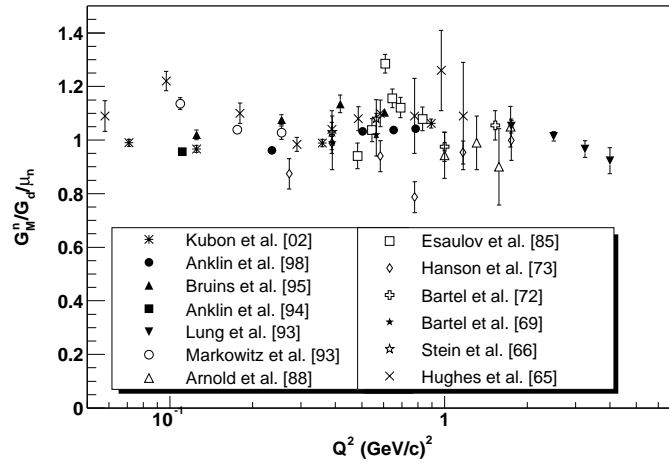


Figure 1.12: World data on  $G_M^n$  from unpolarized electron-deuteron measurements. The figure is from [32]

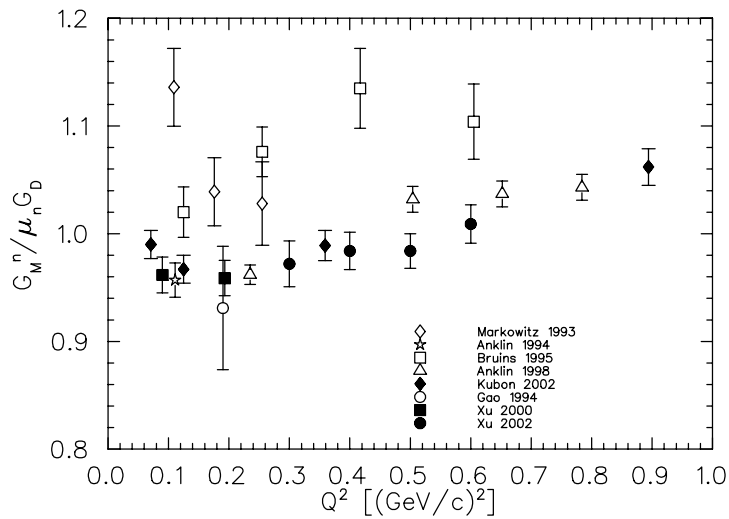


Figure 1.13: World data on  $G_M^n$  from polarized target measurements. The figure is from [32]

Deviations from this “free ratio” assumption are parametrized by the factor  $a(Q^2)$ , which can be calculated from deuteron models, and are small at large  $Q^2$ . Once the model corrections have been applied to  $R$ , the results of previous measurements of the elastic proton scattering cross section and the neutron electric form factor can be used to extract  $G_M^n$ . The ratio method has several advantages. It is insensitive to the luminosity, electron acceptance, reconstruction efficiency and trigger efficiency. The dominant contribution to radiative corrections in elastic electron-nucleon scattering comes from additional photons which couple to the electron, so when the ratio is taken, the radiative corrections very nearly cancel. Sensitivity to the details of the deuteron wave function are also reduced by taking the ratio.

Use of the ratio model requires making an exclusive measurement of e-n scattering, and so requires an accurate measurement of the neutron detection efficiency. Accurate matching of the scattered neutron and proton acceptance is also required. The e5 running period used a dual-cell target, containing collinear deuterium and hydrogen cells. Use of the hydrogen cell allows a simultaneous *in-situ* measurement of the neutron detection efficiency. The ratio method also requires information on the other three form factors, or more precisely, the proton elastic scattering cross section and  $G_E^n$ . The proton cross section has been well measured in the past, and as only the total elastic cross section is needed for the proton, two-photon exchange issues (relevant to the extraction of the proton form factors from elastic scattering data) are not important. While the uncertainties on  $G_E^n$  are large,  $G_E^n$  is small compared to the other form factors, and its contribution to the value of the ratio diminishes as  $Q^2$  becomes larger.

# Chapter 2

## Experimental Setup

### 2.1 The CEBAF Accelerator

The experiment was conducted at the Continuous Electron Beam Accelerator Facility (CEBAF) at Thomas Jefferson National Accelerator facility (TJNAF). CEBAF is a recirculating electron-beam accelerator utilizing two superconducting linear accelerators (linacs) and two bending sections. The accelerator elements and end stations are shown in Fig 2.1.

The linacs are constructed from 338 niobium superconducting radio-frequency cavities (SRF). Eight SRF are grouped into a cryomodule, where their temperature was maintained at 2.08K by a liquid helium bath. Forty-two cryomodules were used in the two linacs, with one-quarter cryomodule used in the injector. The linacs each provide up to approximately 600 MeV of energy per pass (about 1.2 GeV for a complete circuit around the accelerator). The beam can be recirculated up to five times to deliver up to 6 GeV beam of high quality, with a resolution of less than 0.01% and beam spot size at the target of less than 0.5mm. The accelerator is capable of delivering polarized (from a DC photo-emission gun using GaAs cathodes) or unpolarized beam to the three experimental end stations. Electrons at the injector source are chopped at 499 MHz and bunched into 3 sets (each destined for a different end station). The bunches have a relative phase of  $120^\circ$  and are interleaved to form a 1497 MHz beam structure. After acceleration, a normal conducting RF separator is used to kick electron bunches to the appropriate experimental hall, resulting in beam bunch delivery to an end station every 2.0039 ns.

### 2.2 The CLAS spectrometer

#### 2.2.1 Toroidal Magnet

The magnetic field necessary for the momentum analysis of charged tracks is generated by a set of six superconducting coils placed about the beamline. The position of the coils is shown in Fig 2.2

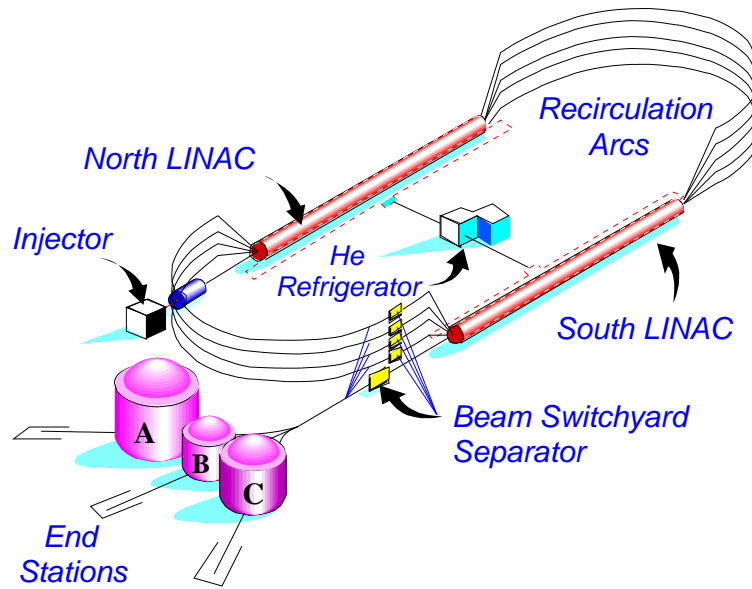


Figure 2.1: The CEBAF accelerator and experimental end stations

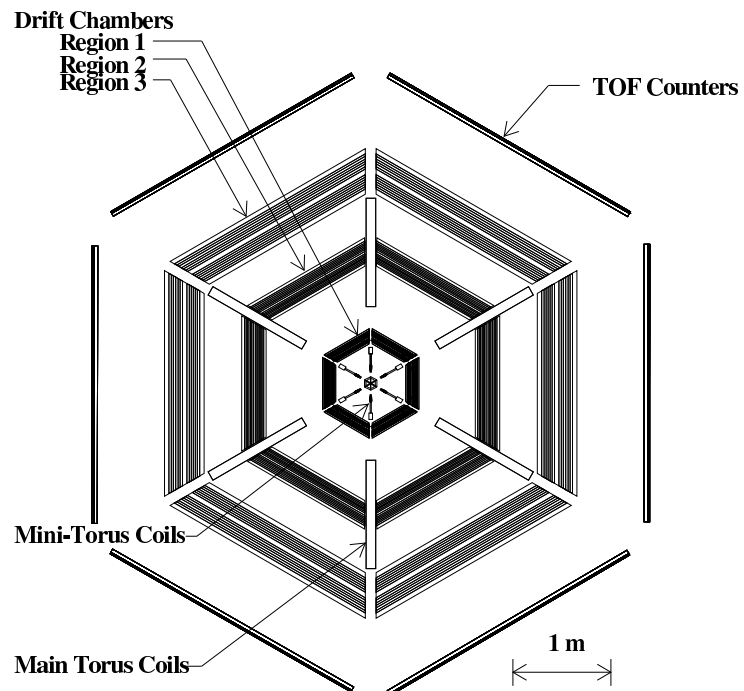


Figure 2.2: The CLAS detector, as seen from upstream, looking down the beamline. The torus coils are shown, dividing the detector into six sectors.

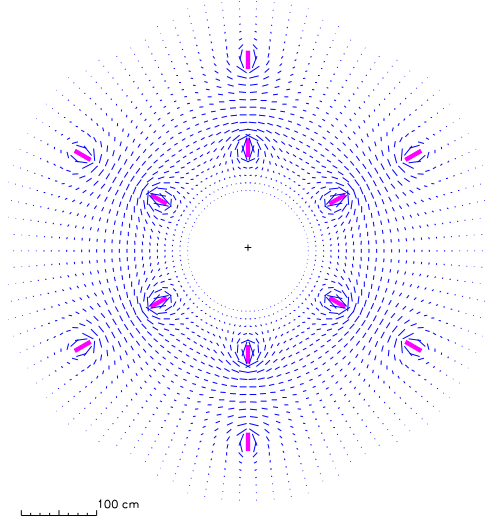


Figure 2.3: Magnetic field vectors for the CLAS magnet transverse to the beam. The length of each segment is proportional to the field strength.

The torus coils generate a toroidal magnetic field, with the field line mostly in the azimuthal direction, circling the beam line. The magnetic field vectors for a typical slice perpendicular to the beam line are shown in Fig 2.3

The torus is constructed from iron-free coils approximately 5m long and 3m tall, using an aluminum stabilized NbTi/Cu conductor enclosed in an aluminum cryostat. Cooling of the coils to 4.5 K is maintained by forcing super-critical helium through cooling tubes located on the inside of the coil windings. The kidney shape of the coils generates a field that is maximal at low polar angle, as can be seen in Fig 2.4. Thus, the field-integral for forward going (typically high momentum) particles is large. The field strength has a maximum value of 3.5T and field-integral ( $\int \vec{B} \cdot d\vec{l}$ ) of 2.5 Tm in the forward direction when operated at the maximum current. The magnet is routinely operated at a current no larger than 3375A, 87% of the design maximum to keep mechanical stresses on the coils within conservative limits.

A second toroidal magnet, the mini-torus, is used during electron runs. The mini-torus generates a weak magnetic field around the target region. The mini-torus field sweeps low-momentum Møller electrons generated by beam interaction in the target toward the beamline and away from the Region 1 drift chambers. The mini-torus, when operated at its nominal 6000A current, generates a magnetic field strength that is 1-5% of that of the main torus, so its effect on higher momentum particles is not large.

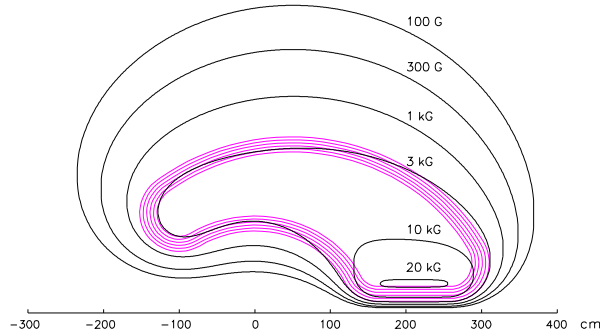


Figure 2.4: Magnetic field contours for the CLAS magnet coils at the maximum current of 3860A

## 2.2.2 Drift Chambers

Each of the six sectors of the spectrometer is equipped with 3 sets of drift chambers(DC) [33] for charged particle tracking. Measurement of the shape of the particle’s track allowed determination of the particles momentum at the scattering vertex. The three drift chamber layers, referred to as Region 1 (R1), Region 2 (R2) and Region 3 (R3), measure the track of a charged particle as it is deflected by the magnetic field. R1, the innermost and smallest section is located in the nearly field-free volume around the target. R2 is located inside the magnetic field of the main torus and is mounted on the torus cryostat. R3 is located furthest from the target, and outside the magnetic field. The placement of the three layers is shown in Fig 2.2. The drift chambers have an angular coverage of  $8^\circ$  to  $140^\circ$  in polar angle, with approximately 80% azimuthal coverage.

The drift chambers are wedge shaped bodies, supporting wires stretched between two endplates, each parallel to the adjacent coil plane. The wires were strung in an alternating pattern of two field wires and one sense wire, with the wire positions shifted by half the nominal sense-wire spacing between successive rows. This resulted in a hexagonal pattern, with six field wires surrounding each sense wire, as shown in Fig 2.5

The drift cell size increases with increasing distance from the target region, with the average sense wire/field wire spacing being 0.7 cm, 1.5 cm and 2.0 cm in R1, R2 and R3 respectively. The wire layers in each chamber are grouped into two “superlayers” of six wire layers each, one axial to the magnetic field, and one tilted at a  $6^\circ$  angle (the “stereo layer”) to provide azimuthal information. Due to space constraints, the stereo superlayer in R1 has only four layers. There is a layer of guard wires surrounding the perimeter of each superlayer to reproduce the field-configuration of an infinite array of drift cells.

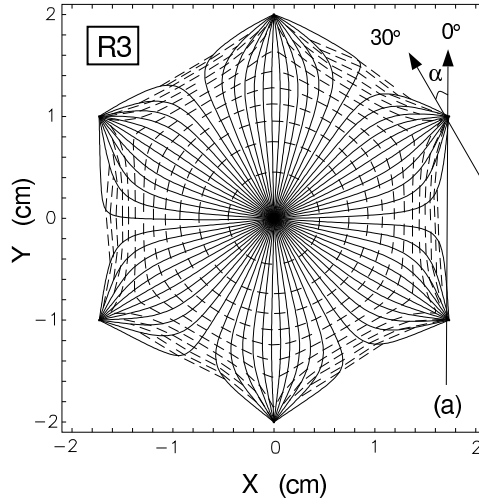


Figure 2.5: An illustration of one drift cell in Region 3. The electric field lines (solid) and isochrones (dashed) are shown.

All three DC layers are filled with a 90% Ar, 10% CO<sub>2</sub> gas mixture, which was chosen for its high saturated drift velocity (greater than  $4 \text{ cm}/\mu\text{s}$ ), high operating plateau and non-flammability. The sense wires in all three layers were  $20 \mu\text{m}$  gold-plated tungsten, and the guard and field wires were  $140 \mu\text{m}$  aluminum.

The tracking is done in two stages. First, the hits in each superlayer are grouped into segments. The found segments from different superlayers are linked to form a track. This first stage (hit-based tracking) is done using only geometrical information about the locations of the hit wires. At the hit-based stage, the momentum measurement is within 5% of the true value. In the second tracking stage (time-based tracking) the timing information from the electron interaction in the SC and the individual wires is used to convert the drift time in each cell to a drift distance. The track parameters are chosen to minimize the quadrature sum of the residuals (difference between drift distance calculated from timing information and drift distance calculated from the track geometry) over the length of the track. After time based tracking, the momentum resolution improves to 0.4%, with a tracking efficiency of greater than 95%. A plot of the r.m.s residuals as a function of distance-of-closest approach can be seen in Fig 2.7.

### 2.2.3 Time of Flight System

Each of the six sectors of the spectrometer is instrumented with a scintillator counter array (SC) [34]. The purpose of the SC system is to make time-of-flight measurements of charged particles. The time-of-flight information, when combined with the momentum measurement from the drift chamber, allows computation of the particle mass.

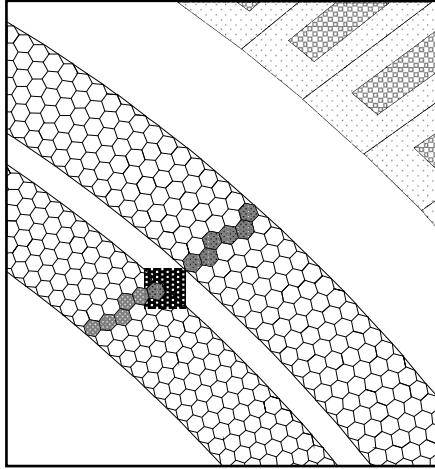


Figure 2.6: The response of the outer(stereo) and inner(axial) superlayers in R3 to the passage of a typical charged particle.

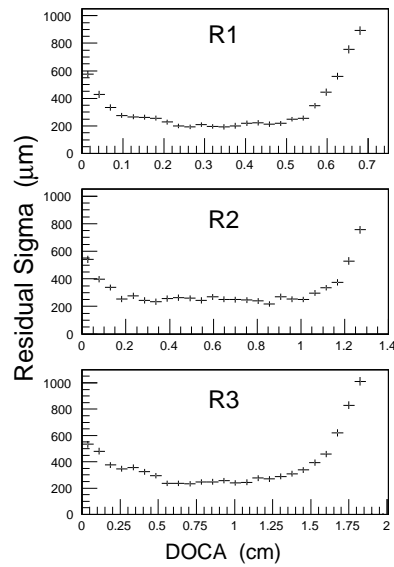


Figure 2.7: The widths of the DC r.m.s residual distributions in each superlayer vs. the distance of closest approach.

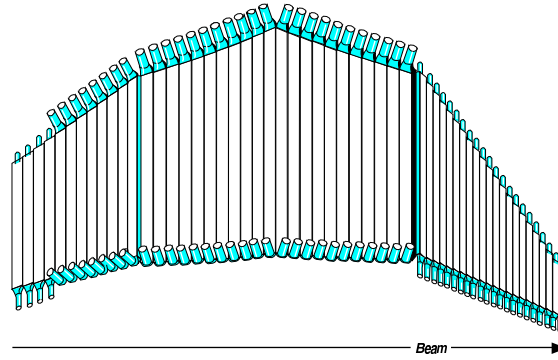


Figure 2.8: A perspective view of the scintillator counters in the Time-of-Flight system.

The SC in each sector is constructed from 57 plastic scintillator bars, grouped into 4 flat panels, as shown in Fig 2.8. The scintillator bars have a uniform 5.08 cm thickness, which produces a large signal for minimum ionizing particles. The forward counters ( $\theta < 45^\circ$ ) in panel 1 are 15 cm wide, while the large angle counters are 22 cm wide. All counters are made from Bicron BC-408 scintillator, and are read out with 2 in (panel 1) or 3 in (large angle) PMTs. The counters are coupled to the PMTs through bent light guides. The bent light guides are necessary to allow mounting the PMT tubes in the shadow of the torus cryostat. All the scintillators were read out on both ends with independent PMTs, except for the last 18 bars, which were coupled together into pairs, forming 9 counters with width of 44 cm.

The timing resolution of the scintillator bars was found to depend on the bar length. The intrinsic resolution was measured by injecting laser light into the center of the bar, and measuring the PMT response. The results are shown in Fig 2.9

In most standard CLAS analysis, the time-of-flight system is used only for charged particles, to make a measurement of particle mass when the timing information is combined with the momentum measurement from the drift chambers. For the  $e5$  analysis, the time-of-flight system will also be used for neutron detection.

## 2.2.4 Cherenkov Counters

Each sector of the spectrometer is instrumented with a threshold Cherenkov Counter (CC) in the forward region ( $\theta < 45^\circ$ ) [35]. The Cherenkov counters are used for electron pion separation. The CC in each sector consists of 36 optical modules, as shown in Fig 2.11.

The 36 optical modules are divided into 18 pairs by the sector midplane. Each of the half-modules is constructed of 3 mirrors, one elliptical, one hyperbolic and one cylindrical. The mirrors are used to focus the Cherenkov light into the light-collecting Winston cone attached to a PMT. The mirror optics were designed to focus only in the azimuthal direction, so that information on the electron polar angle is preserved.

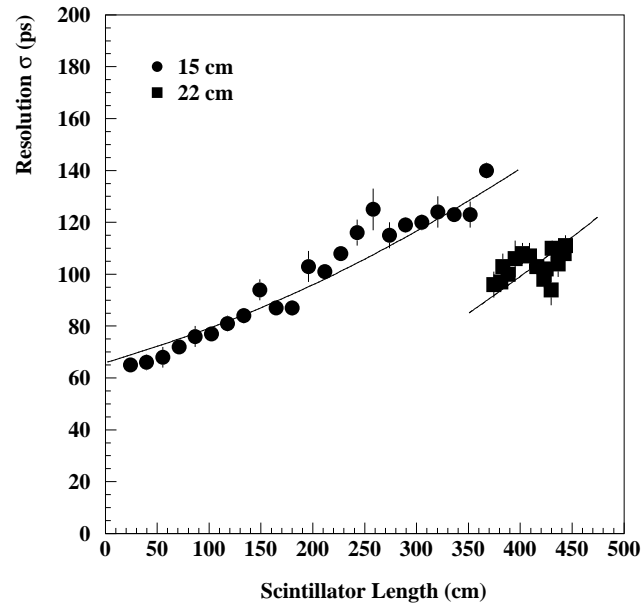


Figure 2.9: The timing resolution of the time-of-flight scintillators versus scintillator length

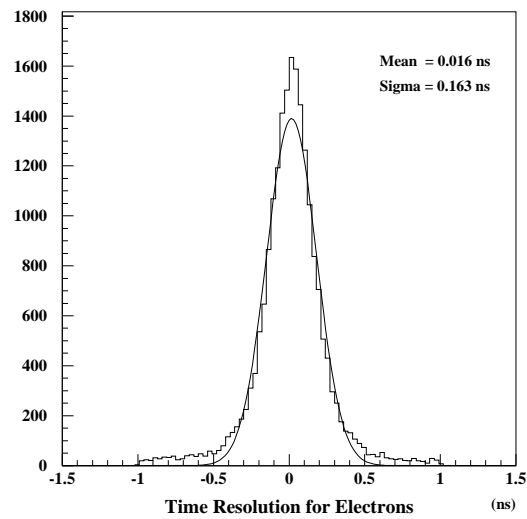


Figure 2.10: The SC timing resolution for electrons

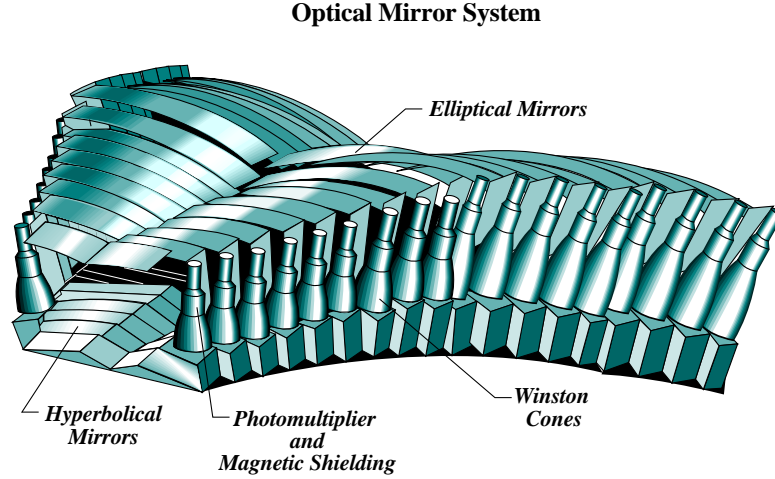


Figure 2.11: An illustration of the 36 modules of the CC in one sector

The mirror support is constructed from a layered Kevlar and vinyl foam structure. The mirror surfaces are Lexan sheets coated with vacuum deposited Al, with a layer of  $MgF_2$  added to inhibit oxidation. A ray tracing of an example light path in the CC module is shown in Fig 2.12

The PMTs are all mounted in the region blocked by the torus coils to minimize the material volume in the path of particles emerging from the target, and are fitted with high-permeability magnetic shields to protect against fringe fields from the torus coils. The gas used in the CC is perfluorobutane ( $C_4F_{10}$ ), which has an index of refraction of 1.00153. This corresponds to a threshold velocity of  $0.99847c$ . This threshold will separate electrons from pions for momenta less than  $2.5 \text{ GeV}/c$ .

### 2.2.5 Forward Electromagnetic Calorimeter

The forward region ( $8^\circ < \theta < 45^\circ$ ) of each sector is instrumented with an electromagnetic sampling calorimeter (EC) [36]. The uses of the EC of interest for this analysis are detection of and triggering on electrons and detection of neutrons (and separation of neutron from photons). The EC is constructed from alternating layers of scintillator strips and lead sheets, with a total thickness of 39 cm of scintillator and 8.4 cm of lead, for a total thickness of 16 radiation lengths. The lead sheets account for 90% of the 16 radiation length thickness.

In each module, the scintillator/lead layers are contained in a volume having the shape of a nearly equilateral triangle. Each module contains 39 layers consisting of 10 mm thick scintillator and 2.2 mm of lead. The module is designed using a projective geometry, pointed at the nominal target position, such that the solid angle subtended by successive layers is approximately constant. The  $\phi$  coverage ranges from 50% at forward angles to approximately 90% at large angles. Each layer consists of 36 scintillator strips oriented parallel to one side of the triangle, with the strip orientation

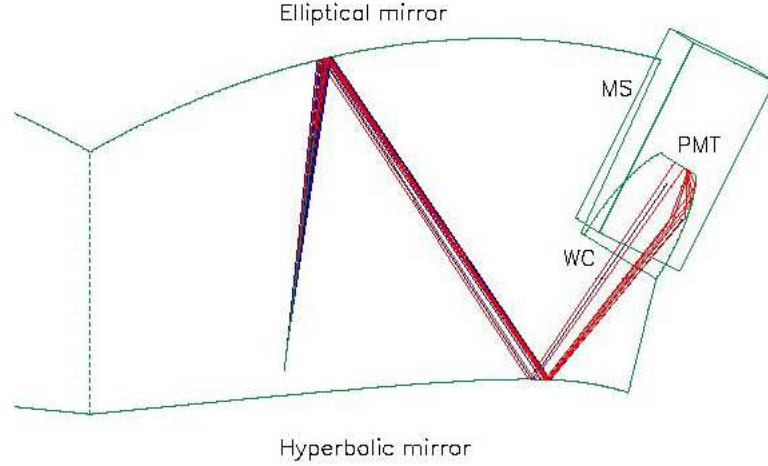


Figure 2.12: Schematic diagram of light path in CC module

being rotated by  $120^\circ$  in each successive layer. The module construction is illustrated in Fig 2.13

The three orientations (or *views*) of scintillator strips are labeled *u*, *v* and *w*. Each view contains 13 layers, which are subdivided into *inner* (5 layers) and *outer* (8 layers) stacks that provide longitudinal sampling. Each of the view/stack combinations are optically ganged and coupled to XP2262 PMTs via fiber optic cables. The optical readout of the EC is illustrated in Fig 2.14. The 1296 PMT channels are read out by FASTBUS crates containing LeCroy 1881M ADC and LeCroy 1872A TDC boards. Leading edge discriminators are used to provide timing signals to the TDC.

To reconstruct a hit in the EC, energy deposition is required in all 3 views of either the inner or outer layers of the module. Adjacent strips are placed into groups in each view if their energy deposit are above a software threshold. After grouping, the centroid and RMS for each group are computed. The intersection points of scintillator groups in different views are found. Intersections which contain groups from all 3 views correspond to hits. The energy deposit and time of the hit are calculated taking into account the path lengths from the hit location to the readout edge (to correct for signal propagation time and attenuation). If one group is involved in more than one hit, its energy is divided between hits with an appropriate weighting. A view of the EC showing reconstructed hits is shown in Fig 2.15

The energy resolution of the forward calorimeter for electrons can be parametrized by:

$$\frac{\sigma}{E} = \frac{10.3\%}{\sqrt{E(\text{GeV})}} \quad (2.1)$$

The average position resolution for electron showers is 2.3 cm (for showers with more than 0.5 GeV of energy deposited in the scintillator). The electron timing resolution averages 200 ps.

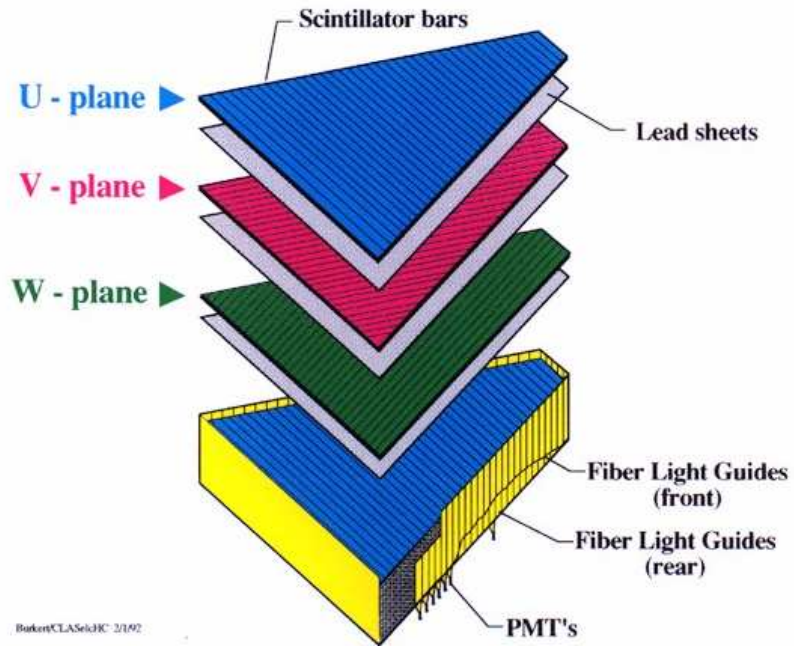


Figure 2.13: Exploded view of one of the EC modules

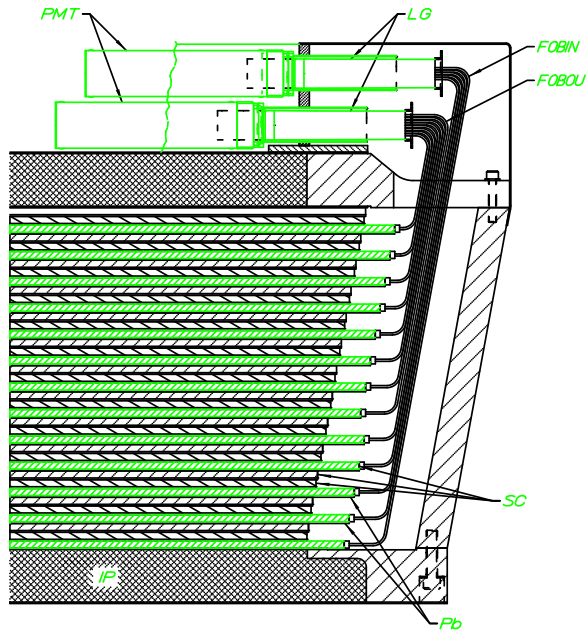


Figure 2.14: Side view of EC module, showing optical connections

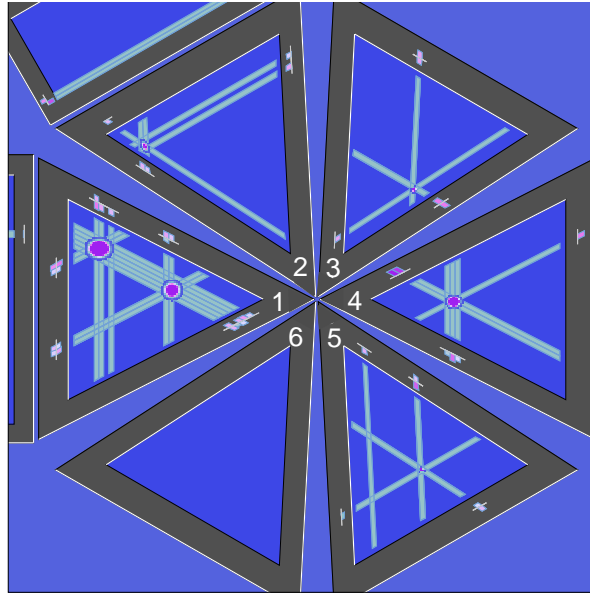


Figure 2.15: Event reconstruction in the EC. In sector 2,3,4,5 a single hit is found, while in sector 1, multiple hits are reconstructed.

### 2.2.6 E5 Target

The e5 running period utilized a novel dual-cell target design, shown in Fig 2.16. The target cells were 6 cm long, with a 3 cm gap between cells. The downstream cell was filled with liquid hydrogen (used for calibration reactions) and centered at the nominal CLAS target position. The upstream cell was filled deuterium for the ratio measurement. The target was constructed from aluminum, with 20 micron aluminum entrance/exit windows. The cooling lines and support structures were attached at the upstream end of the target to minimize the material in the path of scattered particles. A plot of electron vertex position along the beamline, showing the separation of the two target cells is shown in Fig 2.17

### 2.2.7 Trigger and Data Acquisition

The CLAS trigger system uses a hierarchical two-level system, controlled by custom Trigger Supervisor electronics. The first trigger level, Level 1, provides a fast signal based on selected PMT-based detector components such as the Cherenkov or forward calorimeter. The second level, Level 2, uses a rudimentary track-finding algorithm to identify events with charged tracks in the drift chamber. For the e5 running period, only the Level 1 trigger information was used in triggering. The Level 2 trigger was operated in “Late Fail” mode, where the verdict of the Level 2 track finding algorithm was written into the data stream, but was not used to make trigger decisions.

The Level 1 trigger used pipelined memory lookup units (MLUs) to make a fast,

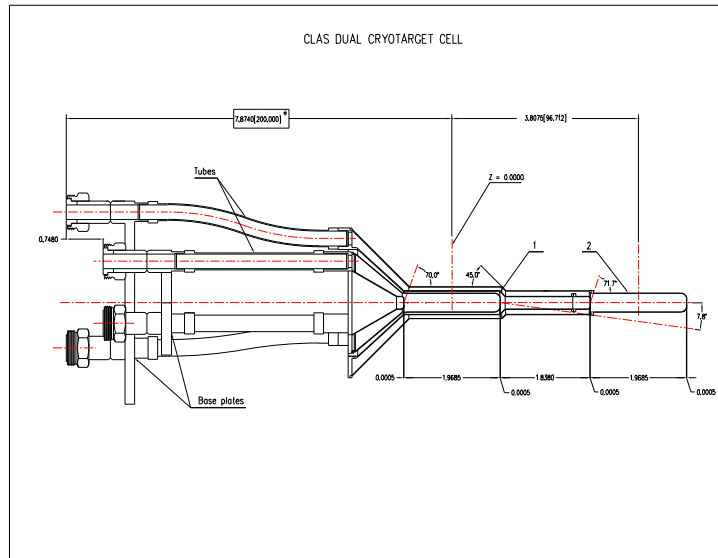


Figure 2.16: An engineering drawing of the E5 dual-cell cryotarget

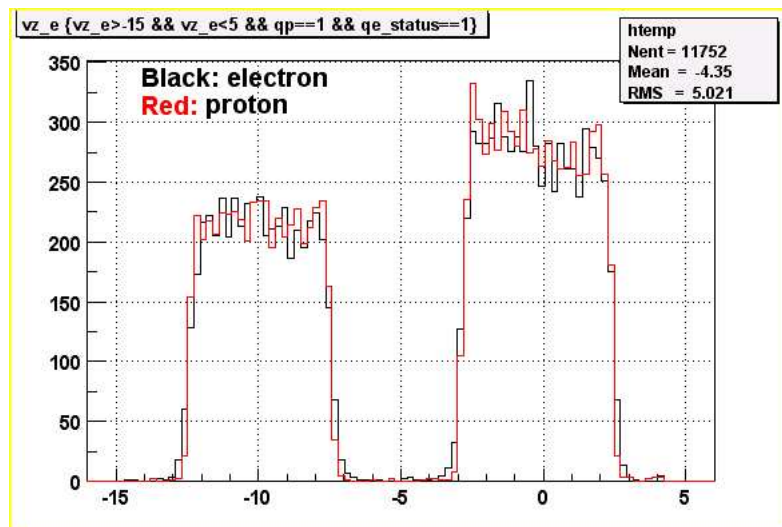


Figure 2.17: Position of the electron and proton vertex along the beamline for the e5 target for ep events.

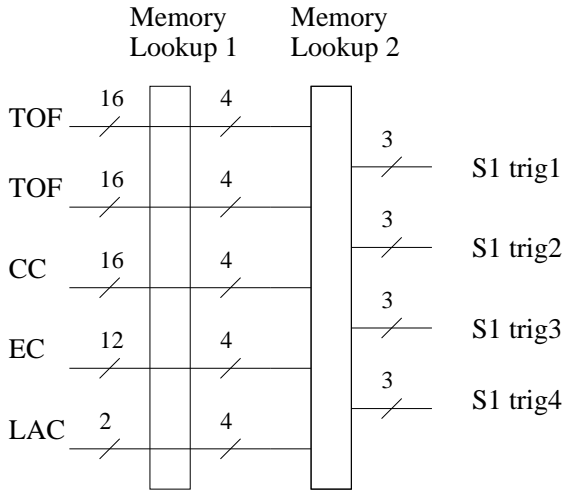


Figure 2.18: Schematic diagram of the first stage of the Level 1 trigger, where 4 trigger blocks are formed from the PMT information in a single sector.

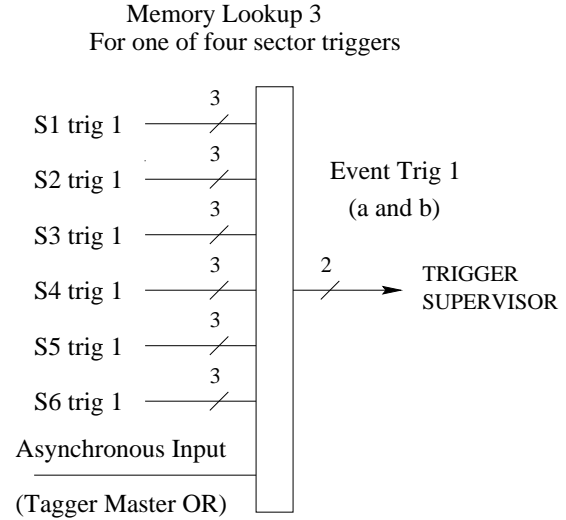


Figure 2.19: Schematic diagram of the second stage of the Level 1 trigger, where information from a single trigger block across six sectors is combined with an asynchronous input to produce an event trigger, which is input to the Trigger Supervisor.

deadtimeless trigger from fast PMT signals. The MLU configuration could be programmed to define a trigger from combinations of signals from the CC, EC and TOF. For each sector, up to 4 trigger results could be generated in response to a coincidence of inputs. The trigger outputs from each of the 6 sectors were used as input to another MLU which could be used to correlate information across all sectors, to search for a loosely specified event topology. A total of eight trigger signals were passed from Level 1 to the Trigger Supervisor. The Level 1 trigger processing time, including delays, was around 90 ns.

The Trigger Supervisor accepted 12 inputs, 8 from the Level 1 trigger, and the rest from various calibration and monitoring sources. A prescaling option was available for the Level 1 inputs, so that detector calibration or monitoring data could be taken concurrently with the physics data. After receiving a trigger from Level 1, the Supervisor sent out a common-start signal to the PMT TDCs, an integrating gate signal to the PMT ADCs and (with added delay) the common-stop signal to the drift chamber TDCs. If the Level 2 trigger were used, the Trigger Supervisor would wait  $3.2 \mu\text{s}$  after receiving a Level 1 to receive a confirmation signal from Level 2. If Level 2 failed, a fast-clear signal would be sent to the electronics, otherwise the usual output signals would be sent.

For the e5 running period, the trigger was configured to select events with electron-like signals. The trigger configuration is listed in Table 2.1. The trigger required hits

Table 2.1: Settings for physics trigger for e5 run period. The Level 1 trigger required a coincidence between EC and CC in a single sector of the form  $CC + EC_{inner} + EC_{total}$ . The Level 2 trigger was used in “Late Fail” mode.

Beam Energy (GeV)	Torus (A)	Level 1 Configuration (mV)				Level 2
		CC	$EC_{inner}$	$EC_{outer}$	$EC_{total}$	
4.232	3375	20	60	99	148	Off
2.558	2250	20	32	96	99	On
2.558	-2250	20	32	96	98	Off

in the forward calorimeter and the Cherenkov in the same sector.

After receiving a signal from the Trigger Supervisor, the Read-Out Controllers (ROCs) were instructed to collect the information for the event. The ROCs read out the information from one crate of electronics each, and the event fragments are sent to the Event Builder. The Event Builder collected the fragments, assembled them into complete events and passed the complete events to the Event Transport (ET) process. The ET served events to a set of clients including various data monitoring processes and online event reconstruction (of a subset of the data). The Event Recorder (ER) collected events off the ET and transferred them to a RAID, from which they were eventually moved to tape for long term storage. A schematic diagram of the data flow for CLAS is shown in Fig. 2.20.

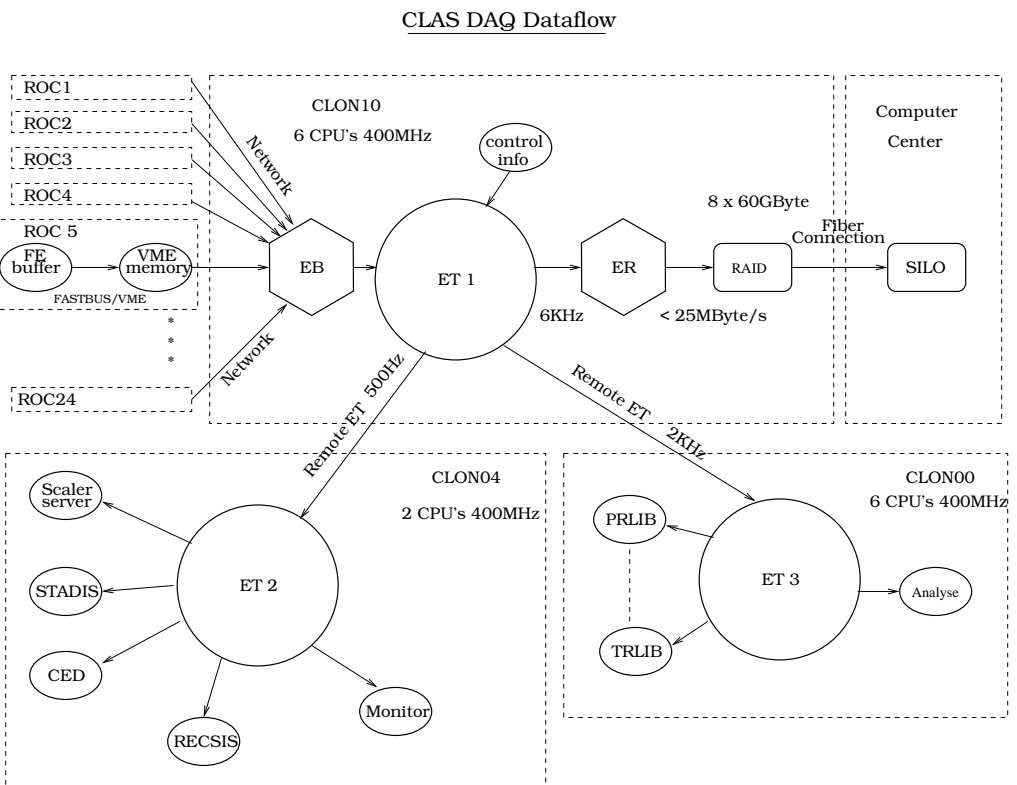


Figure 2.20: A schematic of the CLAS data flow, showing the movement of data from the detectors' Read-Out Controllers, through the Event Builder and into the SILO tape server.

# Chapter 3

## Experiment Analysis

### 3.1 Event Reconstruction

The analysis of the e5 data was performed with a modified version of the CLAS reconstruction software, derived from the “release-4-3” code. The detectors were calibrated (EC timing and energy, SC timing and energy, DC drift time to drift distance conversion) using the standard packages. A set of special “road files” generated for the e5 target and magnetic field configurations was used as an input template to the RECSIS event reconstruction code. RECSIS returned particle charge, momentum, and position values for charged particles in the drift chamber. Details of the tracking code can be found in [37]. Information from other detector packages, such as hit locations and times in the EC and SC, were matched to the DC tracks by the SEB package. The SEB package was modified to write summary information to a MySQL database after processing each file. The reconstructed events were written to BOS files, along with some of the raw event information, to the JLab tape silo.

### 3.2 Run Selection

Files were selected for analysis by examining two quantities recorded in the cooking database, the ratio of protons to electrons originating in the hydrogen target cell, and the ratio of time-based tracks to hit based tracks. The cuts were selected to remove files in which either of these quantities differed too much from the average. Files selected for analysis were required to satisfy:

$$0.9 < \frac{N_p}{N_e} < 1.2 \quad E_{beam} = 4.2 GeV \quad (3.1)$$

$$0.85 < \frac{N_p}{N_e} < 1.0 \quad E_{beam} = 2.5 GeV \quad (3.2)$$

where  $N_p$  is the number of protons and  $N_e$  is the number of electrons.

These cuts are illustrated in Fig. 3.1 and Fig. 3.2.

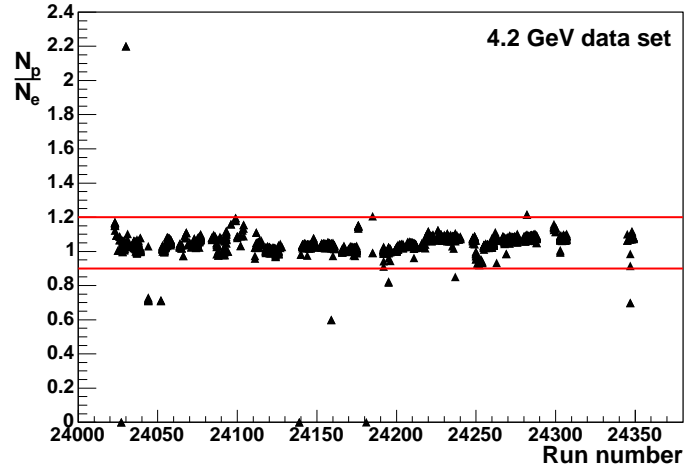


Figure 3.1: The ratio of the number of protons to the number of electrons for events originating in the hydrogen target versus run number. The data are from the 4.2 GeV beam energy data set. The cuts applied are shown in red.

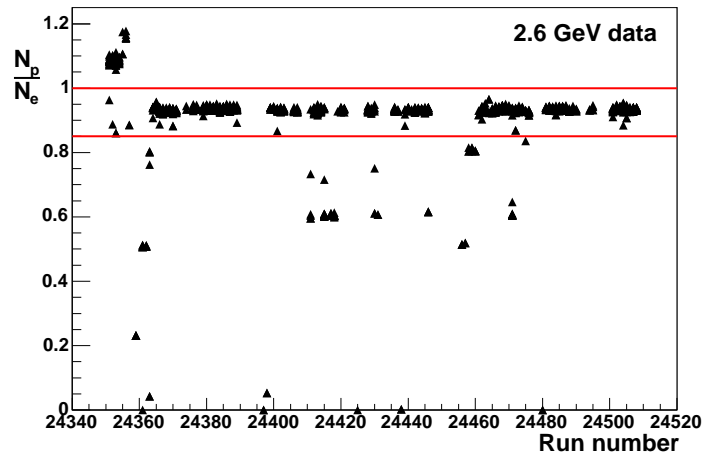


Figure 3.2: The ratio of the number of protons to the number of electrons for events originating in the hydrogen target versus run number. The data are from the 2.5 GeV beam energy data set. The cuts applied are shown in red.

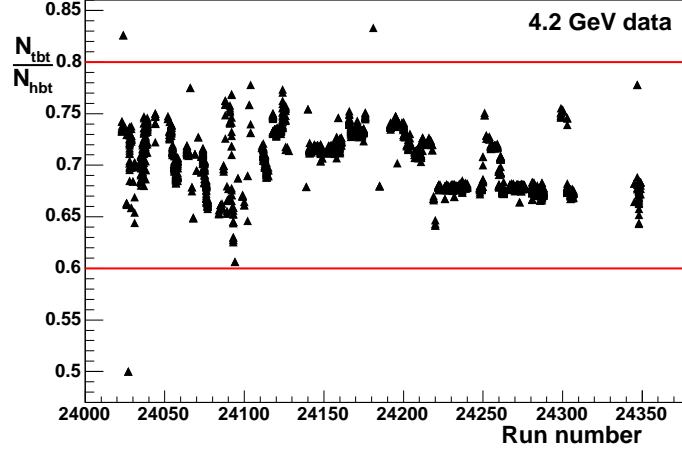


Figure 3.3: The ratio of the number of time-based tracks to the number of hit-based tracks versus run number. The data are from the 4.2 GeV beam energy data set. The cuts applied are shown in red.

Files selected for analysis were also required to satisfy:

$$0.6 < \frac{N_{tbt}}{N_{hbt}} < 0.8 \quad E_{beam} = 4.2 GeV \quad (3.3)$$

$$0.75 < \frac{N_{tbt}}{N_{hbt}} < 0.85 \quad E_{beam} = 2.5 GeV \quad (3.4)$$

where  $N_{tbt}$  is the number of time-based tracks, and  $N_{hbt}$  is the number of hit-based tracks. These cuts are illustrated in Fig. 3.3 and Fig. 3.4.

### 3.3 Neutron Detection Efficiency Measurement

The hydrogen cell of the e5 target allows for an *in-situ* measurement of the neutron detection efficiency of the EC and SC detector systems. The reaction  $ep \rightarrow e\pi^+(n)$  on protons in the hydrogen cell is used as a source of tagged neutrons. Candidate events are selected which have one negative track and one positive track.

#### 3.3.1 Electron Identification

Events with well identified electrons were selected according to the following criteria:

1. Vertex Cut

The z-component of the electron vertex position determined by tracking must satisfy  $-3.0 < v_z < 3.0$  cm. This cut ensures that the electron originated in the hydrogen cell of the target, and removes some of the contamination from events in the target entrance/exit windows.

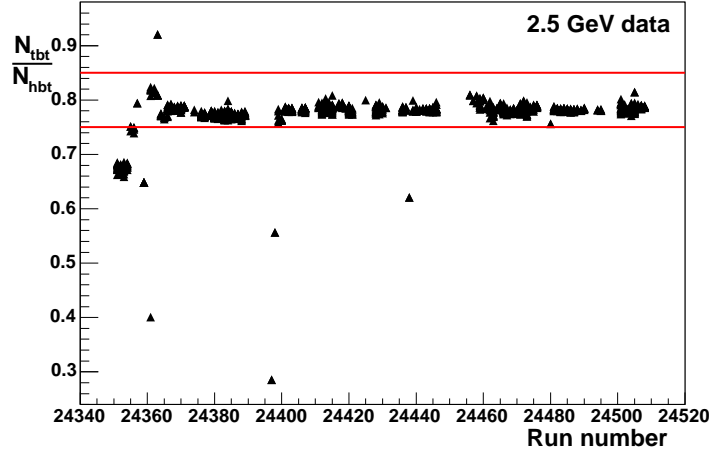


Figure 3.4: The ratio of the number of time-based tracks to the number of hit-based tracks versus run number. The data are from the 2.5 GeV beam energy data set. The cuts applied are shown in red.

## 2. EC fiducial cut

The location of the electron hit on the EC face plane must be at least 10 cm away from any of the three edges of the EC. This cut removes events in which energy from the electron shower leaks out the sides of the calorimeter (95% of the shower is concentrated within 4 cm transverse to the incident track [36]).

## 3. EC minimum energy deposit

The energy deposited in the inner layer of the EC is required to satisfy  $EC_{inner} > 50$  MeV. This cut rejects minimum ionizing particles (MIP) by requiring an energy deposit larger than a MIP would make in traversing the inner layer.

## 4. EC energy/momentum match

The sampling fraction of the EC has been parametrized in terms of the incident electron momentum:

$$f(p) = \frac{0.23p + 0.071p^2 - 0.032p^3}{p} \quad p < 1.0 \text{ GeV}/c \quad (3.5)$$

$$(3.6)$$

$$f(p) = 0.272 \quad p > 1.0 \text{ GeV}/c \quad (3.7)$$

The electron energy determined from the track momentum measured in the DC and the energy deposited in the EC must satisfy the relation:

$$-0.2 < E - \frac{E_{dep}}{f(p)} < 0.15 \text{ GeV}/c \quad (3.8)$$

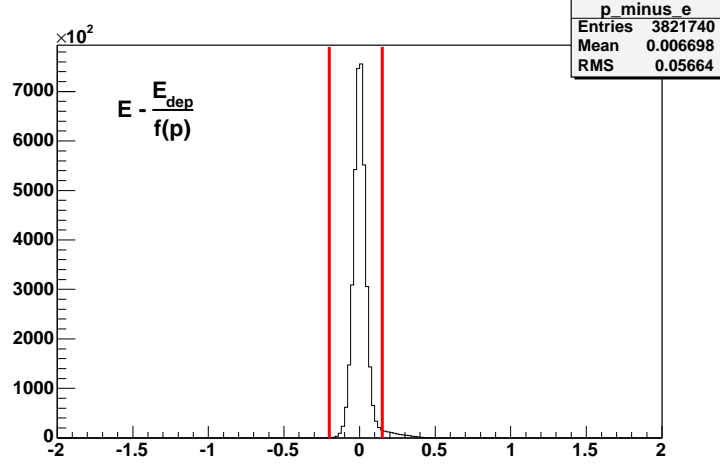


Figure 3.5: The difference between electron energy determined from tracking and sampling-fraction corrected energy deposited in EC. The cut values are shown in red. The data is a sample of the 2.5 GeV data set.

This cut is illustrated for a sample of the 2.5 GeV data set in Fig 3.5.

#### 5. CC hit and photo-electron cut

A hit in the CC, correlated with the DC track, was required, with a minimum of 1.0 for the estimated number of photo-electrons produced, based on the ADC response. This cut is illustrated in Fig 3.6.

### 3.3.2 $\pi^+$ Identification

Positive tracks were identified as  $\pi^+$  by comparing the particle velocity measured from a combination of tracking and time-of-flight information to the velocity expected for a  $\pi^+$  of the measured momentum.

The particle velocity was determined from:

$$\beta_{track} = \frac{l_{\pi}}{c\Delta t} \quad (3.9)$$

where  $l_{\pi}$  is the track length of the  $\pi^+$  candidate measured by the DC, and

$$\Delta t = t_{\pi} - t_0 \quad (3.10)$$

where  $t_{\pi}$  is the time reported by the SC for the particle, and  $t_0$  is the event start time, found from:

$$t_0 = t_{electron} - \frac{l_{electron}}{c}. \quad (3.11)$$

where  $t_{electron}$  is the electron time reported by the SC and  $l_{electron}$  is the electron track length (from the vertex to the SC plane) determined from tracking.

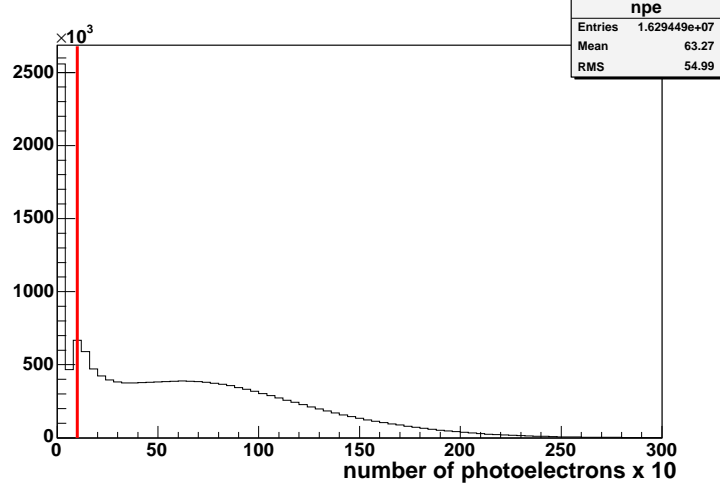


Figure 3.6: The horizontal axis shows 10 times the estimated number of photoelectrons produced in the CC. The cut is shown in red. The data is a sample of the 2.5 GeV data set.

The particle velocity can also be determined from its measured momentum and an assumption regarding its species:

$$\beta_{\pi} = \frac{|\vec{p}|}{\sqrt{|\vec{p}|^2 + M_{\pi}^2}} \quad (3.12)$$

A cut was placed on the difference of these two  $\beta$  values, which required:

$$-0.04 < \Delta\beta < 0.04. \quad (3.13)$$

This cut is illustrated in Fig 3.7.

A CC veto was applied, rejecting any  $\pi^+$  candidate track that had an associated hit in the Cerenkov detector.

### 3.3.3 Neutron selection

Once the event had been identified as having a good electron and  $\pi^+$ , the missing mass in the event was calculated. The 4-momentum of the initial state particles was known:

$$e_{in} = E_0(1, 0, 0, 1) \quad (3.14)$$

$$P = (M_p, 0, 0, 0) \quad (3.15)$$

where  $e_{in}$  is the incoming electron 4-momentum ( $E_0$  is the incident beam energy), and  $P$  is the 4-momentum of the target proton. The final-state was assumed to be composed of an electron,  $\pi^+$  and neutron. The electron and  $\pi^+$  4-momenta were known

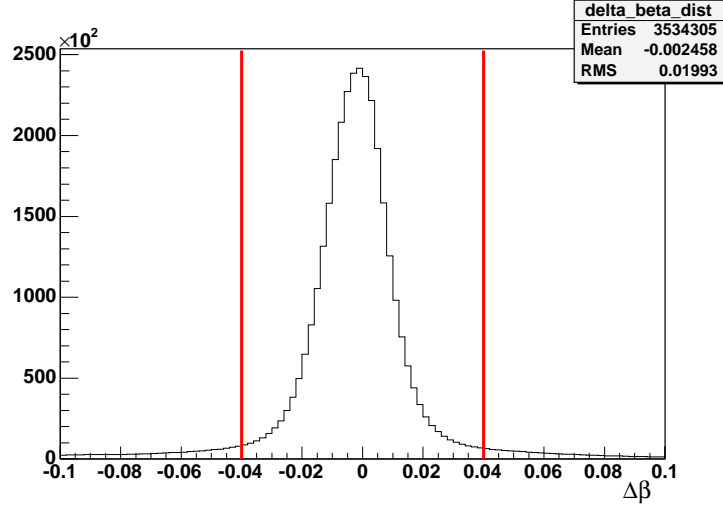


Figure 3.7: The distribution of the difference between  $\beta$  determined from path length and time-of-flight and  $\beta$  determined from the measured momentum and the assumption that the particle is a  $\pi^+$ . The cuts are shown in red. The data is from the 2.5 GeV data set.

from tracking, so the neutron 4-momentum could be determined from conservation of 4-momentum:

$$X_n = e_{in} + P - e_{out} - \pi_{out} \quad (3.16)$$

where  $X_n$  is the neutron 4-momentum and  $e_{out}, \pi_{out}$  are the momentum of the scattered electron and pion. The missing mass was found from:

$$MM = \sqrt{X^2} \quad (3.17)$$

The missing mass for each event was required to satisfy:

$$0.9 < MM < 0.95 \text{ GeV}/c^2 \quad (3.18)$$

The missing mass cut is illustrated in Fig 3.8.

### 3.3.4 Efficiency Measurement in the Forward Calorimeter

#### 3.3.4.1 Neutron selection and sector-wise efficiency measurement

The direction of the neutron in the  $ep \rightarrow e\pi^+(n)$  reaction was determined from Eqn 3.16. A ray was drawn from the electron- $\pi^+$  vertex position to a plane parallel to the EC face. If the point-of-intersection lay outside the triangle defined by the EC face, the event was dropped. An additional fiducial cut required that the point-of-intersection lie more than 60 cm from any EC edge was enforced. In the cases where the reconstructed neutron was expected to intersect the fiducial region of one

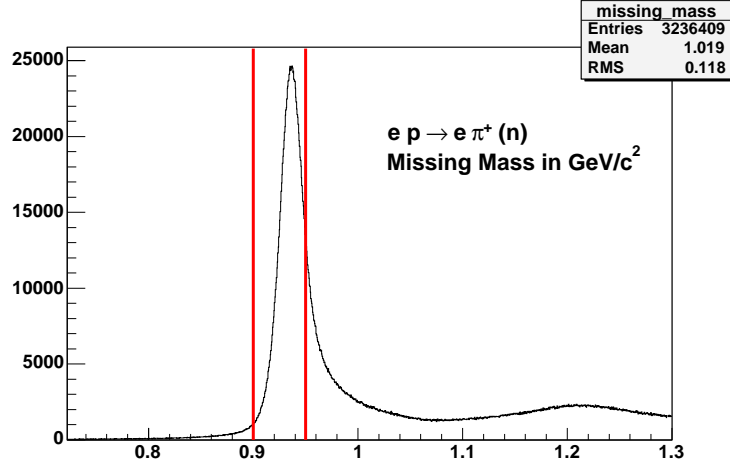


Figure 3.8: Missing mass in the  $ep \rightarrow e\pi^+(n)$  reaction. The neutron selection cut is shown in red. The data is from the 2.5 GeV data set.

of the EC modules, the EC module was searched for neutral hits (hits which have no associated charged tracks) in the vicinity of the expected point-of-intersection. A was applied cut rejecting neutral hits found more than 30 cm (as measured in the EC plane) from the expected point-of-intersection. This cut is illustrated in Fig 3.9.

In the case where a neutral hit was found which satisfied the  $\Delta R$  cut, an additional cut required at least 15 MeV of energy deposited in the calorimeter.

An event in which a good electron and  $\pi^+$  were found, and for which the expected point-of-intersection was within the EC fiducial region was labeled a *reconstructed* event. A reconstructed event which contained a neutron hit which satisfied the  $\Delta R$  cut and the minimum energy deposited cut was labeled a *found* event. The events were binned in neutron momentum and the detection efficiency in each momentum bin was calculated as:

$$\eta_i = \frac{f_i}{r_i} \quad (3.19)$$

where  $\eta_i$  is the efficiency in the  $i^{\text{th}}$  momentum bin, and  $f_i$  and  $r_i$  are the number of found and reconstructed neutron events in the  $i^{\text{th}}$  momentum bin, respectively. The distribution of accepted neutrons in each momentum bin follows a binomial distribution (in each trial, the neutron is either found or not found), with the probability of success being the efficiency at that momentum. The variance on  $r$  for the binomial distribution is given by:

$$V = \left( \frac{r}{r-1} \right) r \left( \frac{f}{r} \right) \left( 1 - \frac{f}{r} \right) \quad (3.20)$$

where  $r$  is the number of trials (the number of reconstructed neutrons) and  $f$  is the number of successes (the number of found neutrons). The estimate for the efficiency

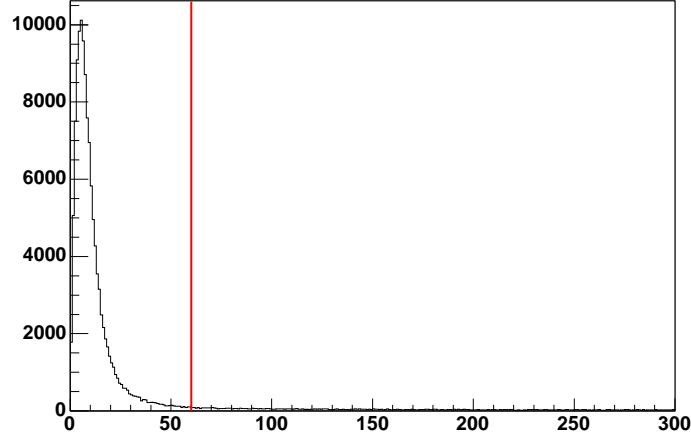


Figure 3.9: The distribution of the distance  $\Delta R$  between the expected point-of-intersection and the observed hit location for neutron candidate events in the EC. The cut applied is shown in red. The data is a sample from the 2.5 GeV dataset.

is  $\frac{f}{r}$ , so the estimate on the error on the efficiency in the  $i^{\text{th}}$  bin is given by:

$$\sigma_i = \sqrt{\left(\frac{f_i}{r_i}\right) \frac{1 - \frac{f_i}{r_i}}{r_i - 1}} \quad (3.21)$$

Fig 3.10 and Fig 3.11 show plots of the neutron detection efficiency in each of the six EC modules, for the 2.5 GeV and 4.2 GeV data sets. Fig 3.12 shows a comparison of the neutron detection efficiency integrated over all six EC modules measured in each data set.

### 3.3.4.2 Efficiency parameterization in the EC

The neutron detection efficiency in each sector was parameterized as a function of the neutron momentum with polynomials of the form:

$$\eta(p) = a_0 + a_1p + a_2p^2 + a_3p^3 \quad (3.22)$$

for  $p < p_t$ , and:

$$\eta(p) = f \quad (3.23)$$

for  $p \geq p_t$ .  $p_t$  was a parameter of the fit, and the parameter  $f$  was determined by requiring that  $\eta(p)$  be continuous at  $p = p_t$ . The fit parameters were obtained using a maximum likelihood method. The following terms will be used in the description of the fitting procedure:

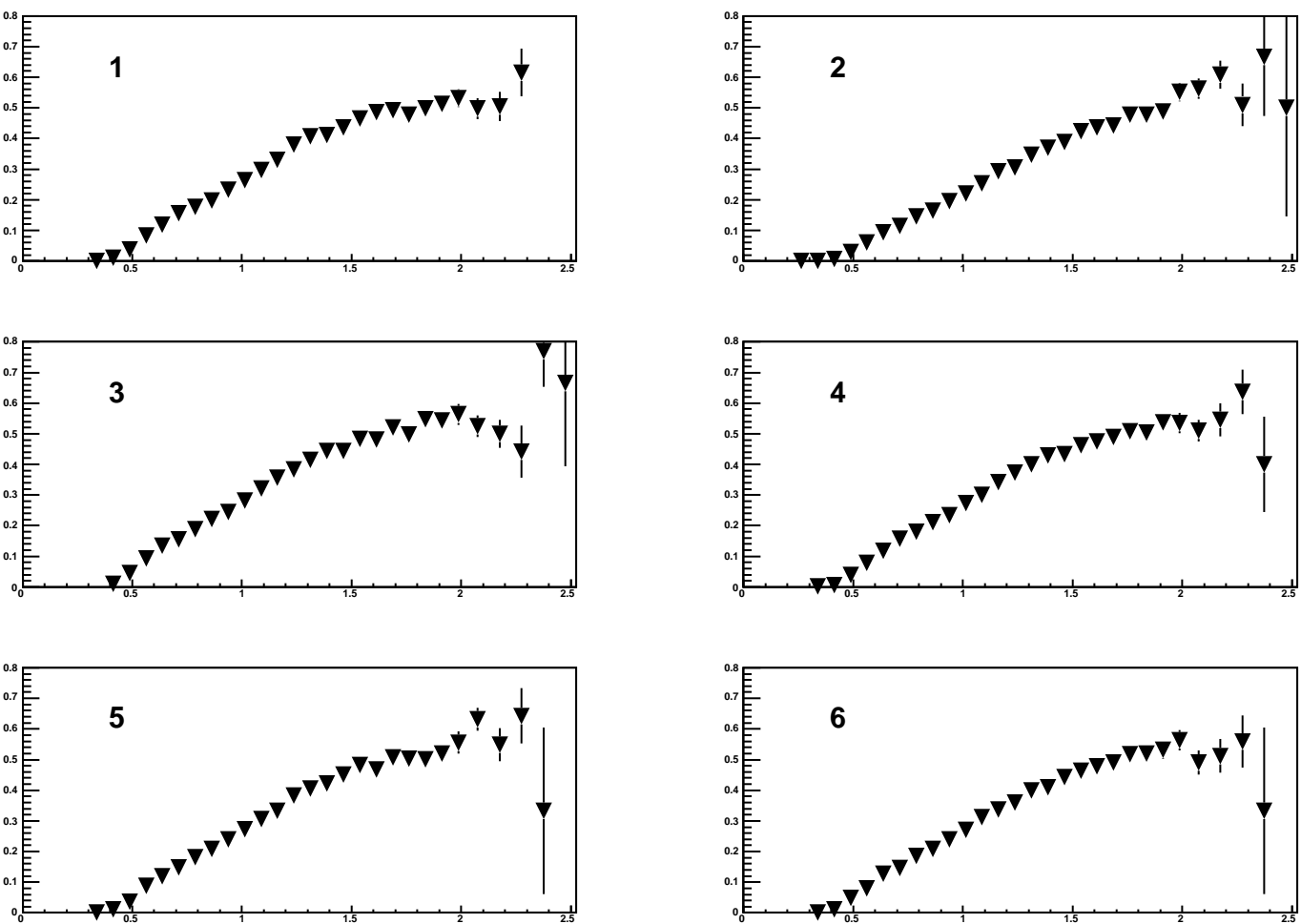


Figure 3.10: EC Neutron detection efficiency, binned in neutron momentum, for each sector in the 2.5 GeV dataset. The sectors numbers are indicated in each panel. The horizontal axis in each panel is the neutron momentum in GeV/c.

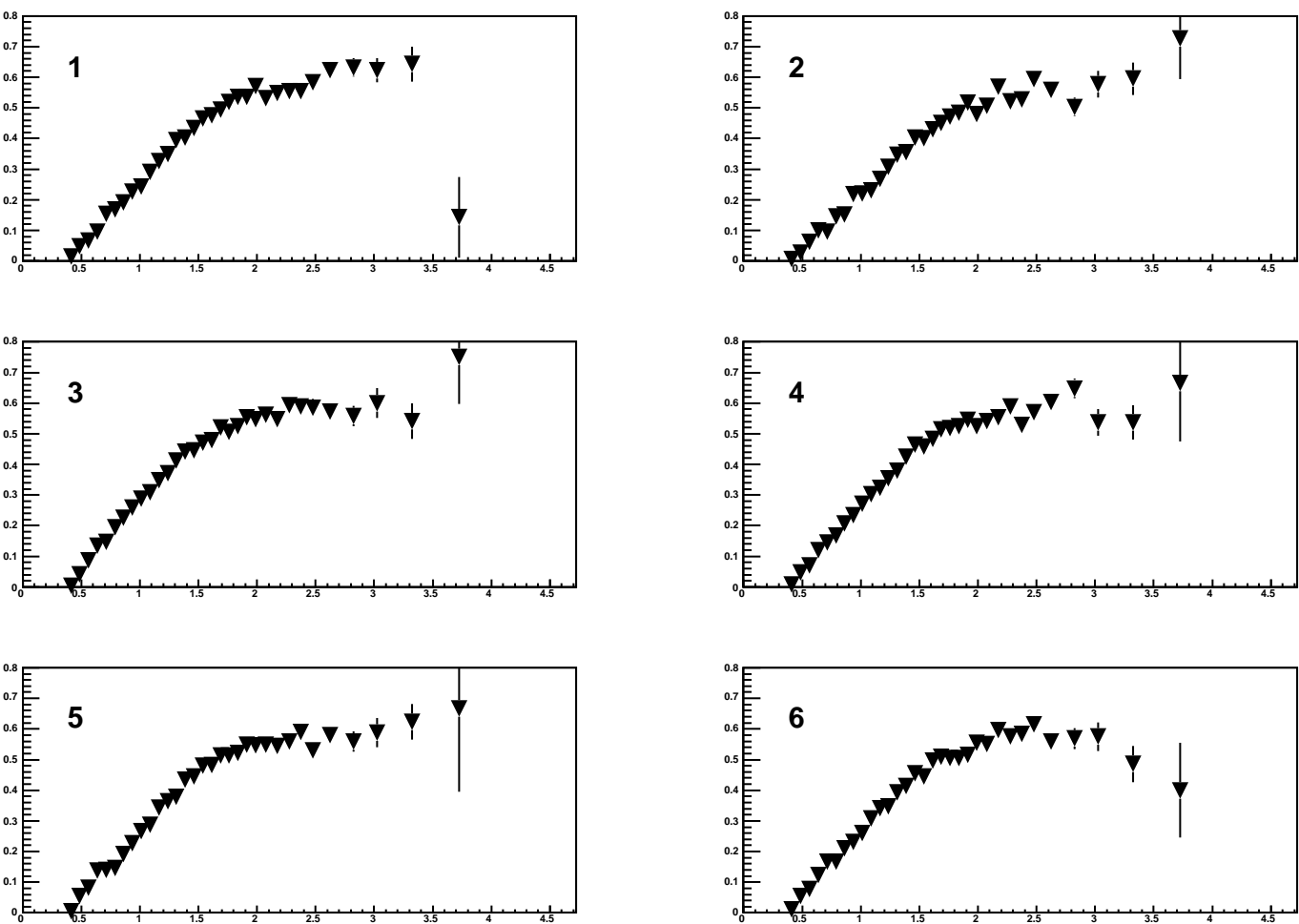


Figure 3.11: EC Neutron detection efficiency, binned in neutron momentum, for each sector in the 4.2 GeV dataset. The sectors numbers are indicated in each panel. The horizontal axis in each panel is the neutron momentum in GeV/c.

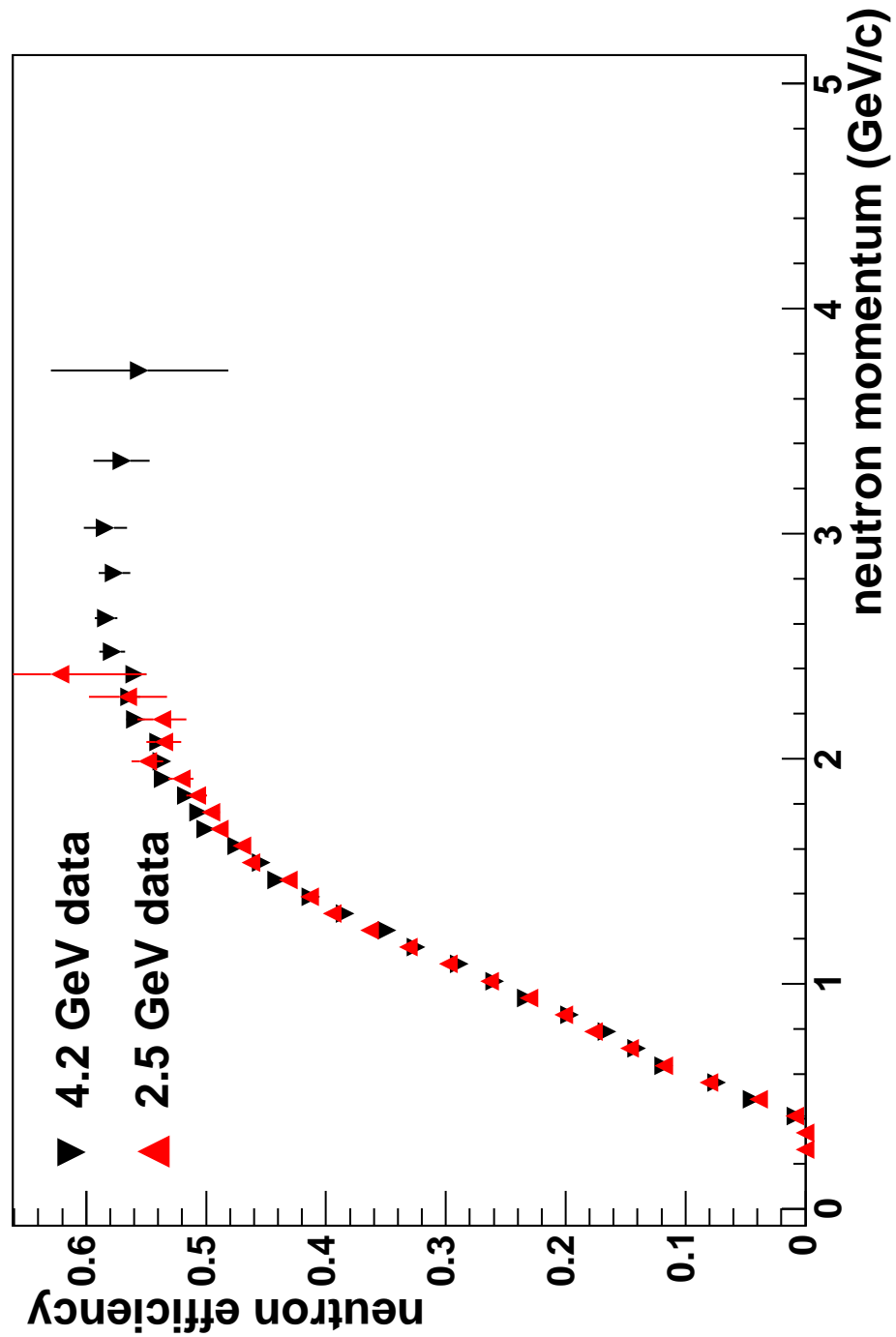


Figure 3.12: A comparison of the neutron detection efficiency in the EC, as measured at two different beam energies. In this figure, the efficiency has been integrated over all six sectors

$r_i$  = number of entries in  $i^{th}$  momentum bin of the reconstructed neutron histogram  
 $f_i$  = number of entries in  $i^{th}$  momentum bin of the found neutron histogram  
 $\eta_i$  = efficiency in  $i^{th}$  momentum bin, defined above.

It is assumed that the number of found neutrons expected to be seen in the  $i^{th}$  momentum bin is:

$$\mu_i = \eta_i r_i. \quad (3.24)$$

From the Poisson distribution, the probability to see  $f_i$  counts when  $\mu_i$  counts are expected is:

$$P_i = \frac{\mu_i^{f_i}}{f_i!} e^{-\mu_i} \quad (3.25)$$

The probability to observe the entire found neutron distribution is then given by the product of the probability of observing  $f_i$  counts in each bin:

$$P = \prod_i \frac{\mu_i^{f_i}}{f_i!} e^{-\mu_i} \quad (3.26)$$

The parameters in the function  $\eta(p)$  are chosen such that  $P$  is maximized. Consider the (negative) natural log of  $P$ :

$$-\ln P = - \sum_i \{f_i \ln \mu_i - \ln f_i! - \mu_i\} \quad (3.27)$$

The second term,  $\sum_i \ln f_i!$ , does not depend on any of the parameters, so it can be treated as a constant. The 5 parameters for  $\eta(p)$  are then obtained by minimizing:

$$-\ln P = - \sum_i \{f_i \ln \mu_i - \mu_i\} + constant \quad (3.28)$$

This minimization procedure was performed, using MINUIT, in each of six sectors. In an effort to account for any possible dependence of the neutron detection efficiency on the position of the neutron hit on the EC face, the EC face was subdivided into smaller units. Each of the three EC views is composed of 36 strips. This division segments the EC face into  $36^2 = 1296$  triangular *pixels*. Sets of 12 adjacent strips in each view were collected together in software to reduce the number of divisions per view to 3. These 3 *superstrips* divide the EC face into  $3^2 = 9$  *superpixels*, as illustrated in Fig 3.13

The uncertainty on the fit at a given momentum was found from the error matrix returned by MINUIT:

$$\sigma_\eta^2 = \sum_{i,j} \epsilon_{ij} \frac{\partial \eta}{\partial a_i} \frac{\partial \eta}{\partial a_j} \quad (3.29)$$

where  $\eta$  is the value of the fitted function function,  $a_i$  is the  $i^{th}$  parameter of the fit, and  $\epsilon_{ij}$  are the values of the error matrix returned by MINUIT. The results of

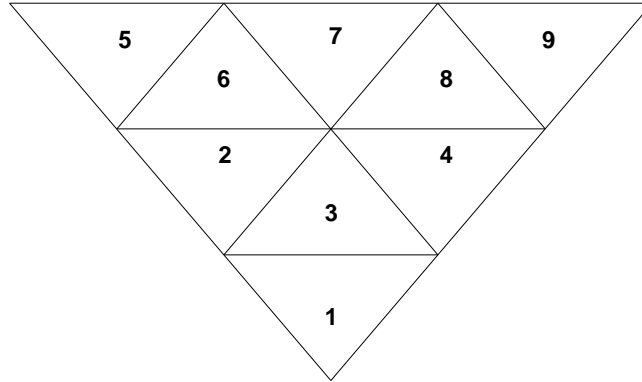


Figure 3.13: Division of the EC face into 9 superpixels. Pixel 1 is located nearest the beam line.

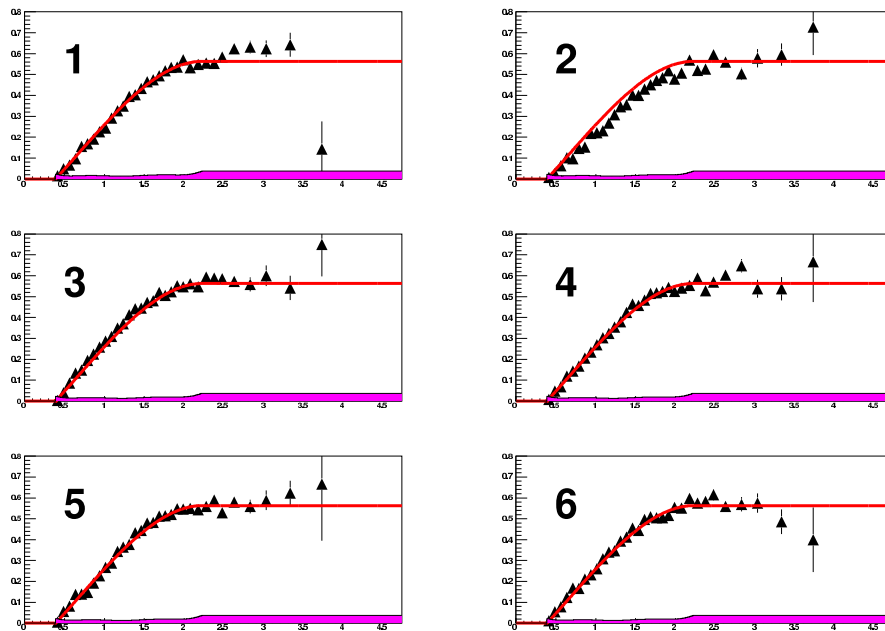


Figure 3.14: The sector-based fits to the EC neutron detection efficiency for the 4.2 GeV data are shown in red. The uncertainty on the fit, scaled up by a factor of 10, is shown by the magenta band. The horizontal axis shows the neutron momentum in GeV/c.

the sector-based fits for the 4.2 GeV data are shown in Fig 3.14. Similar results are obtained in the 2.5 GeV case.

The efficiency function on each superpixel,  $\eta_{sp}$ , was taken to be the product of the efficiency function for that sector multiplied by a scale factor:

$$\eta_{sp}(p) = \alpha \eta_{sector}(p) \quad (3.30)$$

The scale factor  $\alpha$  for each superpixel was found by minimizing the function:

$$\chi^2 = \sum_i \left( \frac{\epsilon_i - \alpha \eta(p_i)}{\sigma_i} \right)^2 \quad (3.31)$$

In this equation,  $\epsilon_i$  is the measured efficiency in the  $i^{th}$  momentum bin for that superpixel,  $\eta(p_i)$  is the efficiency function for the sector evaluated at the center of the  $i^{th}$  momentum bin and  $\sigma_i$  is the error on the measured efficiency in the  $i^{th}$  momentum bin for that superpixel. The value of the scale factor is given by:

$$\alpha = \frac{\sum \frac{\epsilon_i \eta(p_i)}{\sigma_i^2}}{\sum \frac{\eta(p_i)^2}{\sigma_i^2}} \quad (3.32)$$

The uncertainty on the scale factor is given by:

$$\sigma_\alpha^2 = \sum_i \sigma_i^2 \left( \frac{\partial \alpha}{\partial \epsilon_i} \right)^2 \quad (3.33)$$

$$= \frac{1}{\sum \frac{\eta(p_i)^2}{\sigma_i^2}} \quad (3.34)$$

Appendix B contains plots of the measured efficiency and efficiency fits for each of the nine superpixels in each of the six sectors for the 2.5 GeV and 4.2 GeV data sets. The values of the scale factor and error on the scale factor are indicated on the plots.

### 3.3.5 Efficiency Measurement in the Time of Flight system

#### 3.3.5.1 Neutron selection and sector-wise efficiency measurement

The direction of the neutron in the  $ep \rightarrow e\pi^+(n)$  reaction was determined from Eqn 3.16. A ray was drawn from the electron- $\pi^+$  vertex position to each of the planes parallel to the four SC panels in the sector into which the neutron was moving. The point-of-intersection of the neutron in each plane was calculated, and the plane which had the shortest vertex to point-of-intersection distance was used to determine the SC panel hit. This was done to resolve paddle-overlap issues near the panel edges. The point-of-intersection was required to be located on one of the SC paddles in the struck

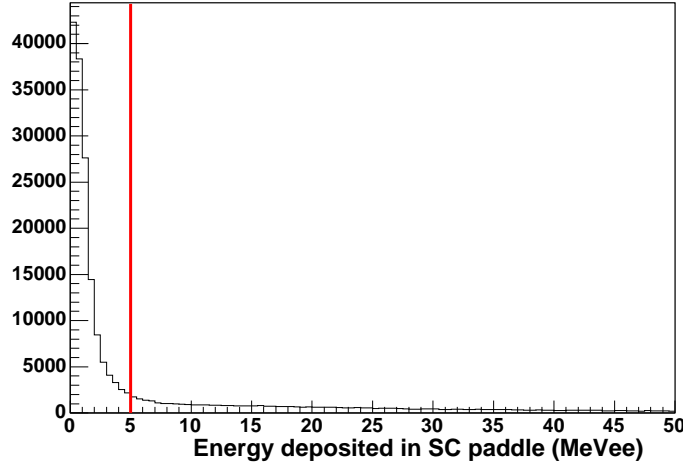


Figure 3.15: The energy deposited in the SC by candidate neutron events. The cut applied is shown in red. Only events with energy greater than 5 MeVee were considered for further analysis. The data shown are a sample from the 2.5 GeV data set.

panel. An additional fiducial cut required that the expected point-of-intersection to be more than 10 cm from either of the two ends of the paddle. In the cases where the reconstructed neutron was expected to intersect the fiducial region of one of the SC panels, that SC panel was searched for neutral hits uncorrelated with any charged track. Events which had SC hits on paddles other than the expected paddle or one of the two paddles adjacent to the expected paddle were rejected. In the case where the neutron was expected to strike a paddle at the edge of a panel, the edge paddles in the adjacent panel were searched as well.

Because generating an SC hit requires an interaction in only a single scintillator, the photon background is higher in the SC than in the EC. Photon rejection was accomplished by cuts on energy deposited and timing. Fig 3.15 shows a plot of the distribution of energy deposited in candidate SC neutron events. A large spike of very low energy events is seen. A cut requiring  $E_{dep} > 5$  MeVee (MeV, electron equivalent) was applied to reject low energy photon background. Because the same  $E_{min}$  cut was applied to SC neutrons in the quasi-elastic analysis, the exact location of this cut could be chosen somewhat arbitrarily.

After rejecting the low energy events, a timing cut was applied. The expected time-of-flight of the neutron was calculated from:

$$t_{expected} = \frac{|\vec{v} - \vec{x}|}{\beta c} \quad (3.35)$$

where  $\vec{v}$  is the electron- $\pi^+$  vertex position and  $\vec{x}$  is the location of the expected point-of-intersection of the neutron and the SC paddle. The measured neutron time-of-flight

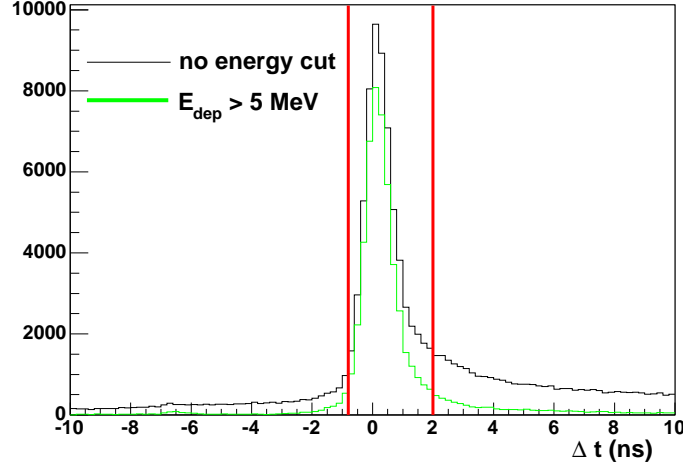


Figure 3.16: The  $\Delta t$  distribution for candidate neutron events in the SC. The black curve shows  $\Delta t$  before application of the  $E_{dep}$  cut. The green curve shows  $\Delta t$  after the  $E_{dep}$  cut. The cuts applied are shown in red. The data shown are a sample from the 2.5 GeV data set.

was calculated from:

$$t_{measured} = t_{sc} - t_0 \quad (3.36)$$

where  $t_{sc}$  is the hit time reported by the SC and  $t_0$  is the event start time defined in Eqn 3.11. A cut was applied requiring

$$-0.8 < \Delta t < 2.0ns \quad (3.37)$$

where  $\Delta t = t_{measured} - t_{expected}$ . The effect of the timing cut is illustrated in Fig 3.16

The events were binned in neutron momentum and the efficiency and uncertainties were calculated as in Eqns 3.19 and 3.21. Fig 3.17 and Fig 3.18 show plots of the neutron detection efficiency in each of the six SC sectors (integrated over all paddles), for the 2.5 GeV and 4.2 GeV data sets. Fig 3.19 shows a comparison of the neutron detection efficiency integrated over all six SC modules measured in each data set.

### 3.3.5.2 Efficiency parametrization in the SC

The neutron detection efficiency in each sector was parametrized as a function of the neutron momentum with a polynomial of the form:

$$\eta(p) = a_0 + a_1p + a_2p^2 + a_3p^3 \quad (3.38)$$

for  $p < p_t$  and:

$$\eta(p) = f \quad (3.39)$$

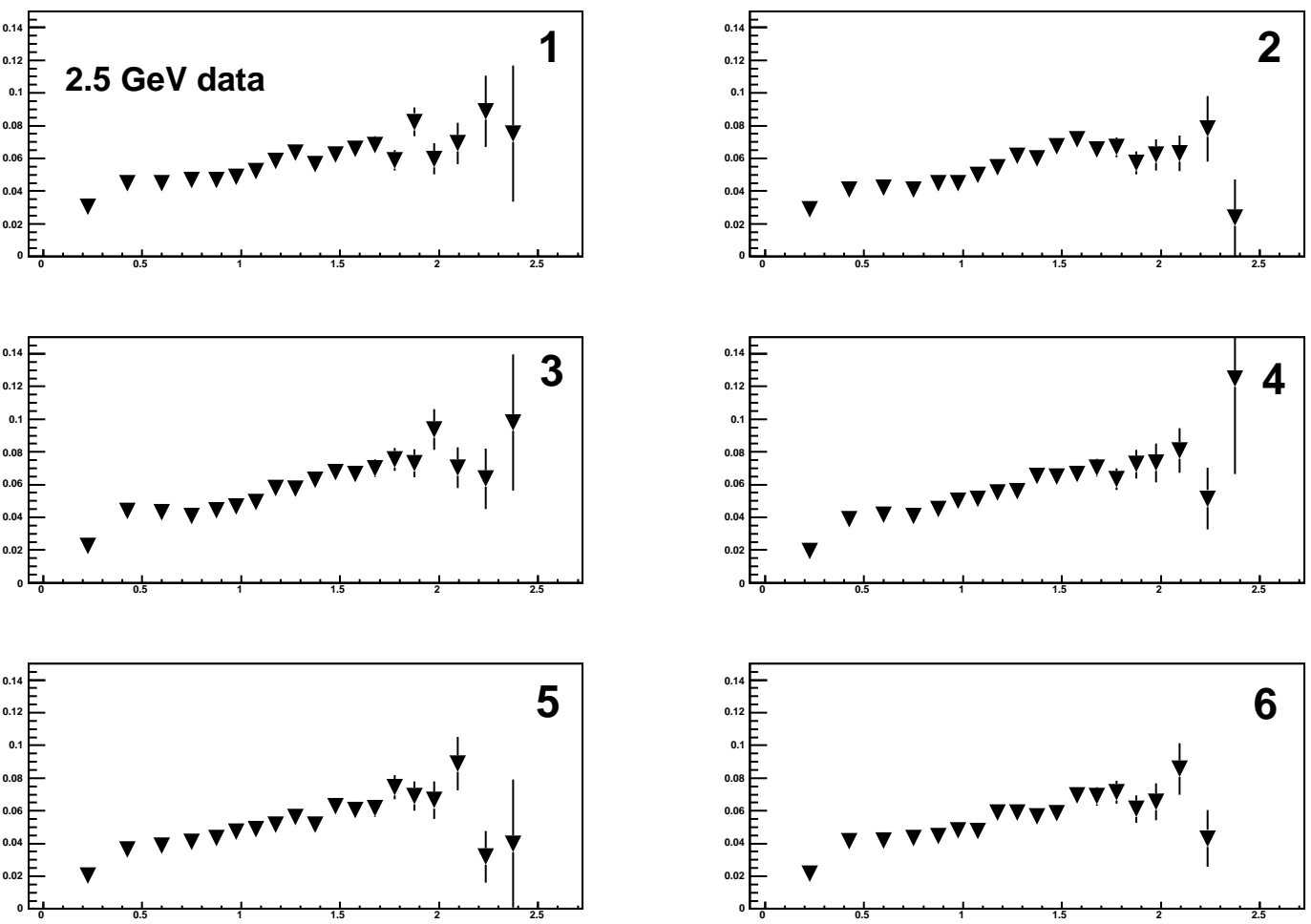


Figure 3.17: SC Neutron detection efficiency, binned in neutron momentum, for each sector in the 2.5 GeV data set. The horizontal axis in each panel is the neutron momentum in GeV/c.

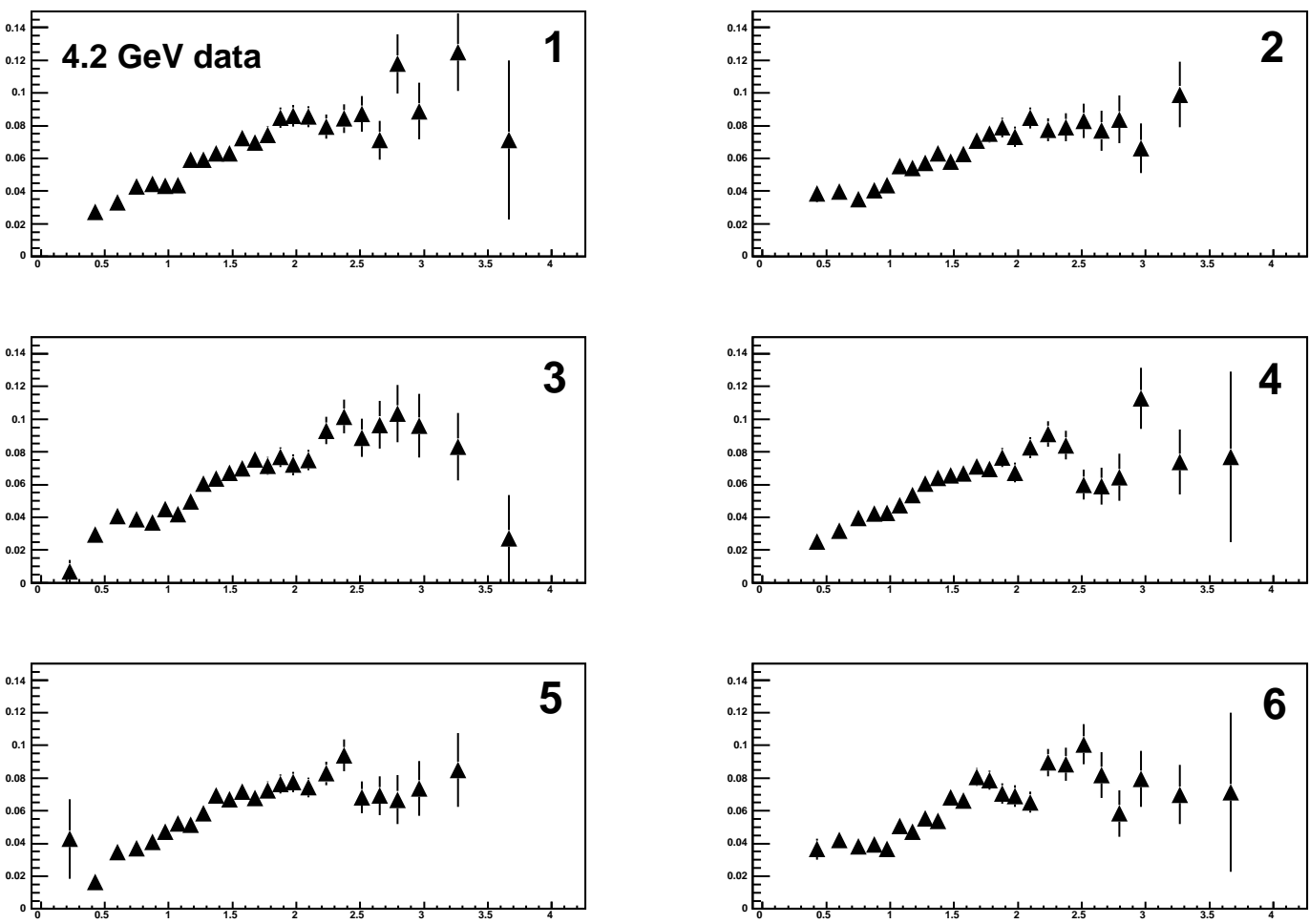


Figure 3.18: SC Neutron detection efficiency, binned in neutron momentum, for each sector in the 4.2 GeV data set. The horizontal axis in each panel is the neutron momentum in GeV/c.

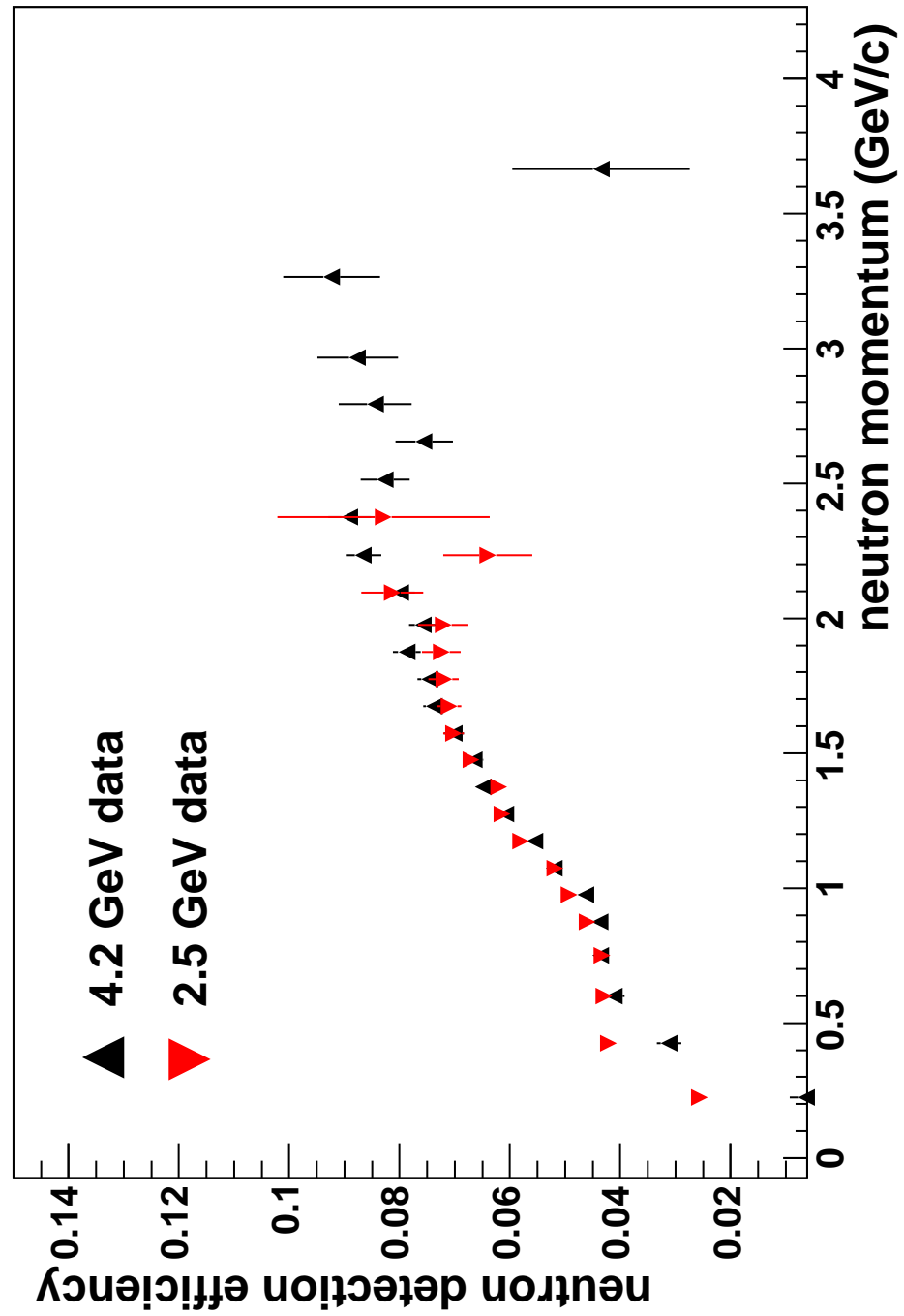


Figure 3.19: A comparison of the neutron detection efficiency in the SC, as measured at two different beam energies. In this figure, the efficiency has been integrated over all six sectors

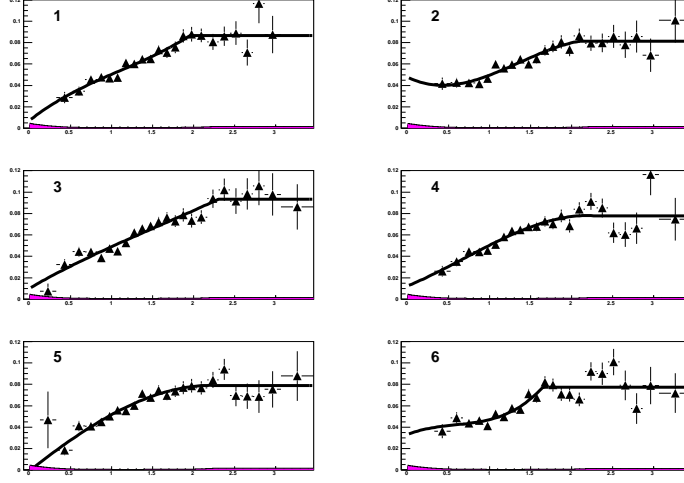


Figure 3.20: The sector-based fits to the SC neutron detection efficiency for the 4.2 GeV data are shown. The uncertainty on the fit is shown by the magenta band. The horizontal axis in each panel shows the neutron momentum in GeV/c.

for  $p \geq p_t$ .  $p_t$  was a parameter of the fit, and  $f$  was determined by requiring  $\eta(p)$  to be continuous at  $p_t$ .

The global efficiency histogram in each sector (containing data from all paddles in the sector) was fitted by this polynomial form using a least-squares fit over the momentum range  $0.0 < p < 1.8$  GeV/c for the 2.5 GeV data set, and  $0.0 < p < 2.8$  GeV/c for the 4.2 GeV data set. The uncertainty on the fit at a given momentum was found from the error matrix returned by MINUIT:

$$\sigma_\eta^2 = \sum_{i,j} \epsilon_{ij} \frac{\partial \eta}{\partial a_i} \frac{\partial \eta}{\partial a_j} \quad (3.40)$$

where  $\eta$  is the value of the fitted function,  $a_i$  is the  $i^{\text{th}}$  parameter of the fit, and  $\epsilon_{ij}$  are the values of the error matrix returned by MINUIT. The fits and associated errors for each of the six sectors in the 4.2 GeV data is shown in Fig 3.20.

In an effort to account for possible paddle-by-paddle variations in the neutron detection efficiency, the efficiency on each paddle,  $\eta_p$ , was taken to be the product of the efficiency function for that sector multiplied by a scale factor:

$$\eta_{\text{paddle}}(p) = \alpha \eta_{\text{sector}}(p). \quad (3.41)$$

The scale factor  $\alpha$  for each paddle was found by minimizing the function:

$$\chi^2 = \sum_i \left( \frac{\epsilon_i - \alpha \eta(p_i)}{\sigma_i} \right)^2 \quad (3.42)$$

In this equation,  $\epsilon_i$  is the measured efficiency in the  $i^{th}$  momentum bin for that paddle,  $\eta(p_i)$  is the efficiency function for the sector evaluated at the center of the  $i^{th}$  momentum bin and  $\sigma_i$  is the error on the measured efficiency in the  $i^{th}$  momentum bin for that paddle. The equation for the value of the scale factor and its error are the same as in the EC case.

Appendix C contains plots of the measured efficiency and efficiency fits for each paddle in each of the six sectors for the 2.3 GeV and 4.2 GeV data sets. Badly-performing paddles were rejected by requiring:

$$0.8 \leq \alpha \leq 1.2 \quad (3.43)$$

Paddles which failed to satisfy this requirement were switched off in software. Paddles with less than 4 data points (for example, sector 4, paddle 29 in Fig C.4) were switched off in software. This cut defined the high-paddle number cut-off. For the 4.2 GeV data, the high-paddle cut-off is 25 or 26 depending on sector, while the cut-off in the 2.5 GeV data set is paddle number 27 or 28 depending on sector.

## 3.4 Proton Detection Efficiency Measurement

The hydrogen cell of the e5 target allows for an *in-situ* measurement of the proton detection efficiency in the SC detector system. Elastic  $ep$  scattering is used as a proton source. Candidate events were selected which had one negative track, and not more than one positive tracks.

### 3.4.1 Electron Identification

The electron selection criteria described in Section 3.3.1 were applied. Once the event was identified as having a good electron, the mass of the recoiling hadronic system was calculated. The 4-momentum of the initial state particles was known:

$$e_{in} = E_0(1, 0, 0, 1) \quad (3.44)$$

$$P = (M_p, 0, 0, 0) \quad (3.45)$$

where  $e_{in}$  is the incoming electron 4-momentum ( $E_0$  is the incident beam energy), and  $P$  is the 4-momentum of the target proton. The final state was taken to be an electron and a recoiling hadronic system. The scattered electron 4-momentum was known from tracking, so the recoil 4-momentum could be determined from conservation of 4-momentum:

$$X_h = e_{in} + P - e_{out} \quad (3.46)$$

where  $X_h$  is the 4-momentum of the hadronic system and  $e_{out}$  is the scattered electron 4-momentum. The square of the invariant mass of the hadronic system was found from:

$$W^2 = X_h^\mu X_{h,\mu}. \quad (3.47)$$

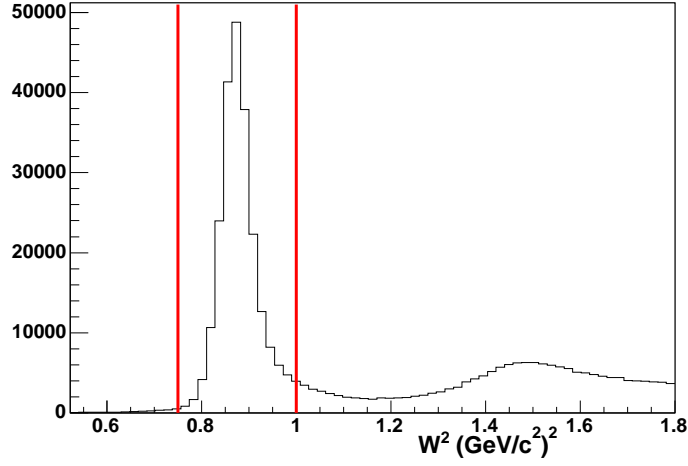


Figure 3.21: The  $W^2$  distribution in candidate  $ep$  elastic events (events with an electron and zero or one charged track). The cuts applied are shown in red. The data shown are a sample of the 2.5 GeV data set.

Elastic events were selected by applying a cut that required

$$0.75 < W^2 < 1.0(\text{GeV}/c^2)^2 \quad (3.48)$$

The distribution of  $W^2$  and the cuts applied are illustrated in Fig. 3.21.

For events which passed the  $W^2$  cut (labeled *reconstructed* events), the paddle the proton was expected to hit was calculated by *swimming* the proton from the electron-beamline vertex position through the mini-torus and main torus magnetic fields out to the SC. The point-of-intersection of the proton in each SC plane was calculated, and the plane which had the shortest vertex to point-of-intersection distance was used to determine the SC panel hit. The point-of-intersection was required to be located on one of the SC paddles in the struck panel. An additional fiducial cut required that the expected point-of-intersection to be more than 10 cm from either of the two ends of the paddle. In those cases where the proton was expected to intersect the SC fiducial region, the SC was searched for hits correlated with a positively-charged track.

### 3.4.2 Proton Identification

Elastic events in which a positive track is found were subjected to a cut requiring the coplanarity of the positive track and the electron. For elastic scattering, the electron and proton azimuthal angles should be  $180^\circ$  apart. Fig 3.22 shows the  $|\Delta\phi|$  distribution for events which passed the  $W^2$  cut. A cut requiring

$$178^\circ < |\Delta\phi| < 182^\circ \quad (3.49)$$

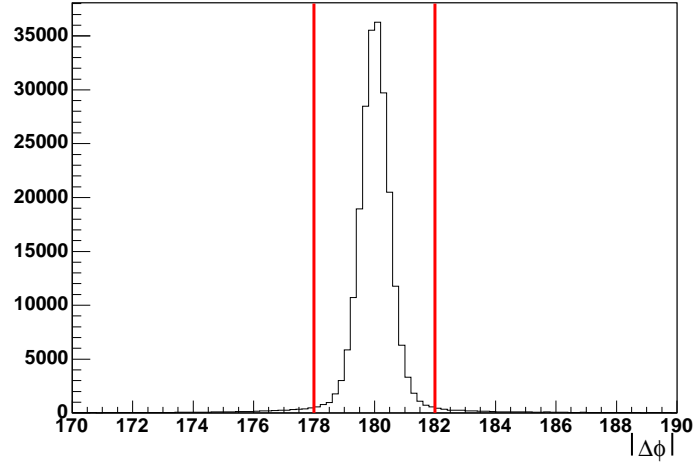


Figure 3.22: The  $\Delta\phi$  distribution for candidate  $ep$  elastic events which passed the  $W^2$  cut. The horizontal axis is in degrees. The cuts applied are shown in red. The data shown are a sample from the 2.5 GeV data set.

was applied.

The SC paddle which the proton hit was required to be the paddle predicted, or one of the two adjacent paddles.

### 3.4.3 Efficiency calculation

Because of the one-to-one relationship between proton scattering angle and proton momentum for elastic scattering, each SC paddle was illuminated by a narrow range of proton momenta. As such, no momentum dependent fitting was attempted. The efficiency on each paddle was calculated by integrating the found and reconstructed protons over the small momentum range covered by the paddle. The errors assigned were binomial, as described in Eqn 3.21. Figs 3.23 and 3.24 show plots of the average proton detection efficiency on each SC paddle in each of the six sectors for the 2.5 and 4.2 GeV data sets.

## 3.5 Momentum Corrections

Fig 3.25 shows  $W^2$  measured in  $ep$  elastic scattering as a function of electron azimuthal angle. Because of uncertainties in the magnetic field map used to reconstruct tracks in the drift chamber, the  $W^2$  determination is flawed, leading to mis-located centroids and strong  $\phi$  dependence in some sectors.

Elastic scattering from the proton target is used to derive a multiplicative correc-

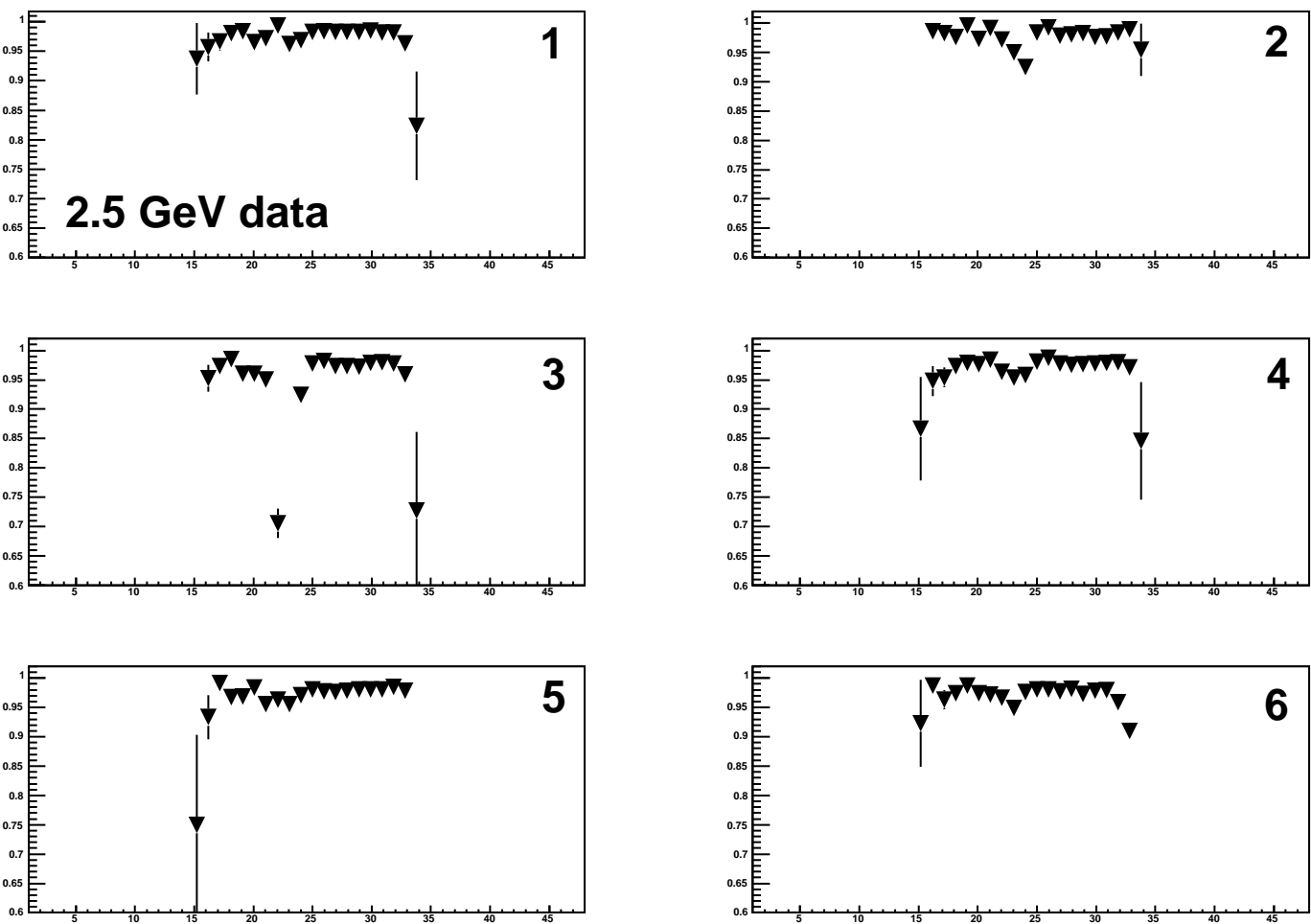


Figure 3.23: Average proton detection efficiency in the SC for the 2.5 GeV data set. The horizontal axis in each panel shows SC paddle number. The sector numbers are indicated in each panel.

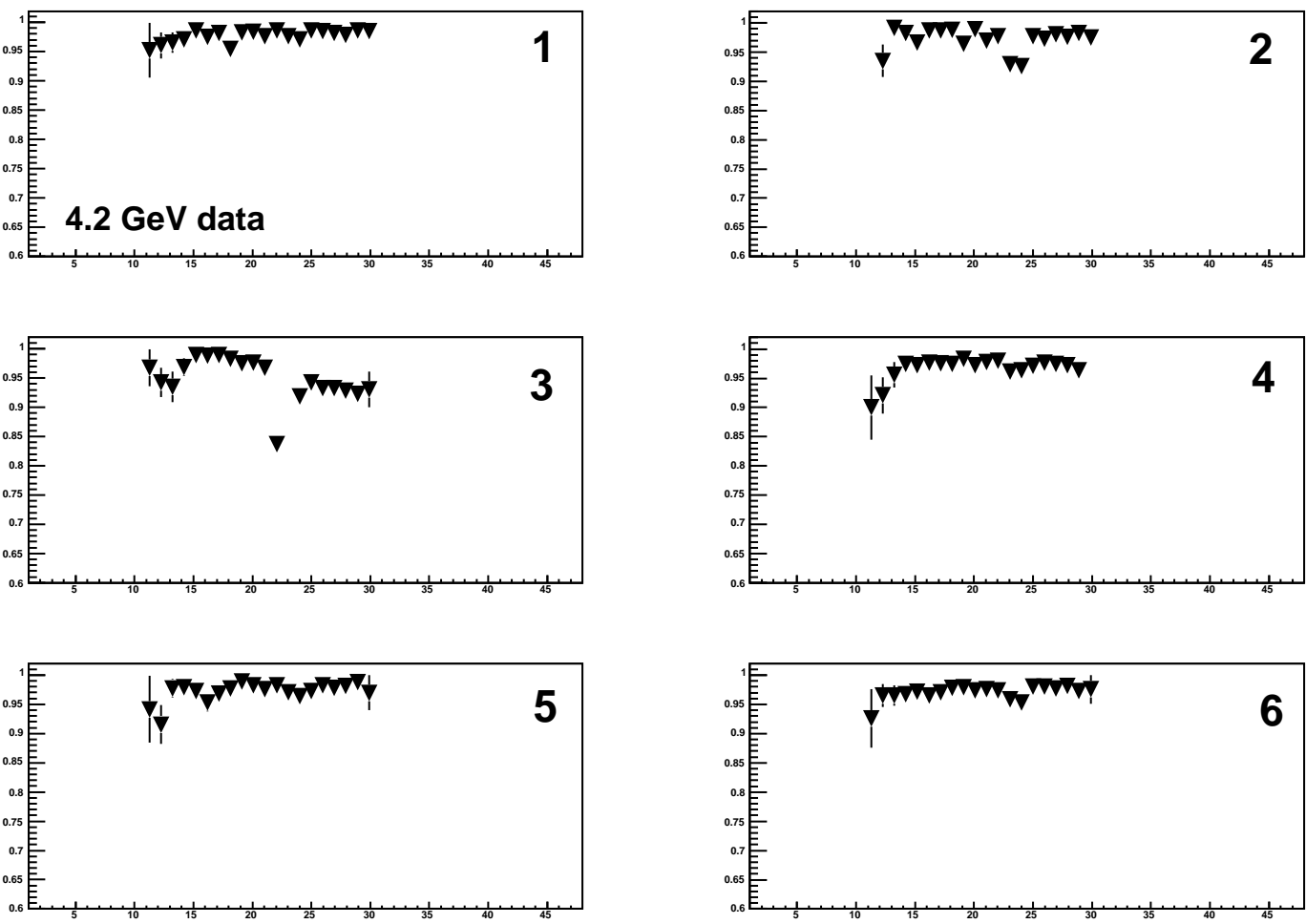


Figure 3.24: Average proton detection efficiency in the SC for the 4.2 GeV data set. The horizontal axis in each panel shows SC paddle number. The sector numbers are indicated in each panel.

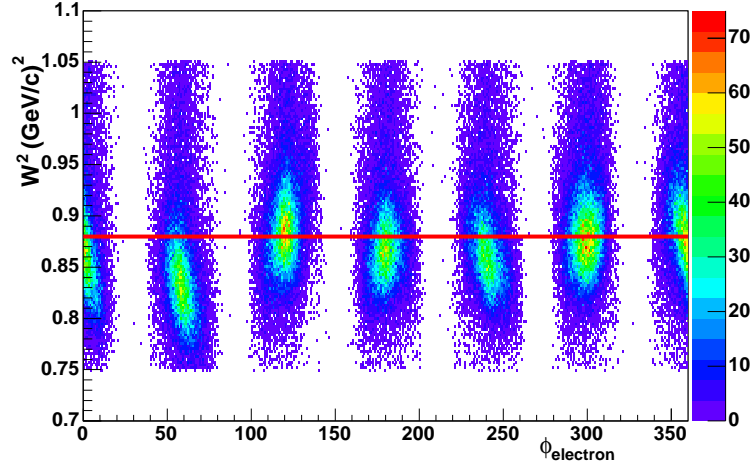


Figure 3.25:  $W^2$  as measured in ep elastic scattering in the 4.2 GeV data set, as a function of electron azimuthal angle. The red line shows the square of the proton mass.

tion to the electron momentum. Conservation of 4-momentum gives:

$$b^\mu + t^\mu = e^\mu + W^\mu \quad (3.50)$$

where  $b^\mu$  is the 4-momentum of the incident beam,  $t^\mu$  is the 4-momentum of the target proton,  $e^\mu$  is the 4-momentum of the scattered electron and  $W^\mu$  is the 4-momentum of the recoiling proton. These vectors have the following values:

$$b^\mu = E_0(1, \hat{z}) \quad (3.51)$$

$$t^\mu = (M_p, 0, 0, 0) \quad (3.52)$$

$$e^\mu = E(1, \hat{e}) \quad (3.53)$$

where  $E_0$  is the incident beam energy,  $E$  is the scattered electron energy and  $\hat{e}$  is the scattered electron direction. The proton invariant mass-squared is found from:

$$W^\mu = e^\mu - b^\mu - t^\mu \quad (3.54)$$

$$= e^\mu - a^\mu \quad (3.55)$$

where  $a^\mu \equiv b^\mu + t^\mu$ .

$$W^2 = (e^\mu - a^\mu)(e_\mu - a_\mu) \quad (3.56)$$

$$= a^2 - 2a^\mu e_\mu \quad (3.57)$$

The mass of the electron has been neglected. The assumption is made that tracking has correctly measured the *direction* of the scattered electron, but that its *energy*

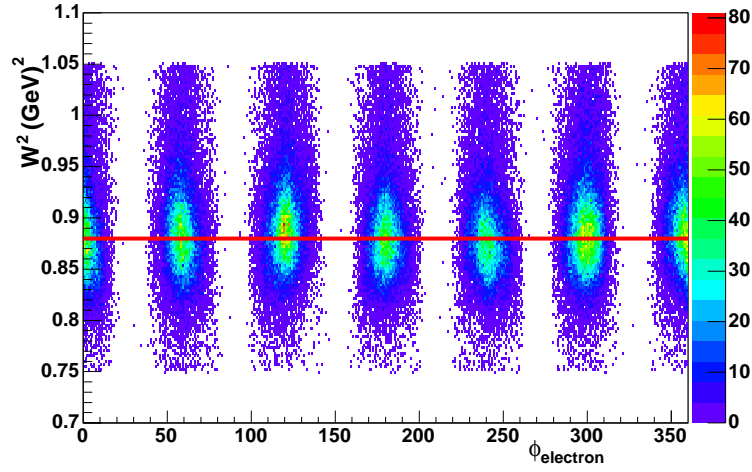


Figure 3.26:  $W^2$  as measured in ep elastic scattering in the 4.2 GeV data set, as a function of electron azimuthal angle, after momentum corrections. The red line shows the square of the proton mass.

may have been mismeasured, so that  $e^\mu$  is replaced by  $\alpha e^\mu$ . A sample of ep elastic events, selected according to the same criteria used in the proton detection efficiency measurement was used to find optimal values for  $\alpha$ . The data in each sector was subdivided in  $\theta$  and  $\phi$  bins. In each bin,  $\alpha$  was determined by minimizing:

$$\chi^2 = \sum_i \left( \frac{W_i^2 - M_p^2}{\sigma_i} \right)^2 \quad (3.58)$$

All events in each bin were weighted evenly. Setting  $\frac{d\chi^2}{d\alpha} = 0$  gives:

$$\alpha = \frac{\sum (a^\mu e_\mu) (a^2 - M_p^2)}{2 \sum (a^\mu e_\mu)^2} \quad (3.59)$$

The results of this procedure are illustrated in Fig 3.26, which shows  $W^2$  as a function of electron azimuthal angle *after* application of the corrections. Notice the reduced  $\phi$  dependence and improved centroid location.

Table 3.1 shows the centroid location in each of the six sectors for the 4.2 GeV data set before and after applying the correction. Table 3.2 shows the centroid locations for the 2.5 GeV data set.

Table 3.1: Comparison of uncorrected and corrected centroid values for  $W^2$  determination from elastic ep scattering in the 4.2 GeV data set. Centroid locations are given in  $\text{GeV}^2$

sector	uncorrected centroid	corrected centroid
1	0.8731	0.8784
2	0.8323	0.8697
3	0.8819	0.8838
4	0.8669	0.8763
5	0.8606	0.8734
6	0.8766	0.8809

Table 3.2: Comparison of uncorrected and corrected centroid values for  $W^2$  determination from elastic ep scattering in the 2.5 GeV data set. Centroid locations are given in  $\text{GeV}^2$

sector	uncorrected centroid	corrected centroid
1	0.8730	0.8793
2	0.8431	0.8790
3	0.8810	0.8825
4	0.8717	0.8793
5	0.8714	0.8792
6	0.8805	0.8821

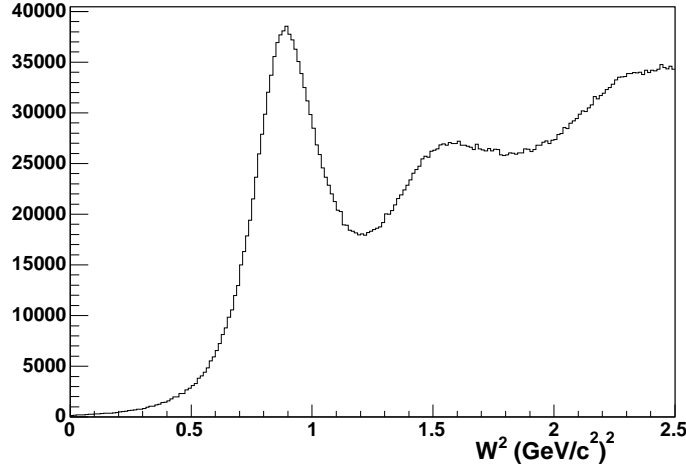


Figure 3.27:  $W^2$  in  $(\text{GeV}/c^2)^2$  for candidate  $D(e, e'n)$  and  $D(e, e'p)$  events after application of electron-based cuts. A quasi-elastic peak is clearly seen, along with a substantial inelastic background. Data from the 4.2 GeV running period is shown.

## 3.6 Quasi-elastic ratio measurement

### 3.6.1 Quasi-elastic electron selection

The cooked files containing all events seen in e5 were filtered down to a smaller set of files containing only  $D(e, e'n)$  and  $D(e, e'p)$  candidates by applying a few cuts based on the electron observed in each event. Events were required to have an electron which satisfied all of the electron selection criteria described in Section 3.4.1. Events which contained any negatively charged tracks in addition to the electron, or more than one positively charged track were discarded. Events in which the z-component of the electron vertex position was outside the deuterium target ( $-12.5 \leq z \leq -8.25$  cm) were discarded. After application of these cuts a substantial inelastic background remained, as shown in Fig 3.27.

### 3.6.2 Quasi-elastic $D(e, e'p)$ selection

To remove the inelastic background, an additional set of cuts were applied to the proton candidates. A  $Q^2$  dependent cut in the  $W^2, \theta_{pq}$  plane ( $\theta_{pq}$  is the angle between the virtual photon direction and the direction of the scattered nucleon at the vertex) was used to isolate events in the quasi-elastic region. The cuts are shown in Fig 3.28 and Fig 3.30 for protons which satisfied the EC fiducial cut described in Section 3.6.5, and in Fig 3.29 and Fig 3.31 for protons which satisfied the SC fiducial cuts described in Sec 3.6.5. The allowed  $W^2$  region is  $0.5 \leq W^2 \leq 1.2(\text{GeV}/c^2)^2$  in all  $Q^2$  bins. The maximum allowed  $\theta_{pq}$  varies from bin to bin and is summarized in Table 3.3 and

Table 3.3:  $Q^2$ -dependent  $\theta_{pq}$  cuts for EC protons in the 4.2 GeV data.

$Q^2$ range	$\theta_{pq}^{maximum}$
1.5,1.75	3.5
1.75,2.0	3.0
2.0,2.5	2.75
2.5,3.0	2.5
3.0,4.5	2.25

Table 3.4:  $Q^2$ -dependent  $\theta_{pq}$  cuts for SC protons in the 4.2 GeV data.

$Q^2$ range	$\theta_{pq}^{maximum}$
1.0,1.5	4.5
1.5,2.0	4.0
2.0,2.5	3.5
2.5,3.0	3.0
3.0,4.5	2.5

Table 3.4 for the 4.2 GeV data, and in Table 3.5 and Table 3.6 for the 2.5 GeV data.

### 3.6.3 Quasi-elastic $D(e, e'n)$ selection

In the  $D(e, e'n)$  channel the same electron selection criteria and  $Q^2$ -dependent cuts in the  $W^2, \theta_{pq}$  plane used in the  $D(e, e'p)$  channel were applied. To suppress accidentals in the SC, a cut requiring that the energy deposited in an SC paddle exceed 5 MeVee was applied. This is the same energy deposited cut that was applied in the SC neutron detection efficiency calibration.

### 3.6.4 Rejection of unreconstructed proton tracks

The energy-deposited spectrum of protons (from the  $D(e, e'p)$  reaction) traversing the SC array is shown in Fig 3.32. The energy-deposited spectrum of quasi-elastic neutron candidates in the SC is shown in Fig 3.33. The peak near  $E_{dep} \approx 0$  is most likely caused by low energy photons, and is excluded by the  $E_{min} > 5$  MeVee cut

Table 3.5:  $Q^2$ -dependent  $\theta_{pq}$  cuts for EC protons in the 2.5 GeV data.

$Q^2$ range	$\theta_{pq}^{maximum}$
1.25,1.75	3.5
1.75,2.0	3.0
2.0,2.25	2.75
2.25,2.5	3.0

Table 3.6:  $Q^2$ -dependent  $\theta_{pq}$  cuts for SC protons in the 2.5 GeV data.

$Q^2$ range	$\theta_{pq}^{maximum}$
0.5,0.75	6.0
0.75,1.0	5.0
1.0,1.5	4.0
1.5,2.5	3.5

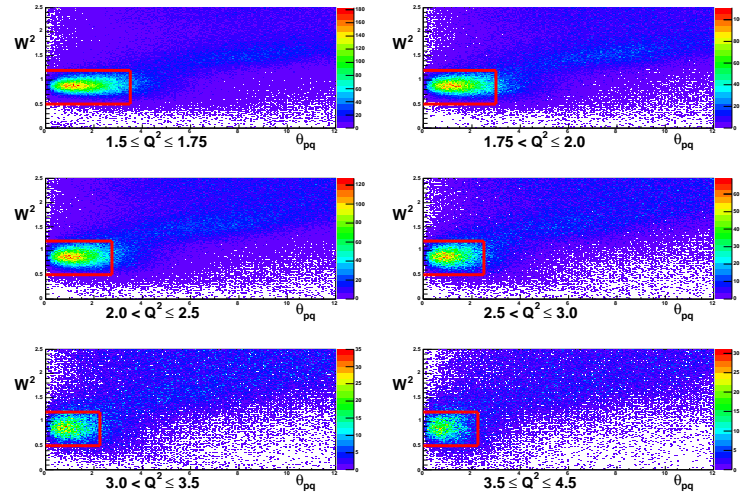


Figure 3.28: Quasi-elastic proton selection cuts for EC protons in the 4.2 GeV data set. Events outside the red box are discarded. In each  $Q^2$  bin, the horizontal axis is  $\theta_{pq}$  (the angle between the virtual photon direction and the scattered proton direction) in degrees and the vertical axis is  $W^2$  in  $(GeV/c^2)^2$

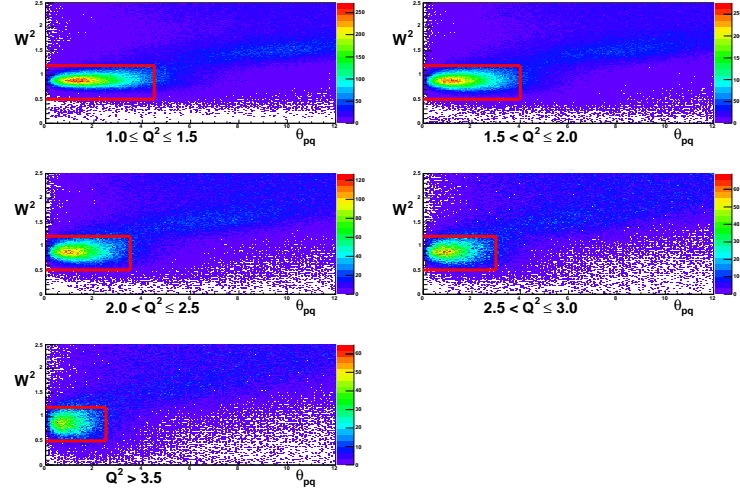


Figure 3.29: Quasi-elastic proton selection cuts for SC protons in the 4.2 GeV data set. Events outside the red box are discarded. In each  $Q^2$  bin, the horizontal axis is  $\theta_{pq}$  (the angle between the virtual photon direction and the scattered proton direction) in degrees and the vertical axis is  $W^2$  in  $(\text{GeV}/c^2)^2$

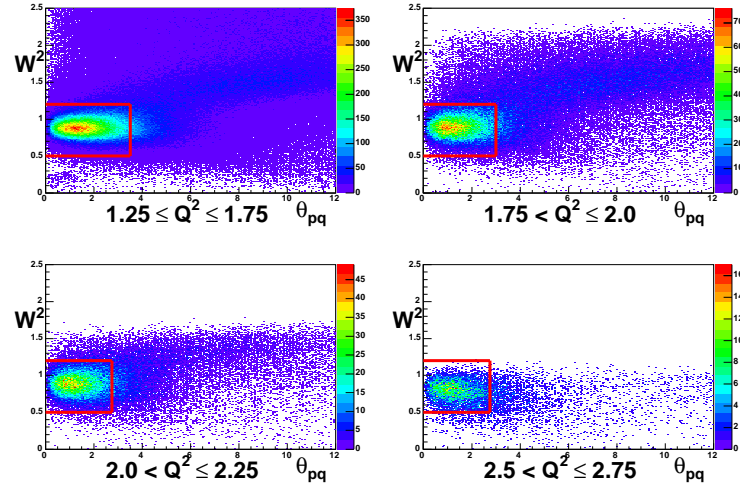


Figure 3.30: Quasi-elastic proton selection cuts for EC protons in the 2.5 GeV data set. Events outside the red box are discarded. In each  $Q^2$  bin, the horizontal axis is  $\theta_{pq}$  (the angle between the virtual photon direction and the scattered proton direction) in degrees and the vertical axis is  $W^2$  in  $(\text{GeV}/c^2)^2$

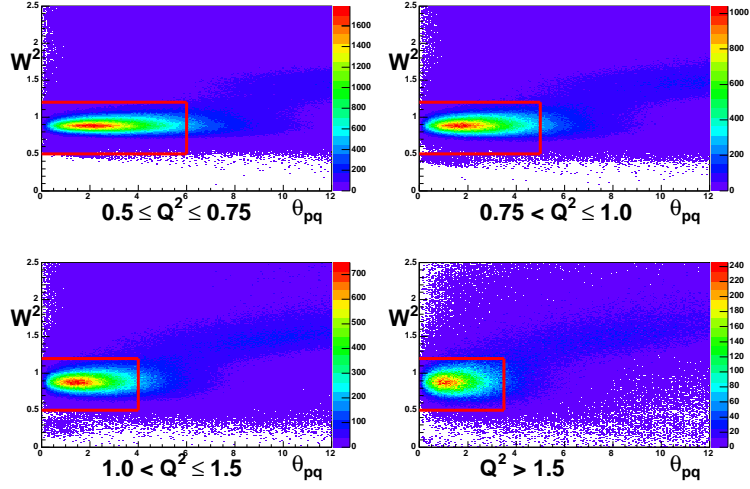


Figure 3.31: Quasi-elastic proton selection cuts for SC protons in the 2.5 GeV data set. Events outside the red box are discarded. In each  $Q^2$  bin, the horizontal axis is  $\theta_{pq}$  (the angle between the virtual photon direction and the scattered proton direction) in degrees and the vertical axis is  $W^2$  in  $(GeV/c^2)^2$

applied to neutrons in both the calibration and quasi-elastic reactions. A second peak in the neutron distribution is seen in the region of  $E_{dep} \approx 12$  MeV. This second peak is unexpected, and occurs at approximately the energy that would be expected for protons.

A sample of events in the region of this peak ( $8 < E_{dep} < 14$  MeV) were inspected visually using the event-display program CED. While some looked normal, others appeared to have partial positive tracks in the sector opposite the electron, as shown in Figs 3.34, 3.35, and 3.36. All of these partial tracks were missing data in one or more DC superlayers, and were not reconstructed by the tracking algorithm. The unreconstructed proton tracks were rejected by counting the number of active DC wires, in each DC region, inside a  $\pm 5^\circ$  window around the expected proton trajectory. SC neutron candidate events that had an energy deposited in the area around the expected proton energy were rejected if they also had either: 1) 7 active wires in Region 1 and 9 or more active wires in either Region 2 or Region 3, or 2) more than 9 active wires in Region 2 and Region 3 were rejected. The effect of this cut is illustrated in Fig 3.37.

### 3.6.5 Acceptance matching and fiducial cuts

To ensure that the  $\sigma_n/\sigma_p$  ratio is measured correctly, it is necessary to take some care that the range of solid angle over which the neutrons are accepted is the same as that over which the protons are accepted. A common fiducial region was enforced by applying an identical fiducial cut to proton and neutron candidate events. In

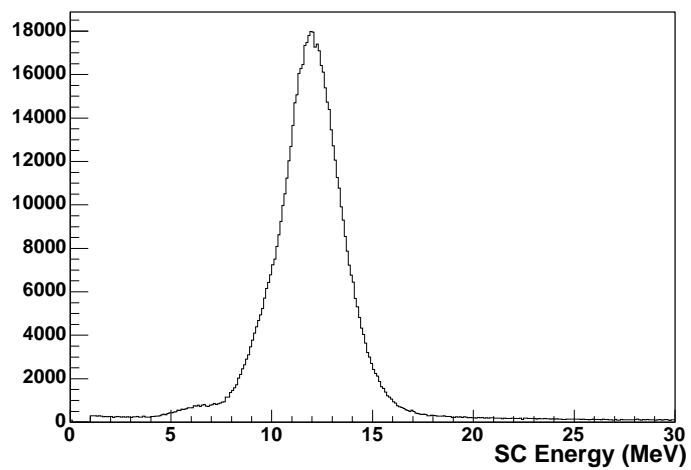


Figure 3.32: Energy deposited in the SC by protons from the  $D(e, e'p)$  reaction

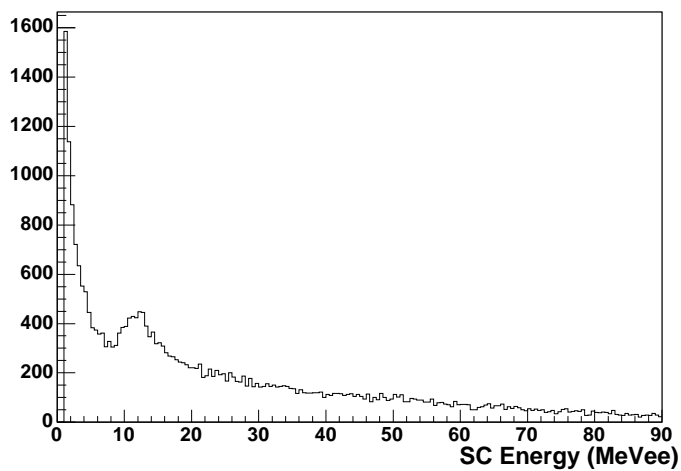


Figure 3.33: Energy deposited in the SC by quasi-elastic neutron candidates.

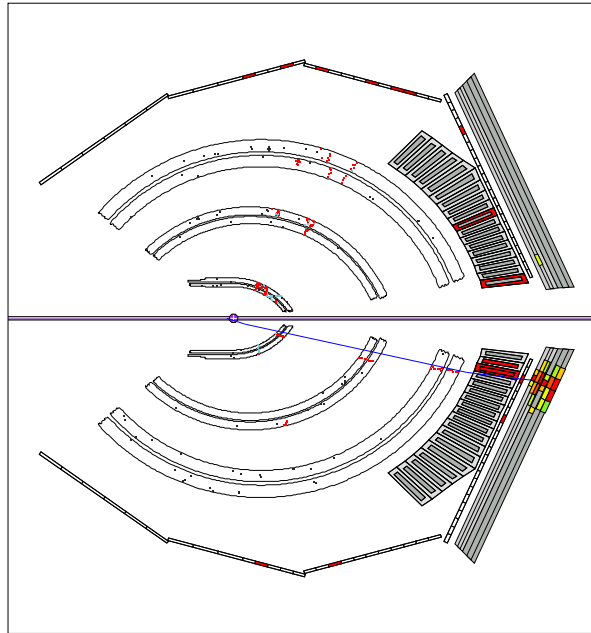


Figure 3.34: CED representation of an unreconstructed proton event.

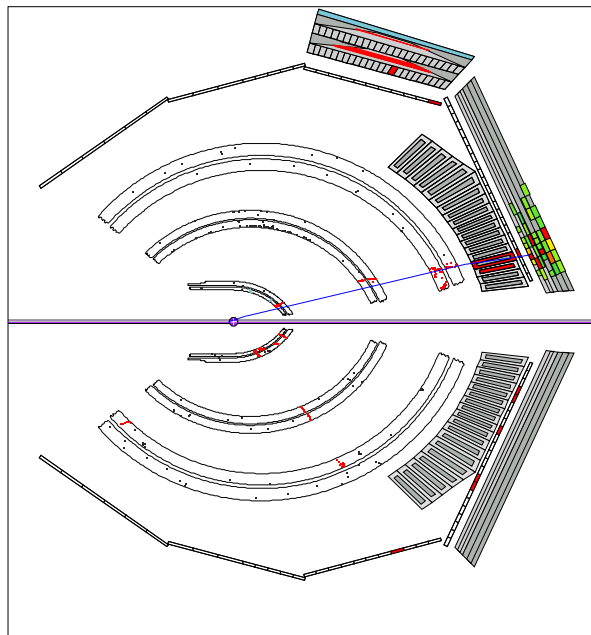


Figure 3.35: CED representation of an unreconstructed proton event.

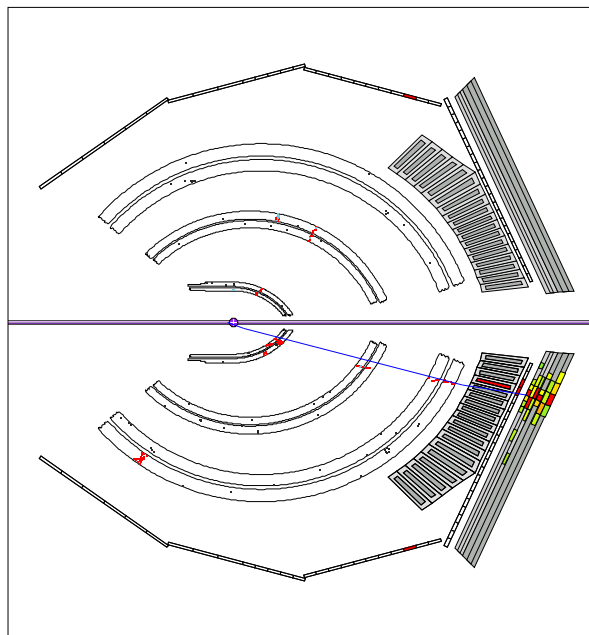


Figure 3.36: CED representation of an unreconstructed proton event.

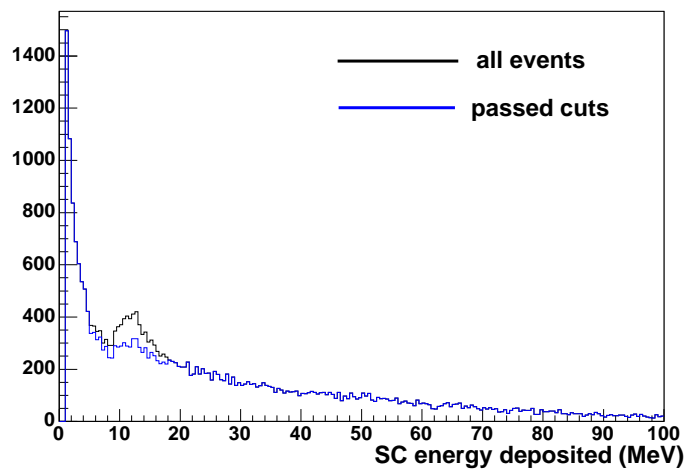


Figure 3.37: SC energy deposit spectrum for candidate neutral events before and after applying DC wire-based unreconstructed proton rejection cut.

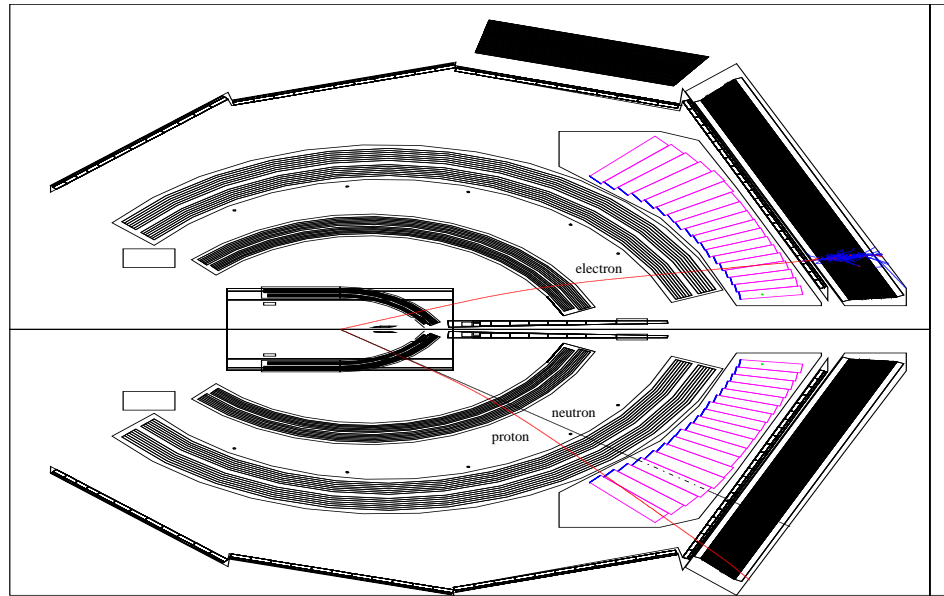


Figure 3.38: An illustration of the acceptance matching technique. From the scattered electron (inbending red track) kinematics, the 3-momentum of a stationary target nucleon was determined. This nucleon was required to strike the active region of the acceptance if it were either a neutron (black track) or a proton (outbending red track). This illustration shows an acceptable event from the 4.2 GeV EC neutron measurement.

each event, the expected nucleon 3-momentum (assuming a stationary target) was determined from the electron kinematics. The possibility that the struck nucleon was a neutron was considered first. This neutron was traced out to either the EC or SC plane, depending on which analysis was being performed. If this expected neutron failed to intersect a good SC paddle (a paddle with neutron detection efficiency greater than 1% and whose neighbors also had efficiency greater than 1%), or a good EC pixel (a pixel with neutron detection efficiency greater than 5%), the event was discarded for the SC or EC analysis, respectively. Next, the possibility that the struck nucleon was a proton was considered. A proton with the expected nucleon 3-momentum was swum through the magnetic field out to the SC plane, where it was required to strike an SC paddle whose efficiency was greater than 85%, and whose neighboring paddles also had efficiency greater than 85%. Events which failed this cut were also discarded for both the SC and EC analysis. The struck nucleon was required to satisfy the .AND. of both of these conditions: expected neutron went into allowed region, expected proton went into allowed region. The double particle-tracking used to evaluate the fiducial cut is illustrated in Fig 3.38. The distribution of events in the  $\theta_{expected}, \phi_{expected}$  plane for the EC neutron analysis of the 4.2 GeV data is shown in Fig 3.39.

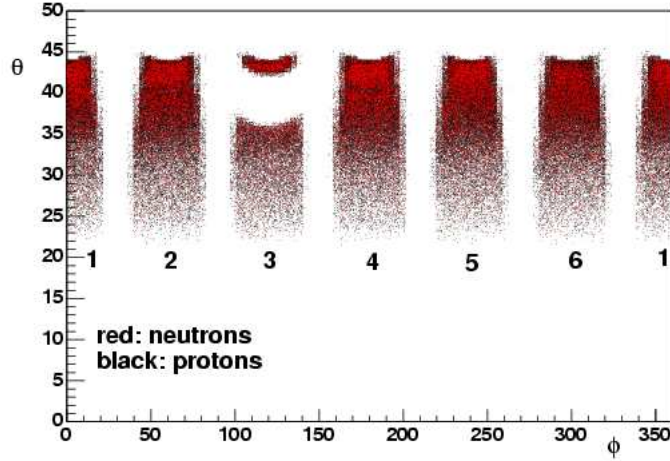


Figure 3.39: The distribution of neutron and proton events in the  $\theta_{expected}, \phi_{expected}$  plane for the EC neutron analysis of the 4.2 GeV data. The gap in sector 3 is caused by a dead TOF paddle and its adjacent paddles which were switched off in software.

### 3.6.6 Efficiency corrections and Ratio calculation

#### 3.6.6.1 Event-by-event efficiency corrections

Events which satisfy the quasi-elastic selection cuts and the fiducial cuts are filled into two histograms, binned in  $Q^2$ , one for neutron events and one for proton events. The entries to these histograms were weighted by the reciprocal of the detection efficiency of the detector element in which they were found: EC pixel or SC paddle for neutrons, SC paddle for protons. Any events which are found in poorly performing detector elements (EC neutron detection efficiency below 5%, SC neutron detection efficiency below 1%, proton detection efficiency below 85%) are discarded. The average efficiency correction, binned in  $Q^2$ , for the detectors are shown in Fig 3.40, Fig 3.41 and Fig 3.42.

#### 3.6.6.2 Statistical Error Analysis for Neutron Histograms

The contents of each of the  $Q^2$  bins in the neutron histogram are:

$$b_i = \sum_{j=1}^{N_i} \frac{1}{\alpha_j \eta_j} \quad (3.60)$$

where  $b_i$  is the entry in the  $i^{th}$   $Q^2$  bin,  $N_i$  is the number of events seen in the  $i^{th}$   $Q^2$  bin,  $\alpha_j$  is the scale factor on the detector element in which the  $j^{th}$  event was found (SC paddle or EC superpixel), and  $\eta_j$  is the value of the efficiency fit evaluated at momentum  $p_j$ . In each  $Q^2$  bin, only a limited number of detector elements contribute.

For the purpose of determining the statistical error on  $b_i$ , the expression for the bin content can be rewritten as:

$$b_i = \sum_{k=1}^{N_d} \frac{n_k}{\alpha_k} f_k \quad (3.61)$$

where the index  $k$  denotes the detector element in which the neutron was detected (SC paddle or EC superpixel),  $N_d$  is the number of active detector elements in the  $i^{\text{th}}$   $Q^2$  bin,  $n_k$  is the number of counts seen in the  $k^{\text{th}}$  detector element,  $\alpha_k$  is the scale factor for the  $k^{\text{th}}$  detector element, and

$$f_k = \left\langle \frac{1}{\eta(p)} \right\rangle \quad (3.62)$$

is the reciprocal of the efficiency parametrization associated with the  $k^{\text{th}}$  detector element, averaged over the momentum range covered by the  $i^{\text{th}}$   $Q^2$  bin.

The uncertainty on  $b_i$  can then be written as:

$$\sigma_{b_i}^2 = \sum_{k=1}^{N_d} \left\{ \sigma_{n_k}^2 \left( \frac{\partial b_i}{\partial n_k} \right)^2 + \sigma_{\alpha_k}^2 \left( \frac{\partial b_i}{\partial \alpha_k} \right)^2 + \sigma_{f_k}^2 \left( \frac{\partial b_i}{\partial f_k} \right)^2 \right\} \quad (3.63)$$

The  $\sigma_{f_k}$  term is small compared to the others and will be neglected. Setting  $\sigma_{n_k}^2 = n_k$  gives:

$$\sigma_{b_i}^2 = \sum_{k=1}^{N_d} \left\{ n_k \left( \frac{f_k}{\alpha_k} \right)^2 + \sigma_{\alpha_k}^2 \left( \frac{n_k f_k}{\alpha_k^2} \right)^2 \right\} \quad (3.64)$$

$$= \sum_{k=1}^{N_d} \frac{n_k f_k^2}{\alpha_k^2} \left( 1 + \frac{n_k \sigma_{\alpha_k}^2}{\alpha_k^2} \right) \quad (3.65)$$

### 3.6.6.3 Statistical Error Analysis for Proton Histograms

The contents of each of the  $Q^2$  bins in the proton histogram are:

$$b_i = \sum_{j=1}^{N_i} \frac{1}{\epsilon_j} \quad (3.66)$$

where  $b_i$  is the entry in the  $i^{\text{th}}$   $Q^2$  bin,  $N_i$  is the number of events seen in the  $i^{\text{th}}$   $Q^2$  bin and  $\epsilon_j$  is the proton efficiency on the  $j^{\text{th}}$  paddle. As in the neutron case, only a few SC paddles are active in a given  $Q^2$  bin, so that the bin contents can be rewritten as:

$$b_i = \sum_{k=1}^{N_d} \frac{n_k}{\epsilon_k} \quad (3.67)$$

where the index  $k$  denotes the SC paddle in which the proton was detected,  $N_d$  is the number of SC paddles active in the  $i^{\text{th}}$   $Q^2$  bin,  $n_k$  is the number of protons found in paddle  $k$ , and  $\epsilon_k$  is the detection efficiency of the  $k^{\text{th}}$  paddle. Recall that for proton detection, the detection efficiency on each SC paddle is taken to be momentum *independent*. The uncertainty on  $b_i$  is then given by:

$$\sigma_{b_i}^2 = \sum_{k=1}^{N_d} \left\{ \sigma_{n_k}^2 \left( \frac{\partial b_i}{\partial n_k} \right)^2 + \sigma_{\epsilon_k}^2 \left( \frac{\partial b_i}{\partial \epsilon_k} \right)^2 \right\} \quad (3.68)$$

$$= \sum_{k=1}^{N_d} \left\{ \frac{n_k}{\epsilon_k^2} + \frac{\sigma_{\epsilon_k}^2 n_k^2}{\epsilon_k^4} \right\} \quad (3.69)$$

$$= \sum_{k=1}^{N_d} \frac{n_k}{\epsilon_k^2} \left( 1 + \frac{\sigma_{\epsilon_k}^2 n_k}{\epsilon_k^2} \right) \quad (3.70)$$

where we have set  $\sigma_{n_k}^2 = n_k$ . The uncertainty on the efficiency  $\sigma_{\epsilon_k}$  is taken to be the binomial uncertainty on the appropriate bin in the efficiency histogram.

#### 3.6.6.4 Statistical Error Analysis for Ratio Histograms

The  $\sigma_n/\sigma_p$  ratio histogram was constructed by dividing the neutron and proton histograms bin-by-bin, so that the contents of each bin in the ratio histogram are:

$$R_i = \frac{b_i^{\text{neutron}}}{b_i^{\text{proton}}} \quad (3.71)$$

where  $b_i^{\text{neutron}}$  is the efficiency-weighted number of neutron events found in the  $i^{\text{th}}$   $Q^2$  bin and  $b_i^{\text{proton}}$  is the efficiency-weighted number of proton events found in the  $i^{\text{th}}$   $Q^2$  bin. The uncertainty on each bin in the ratio histogram is given by the usual propagation of errors formula:

$$\frac{\sigma_R^2}{R^2} = \frac{\sigma_n^2}{n^2} + \frac{\sigma_p^2}{p^2} \quad (3.72)$$

where  $R$  is the value of the ratio histogram in that bin,  $n$  is the weighted number of neutron entries in that bin and  $p$  is the weighted number of proton entries in that bin ( $n$  and  $p$  correspond to  $b_i^{\text{neutron}}$  and  $b_i^{\text{proton}}$  in Eqn 3.71).

#### 3.6.6.5 Uncorrected Ratio Histograms

The  $\sigma_n/\sigma_p$  ratio histograms from the 4.2 GeV data set are shown in Fig 3.43 and the ratio histograms from the 2.5 GeV data set are shown in Fig 3.44. Note that a comparison of the  $\sigma_n/\sigma_p$  ratio at two different beam energies is not appropriate. There are beam energy dependent terms in the elastic cross section, so even if identical values of  $G_M^n$  were determined at the two beam energies, identical values of  $\sigma_n/\sigma_p$  would not be found. Notice that the EC and SC ratio values at low  $Q^2$  values in

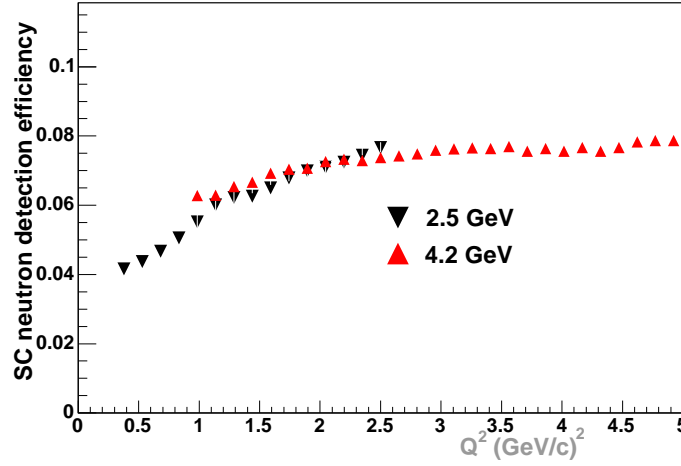


Figure 3.40: The average efficiency correction applied to SC neutrons, binned in  $Q^2$  for the two beam energy settings.

each of these plots do not agree. Additional corrections need to be applied to the measured ratio before  $G_M^n$  can be extracted.

## 3.7 Corrections to Quasi-elastic ratio

### 3.7.1 Uncalibrated SC paddles

The calibration reaction  $ep \rightarrow e\pi^+(n)$  fully illuminates the EC face, allowing the calibration of all the EC pixels. The reaction does not fully illuminate the range of SC paddles where quasi-elastically scattered neutrons are found. A glance at Appendix C will show that the calibration reaction provides calibration data on paddles numbered as high as 25 in the 4.2 GeV data, and as high as 28 in the 2.5 GeV data. Neutron candidates scattered from the  $D_2$  target can be found at higher paddle number than the calibration cut-off. Fig 3.45 shows a plot of the number of neutron candidates in each SC paddle for the 4.2 GeV data set. The neutron population extends up to paddle number 30. The proton calibration reaction  $ep \rightarrow ep$  illuminates the same set of paddles as the quasi-elastic reaction, so there is no uncalibrated paddle problem for protons.

### 3.7.2 Losses due to Fermi motion of the target

If the target nucleon was stationary, there would be a one-to-one relation between  $Q^2$  and nucleon scattering angle, and all of the uncalibrated paddles could be switched off in software and all of the calibrated paddles used. When the target nucleon is in motion, as it is in the deuterium nucleus, the one-to-one relationship between

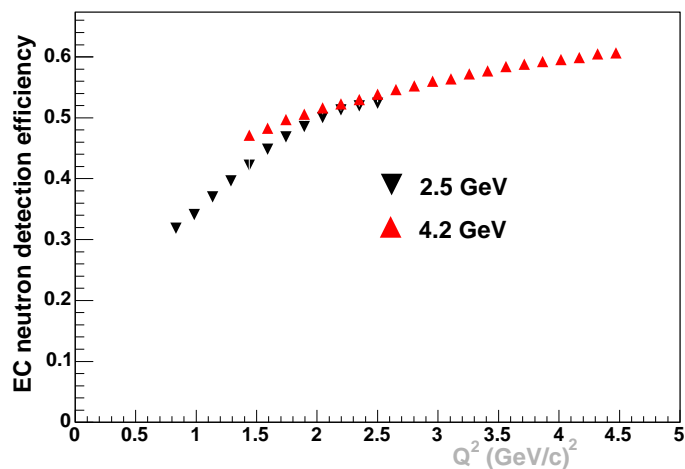


Figure 3.41: The average efficiency correction applied to EC neutrons, binned in  $Q^2$  for the two beam energy settings.

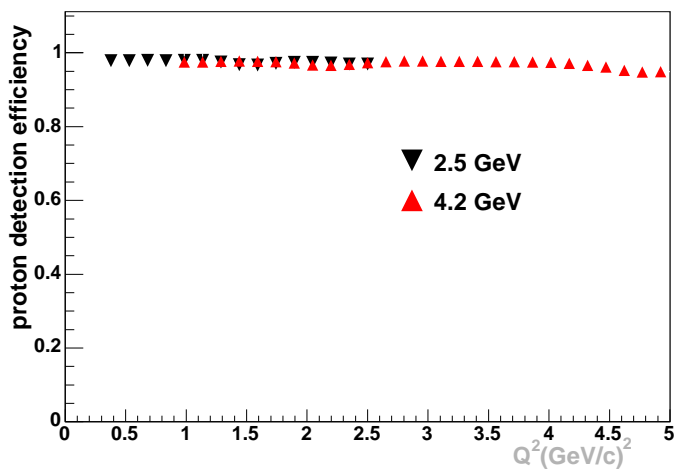


Figure 3.42: The average efficiency correction applied to protons, binned in  $Q^2$  for the two beam energy settings.

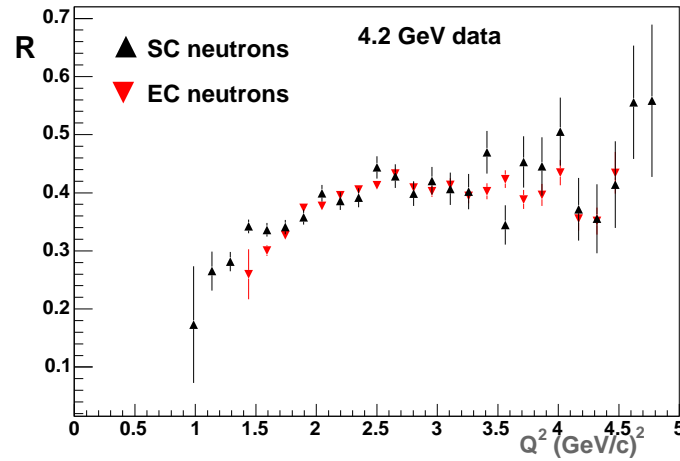


Figure 3.43: The  $\sigma_n/\sigma_p$  ratio  $R$ , as measured in the 4.2 GeV data set for both EC neutrons (red triangles) and SC neutrons (black triangles), binned in  $Q^2$ .

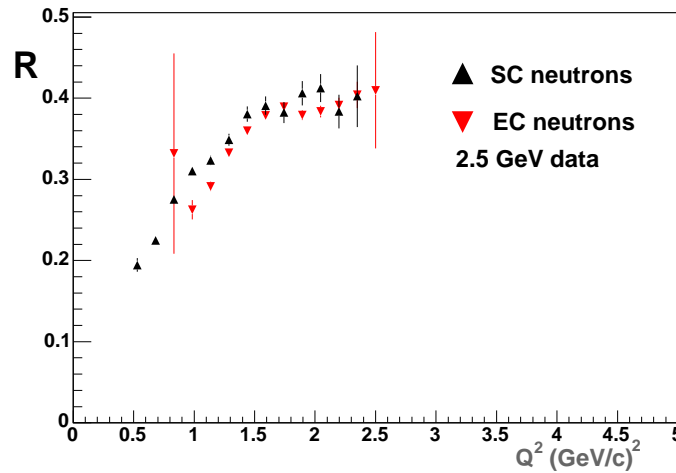


Figure 3.44: The  $\sigma_n/\sigma_p$  ratio  $R$ , as measured in the 2.5 GeV data set for both EC neutrons (red triangles) and SC neutrons (black triangles), binned in  $Q^2$ .

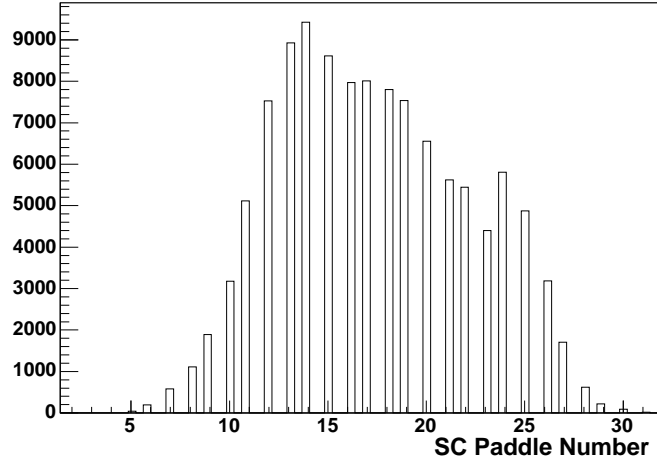


Figure 3.45: Neutron candidate events from the  $D_2$  target, binned by SC paddle number, from the 4.2 GeV data set.

$Q^2$  and scattering angle in elastic scattering is broken. Simply switching off the uncalibrated paddles will give an incorrect measure of the  $\frac{\sigma_n}{\sigma_p}$  ratio at low  $Q^2$  (low  $Q^2$  corresponds to high SC paddle numbers) because of the effects of the target Fermi motion. Neutrons which, based on the electron kinematics, would be expected to strike a paddle near the edge of the calibrated region, may in fact strike uncalibrated paddles due to the additional effect of the Fermi motion. Such a neutron would not be counted, incorrectly lowering the cross-section ratio. A similar loss is not suffered by the protons, because the calibrated proton paddles cover the range of the quasi-elastic reaction. Note that there is no corresponding Fermi induced migration of neutrons *into* the acceptance, due to the requirement that acceptable events must have a predicted nucleon location *inside* the acceptance.

A similar effect is seen in the EC, where neutrons which are expected to strike near the edge of the EC can be moved out of the EC acceptance by Fermi effects. Again, a similar problem is not seen for the protons because the angular coverage of the SC is significantly larger than that of the EC.

This phenomena of particles migrating out of the acceptance due to Fermi effects can be removed in two ways. A fiducial cut which restricts the expected nucleon location to regions of the acceptance sufficiently far away from the edge that Fermi effects are not large enough to move the nucleon out of the acceptance could be applied. Such a cut would have the effect of raising the value of the minimum  $Q^2$  accessible to the measurement. Alternatively, a Monte-Carlo calculation could be used to estimate the fraction of nucleons expected to be removed from the acceptance by Fermi effects. The second option is used in this analysis.

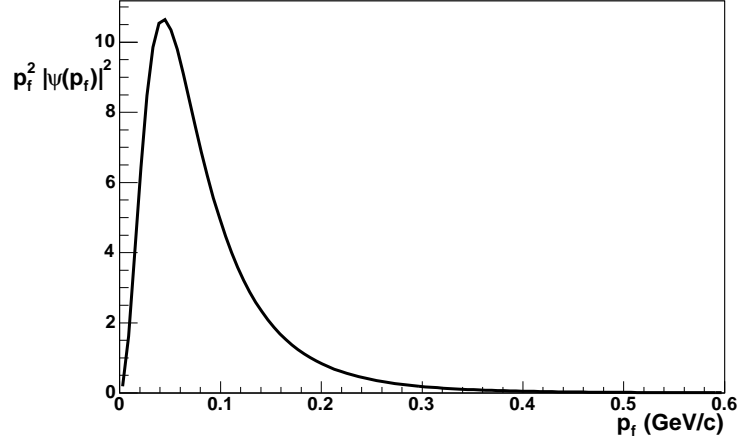


Figure 3.46: The Hulthen distribution for the nucleon Fermi momentum in the deuteron.

### 3.7.3 Quasi-elastic event generator

The angular distribution of neutrons and protons quasi-elastically scattered from the deuteron was simulated using the Hulthen model of the deuteron wave function. The Hulthen model prediction for the nucleon Fermi momentum distribution is shown in Fig 3.46.

Equation 1.8 gives the elastic electron-nucleon scattering cross-section in terms of the Lorentz invariant  $Q^2$  and the energy of the incident electron beam for a nucleon at rest. This equation was used to evaluate quasi-elastic scattering from a moving nucleon in a deuteron (off-shell effects were neglected). To do this, it was first necessary to transform from the lab frame, in which both the electron and the nucleon are in motion, to the nucleon rest frame. Fig 3.47 shows the effect of the boost to the nucleon rest frame on the electron beam energy for a 4.2 GeV incident beam, binned in the magnitude of the Fermi momentum and the cosine of the angle between the Fermi momentum and the incident electron.

The lab frame and rest frame cross sections are related by:

$$\frac{d\sigma}{d\Omega_l} = \frac{d\sigma}{d\Omega_r} \frac{d\Omega_r}{d\Omega_l} \quad (3.73)$$

$$= \frac{d\sigma}{d\Omega_r} \frac{\sin \theta_r}{\sin \theta_l} \frac{d\theta_r}{d\theta_l} \quad (3.74)$$

where the subscripts  $l, r$  denote the lab frame and rest frame respectively.

Equation 3.73 was integrated over polar angle:

$$\int_{d\theta_l} \frac{d\sigma}{d\theta_l} d\theta_l = \int_{d\theta_r} \frac{d\sigma}{d\theta_r} \frac{\sin \theta_r}{\sin \theta_l} \frac{d\theta_r}{d\theta_l} d\theta_r \quad (3.75)$$

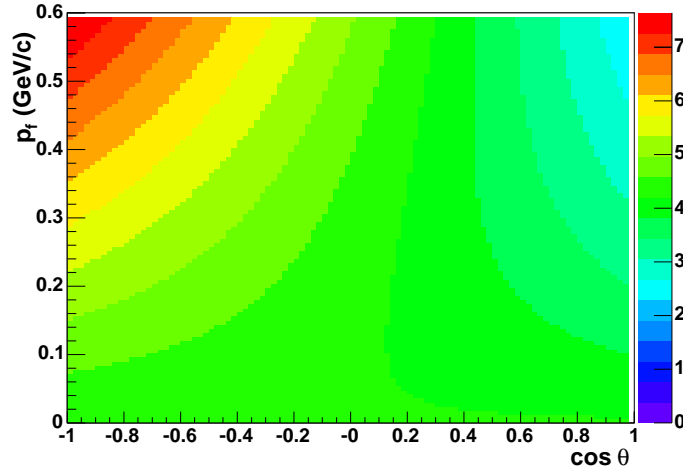


Figure 3.47: The horizontal axis shows the cosine of the angle between the momenta of the incident 4.2 GeV electron and the moving nucleon (the angle in the lab frame). The vertical axis shows the magnitude of the Fermi momentum in GeV/c. The color z-axis shows the energy of the incident electron in the nucleon rest frame, in GeV.

The integration on the left in Eqn 3.75 is over an angular range roughly covering the CLAS acceptance: full azimuthal coverage, 14 to 52 degrees in polar angle for the 4.2 GeV incident beam energy, 12 to 52 degrees in polar angle for the 2.5 GeV incident beam energy. The integration on the right is over the equivalent angular range in the rest frame. The kinematic relations between the lab frame and the rest frame are derived in Appendix D. The Brash parametrization of the form factors is used in evaluation of the integral on the right. The integrated lab-frame cross-section was determined for a range of  $p_f$ ,  $\cos \theta_f$  values. Fig 3.48 shows the integrated cross-section as a function of the magnitude of the Fermi momentum and the cosine of the angle between the incident electron and the Fermi momentum in the lab frame for electron-neutron scattering, and Fig 3.49 shows the same for the electron-proton case. The electron-neutron and electron-proton elastic scattering cross-sections as a function of scattering angle in the rest frame are shown in Fig 3.50. Note that the cross-section peaks for large Fermi momentum nucleons in the  $\cos \theta_{pq} \approx 1$  region, where the electron beam energy in the nucleon rest frame is smallest.

Each cell in Fig 3.48 and Fig 3.49 was multiplied by the value of the Hulthen function (shown in Fig 3.46) at the appropriate momentum. This generated a two-dimensional histogram for which the relative weighting of the cells should give the relative probability for quasi-elastic scattering at those values of  $p_f$  and  $\cos \theta$ . Fig 3.51 and Fig 3.52 show the weight tables for electron-neutron and electron-proton scattering, respectively.

The kinematics of quasi-elastic scattering are treated using a spectator approximation in which the deuteron is composed of two on-shell nucleons, one moving with

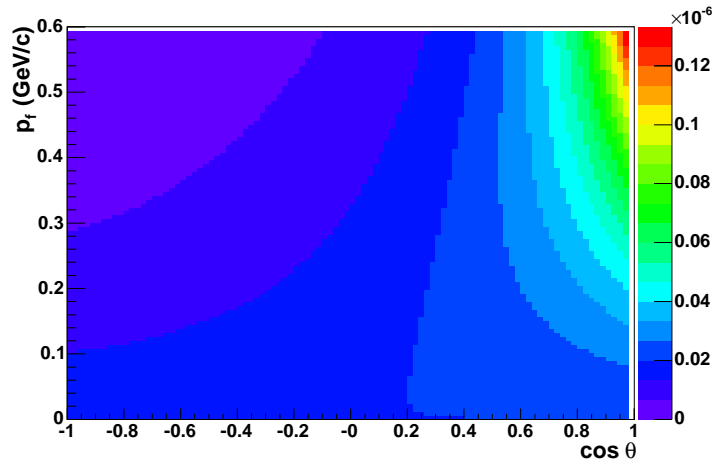


Figure 3.48: Electron-Neutron Scattering: The horizontal axis shows the cosine of the angle between the incident 4.2 GeV electron and the moving nucleon (the angle in the lab frame). The vertical axis shows the magnitude of the Fermi momentum in GeV/c. The color z-axis shows the integrated electron-neutron scattering cross section (in the nucleon rest frame) in units of  $1/\text{GeV}^2$ .

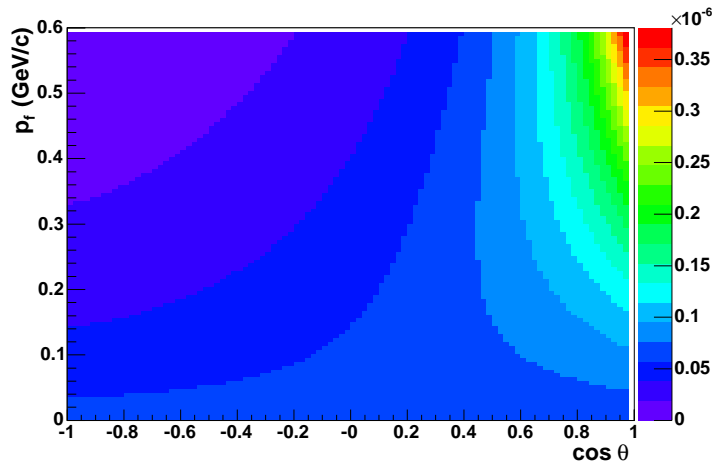


Figure 3.49: Electron-Proton Scattering: The horizontal axis shows the cosine of the angle between the incident 4.2 GeV electron and the moving nucleon (the angle in the lab frame). The vertical axis shows the magnitude of the Fermi momentum in GeV/c. The color z-axis shows the integrated electron-proton scattering cross section (in the nucleon rest frame) in units of  $1/\text{GeV}^2$ .

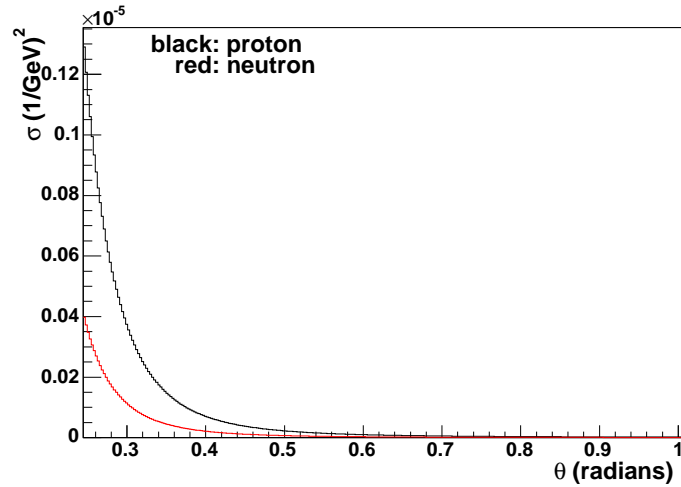


Figure 3.50: The cross-section for elastic electron-proton (black curve) and electron-neutron (red curve) as a function of scattering angle (in radians). The Brash parametrization [38] of the form factors was used. Notice the suppressed zero on the horizontal axis. As  $\theta \rightarrow 0$ ,  $\sigma \rightarrow 0$  for the e-n case, and  $\sigma \rightarrow \infty$  for the e-p case. An incident beam energy of 4.2 GeV was used to generate this figure.

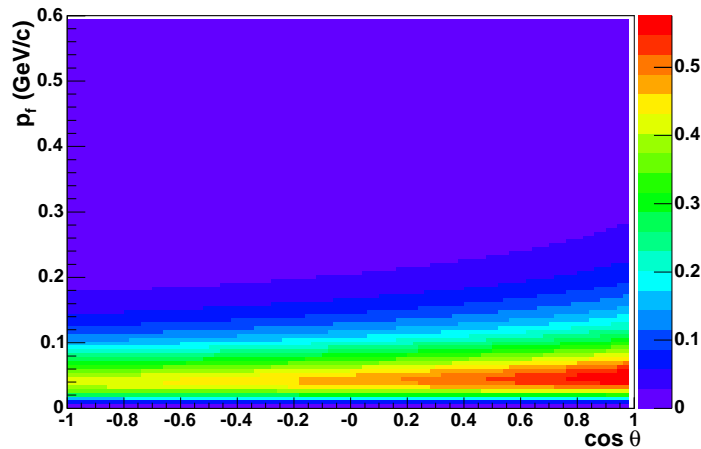


Figure 3.51: Electron-Neutron Scattering: The horizontal axis shows the cosine of the angle between the incident 4.2 GeV electron and the moving nucleon (the angle in the lab frame). The vertical axis shows the magnitude of the Fermi momentum in GeV/c. The color z-axis shows the product of the integrated cross-section and the Hulthen distribution for the electron-neutron case.

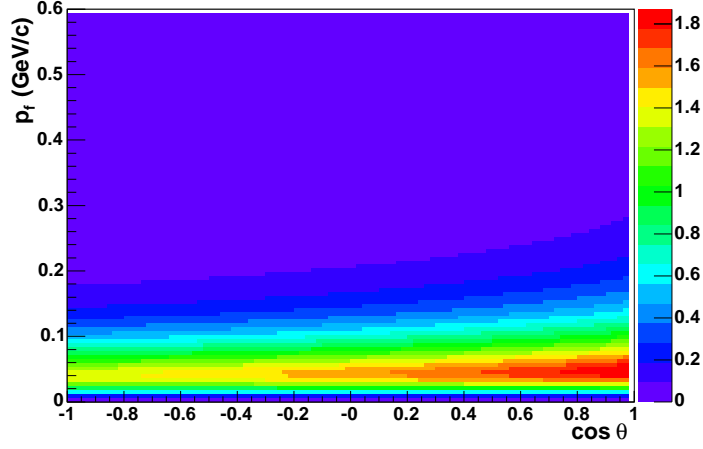


Figure 3.52: Electron-Proton Scattering: The horizontal axis shows the cosine of the angle between the incident 4.2 GeV electron and the moving nucleon (the angle in the lab frame). The vertical axis shows the magnitude of the Fermi momentum in GeV/c. The color z-axis shows the product of the integrated cross-section and the Hulthen distribution for the electron-proton case.

Fermi momentum  $\vec{p}_f$ , the other moving with momentum  $-\vec{p}_f$ . The virtual photon interacts with one of the moving nucleons and the other is unaffected. For simplicity, the nucleons are taken to have the same mass,  $M_N = (1/2)(M_{neutron} + M_{proton})$ . Conservation of energy in the lab frame gives:

$$E_0 + M_D = E_S + E_I + E' \quad (3.76)$$

$$= \sqrt{p_f^2 + M_N^2} + \sqrt{p_I^2 + M_N^2} + E' \quad (3.77)$$

where  $M_D$  is the deuteron mass,  $E_0$  is the incident electron beam energy,  $E_S$  is the energy of the spectator nucleon in the final state,  $E_I$  is the energy of the interacting nucleon in the final state,  $E'$  is the energy of the scattered electron,  $p_f$  is the magnitude of the Fermi momentum and  $p_I$  is the magnitude of the momentum of the interacting nucleon in the final state. Since the virtual photon interacts with only the one nucleon,

$$\vec{p}_I = \vec{p}_f + \vec{q} \quad (3.78)$$

where  $\vec{q}$  is the three-momentum transferred by the virtual photon.

Conservation of momentum in the lab frame gives:

$$E_0 \hat{z} + \vec{p}_f = E' \hat{e} + p_I \hat{n} \quad (3.79)$$

where  $\hat{z}$  is the direction of the incident electron,  $\hat{e}$  is the direction of the scattered electron, and  $\hat{n}$  is the direction of the scattered nucleon (the spectator nucleon has momentum  $-\vec{p}_f$  in the initial and final states).

To generate a quasi-elastic scattering event (either e-n or e-p), a pair of values  $(p_f, \cos \theta)$  are generated randomly, weighted according to the histogram shown in Fig 3.51 for neutrons or Fig 3.52 for protons. The  $\phi$  value for the Fermi momentum is chosen randomly in the range 0 to  $2\pi$ . A rest frame electron scattering angle is chosen randomly according to the distributions shown in Fig 3.50 (with the azimuthal angle taken randomly between 0 and  $2\pi$ ). The rest frame scattering angle is transformed to the lab frame angle using the kinematic relations in Appendix D. This fixes  $\hat{e}$ , the direction of the scattered electron. The solution now proceeds iteratively. A first guess for  $E'$  is made, taking  $E'$  to be equal to the value for an electron *elastically* scattered at the selected scattering angle. With this choice for  $E'$ , Eqn 3.79 can be solved for the scattered nucleon momentum:

$$\vec{p}_I = E_0 \hat{z} + \vec{p}_f - E' \hat{e} \quad (3.80)$$

The value of  $p_I$  determined from the momentum equation is used to derive a new value of  $E'$  from Eqn 3.77. This procedure is iterated until  $|\Delta E'| \leq 0.0001$ , which is usually accomplished in 3 or fewer iterations.

The event generator produces 3-momentum vectors for the scattered electron and scattered nucleon. From the incident and scattered electron 3-momenta,  $W^2$  can be calculated, as well as the virtual photon direction. Fig 3.54 shows a 2-dimensional histogram of event generator output, plotting  $W^2$  vs  $\theta_{pq}$  (the angle between the virtual photon direction and the scattered nucleon direction).

### 3.7.4 Fermi Loss Corrections

The quasi-elastic event generator was used to produce a set of simulated e-n and e-p events. The electron-nucleon vertex position was chosen randomly along the beamline in the z-range of the deuterium target cell,  $-12.5 \leq z \leq -8.25$  cm. The electron was tracked through the magnetic field and was required to strike the active region of the EC.

#### 3.7.4.1 SC Fermi Loss Correction

In either the e-n or e-p case, two histograms were filled. In the first, events in which the nucleon would be *expected* to be found inside the SC acceptance (i.e. to strike an SC paddle whose detection efficiency exceeded the minimum efficiency cut of 0.5% for neutrons or 85% for protons) were binned in  $Q^2$ . The expected nucleon location was calculated using only information taken from the electron kinematics (the only information which would be available in the real data). A second histogram, also binned in  $Q^2$  was filled with events where the scattered nucleon would *actually*

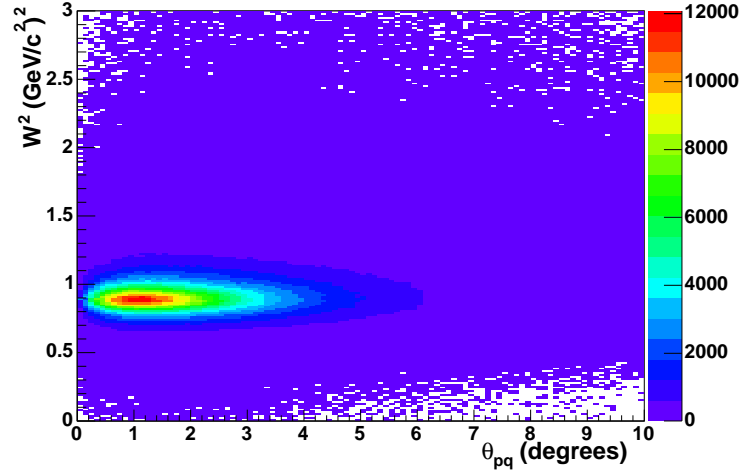


Figure 3.53: Quasi-elastic event generator output. The horizontal axis shows  $\theta_{pq}$  (the angle between the virtual photon direction and the scattered nucleon direction) in degrees. The vertical axis shows  $W^2$  in  $(\text{GeV}/c^2)^2$ . The figure was produced using an incident beam energy of 4.2 GeV and covers  $0.9 \leq Q^2 \leq 4.5 \text{ GeV}/c^2$ .

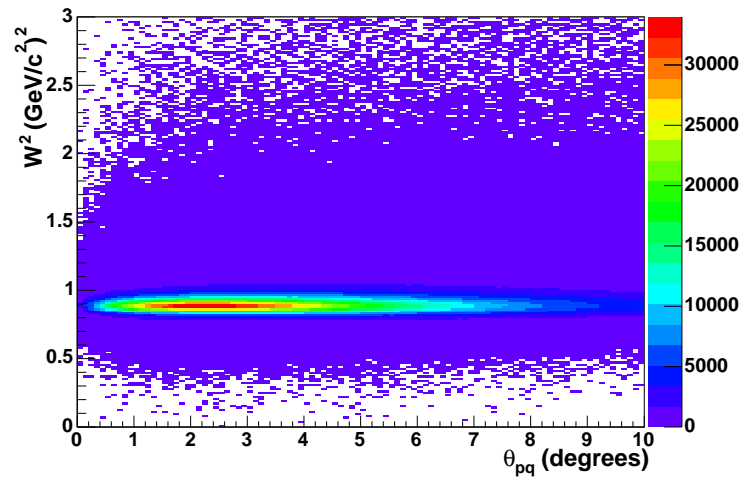


Figure 3.54: Quasi-elastic event generator output. The horizontal axis shows  $\theta_{pq}$  (the angle between the virtual photon direction and the scattered nucleon direction) in degrees. The vertical axis shows  $W^2$  in  $(\text{GeV}/c^2)^2$ . The figure was produced using an incident beam energy of 2.5 GeV and covers  $0.4 \leq Q^2 \leq 2.5 \text{ GeV}/c^2$ .

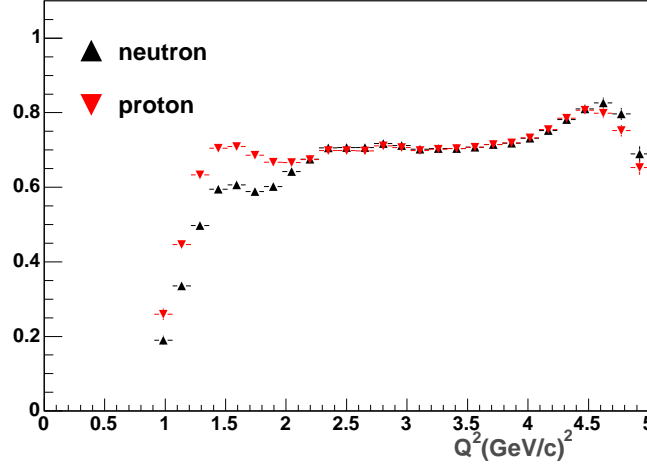


Figure 3.55: The fraction of nucleons scattered at the indicated  $Q^2$  which scattered into the SC acceptance and satisfied the  $\theta_{pq}$  cuts, as determined by the simulation. The black points show the neutron fraction, the red points show the proton fraction. An incident beam energy of 4.2 GeV was used to generate these points.

be found inside the acceptance and satisfy the  $\theta_{pq}$  cuts. This determination used the information about the scattered nucleon 3-momentum from the event generator, information that is *not* available in the real data. The ratio of these two histograms gives the fraction of nucleons that are lost due to the effects of Fermi motion moving the scattered nucleons outside the acceptance. Fig 3.55 shows plots of the loss factor for both neutrons and protons in the 4.2 GeV data set, and Fig 3.56 shows the same for the 2.5 GeV data.

To correct for the effects of the Fermi loss, each  $Q^2$  bin in the e-n/e-p ratio histogram is multiplied by the correction factor determined by the Fermi loss histograms:

$$R_{corrected}^{SC}(Q^2) = \frac{f_{proton}^{SC}(Q^2)}{f_{neutron}^{SC}(Q^2)} R_{observed}^{SC}(Q^2) = f_{fermi}^{SC}(Q^2) R_{observed}^{SC}(Q^2) \quad (3.81)$$

where  $f_{proton}^{SC}$ ,  $f_{neutron}^{SC}$  are taken from the histograms in Fig 3.55 or Fig 3.56. The correction factor for the 4.2 GeV data is shown in Fig 3.57 and for the 2.5 GeV data in Fig 3.58.

### 3.7.4.2 EC Fermi Loss Correction

The Fermi loss correction for the EC was simulated in a fashion analogous to the SC. Two histograms were filled. In the first, events in which the *expected* nucleon satisfied the acceptance matching cuts (the expected neutron intersects the EC and the expected proton strikes an active SC paddle) were binned in  $Q^2$ . In the second,

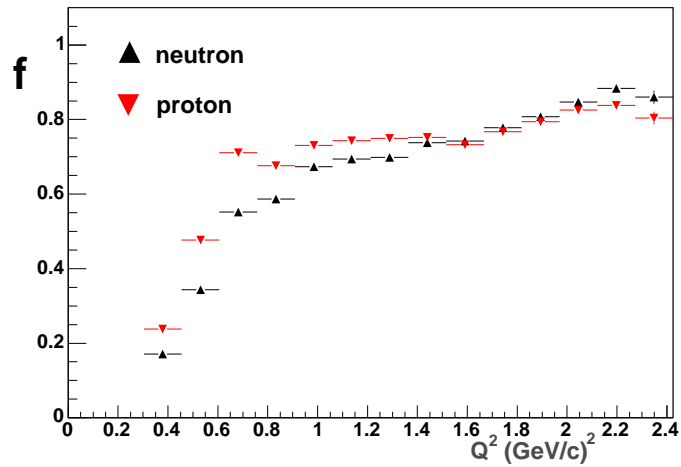


Figure 3.56: The fraction of nucleons scattered at the indicated  $Q^2$  which scattered into the SC acceptance and satisfied the  $\theta_{pq}$  cuts, as determined by the simulation. The black points show the neutron fraction, the red points show the proton fraction. An incident beam energy of 2.5 GeV was used to generate these points.

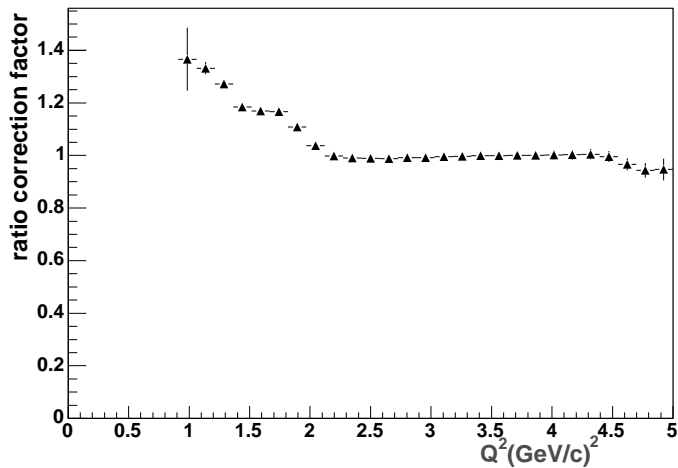


Figure 3.57: The correction factor to the e-n/e-p ratio for Fermi loss in the SC, for the 4.2 GeV data.

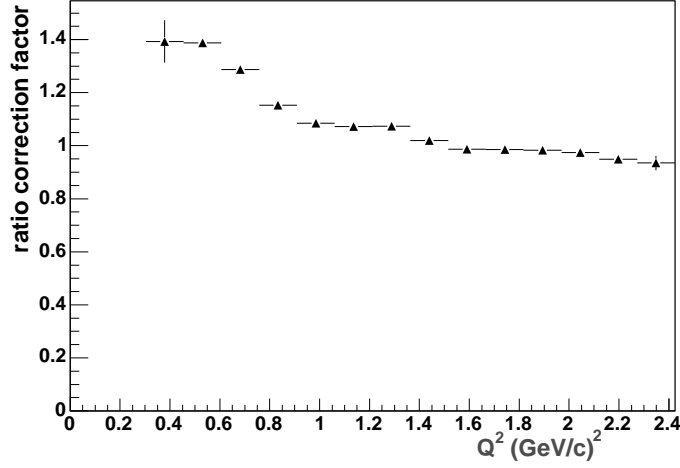


Figure 3.58: The correction factor to the e-n/e-p ratio for Fermi loss in the SC, for the 2.5 GeV data.

events in which the *real* nucleon was found in the acceptance (EC for neutrons, active SC paddle for protons) and satisfied the  $\theta_{pq}$  cut were binned in  $Q^2$ . Fig 3.59 shows the loss factor for protons and neutrons in the 4.2 GeV data set, and Fig 3.60 shows the same for the 2.5 GeV data. The correction to the e-n/e-p ratio for the EC measurement is shown in Fig 3.61 for the 4.2 GeV data, and in Fig 3.62 for the 2.5 GeV data. The Fermi loss correction for the EC is similar to the SC case:

$$R_{corrected}^{EC}(Q^2) = \frac{f_{proton}^{EC}(Q^2)}{f_{neutron}^{EC}(Q^2)} R_{observed}^{EC}(Q^2) = f_{fermi}^{EC}(Q^2) R_{observed}^{EC}(Q^2) \quad (3.82)$$

where  $f_{proton}^{EC}$ ,  $f_{neutron}^{EC}$  are taken from the histograms in Fig 3.59 or Fig 3.60. The correction factor for the 4.2 GeV data is shown in Fig 3.61 and for the 2.5 GeV data in Fig 3.62.

The effect of applying the Fermi loss corrections to the  $\sigma_n/\sigma_p$  ratio histograms are shown in Fig 3.63 for the 4.2 GeV data and in Fig 3.64. Notice that the corrections have removed most of the disagreement between the EC and SC values at low  $Q^2$  in each of the plots. The effect of the Fermi corrections is even more striking when its effect on  $G_M^n$  is considered in Section 4.1.

### 3.7.5 Radiative Corrections

If diagrams beyond the lowest order Born term, containing more than a single virtual or real photon, are considered, the scattering cross section is modified from its single photon value by a multiplicative factor:  $\sigma = \sigma_0(1 + \delta)$ , where  $\sigma_0$  is the single photon

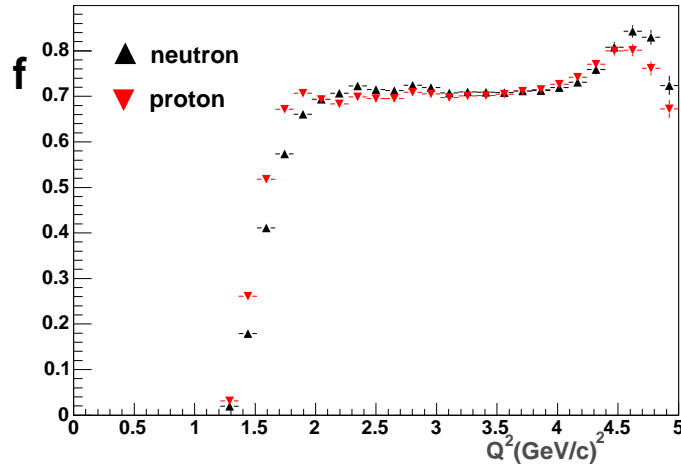


Figure 3.59: The fraction of nucleons scattered at the indicated  $Q^2$  which scattered into the EC acceptance and satisfied the  $\theta_{pq}$  cuts, as determined by the simulation. The black points show the neutron fraction, the red points show the proton fraction. An incident beam energy of 4.2 GeV was used to generate these points.

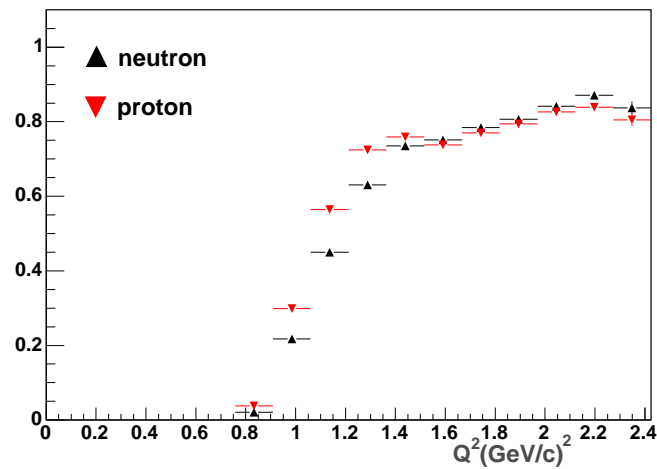


Figure 3.60: The fraction of nucleons scattered at the indicated  $Q^2$  which scattered into the EC acceptance and satisfied the  $\theta_{pq}$  cuts, as determined by the simulation. The black points show the neutron fraction, the red points show the proton fraction. An incident beam energy of 2.5 GeV was used to generate these points.

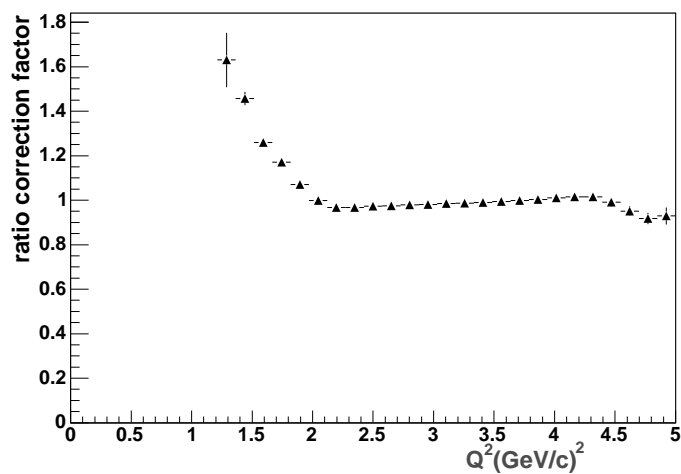


Figure 3.61: The correction factor to the e-n/e-p ratio for Fermi loss in the EC, for the 4.2 GeV data.

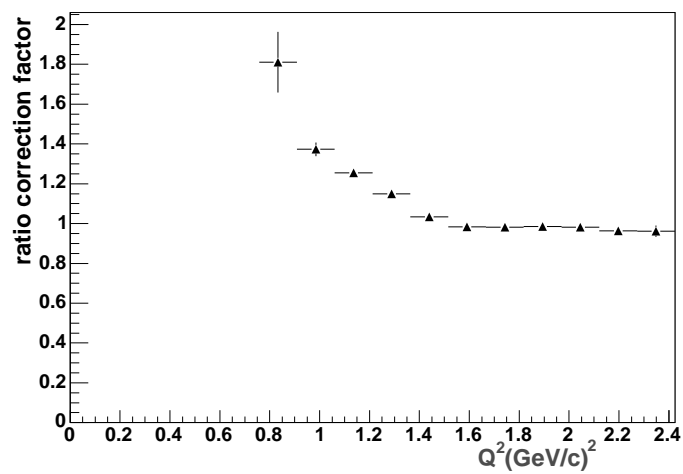


Figure 3.62: The correction factor to the e-n/e-p ratio for Fermi loss in the EC, for the 2.5 GeV data.

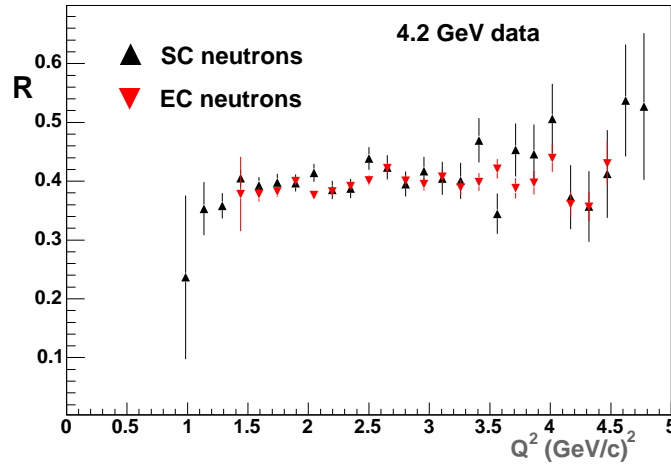


Figure 3.63: The  $\sigma_n/\sigma_p$  ratio  $R$ , as measured in the 4.2 GeV data set for both EC neutrons (red triangles) and SC neutrons (black triangles), binned in  $Q^2$ . The Fermi loss corrections have been applied.

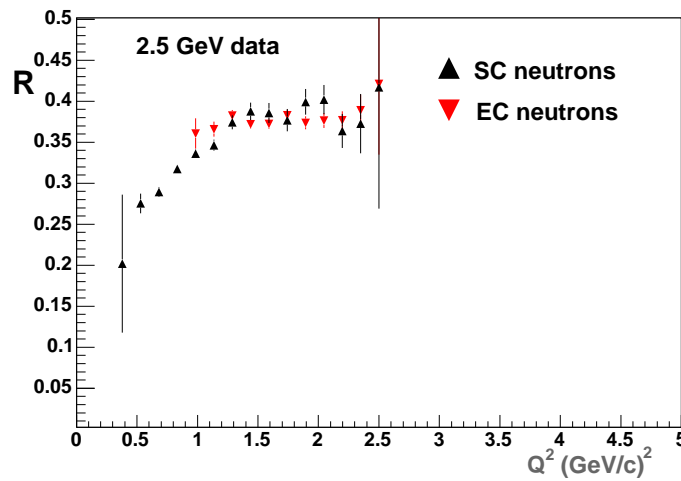


Figure 3.64: The  $\sigma_n/\sigma_p$  ratio  $R$ , as measured in the 2.5 GeV data set for both EC neutrons (red triangles) and SC neutrons (black triangles), binned in  $Q^2$ . The Fermi loss corrections have been applied.

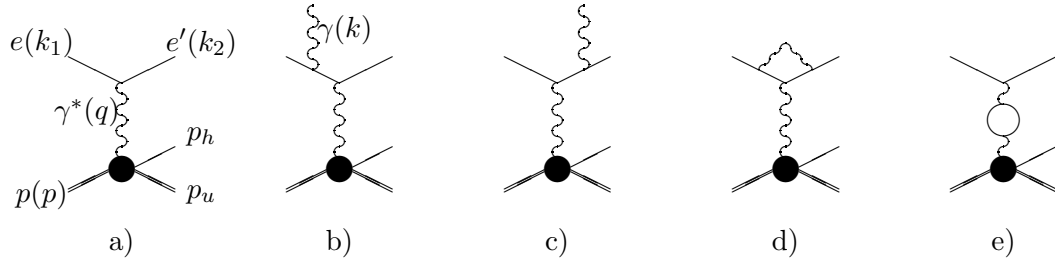


Figure 3.65: Feynman diagrams contributing to the Born and the next-order cross sections. a) Born process, b) and c) Bremsstrahlung, d) Vertex correction, and e) Vacuum polarization.  $p_h$  is the momentum of the detected hadron,  $p_u$  is the momentum of the undetected hadron.

exchange cross-section, and  $\delta$  is due to the effect of higher-order diagrams. Various schemes for computing the correction factor  $(1 + \delta)$  have been put forward.

The traditional Mo and Tsai [39] approach to radiative corrections was developed for use in *inclusive* scattering, and cannot properly be applied to the scattering measurement from which  $G_M^n$  is extracted. The measurement of the quasi-elastically scattered hadron, in addition to the electron, reduces the phase space allowed for the radiated photon. In addition, only two structure functions contribute in the case of exclusive scattering, while for unpolarized inclusive scattering, four structure functions can contribute.

The radiative corrections for this analysis were performed using the approach of Afanasev *et al.* [40], which was originally developed for exclusive pion electroproduction. The model includes, in addition to the Born term, diagrams for initial and final state electron Bremsstrahlung, electron vertex correction, and vacuum polarization. The diagrams included are shown in Fig 3.65. Note that two-photon exchange diagrams are not included.

Afanasev *et al.* wrote a computer code EXCLURAD to numerically evaluate the radiative corrections. The EXCLURAD code generates the ratio of the radiated cross section at a given value of  $Q^2, W, \cos \theta_{pq}, \phi_{pq}$  to the PWIA result ( $\theta_{pq}, \phi_{pq}$  are the polar and azimuthal angles between the virtual photon direction and the direction of the detected hadron). For the  $G_M^n$  analysis, the reactions of interest are  $D(e, e'p)n$  and  $d(e, e'n)p$ , not pion production on a proton target. To accommodate the change in final state hadron species, the EXCLURAD code was modified. The masses of the target, detected and undetected final state hadrons were changed to values appropriate for deuteron breakup. The DEEP code of Van Orden *et al.* [41], a relativistic deuteron model, was installed to calculate response functions at the deuteron-virtual photon vertex.

The EXCLURAD/DEEP code was used to generate surfaces in  $\cos \theta_{pq}$  and  $\phi_{pq}$  at a variety of  $Q^2$  points, as shown in Fig 3.66. At each  $Q^2$  value, this surface is

Table 3.7: Radiative correction values for 2.5 GeV data.

$Q^2$	$1 + \delta_n$	$1 + \delta_p$	$f_{rad}$
1	0.7956	0.7957	0.9999
2.35	0.8273	0.8273	1.0000
2.45	0.8421	0.8424	0.9996
2.55	0.8568	0.8583	0.9983

Table 3.8: Radiative correction values for 4.2 GeV data.

$Q^2$	$1 + \delta_n$	$1 + \delta_p$	$f_{rad}$
4.0	0.82691	0.82691	1.0000
5.0	0.85310	0.85310	1.0000

integrated over the range of  $\cos\theta_{pq}$  accepted for that  $Q^2$  (see previous section) and over the full range of  $\phi_{pq}$  (Monte Carlo studies and analysis of the quasi-elastic data both confirm the full  $\phi_{pq}$  coverage of the detector). The calculation at each  $Q^2$  point is performed twice, once for the case where the detected hadron is the proton, once for the case where the detected hadron is the neutron. Note that while the radiative correction factor ( $1+\delta$ ) may be as large as 1.3 for either of the two final states, what is required for the  $G_M^m$  analysis is the ratio of the  $D(e, e'p)n$  and  $D(e, e'n)p$  corrections:

$$f_{radiative}(Q^2) = \frac{1 + \delta_n(Q^2)}{1 + \delta_p(Q^2)} \quad (3.83)$$

where the subscript indicates either the correction to the cross section ratio (*radiative*), or the hadron species (n,p). The corrections to the two hadron species, while individually large in some cases, are numerically close to each other. This is shown in Fig 3.67. The ratio of the curves in Fig 3.67 is shown in Fig 3.68. The radiative correction factors  $1 + \delta_n$ ,  $1 + \delta_p$  and  $f_{radiative}$  are shown for several  $Q^2$  points in Table 3.7 for the 2.5 GeV data and in Table 3.8 for the 4.2 GeV data. The largest radiative correction value seen in the two tables is 0.9983. The radiative correction at each value of  $Q^2$  was taken to be exactly unity, with a systematic uncertainty of 0.17% assigned at each value of  $Q^2$ .

### 3.7.6 Nuclear Corrections

The quantity of interest in this analysis is the ratio of e-n/e-p scattering from *free* nucleons. What is measured is the quasi-elastic e-n/e-p ratio from nucleons bound in the deuteron. This quantity is related to the measured ratio by a correction factor:

$$R_{corrected}(Q^2) = f_{nuclear}(Q^2)R_{observed}(Q^2) \quad (3.84)$$

The correction factor  $f_{nuclear}(Q^2)$  must be determined by theoretical calculation. It would be ideal to perform this calculation in a fully relativistic framework, starting

$$E=4.232 \text{ GeV}, W=2.417 \text{ GeV}, Q^2=4.0 \text{ GeV}^2$$

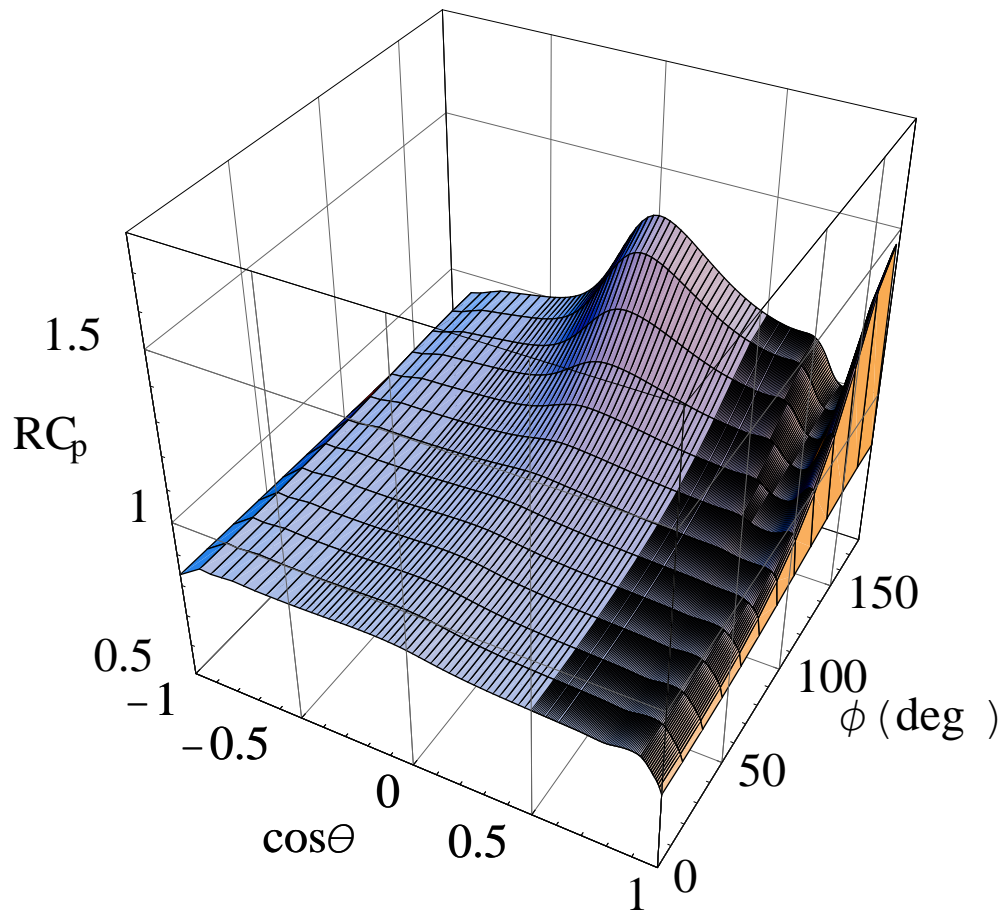


Figure 3.66: Radiative correction for quasi-elastic  $D(e, e'p)n$  scattering as a function of  $\cos\theta_{pq}$  and  $\phi_{pq}$ . The figure was made using an incident beam energy of 4.23 GeV, and shows the correction for scattering at  $Q^2 = 4.0 \text{ GeV}^2$

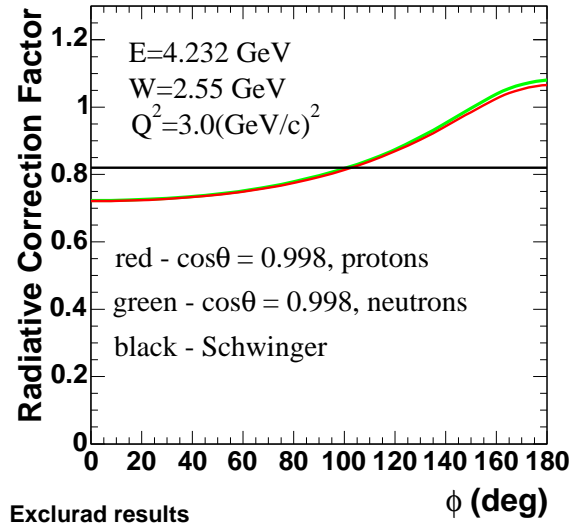


Figure 3.67: A comparison of the radiative correction factor for  $D(e, e'p)n$  and  $D(e, e'n)p$ , as a function of  $\phi_{pq}$ . The curves shown were generated for a beam energy of 4.232 GeV and  $Q^2$  of 3.0 (GeV/c)<sup>2</sup>. Also shown for comparison are the results of the Schwinger model [42], which calculates the correction for inclusive scattering off a fixed potential.

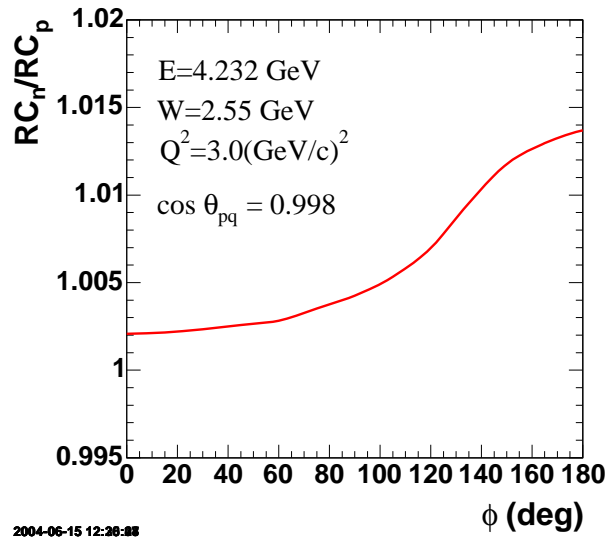


Figure 3.68: The ratio of the  $D(e, e'p)n$  and  $D(e, e'n)p$  radiative correction curves shown in Fig. 3.67. When averaged over  $\phi_{pq}$ , this curve gives the radiative correction to the quasi-elastic ratio at  $Q^2 = 3.0(\text{GeV}/c)^2$ .

from a Lagrangian. Such an approach would automatically include a proper relativistic treatment of the nuclear dynamics and electromagnetic current. However, a fully relativistic treatment is not available. In practice, electron scattering from nuclei is usually treated by taking the nuclear initial state as the solution to a bound-state Schrodinger equation, and the final state is calculated using optical potentials or a multiple-scattering approach. The electromagnetic current is subjected to a non-relativistic reduction in this case. The theoretical calculations for this analysis were carried out by Jeschonnek [43], using the procedure described in [44], [45], [46], and by Arenhövel [47].

For relativistic scattering, the cross-section in the lab frame can be written as [48]:

$$\left( \frac{d\sigma^5}{d\epsilon' d\Omega_e d\Omega_N} \right)_{fi}^h = \frac{m_N m_f p_N}{8\pi^3 m_i} \sigma_{Mott} f_{rec}^{-1} \left[ (v_L R_{fi}^L + v_T R_{fi}^T + v_{TT} R_{fi}^{TT} + v_{TL} R_{fi}^{TL}) + h (v_{T'} R_{fi}^{T'} + v_{TL'} R_{fi}^{TL'}) \right], \quad (3.85)$$

where  $m_i$ ,  $m_N$  and  $m_f$  are the masses of the target nucleus, the ejectile nucleon and the residual system,  $p_N$  and  $\Omega_N$  are the momentum and solid angle of the ejectile,  $\epsilon'$  is the energy of the detected electron and  $\Omega_e$  is its solid angle. The helicity of the electron is denoted by  $h$ . The Mott cross section is (setting  $\hbar = c = 1$ ):

$$\sigma_{Mott} = \left( \frac{\alpha \cos(\theta_e/2)}{2\varepsilon \sin^2(\theta_e/2)} \right)^2 \quad (3.86)$$

and the recoil factor is given by

$$f_{rec} = \left| 1 + \frac{\omega p_x - E_x q \cos \theta_x}{m_i p_x} \right|. \quad (3.87)$$

The coefficients  $v_k$  are constructed from elements of the lepton tensor, and convey information about the polarization state of the virtual photon (for example, the  $v_{LT}$  term is generated by interference between longitudinal and transverse modes of the virtual photon). The  $R^k$  are the nuclear response functions and contain information on the nucleon electromagnetic current. In terms of the nucleon current 4-vector  $(\rho, \vec{J})$ , the  $R^k$  are:

$$\begin{aligned} R_{fi}^L &\equiv |\rho(\vec{q})_{fi}|^2 \\ R_{fi}^T &\equiv |J_+(\vec{q})_{fi}|^2 + |J_-(\vec{q})_{fi}|^2 \\ R_{fi}^{TT} &\equiv 2 \Re [J_+(\vec{q})_{fi} J_-(\vec{q})_{fi}] \\ R_{fi}^{TL} &\equiv -2 \Re [\rho^*(\vec{q})_{fi} (J_+(\vec{q})_{fi} - J_-(\vec{q})_{fi})] \\ R_{fi}^{T'} &\equiv |J_+(\vec{q})_{fi}|^2 - |J_-(\vec{q})_{fi}|^2 \\ R_{fi}^{TL'} &\equiv -2 \Re [\rho^*(\vec{q})_{fi} (J_+(\vec{q})_{fi} + J_-(\vec{q})_{fi})], \end{aligned} \quad (3.88)$$

The  $J_{\pm}$  are the spherical components of the current 3-vector [49].

In the non-relativistic case, the lab-frame cross-section in the Plane-Wave Impulse Approximation(PWIA) can be written:

$$\frac{d^5\sigma}{d\epsilon' d\Omega_e d\Omega_N} = \frac{m_N m_f p_N}{m_i} \sigma_{eN} f_{rec}^{-1} n(\vec{p}), \quad (3.89)$$

where  $n(\vec{p})$  is the nucleon momentum distribution (evaluated at the value of  $\vec{p}$  determined by the reaction kinematics), and the  $eN$  cross section is given by

$$\sigma_{eN} = \sigma_{Mott} \sum_k v_k R_k^{sn}. \quad (3.90)$$

The  $sn$  superscript indicates the single-nucleon response function. The single-nucleon response functions are related to the nuclear responses by

$$R_K^{nucleus} = (2\pi)^3 R_k^{single\ nucleon} n(\vec{p}) \quad (3.91)$$

Combining these, one has:

$$\frac{d^5\sigma}{d\epsilon' d\Omega_e d\Omega_N} = \frac{m_N m_f p_N}{m_i} f_{rec}^{-1} \sigma_{Mott} n(\vec{p}) \sum_k v_k R_k^{single\ nucleon} \quad (3.92)$$

The momentum distribution  $n(\vec{p})$  is obtained by Fourier transform of the nuclear wave function:

$$n(\vec{p}) = \frac{1}{2\pi^2} (u(p)^2 + w(p)^2) \quad (3.93)$$

where  $u(p), w(p)$  are the S-wave and D-wave components of the deuteron wave function in momentum space, and the normalization condition is

$$\int d^3\vec{p} n(\vec{p}) = 1 \quad (3.94)$$

The AV18 deuteron wave function [50] was used in the calculation.

The electromagnetic current operator for the nucleon is given by:

$$J^\mu(P\Lambda; P'\Lambda') = \bar{u}(P'\Lambda') \left[ F_1 \gamma^\mu + \frac{i}{2m_N} F_2 \sigma^{\mu\nu} Q_\nu \right] u(P\Lambda) \quad (3.95)$$

where  $P, P'$  indicate the four-momenta of the nucleon, and  $\Lambda, \Lambda'$  indicate the nucleon spin state. A non-relativistic reduction of the current operator is carried out in [45], after which the nuclear response functions can be written in terms of the Sachs form-

factors:

$$\begin{aligned}
R_L^{sn} &= f_o^2(\xi_o^2 + \kappa^2\delta^2\xi_o'^2) \\
&= \frac{\kappa^2}{\tau}(G_E^2 + \delta^2W_2) \\
R_T^{sn} &= f_o^2(2\kappa^2\xi_1'^2 + \kappa^4\delta^2\xi_2'^2 + \delta^2\xi_1^2 + \kappa^2\delta^4\xi_3'^2 - 2\kappa^2\delta^2\xi_1'\xi_3') \\
&= 2W_1 + \delta^2W_2 \\
R_{TT}^{sn} &= f_o^2(\kappa^4\delta^2\xi_2'^2 + 2\kappa^2\delta^2\xi_1'\xi_3' - \delta^2\xi_1^2 - \kappa^2\delta^4\xi_3'^2) \cos(2\varphi) \\
&= -\delta^2W_2 \cos(2\varphi) \\
R_{TL}^{sn} &= 2\sqrt{2} \cos(\varphi) f_o^2(\delta\xi_o\xi_1 + \kappa^2\delta\xi_o'(\xi_1' - \delta^2\xi_3')) \\
&= 2\sqrt{2} \cos(\varphi) \frac{\kappa}{\sqrt{\tau}} \sqrt{1 + \tau + \delta^2} \delta W_2
\end{aligned} \tag{3.96}$$

where the  $W_1 = \tau G_M^2$  and  $W_2 = \frac{1}{1+\tau}(G_E^2 + \tau G_M^2)$ . The other factors are kinematic terms:

$$\begin{aligned}
\kappa &= \frac{|\vec{q}|}{2m_N} \\
\delta &= \frac{p_\perp}{m_N} \\
\lambda &= \frac{\omega}{2m_N} \\
\tau &= \kappa^2 - \lambda^2 = \frac{Q^2}{(2M_N)^2}
\end{aligned} \tag{3.97}$$

The dipole parametrization was used for all form factors in the calculation, except  $G_E^m$  which was set to 0.

It is possible for the struck nucleon to interact strongly with other nucleons as it exits the nucleus, as shown in Fig 3.69. The inclusion of Final-State Interactions (FSI) changes the matrix element of interest from  $\mathcal{M}_{fi} = \langle f | J_{em} | i \rangle$  to  $\mathcal{M}_{fi} = \langle f | S J_{em} | i \rangle$ , where  $S$  is the FSI operator. The final-state interactions were calculated in the context of Glauber theory [46]. In this framework, the FSI operator for interaction with a single spectator nucleon takes the form:

$$S(\vec{r}) = 1 - \theta(z) \cdot \Gamma(\vec{b}), \tag{3.98}$$

where the distance  $\vec{r}$  between the two interacting nucleons is decomposed into longitudinal and transverse parts:  $\vec{r} = \vec{b} + z \cdot \hat{q}$ , where  $\hat{q}$  indicates the direction of the virtual photon's momentum. The  $\theta$  function restricts the interaction to nucleons in the struck nucleon's forward hemisphere.  $\Gamma(b)$  is called the profile function, and is related to the nucleon-nucleon scattering amplitude via a Fourier transform:

$$\Gamma(\vec{b}) = \frac{1}{2\pi i k} \int d^2 \vec{l} \exp(-i\vec{l} \cdot \vec{b}) f(\vec{l}). \tag{3.99}$$

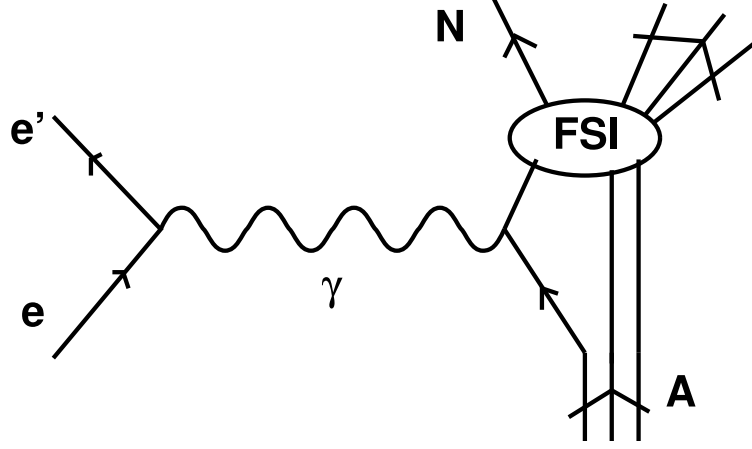


Figure 3.69: Diagrammatic representation of final-state interactions in the  $A(e,e'N)A-1$  single nucleon knockout reaction. The figure is from [46].

where  $\vec{k}$  is the incident nucleon momentum,  $\vec{k}'$  is the outgoing nucleon's momentum, and  $\vec{l} = \vec{k} - \vec{k}'$  is the momentum transferred in the nucleon-nucleon scattering. The most general form for the NN scattering amplitude (subject to the constraints of parity conservation, isospin invariance and the Pauli principle) is given by:

$$f(\vec{l}) = A(\vec{l}) + B(\vec{l}) (\vec{\sigma}_1 + \vec{\sigma}_2) \cdot \hat{n} + C(\vec{l}) (\vec{\sigma}_1 \cdot \hat{n}) (\vec{\sigma}_2 \cdot \hat{n}) + D(\vec{l}) (\vec{\sigma}_1 \cdot \hat{m}) (\vec{\sigma}_2 \cdot \hat{m}) + E(\vec{l}) (\vec{\sigma}_1 \cdot \hat{h}) (\vec{\sigma}_2 \cdot \hat{h}). \quad (3.100)$$

The nucleon spin operators are denoted by  $\vec{\sigma}_1$  and  $\vec{\sigma}_2$ , and  $\hat{n} \equiv \vec{k} \times \vec{k}' / |\vec{k} \times \vec{k}'|$ ,  $\hat{m} \equiv (\vec{k} - \vec{k}') / |\vec{k} - \vec{k}'|$ , and  $\hat{h} \equiv (\vec{k} + \vec{k}') / |\vec{k} + \vec{k}'|$ . In the approach used in [46], the amplitudes  $C, D, E$  are neglected (many implementations of Glauber theory also neglect  $B$ , keeping only the central amplitude  $A$ ), keeping only the central and spin-orbit terms  $A(l)$  and  $B(l)$ , which are parametrized in term of the results of phase shift analysis of NN scattering data:

$$A(l) = \frac{k \sigma_{tot}^{NN}}{4\pi} (\rho + i) \exp(-0.5 l^2 b_o^2) \quad (3.101)$$

$$(3.102)$$

where  $\sigma_{tot}^{NN}$  is the total NN cross-section,  $b_o$  is the diffractive slope and  $\rho$  is the ratio of the real to imaginary parts of the forward elastic amplitude.  $B(l)$  is parametrized in a similar fashion. The inclusion of the spin-orbit amplitude  $B(l)$  is significant for calculating FSI effects in the extraction of the  $R_{TT}$  and  $R_{LT}$  structure functions, but is not significant for the e-n/e-p ratio measurement since the TT and LT structure functions only contribute the total cross-section at the 1% level.

With a model chosen for the nuclear ground state and a prescription for the non-relativistic reduction of the electromagnetic current and a treatment of the final-state

Table 3.9: Nuclear corrections to e-n/e-p ratio from the Jeschonnek model.

$Q^2$	$f_{nuclear}$
1	0.999796
2	0.999714
3	0.999655
4	0.999624
5	0.999619

interactions, the correction to the ratio measurement was calculated by evaluating the ratio  $\sigma_{Full}/\sigma_{PWIA}$  for e-n and e-p scattering, where the “Full” calculations includes all FSI. The ratio of the e-n to e-p correction factors was taken, yielding the correction factor for the e-n/e-p ratio. The results for the 4.2 GeV beam energy are shown in Table 3.9.

The Jeschonnek model is not expected to be valid below  $Q^2 = 1$  (GeV/c)<sup>2</sup> at the lowest. The corrections at lower  $Q^2$  were supplied by the Arenhövel model [47]. The Arenhövel model is a non-relativistic deuteron electro-disintegration model. The Plane Wave Born Approximation (PWBA) is used. The PWBA is similar to the PWIA, but it also includes diagrams where the detected nucleon was *not* the struck nucleon. These diagrams are significant only at low- $Q^2$ . The model includes a treatment final-state interactions, and correction for relativistic effects. Some features not present in the Jeschonnek model are meson-exchange currents (MEC) to account for the possibility of the virtual photon coupling to mesons inside the deuteron, and isobar configurations (IC) to describe the virtual excitation of nucleon resonances, such as  $N\Delta$  or  $\Delta\Delta$ . The Bonn potential is used to model the nucleon-nucleon interaction. The correction factors were derived by comparing the full calculation to the PWBA(no FSI,MC,IC) in the quasi-elastic region. The calculated cross sections were integrated over a range of  $\theta_{pq}$  values used in the analysis, and the ratio of the full-to-PWBA integrated cross sections ratios for the neutron and proton was calculated. The results of the calculation are shown in Fig 3.70.

The Arenhövel model is not expected to be valid above  $Q^2 = 1$  (GeV/c)<sup>2</sup>. The predicted correction factors for the 2.5 GeV beam energy are shown in Table 3.10. Calculations for the 4.2 GeV beam energy were available only at one  $Q^2$  value,  $Q^2 = 0.811$ (GeV/c)<sup>2</sup>. The correction values for the two beam energies are shown in Fig 3.71. The figure shows a second order polynomial fit to the 2.5 GeV calculations, and the lone 4.2 GeV calculation. The nuclear correction at both beam energies will be performed using the fit shown in Fig 3.71.

It is seen that the two models disagree at  $Q^2 = 1$ (GeV/c)<sup>2</sup>, which is at the edge of the expected validity for both models. At  $Q^2 = 1$  (GeV/c)<sup>2</sup>, the average correction is 0.994, or a 0.6% correction. The average correction was used at this  $Q^2$  point, with a 100% uncertainty on the correction, so that a systematic uncertainty of 0.6% was assigned to the correction factor. This 0.6% systematic error was assigned to the

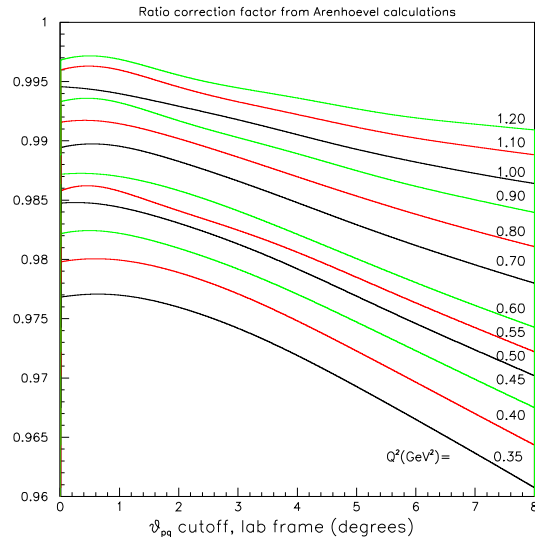


Figure 3.70: The e-n/e-p ratio correction factor, from the Arenhövel model, as a function of the  $\theta_{pq}$  cutoff, for several values of  $Q^2$ . The data shown is for the 2.5 GeV beam energy. The figure is from [51]

Table 3.10: Nuclear corrections to e-n/e-p ratio from the Arenhovel model, for a 2.5 GeV beam energy.

$Q^2$	$f_{nuclear}$
0.5	0.977
0.75	0.983
1.0	0.989
1.2	0.993

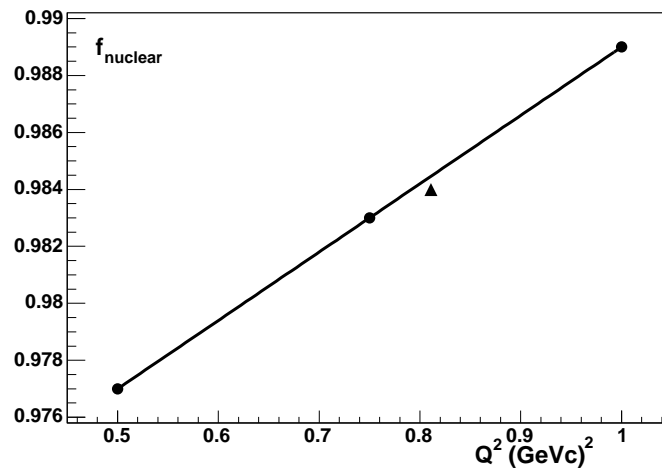


Figure 3.71: Nuclear correction factor for a 2.5 GeV energy beam (circles), and a 4.2 GeV beam (triangle). The curve is a second order polynomial fit to the 2.5 GeV points.

correction factor at all values of  $Q^2$ .

# Chapter 4

## Experiment Results

### 4.1 $G_M^n$ extraction from ratio

The corrected n/p ratio,

$$R_{corrected}(Q^2) = f_{nuclear}(Q^2)f_{radiative}(Q^2)f_{fermi}(Q^2)R_{observed}(Q^2) \quad (4.1)$$

is related to  $G_M^n$  through Eqn 1.12:

$$R_{corrected} = \frac{\sigma_{mott}^n \left( G_{E,n}^2 + \frac{\tau_n}{\epsilon_n} G_{M,n}^2 \right) \left( \frac{1}{1+\tau_n} \right)}{\sigma_{mott}^p \left( G_{E,p}^2 + \frac{\tau_p}{\epsilon_p} G_{M,p}^2 \right) \left( \frac{1}{1+\tau_p} \right)} \quad (4.2)$$

where super- or subscript  $n,p$  denote neutron or proton quantities. The kinematic variable  $\tau, \epsilon$  and the Mott cross section  $\sigma_{mott}$  are as previously defined.  $Q^2$  dependence of all quantities is assumed. Solving the equation above for  $G_M^n$  gives:

$$G_M^n = \sqrt{\left[ R_{corrected} \left( \frac{\sigma_{mott}^p}{\sigma_{mott}^n} \right) \left( \frac{1 + \tau_n}{1 + \tau_p} \right) \left( G_{E,p}^2 + \frac{\tau_p}{\epsilon_p} G_{M,p}^2 \right) - G_{E,n}^2 \right] \frac{\epsilon_n}{\tau_n}} \quad (4.3)$$

The Arrington parametrization [52] was used to evaluate the proton form factors and the Galster parametrization was used for  $G_E^n$ .

The  $G_M^n$  extraction was performed separately for each of the four measurements (2.5 and 4.2 GeV beam energy, SC and EC neutron detection). These four measurements are essentially independent. Two independent detector systems were used for detection of neutrons. Protons were detected in the DC/SC in all cases, however different regions of the drift chambers and SC panel were sampled at the two different beam energies. A comparison of the results from the four extractions is shown in Fig 4.1. The overlap of the four semi-independent measurements over a range of  $Q^2$  values suggests that systematic errors are under control. The necessity of applying the Fermi-momentum correction is shown by Fig 4.2, which shows a comparison of the four  $G_M^n$  measurements with *no* Fermi corrections applied.

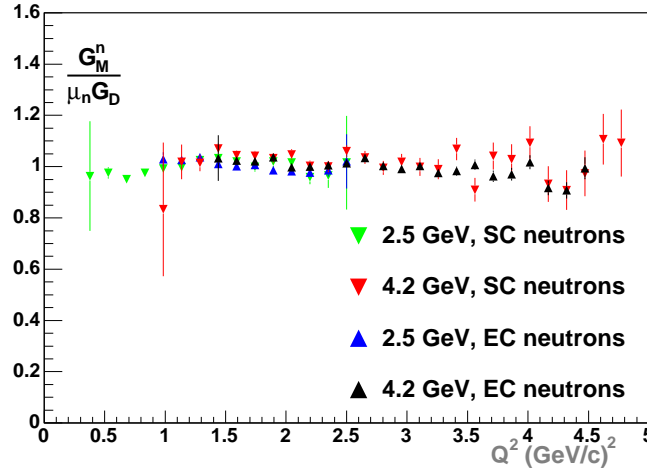


Figure 4.1: Comparison of  $G_M^n$  as a function of  $Q^2$  for four different measurements.  $G_M^n$  has been scaled to the dipole in this figure.

The  $G_M^n$  data from the four separate measurements were combined to form a weighted average. The weighting in each  $Q^2$  bin was chosen to minimize:

$$\chi^2 = \sum_j \frac{(x_j - \bar{x})^2}{\sigma_j^2} \quad (4.4)$$

where  $x_j$  and  $\sigma_j$  are the  $G_M^n$  value and statistical error associated with the  $j^{\text{th}}$  measurement contributing in that  $Q^2$  bin ( $j$  is an integer between 1 and 4). Setting  $\partial\chi^2/\partial\bar{x} = 0$  in Eqn 4.4 and solving for  $\bar{x}$  gives:

$$\bar{x} = \frac{\sum_j \frac{x_j}{\sigma_j^2}}{\sum_j \frac{1}{\sigma_j^2}} \quad (4.5)$$

The statistical error on each point in the weighted average was determined from:

$$\sigma_{\bar{x}}^2 = \sum_j \left(\frac{\partial\bar{x}}{\partial x_j}\right)^2 \sigma_j^2 \quad (4.6)$$

$$= \frac{1}{\sum_j \frac{1}{\sigma_j^2}} \quad (4.7)$$

The combined  $G_M^n$  histogram is shown in Fig 4.3. Tables giving numerical values for the four individual measurements, and the weighted average are shown in Appendix A.

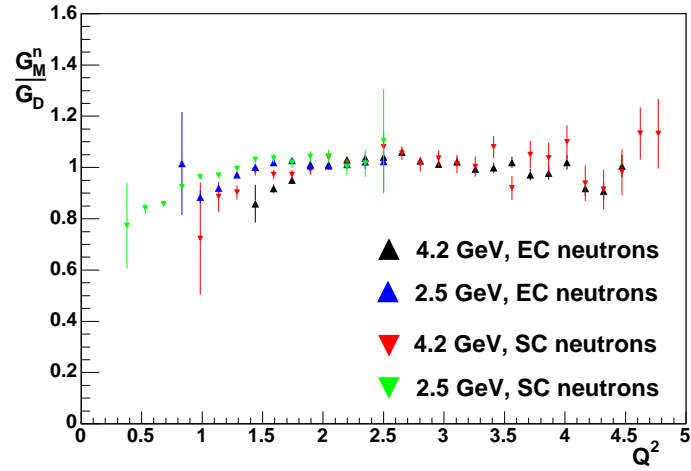


Figure 4.2: Comparison of  $G_M^n$  as a function of  $Q^2$  for four different measurements. The Fermi correction have *not* been applied.

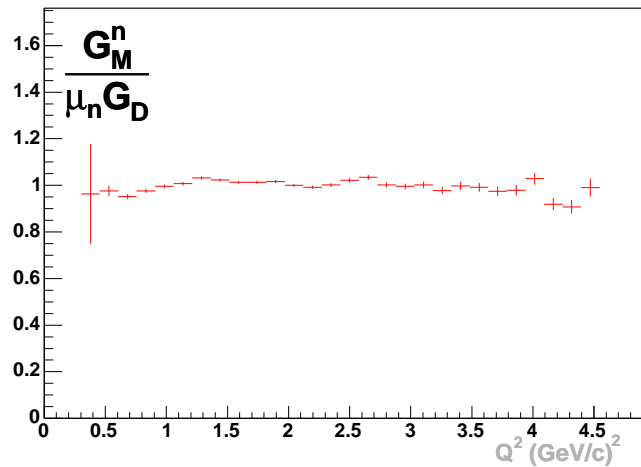


Figure 4.3: Weighted average  $G_M^n$ , binned in  $Q^2$  obtained by combining data from the four separate  $G_M^n$  measurements.  $G_M^n$  has been scaled to the dipole.

## 4.2 Systematic Errors

For the purpose of evaluating systematic errors, Eqn 4.3 can be simplified to:

$$G_M^n = \sqrt{(\sigma_p R_c - G_{E,n}^2) \frac{\epsilon}{\tau}} \quad (4.8)$$

by making the approximations

$$\frac{\sigma_{mott}^p}{\sigma_{mott}^n} \approx 1 \quad (4.9)$$

$$\frac{1 + \tau_n}{1 + \tau_p} \approx 1. \quad (4.10)$$

In Eqn 4.8,  $\sigma_p$  is the reduced proton cross section,  $\sigma_p = G_{E,p}^2 + \frac{\tau}{\epsilon} G_{M,p}^2$  and  $R_c$  is the corrected ratio. The corrected ratio is a function of a variety of parameters (location of cuts on missing mass in the calibration reaction, choice of cuts on  $\theta_{pq}$ ,  $W^2$ , acceptance matching, radiative correction, etc). This dependence on multiple parameters is summarized by writing:

$$R_c = R_c(\vec{f}). \quad (4.11)$$

All of the terms in Eqn 4.8 are understood to have a  $Q^2$  dependence.

The standard propagation of errors formula is applied:

$$(\delta G_M^n)^2 = \left(\frac{\partial G_M^n}{\partial \sigma_p}\right)^2 (\delta \sigma_p)^2 + \left(\frac{\partial G_M^n}{\partial G_E^n}\right)^2 (\delta G_E^n)^2 + \sum_i \left(\frac{\partial G_M^n}{\partial f_i}\right)^2 (\delta f_i)^2. \quad (4.12)$$

The errors are taken to be uncorrelated, so terms of the form  $\frac{\partial^2 G_M^n}{\partial a \partial b}$  are not considered.

### 4.2.1 Systematic error due to uncertainty in Proton cross-section

Consider the  $\sigma_p$  term in Eqn 4.12:

$$(\delta G_M^n)_p = \frac{\partial G_M^n}{\partial \sigma_p} \delta \sigma_p. \quad (4.13)$$

We have:

$$\frac{\partial G_M^n}{\partial \sigma_p} = \frac{1}{2} \frac{1}{G_M^n} R_c \frac{\epsilon}{\tau} \quad (4.14)$$

and the fractional error on  $G_M^n$  due to uncertainty in the proton reduced cross-section is:

$$\frac{(\delta G_M^n)_p}{G_M^n} = \frac{1}{2} \frac{1}{G_{M,n}^2} R_c \frac{\epsilon}{\tau} \delta \sigma_p \quad (4.15)$$

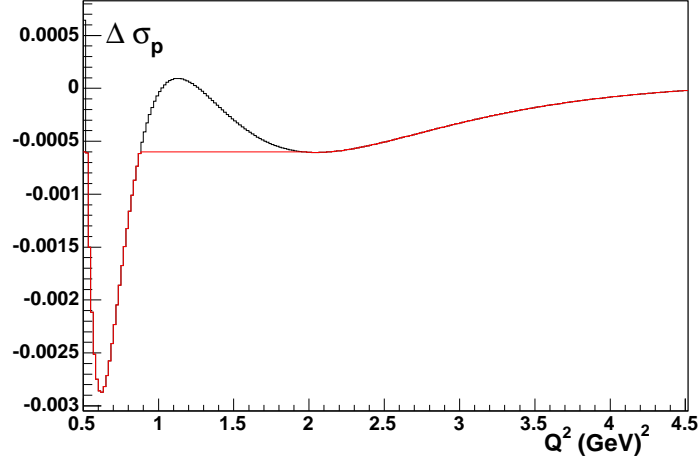


Figure 4.4: The difference in the proton reduced cross section  $\sigma_p$ , as determined from the Bosted and Arrington parameterizations. The black curve shows  $\sigma_p^{arrington} - \sigma_p^{bosted}$ . The red curve shows the value of  $\delta$  used to estimate the systematic error.

To estimate this contribution, we assume:  $G_M^n \approx \mu_n G_D$ , take  $R_c$  from the measurement, and take  $\delta\sigma_p$  to be the difference in  $\sigma_p$  as determined by the Arrington [52] and Bosted [53] parameterizations:

$$\delta\sigma_p = \sigma_p^{arrington} - \sigma_p^{bosted} \quad (4.16)$$

The difference in these two parameterizations is shown by the black curve in Fig 4.4. The parameterizations cross at  $Q^2 \approx 1.1$  GeV/c, giving a value of  $\delta = 0$ . To avoid this unrealistic estimate of  $\delta$ , a value of  $\delta = -0.0006$  is used in the region of the crossing. This substitution is shown by the red curve in Fig 4.4.

Using the  $\delta\sigma_p$  values shown in Fig 4.4 in Eqn 4.15, the estimated systematic uncertainty on  $G_M^n$  caused by the uncertainty in the proton reduced cross-section can be determined. The relative size of the difference in the two parameterizations is shown in Fig 4.5. The fractional uncertainty on  $G_M^n$ , expressed as a percentage, is shown in Fig 4.6 for the 4.2 GeV data, and in Fig 4.7 for the 2.5 GeV data.

### 4.2.2 Systematic error due to uncertainty in $G_E^n$

Consider the  $G_E^n$  term in Eqn 4.12:

$$(\delta G_M^n)_E = \frac{\partial G_M^n}{\partial G_E^n} \delta G_E^n \quad (4.17)$$

We have:

$$\frac{\partial G_M^n}{\partial G_E^n} = \frac{G_E^n \epsilon}{G_M^n \tau} \quad (4.18)$$

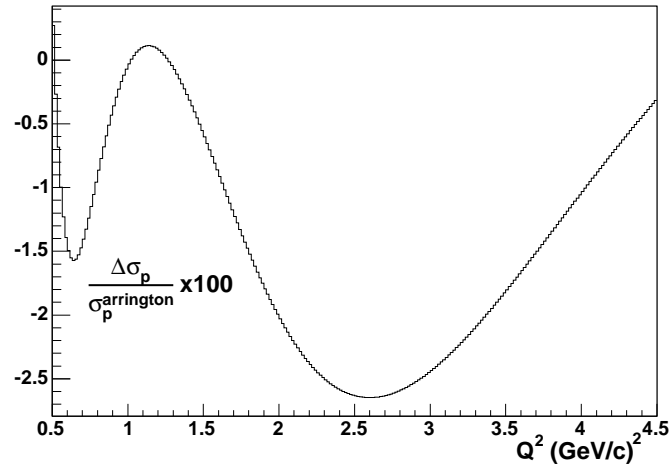


Figure 4.5: The relative difference in the proton reduced cross section  $\sigma_p$ , as determined from the Bosted and Arrington parameterizations, scaled to the Arrington result.

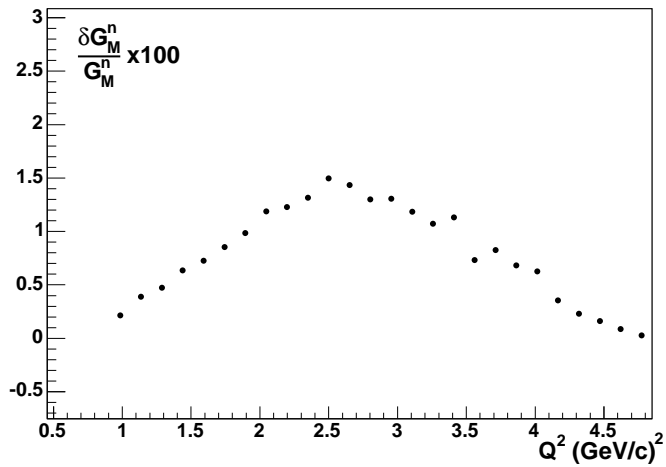


Figure 4.6: The systematic error on  $G_M^n$  due to uncertainties in the reduced proton cross-section, expressed as a percent error, for the 4.2 GeV beam energy.

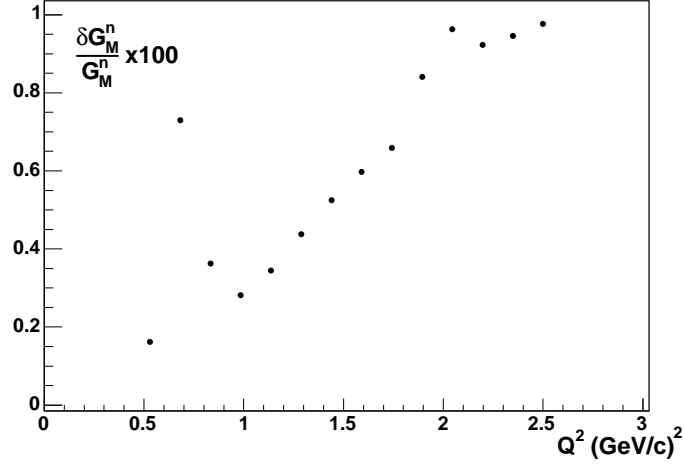


Figure 4.7: The systematic error on  $G_M^n$  due to uncertainties in the reduced proton cross-section, expressed as a percent error, for the 2.5 GeV beam energy.

and the fractional error on  $G_M^n$  due to uncertainty in the neutron electric form factor is:

$$\frac{(\delta G_M^n)_E}{G_M^n} = \frac{G_E^n}{G_{M,n}^2} \frac{\epsilon}{\tau} \delta G_E^n \quad (4.19)$$

To estimate this contribution, we assume  $G_M^n \approx \mu_N G_D$ , and use the Galster parametrization for  $G_E^n$ :

$$G_E^n \approx \frac{\mu_n \tau G_D}{1 + \eta \tau} \quad (4.20)$$

where  $\eta = 5.6$ . With this, we have:

$$\frac{\delta G_M^n}{G_M^n} = \frac{\epsilon}{\mu_n (1 + \eta \tau) G_D} \delta G_E^n \quad (4.21)$$

We take  $\delta G_E^n$  to be the difference between the Galster parametrization and the Lomon [9] model prediction:

$$\delta G_E^n = G_{E,galster}^n - G_{E,lomon}^n \quad (4.22)$$

The Galster and Lomon results are shown in Fig 4.8, along with the high- $Q^2$   $G_E^n$  data of Lung [24] and Schiavilla and Sick [54]. The two parameterizations cross at  $Q^2 \approx 0.7 \text{ GeV/c}$ . This would give the unrealistic result of  $\delta G_M^n = 0$  at the crossing point, and predict unreasonably small errors in the neighborhood of the crossing. To avoid this,  $\delta G_E^n$  in the region  $0.6 \leq Q^2 \leq 1.2 \text{ GeV/c}$  was assigned a value of 0.0036, equal to the value of  $\delta G_E^n$  at  $Q^2 = 1.2 \text{ GeV/c}$ .

The estimated systematic uncertainty on  $G_M^n$  caused by uncertainty in  $G_E^n$  is shown in Fig 4.9 for the 4.2 GeV data, and in Fig 4.10 for the 2.5 GeV data.

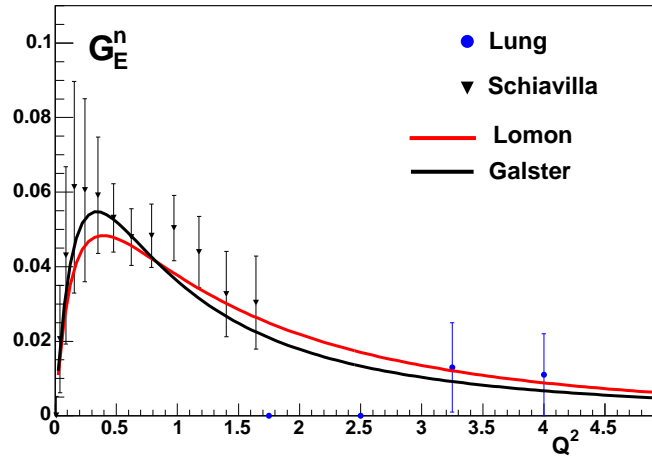


Figure 4.8: The Galster parametrization of  $G_E^n$ , along with the Lomon [9] model prediction and data from Lung [24] and Schiavilla [54].

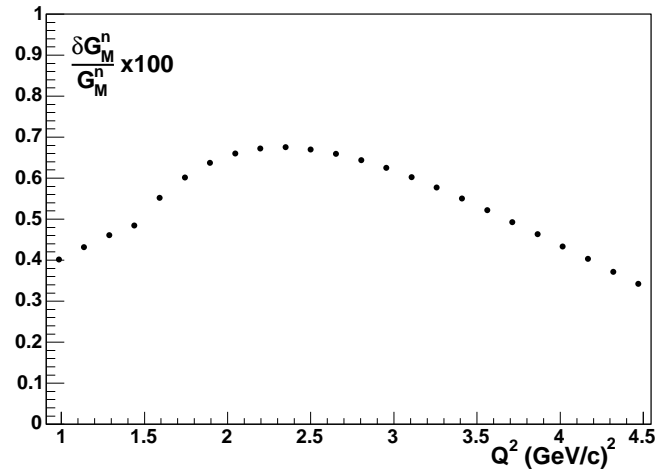


Figure 4.9: The estimated systematic error on  $G_M^n$  due to uncertainties in  $G_E^n$ , expressed as a percent error, for the 4.2 GeV data.

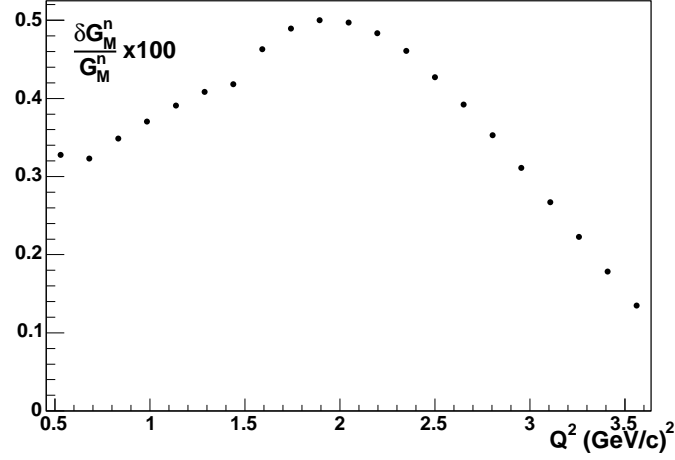


Figure 4.10: The estimated systematic error on  $G_M^n$  due to uncertainties in  $G_E^n$ , expressed as a percent error, for the 2.5 GeV data.

### 4.2.3 Other sources of systematic error

Consider the  $R_c(\vec{f})$  term in Eqn 4.12. The uncertainty in  $G_M^n$  due to the set of parameters  $\vec{f}$  is:

$$(\delta G_M^n)_R^2 = \sum_i \left( \frac{\partial G_M^n}{\partial f_i} \right)^2 (\delta f_i)^2 \quad (4.23)$$

$$= \sum_i \left( \frac{\partial G_M^n}{\partial R_c} \frac{\partial R_c}{\partial f_i} \right)^2 (\delta f_i)^2 \quad (4.24)$$

$$= \sum_i \left( \frac{\sigma_{p\epsilon}}{2G_M^n \tau} \frac{\partial R_c}{\partial f_i} \right)^2 (\delta f_i)^2 \quad (4.25)$$

The functional dependence of  $R_c$  on some of the  $f_i$  is not always clear, so we approximate:

$$\frac{\partial R_c}{\partial f_i} \approx \frac{\delta R_c}{\delta f_i} \quad (4.26)$$

and obtain

$$\left( \frac{\delta G_M^n}{G_M^n} \right)^2 = \sum_i \left( \frac{\sigma_{p\epsilon}}{2\mu_n^2 G_D^2 \tau} \right)^2 (\delta R_c)_i^2 \quad (4.27)$$

where we have used the approximation  $G_M^n \approx \mu_n G_D$  in the denominator on the right hand side, and  $(\delta R_c)_i$  is the variation in  $R_c$  induced by varying parameter  $f_i$ .

#### 4.2.3.1 Accidental background in neutron detection

The presence of accidental background in the  $ep \rightarrow e\pi^+(n)$  reaction was investigated by re-analyzing the calibration data. The assumption was made that the accidental

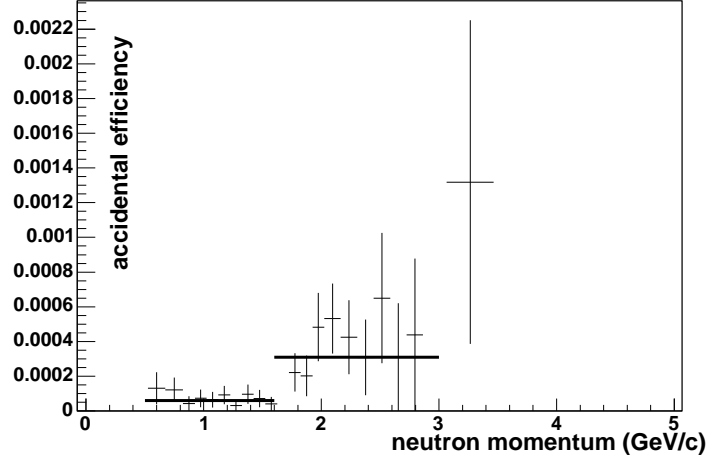


Figure 4.11: Accidental contribution to the neutron detection efficiency in the SC, for the 4.2 GeV data. The horizontal lines are fits of a constant to the data

background was the same in each of the six sectors. On an event-by-event basis, the reconstructed neutron 3-momentum was rotated around the beam-axis by a random multiple of  $60^\circ$  into some sector other than the original sector. The rest of the neutron detection efficiency analysis was carried out as usual. Any non-zero efficiency measured by this procedure must be due to accidental background. It was found that for the EC, no accidental efficiency was observed. For the SC, the accidental efficiencies are shown in Fig 4.11 and Fig 4.12 for the 4.2 GeV and 2.5 GeV data respectively.

The accidental efficiency was fitted with a constant

$$\eta_{accidental} = 7.5 \times 10^{-5} \quad (4.28)$$

for the 2.5 GeV case, and

$$\eta_{accidental} = \begin{cases} 6.05 \times 10^{-5} & p < 1.6 \text{ GeV}/c \\ 3.1 \times 10^{-4} & p > 1.6 \text{ GeV}/c \end{cases} \quad (4.29)$$

for the 4.2 GeV case. The accidental contribution to the efficiency is treated as a systematic error, using

$$\delta R_c = R_0 \left( \frac{1}{\eta} - \frac{1}{\eta - \eta'} \right) \quad (4.30)$$

where  $R_0$  is the measured ratio with no neutron detection efficiency applied,  $\eta$  is the normal neutron detection efficiency, and  $\eta'$  is the estimated accidental efficiency given above. All of these quantities have an understood  $Q^2$  dependence. This expression for  $\delta R_c$  is inserted into Eqn 4.27. The resulting systematic error is shown in Fig 4.13 for the 4.2 GeV data and Fig 4.14 for the 2.5 GeV data.

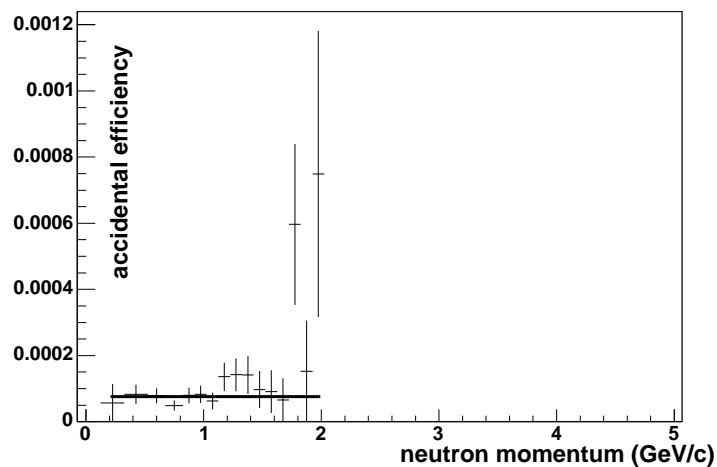


Figure 4.12: Accidental contribution to the neutron detection efficiency in the SC, for the 2.5 GeV data. The horizontal line is a fit of a constant to the data.

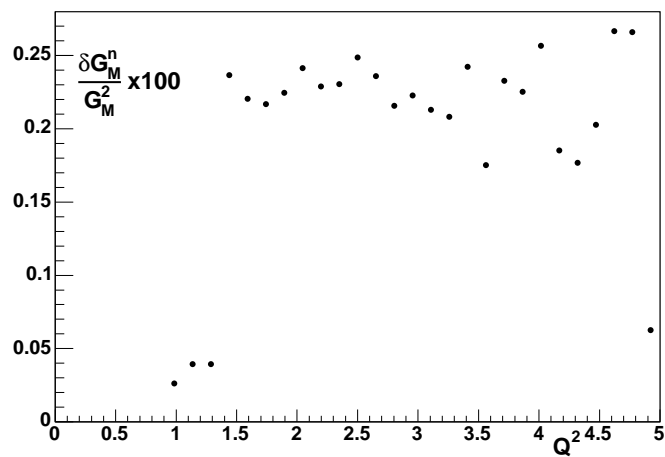


Figure 4.13: Fractional systematic error on  $G_M^n$  due to accidental background in the SC neutron detection efficiency, for the 4.2 GeV data.

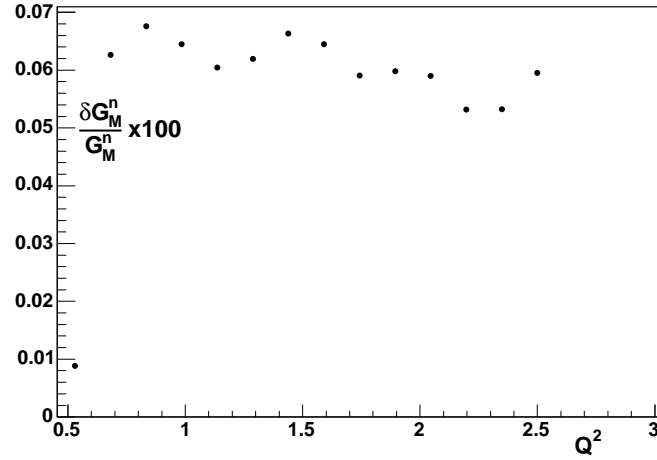


Figure 4.14: Fractional systematic error on  $G_M^n$  due to accidental background in the SC neutron detection efficiency, for the 2.5 GeV data.

#### 4.2.3.2 Missing mass cut in neutron detection efficiency measurement

The neutron missing mass peak observed in the  $ep \rightarrow e\pi^+(n)$  reaction does not show a Gaussian shape, but has a tail toward higher missing mass. The upper end of the missing mass cut was set to avoid this region. The tail may be caused by detector resolution effects (mismeasurement of the electron or  $\pi^+$  momentum will generate an incorrect value for the missing mass), radiative effects, or the presence of misidentified non- $e\pi^+n$  states contaminating the signal. The GSIM Monte Carlo package was used to investigate the presence of background channels contributing to the neutron missing mass peak. The CELEG event generator was used, with all resonance channels active. The gpp package was used for resolution smearing according to two prescriptions: the default setting, and smearing the Distance Of Closest Approach (DOCA) in drift chambers regions (R1,R2,R3) by a factor of (2.0,2.5,3.0) relative to the default values, respectively. Previous analyses [55] have indicated that the default DOCA smearing performed by gpp is inadequate and the values listed give a better agreement between real data and simulation. The smeared GSIM events are then cooked and analyzed using the same procedure as described for the real data. The results of the default DOCA-smearing setting are shown in Fig 4.16 and the extra-smearing results are shown in Fig 4.17.

Neither of the two DOCA settings seems to get the missing mass distribution quite right. A detailed study of which GSIM/GPP settings optimize the simulation performance for this reaction channel was not made. From the simulation results presented, it appears that non- $e\pi^+n$  channels do not contribute a significant background in the  $0.9\text{GeV} \leq MM \leq 1.0\text{GeV}$  region. The skewing of the observed missing mass spectrum appears to be due to detector resolution effects. An investigation was

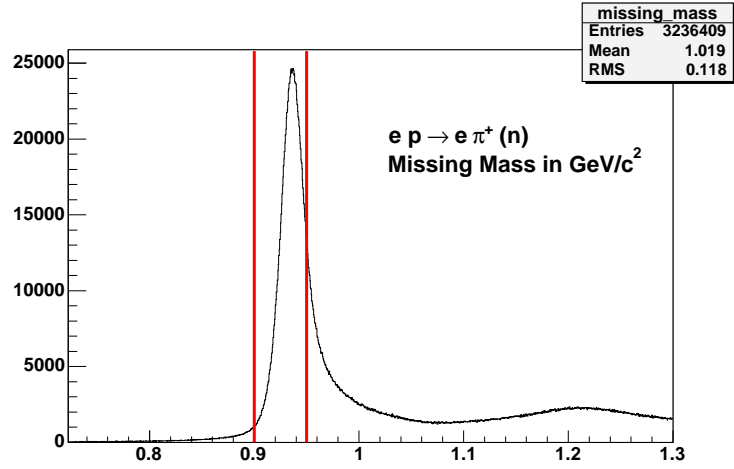


Figure 4.15: The observed missing mass distribution in the  $ep \rightarrow e\pi^+(n)$  reaction.

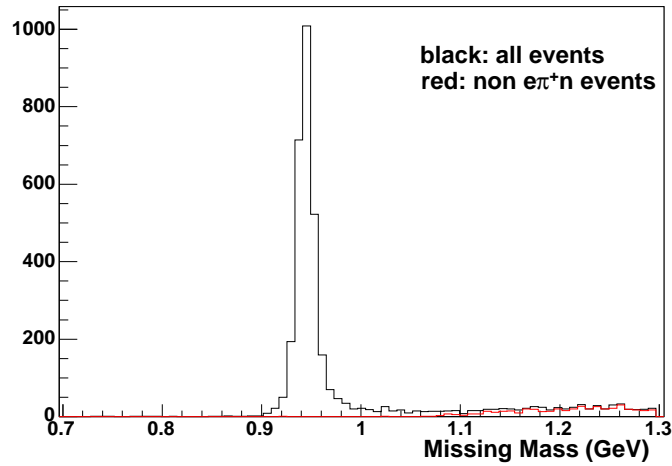


Figure 4.16: Missing mass spectrum in the  $ep \rightarrow e\pi^+(n)$  reaction, generated from CELEG/GSIM, with default DOCA smearing.

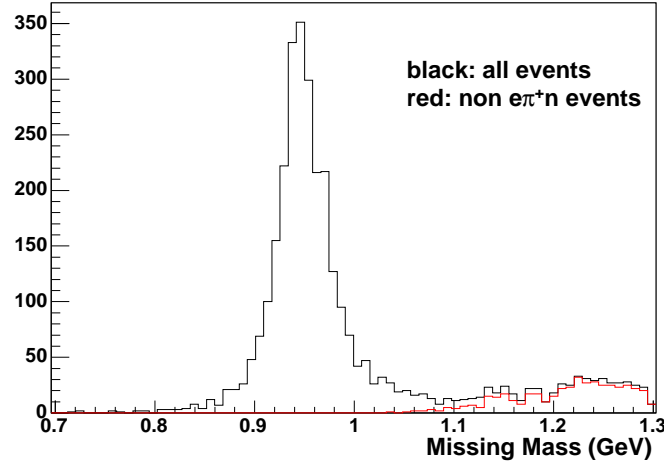


Figure 4.17: Missing mass spectrum in the  $ep \rightarrow e\pi^+(n)$  reaction, generated from CELEG/GSIM, with extra DOCA smearing factor (2.0,2.5,3.0) in (R1,R2,R3).

made of how far the upper limit of the missing mass cut can be pushed before the measured efficiency begins to degrade due to the angle between the reconstructed and real neutron 3-momentum becoming too large. The missing mass peak was sliced into several sections, and the EC neutron detection efficiency was measured for each section, using the 4.2 GeV data. The results are shown in Figs 4.18, 4.19, 4.20.

Consistent results were obtained for missing mass slices in the 0.9 to 0.96 range, but beyond that, the performance began to degrade. To assess the effect of changes in the location of the upper bound of the missing mass cut on  $G_M^n$ , Eqn 4.27 was used with:

$$\delta R_c = R_0 \frac{1}{2} \left( \frac{1}{\eta_{94}} - \frac{1}{\eta_{96}} \right) \quad (4.31)$$

where  $\eta_{94}$  is the efficiency evaluated using the missing mass region  $0.9 < MM < 0.94$ , and  $\eta_{96}$  is the efficiency evaluated using the missing mass region  $0.9 < MM < 0.96$ . The cuts were chosen to bracket the cut value of 0.95 used in the analysis. The upper value of 0.96 was chosen as the largest value of the cut at which sensible efficiency results are obtained. Since the shape of the efficiency curve doesn't vary much for cut values below 0.95, a value of 0.94 was chosen for symmetry. The resulting error estimates are shown in Fig 4.21 for the 4.2 GeV data and Fig 4.22 for the 2.5 GeV data.

#### 4.2.3.3 Distance cut in EC calibration neutron selection

In the neutron detection efficiency calibration, a cut was applied requiring that any neutron from the  $ep \rightarrow e\pi^+(n)$  reaction found in the EC satisfy the cut  $\Delta R < 60$  cm where  $\Delta R$  is the distance between the observed hit location and the hit location

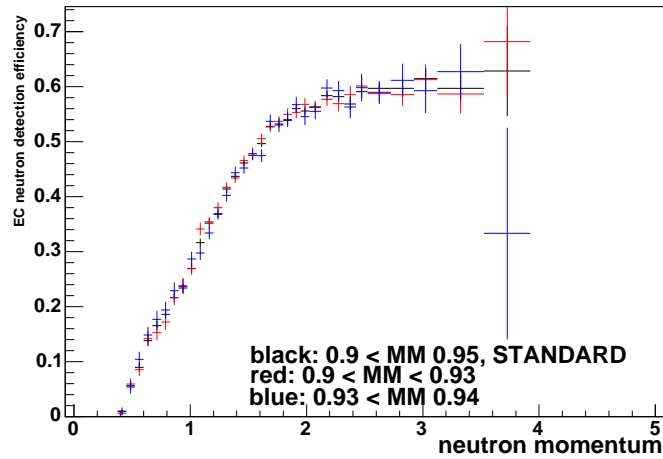


Figure 4.18: The EC neutron detection efficiency in the 4.2 GeV data, for various slices of the neutron missing mass peak. The black points show the standard cut,  $0.9 < MM < 0.95$ .

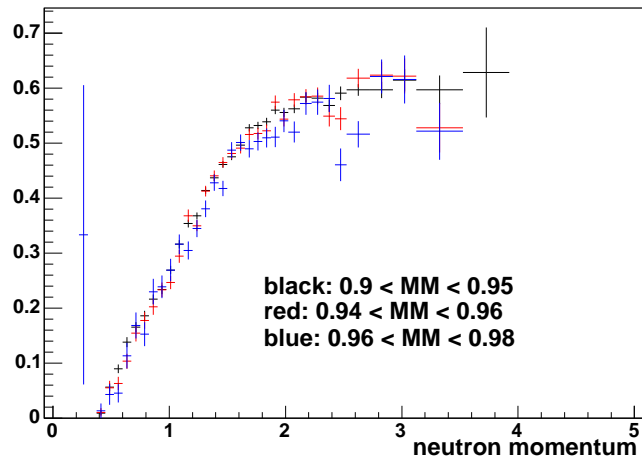


Figure 4.19: The EC neutron detection efficiency in the 4.2 GeV data, for various slices of the neutron missing mass peak. The black points show the standard cut,  $0.9 < MM < 0.95$ .

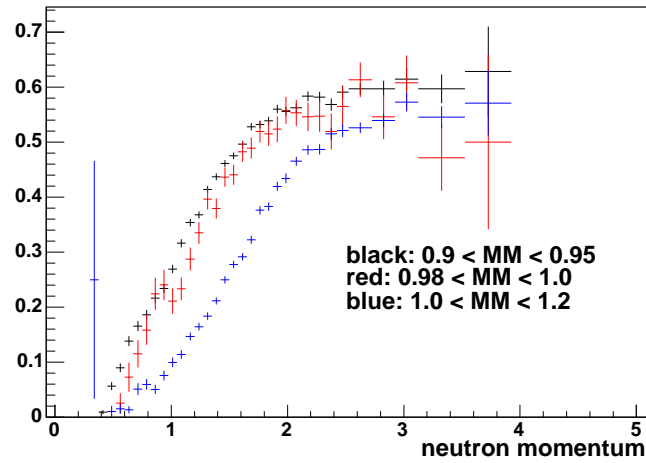


Figure 4.20: The EC neutron detection efficiency in the 4.2 GeV data, for various slices of the neutron missing mass peak. The black points show the standard cut,  $0.9 < MM < 0.95$ .

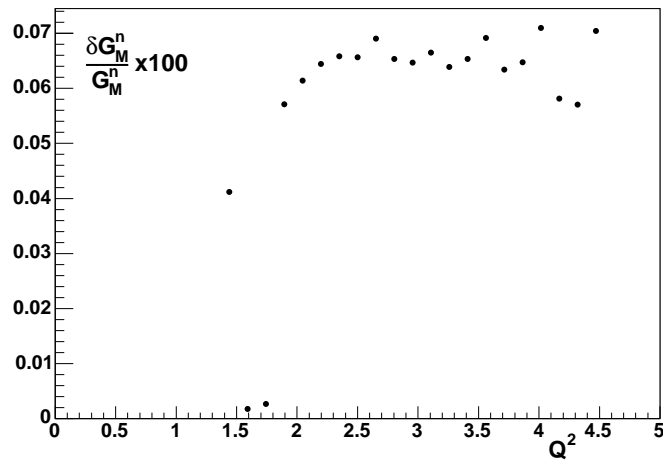


Figure 4.21: Estimated fractional systematic error on  $G_M^n$  due to the selection of the upper edge of the missing mass cut in the  $ep \rightarrow e\pi^+(n)$  reaction, for the 4.2 GeV EC data.

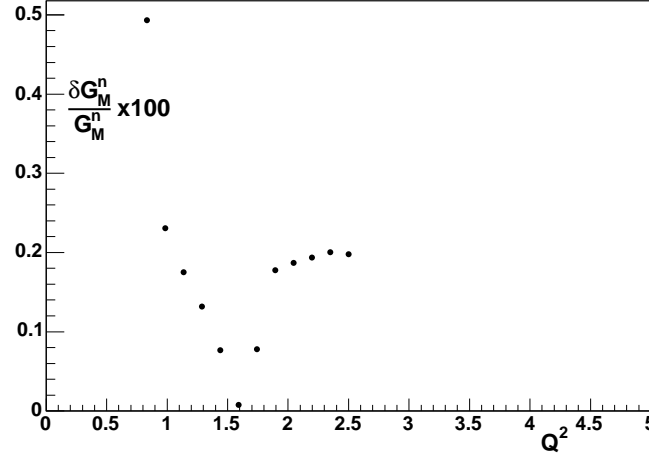


Figure 4.22: Estimated fractional systematic error on  $G_M^n$  due to the selection of the upper edge of the missing mass cut in the  $ep \rightarrow e\pi^+(n)$  reaction, for the 2.5 GeV EC data.

expected from the neutron missing momentum. The accuracy of the position reconstruction in the EC is estimated to be  $\approx 0.5$  degrees [56]. A value of 525 cm was taken as a typical target to calorimeter distance, giving a position resolution of  $\approx 4.5$  cm. The fractional uncertainty in  $G_M^n$  due to this cut is estimated from Eqn 4.27 with:

$$\delta R = \frac{1}{2}R_0\left(\frac{1}{\eta_1} - \frac{1}{\eta_2}\right) \quad (4.32)$$

where  $\eta_1$  is the global EC efficiency evaluated with a  $\Delta R < 55.5$  cm cut, and  $\eta_2$  is the global EC efficiency evaluated with a  $\Delta R < 64.5$  cm cut. The global efficiencies for the two  $\Delta R$  selections are shown in Fig 4.23 and 4.24 for the 4.2 GeV and 2.5 GeV data respectively. The estimated systematic errors for the 4.2 and 2.5 GeV data are shown in Fig 4.25 and 4.26.

#### 4.2.3.4 EC neutron detection efficiency parametrization

The neutron detection efficiency in the EC is parametrized by a third order polynomial at low neutron momentum, and a flat line at high momentum, as described in Section 3.3.4.2. To investigate the sensitivity to the details of this fit, the fitting procedure was modified by switching off the  $p^3$  term in the fitting function. The standard fit applied to the global efficiency data is shown in Fig 4.27, along with the modified fit. The systematic error is estimated by using Eqn 4.27 with:

$$\delta R = |R_{standard} - R_{modified}| \quad (4.33)$$

The estimated systematic error due to the parametrization of the EC neutron detection efficiency is shown in Fig 4.28 for the 4.2 GeV data. Based on the results

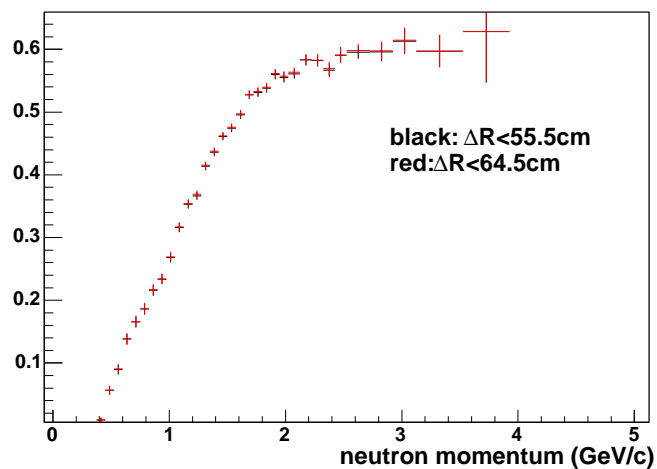


Figure 4.23: Comparison of EC neutron detection efficiency, integrated over all sectors, for two choices of the  $\Delta R$  cut, from the 4.2 GeV data.

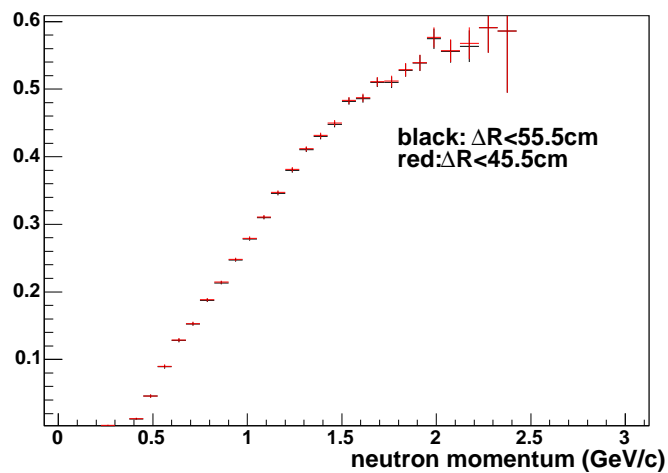


Figure 4.24: Comparison of EC neutron detection efficiency, integrated over all sectors, for two choices of the  $\Delta R$  cut, from the 2.5 GeV data.

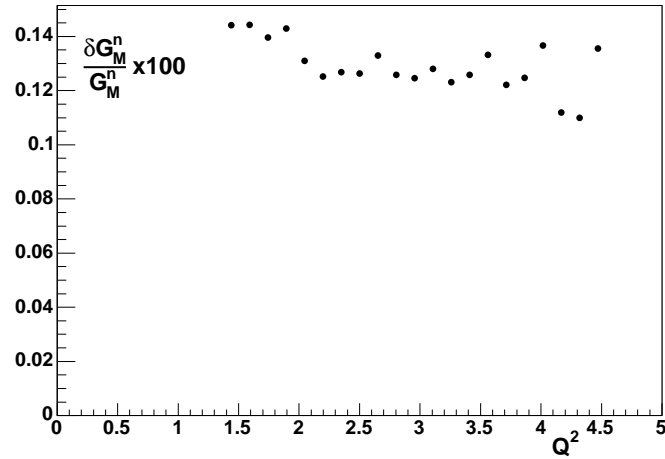


Figure 4.25: Estimated fractional systematic error on  $G_M^n$  due to the choice of  $\Delta R$  cuts in EC neutron selection in the calibration reaction in the 4.2 GeV data.

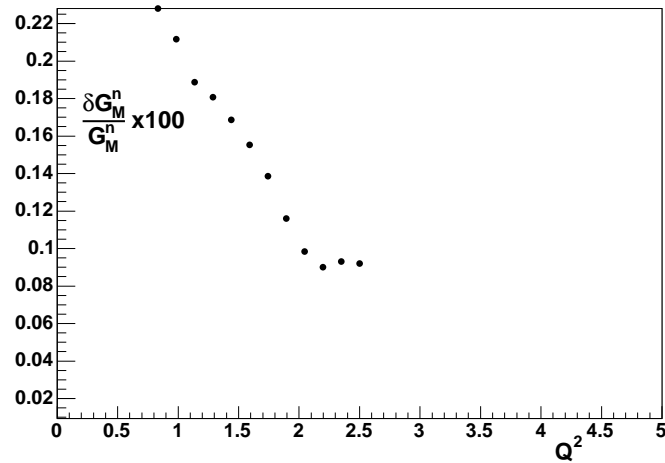


Figure 4.26: Estimated fractional systematic error on  $G_M^n$  due to the choice of  $\Delta R$  cuts in EC neutron selection in the calibration reaction in the 2.5 GeV data.

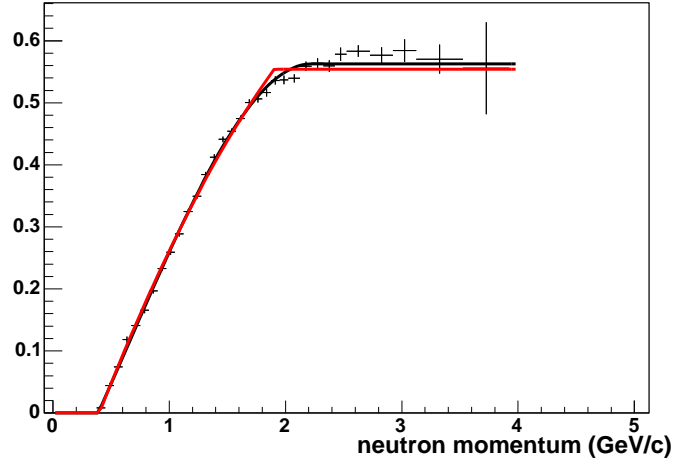


Figure 4.27: The black curve shows the global EC neutron detection efficiency data, fitted by the third order standard fit. The red curve shows the modified fit, obtained by switching off the  $p^3$  term.

shown in the figure, a flat systematic uncertainty of 1.0% is assigned at all  $Q^2$  values for the 4.2 GeV data. A similar procedure was carried out for the 2.5 GeV data. The comparison of the standard and modified fits is shown in Fig 4.29. The systematic error induced by varying the fit is shown in Fig 4.30. Based on this figure, a flat systematic uncertainty of 1.5% was assigned at all values of  $Q^2$  for the 2.5 GeV data.

In the standard fitting procedure, the point at which the efficiency function switches from a third-order polynomial to a constant is left as a parameter of the fit. To test the sensitivity to the selection of the location of the switching point, a series of fits was performed where the location of the switching point was fixed. For reasonable values of the switching point (between 1.9 and 2.4 GeV/c in neutron momentum), it was found that the value of the fit for momenta *below* the switching point was essentially unchanged. For momenta above the switching point, variations in efficiency of up to 2% of the standard value could be produced. As  $G_M^n$  varies with the square root of the efficiency, a systematic error of 1% was assigned for  $Q^2$  values greater than 2 (GeV/c)<sup>2</sup>. This error was treated as an independent error.

#### 4.2.3.5 SC neutron detection efficiency parametrization

The neutron detection efficiency in the SC is parametrized by a third order polynomial at low neutron momentum, and a flat line at higher momentum, as described in Sec 3.3.5.1. To investigate the sensitivity to the details of this fit, the fitting procedure was modified by switching off the  $p^3$  and  $p^2$  terms in the fit. The standard fit applied to the global SC data is shown in Fig 4.31, and the modified fit is shown in Fig 4.32.

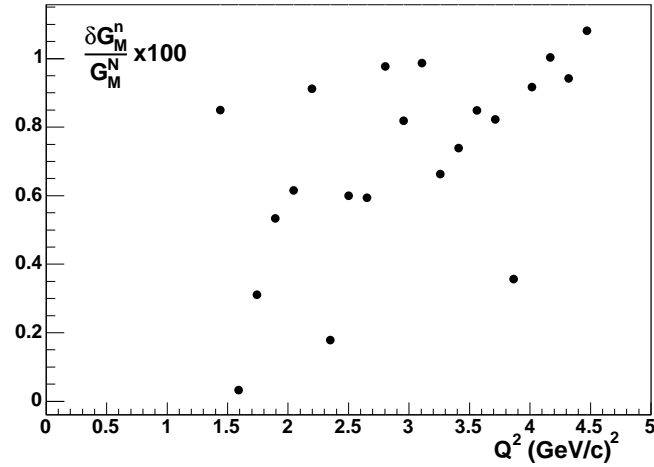


Figure 4.28: The estimated fractional systematic error on  $G_M^n$ , due to the parametrization of the EC neutron detection efficiency.

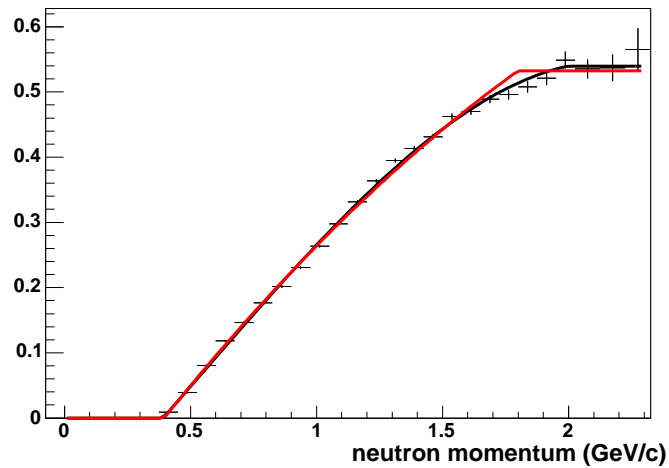


Figure 4.29: The black curve shows the 2.5 GeV global EC neutron detection efficiency data, fitted by the third order standard fit. The red curve shows the modified fit, obtained by switching off the  $p^3$  term.

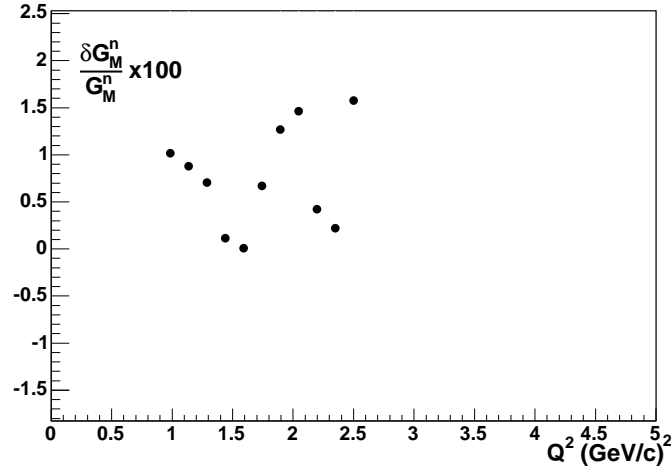


Figure 4.30: The estimated fractional systematic error on  $G_M^n$ , due to the parametrization of the EC neutron detection efficiency.

The systematic error is estimated by using Eqn 4.27 using:

$$\delta R = |R_{standard} - R_{modified}| \quad (4.34)$$

The estimated systematic error due to the parametrization of the SC neutron detection efficiency is shown in Fig 4.33. Based on this plot, a flat systematic error of 2% was assigned at all values of  $Q^2$  for the both the 4.2 GeV data and the 2.5 GeV data (results similar to Fig 4.33 were obtained for the 2.5 GeV data).

In the standard fitting procedure, the point at which the efficiency function switches from a third-order polynomial to a constant is left as a parameter of the fit. To test the sensitivity to the selection of the location of the switching point, a series of fits was performed where the location of the switching point was fixed. For reasonable values of the switching point (between 1.4 and 1.7 GeV/c in neutron momentum), it was found that the value of the fit for momenta *below* the switching point was essentially unchanged. For momenta above the switching point, variations in efficiency of up to 3.5% of the standard value could be produced. As  $G_M^n$  varies with the square root of the efficiency, a systematic error of 1.74% was assigned for  $Q^2$  values greater than 1 (GeV/c)<sup>2</sup>. This error was treated as an independent error.

#### 4.2.3.6 Proton detection efficiency

A comparison was made of the momentum-averaged proton detection efficiency on SC paddles which were used in both the 4.2 GeV and 2.5 GeV analyses. The relative difference in efficiency on each paddle is shown in Fig 4.34. From the scattered points in Fig 4.34, a systematic uncertainty of 0.75% was assigned to the proton detection

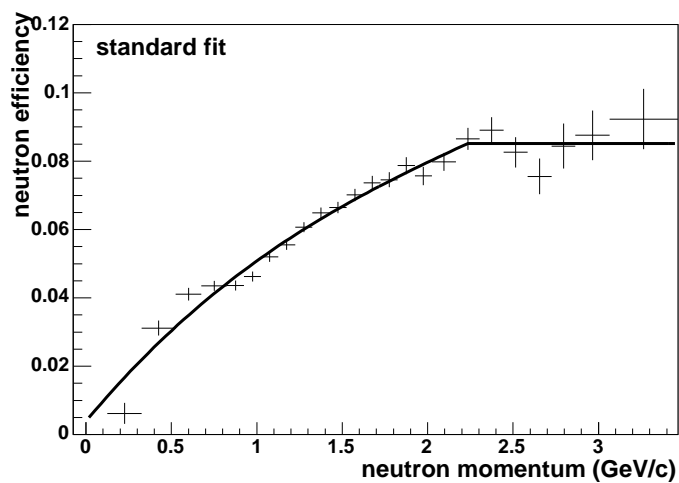


Figure 4.31: The global SC neutron detection efficiency data, fitted by the third order standard fit.

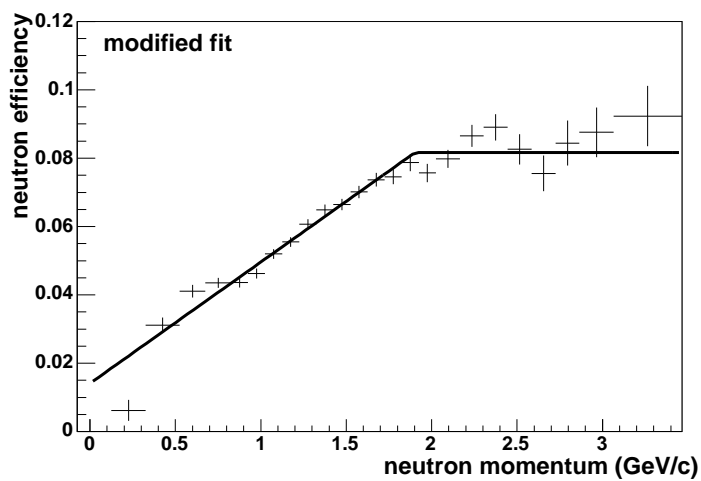


Figure 4.32: The global SC neutron detection efficiency data, fitted by the first order modified fit.

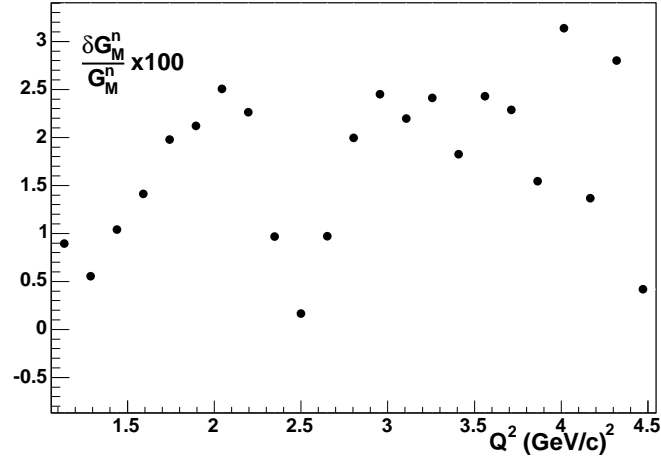


Figure 4.33: The estimated fractional systematic error on  $G_M^n$ , due to the parametrization of the SC neutron detection efficiency.

efficiency. The systematic error on  $G_M^n$  was determined from Eqn 4.27 using:

$$\delta R_c = \delta \eta_p R_0 \quad (4.35)$$

where  $\delta \eta_p = 0.0075$  and  $R_0$  is the measured ratio with no proton detection efficiency applied. The systematic error is shown in Fig 4.35 for the 4.2 GeV data, and in Fig 4.36 for the 2.5 GeV data.

#### 4.2.3.7 Accidental background in quasi-elastic events

The presence of accidental background in the quasi-elastic channel was investigated using the same technique applied in the neutron detection efficiency case. The expected neutron 3-momentum vector was rotated about the beam-axis by a multiple of  $60^\circ$ , placing the expected hit location in a sector where the neutron ought not to have been seen. Any neutral hits found after this rotation were attributed to accidental background. The accidental rate was assumed to be the same in all sectors.

The result of the procedure was that no significant background was found. Any neutrals found after the rotation were rejected by some combination of the cuts on energy deposited,  $W^2$  or  $\theta_{pq}$ . Fig 4.37 shows the  $\theta_{pq}$  spectrum for rotated quasi-elastic events in the SC. Similar results were obtained for both beam energies, in the EC and the SC.

#### 4.2.3.8 Acceptance/Fermi loss correction

To test the sensitivity of the ratio measurement to the details of the Fermi loss correction procedure, the shape of the nucleon momentum distribution was altered.

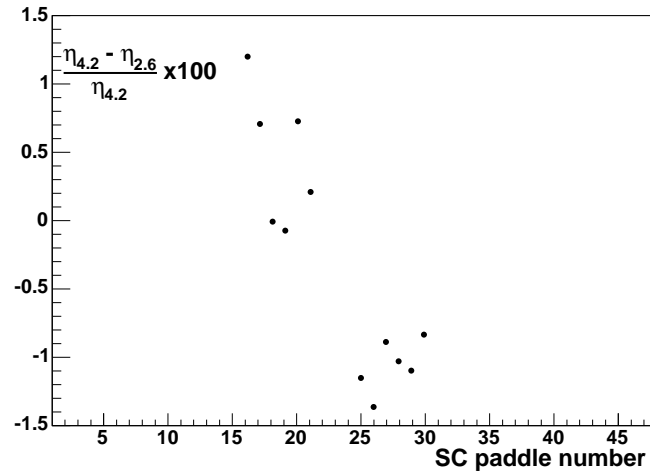


Figure 4.34: The relative difference in the average proton detection efficiency in the 4.2 GeV and 2.5 GeV data sets.

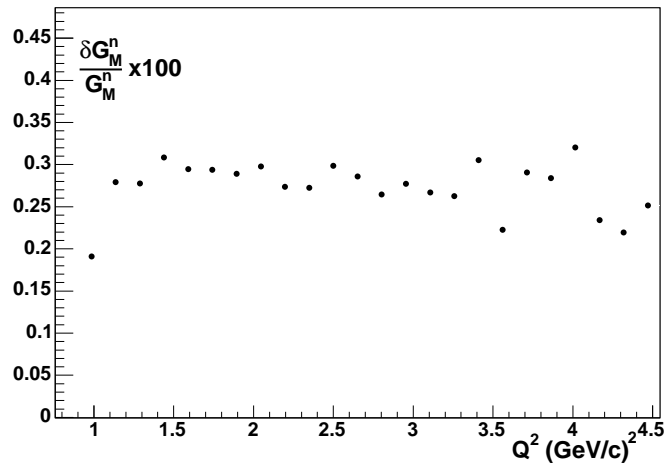


Figure 4.35: Estimated fractional systematic error on  $G_M^n$  due to uncertainties in the proton efficiency correction in the 4.2 GeV data set.

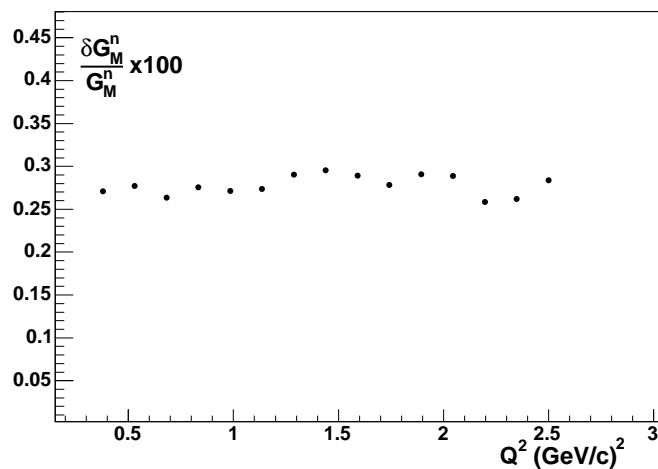


Figure 4.36: Estimated fractional systematic error on  $G_M^n$  due to uncertainties in the proton efficiency correction in the 2.5 GeV data set.

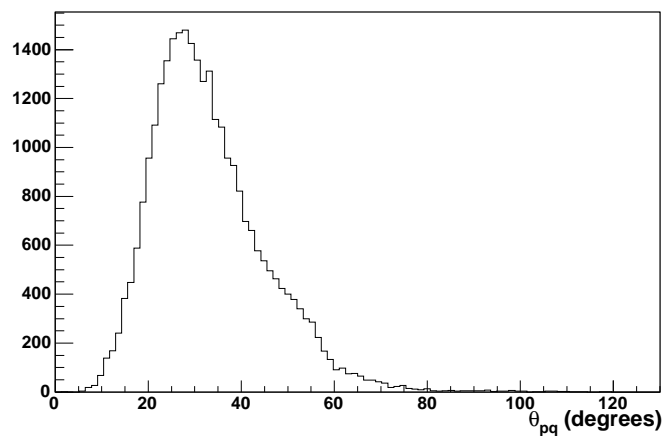


Figure 4.37:  $\theta_{pq}$  spectrum for quasi-elastic e-n candidate events in the SC, *after* the expected neutron momentum vector was rotated about the beam axis into an adjacent sector.

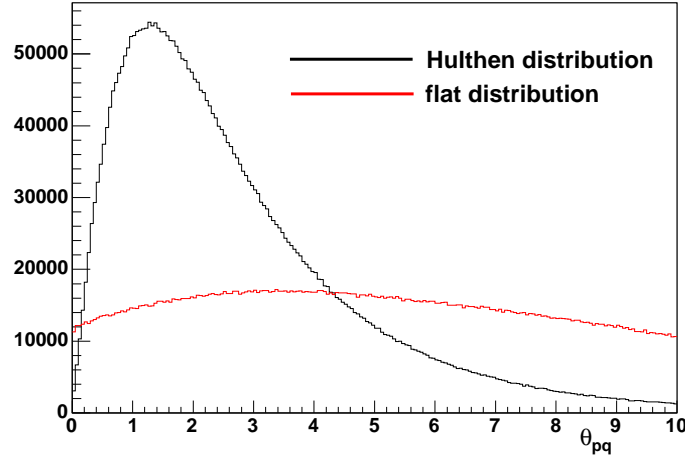


Figure 4.38: A comparison of the  $\theta_{pq}$  distributions obtained from the deuteron model, for the Hulthen (black line) and flat (red line) nucleon momentum distributions.

The most severe alteration that was tested replaced the Hulthen distribution shown in Fig 3.46 with a flat distribution that assigned the nucleon an equal probability of being found with any momentum between 0 and  $600\text{MeV}/c$ . The  $\theta_{pq}$  distributions obtained from the Hulthen and flat nucleon momentum distributions are shown in Fig 4.38. The shape of the  $\theta_{pq}$  distribution observed for e-p quasi-elastics was seen to be consistent with the event-generator prediction, so the comparison to the flat distribution should be seen as an extreme case.

The shape of the loss fraction curves for neutrons and protons (the standard loss fraction curves were shown in Fig 3.55 and 3.56) were found to have a significant dependence on the shape of the nucleon momentum distribution used. A comparison of the Hulthen and flat distribution results is shown in Fig 4.39 for SC neutrons in the 4.2 GeV data, and in Fig 4.40 for protons in the 4.2 GeV data. The correction to the ratio was found to have only a weak dependence on the shape of the nucleon momentum distribution, as shown in Fig 4.41 for the 4.2 GeV SC neutron data. The fractional difference in the correction factor obtained from the two different momentum distributions is shown in Fig 4.42

Other variations, less pathological than the flat distribution, on the shape of the nucleon momentum distribution were considered, generally giving variations in the correction factor less extreme than those obtained from the flat distribution. Based on these results, a systematic uncertainty of 0.25% is assigned to the correction factor in those  $Q^2$  regions where the correction is less than 5%, and an uncertainty of 1.5% is assigned when the correction is larger than 5%. Using

$$\delta R = \delta f R \quad (4.36)$$

where  $\delta f = 0.005$  or  $0.015$  depending on  $Q^2$ , in Eqn 4.27 gives the systematic error

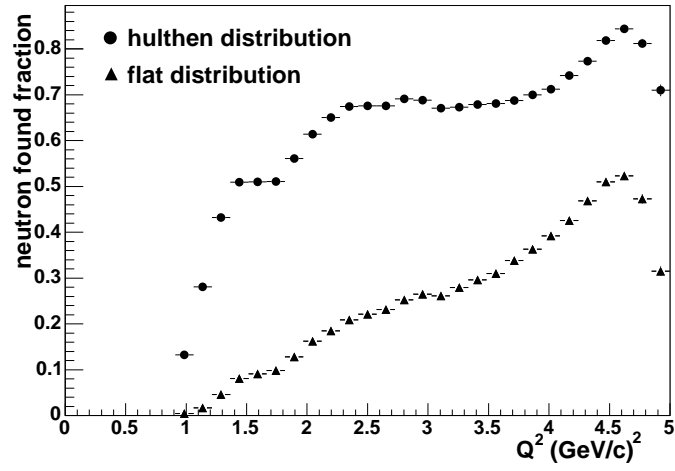


Figure 4.39: A comparison of the neutron loss fraction obtained from the Hulthen and flat distributions for SC neutrons in the 4.2 GeV data set.

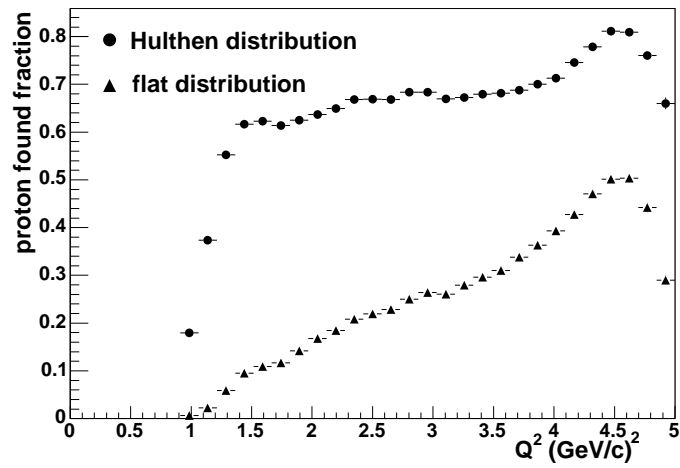


Figure 4.40: A comparison of the proton loss fraction obtained from the Hulthen and flat distributions in the 4.2 GeV data set.

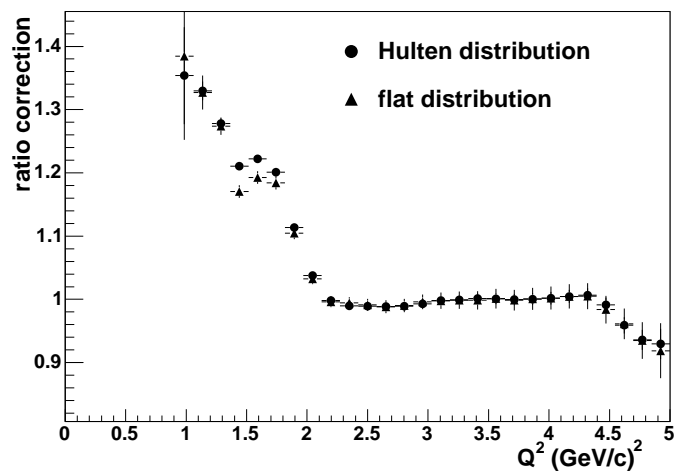


Figure 4.41: A comparison of the ratio correction factor obtained from the Hulthen and flat nucleon momentum distributions in the 4.2 GeV data.

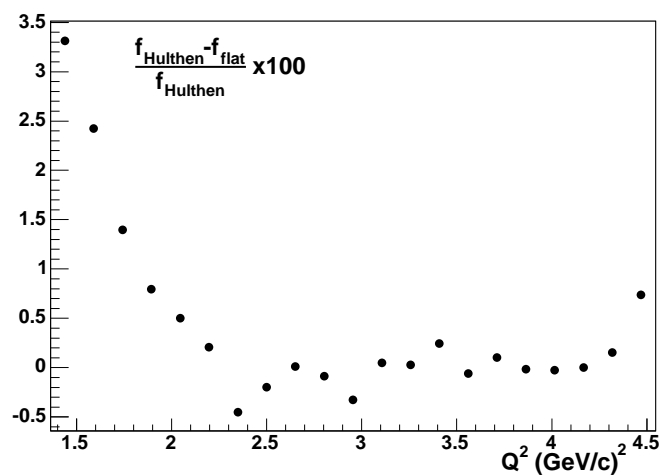


Figure 4.42: The fractional difference in the ratio correction factor obtained from the Hulthen and flat nucleon momentum distributions.

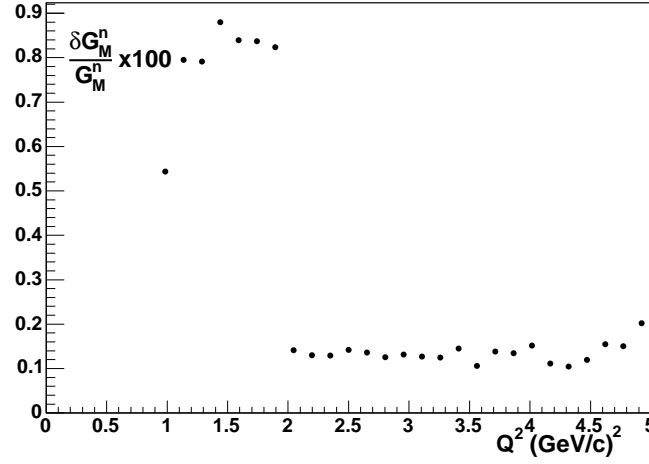


Figure 4.43: The estimated fractional systematic error on  $G_M^n$  due to uncertainties in the acceptance/Fermi-motion correction, for the 4.2 GeV data.

estimates shown in Fig 4.43 and Fig 4.44.

#### 4.2.3.9 $\theta_{pq}$ cut

The value of the  $\theta_{pq}$  cut used in the quasi-elastic event selection was varied by 10% in each direction. The systematic error was calculated using Eqn 4.27 with:

$$\delta R = \frac{1}{2}(R_{110} - R_{90}) \quad (4.37)$$

where  $R_{110}$  is the ratio evaluated with the  $\theta_{pq}$  cut 10% larger, and  $R_{90}$  is the ratio evaluated with the  $\theta_{pq}$  cut 10% smaller. The systematic error estimates obtained from this procedure are shown in Fig 4.45 and Fig 4.46 for the 4.2 GeV data, and Fig 4.47 and Fig 4.48 for the 2.5 GeV data.

#### 4.2.3.10 Nuclear Corrections

As mentioned in section 3.7.6, a systematic error of 0.6% was assigned to the nuclear correction factor at all values of  $Q^2$ . The systematic error on  $G_M^n$  was calculated using Eqn 4.27 with:

$$\delta R = 0.006R \quad (4.38)$$

The fractional systematic error on  $G_M^n$  due to systematic uncertainties in the nuclear correction is shown in Fig 4.49 for the 4.2 GeV data, and in Fig 4.50 for the 2.5 GeV data.

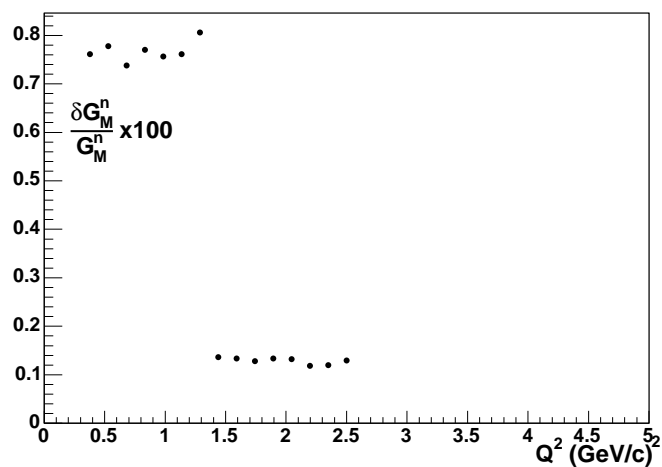


Figure 4.44: The estimated fractional systematic error on  $G_M^n$  due to uncertainties in the acceptance/Fermi-motion correction, for the 2.5 GeV data.

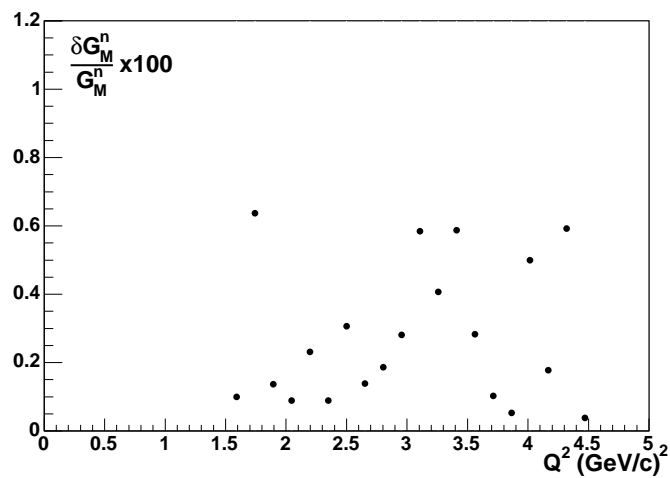


Figure 4.45: Estimated systematic error induced by variation in the  $\theta_{pq}$  cut, for EC neutrons in the 4.2 GeV data set.

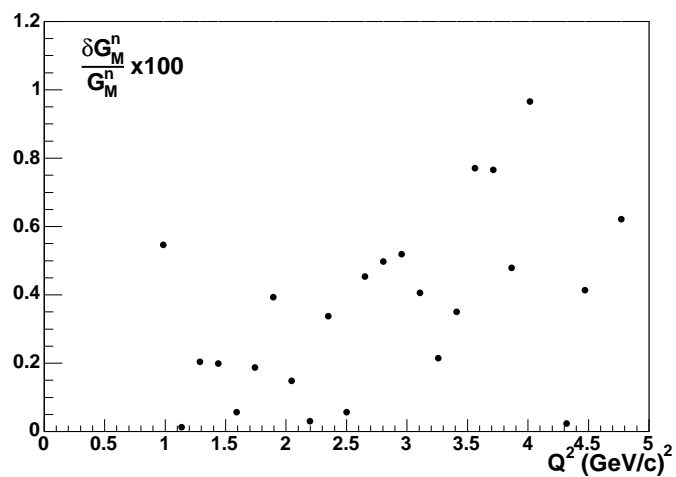


Figure 4.46: Estimated systematic error induced by variation in the  $\theta_{pq}$  cut, for SC neutrons in the 4.2 GeV data set.

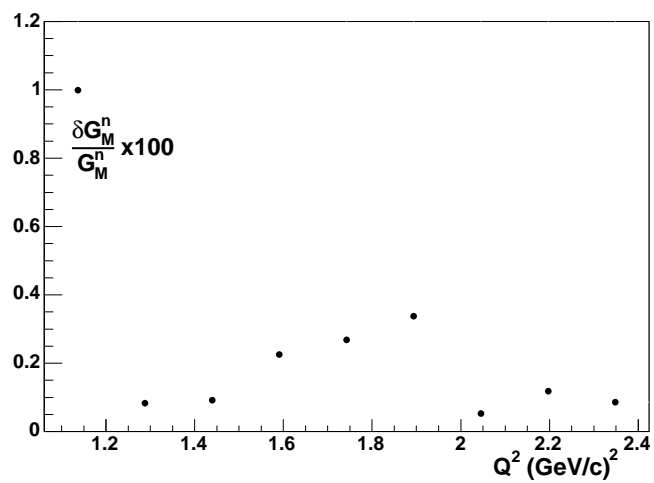


Figure 4.47: Estimated systematic error induced by variation in the  $\theta_{pq}$  cut, for EC neutrons in the 2.5 GeV data set.

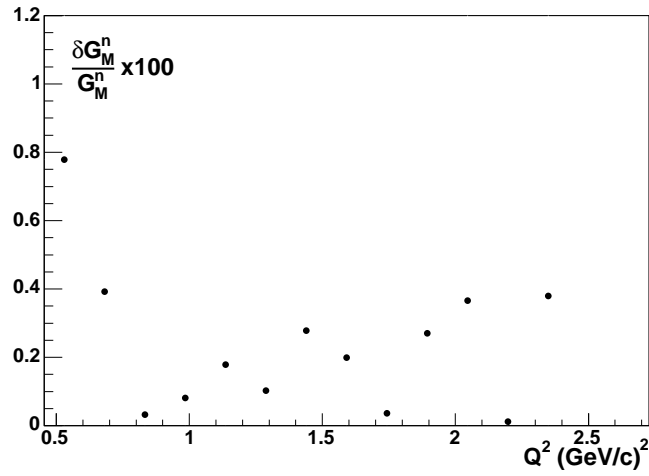


Figure 4.48: Estimated systematic error induced by variation in the  $\theta_{pq}$  cut, for SC neutrons in the 2.5 GeV data set.

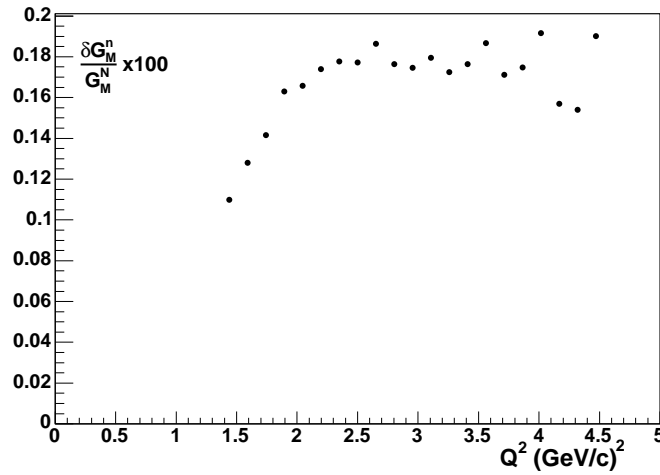


Figure 4.49: Estimated fractional systematic error induced in  $G_M^n$  by systematic error on the nuclear correction, for the 4.2 GeV data set.

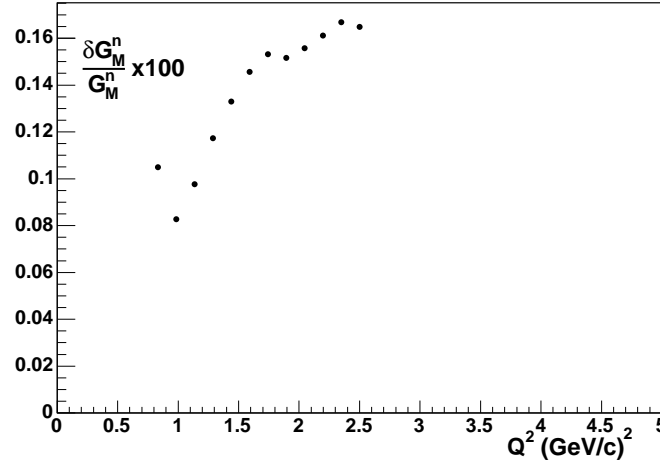


Figure 4.50: Estimated fractional systematic error on  $G_M^n$  induced by systematic error on the nuclear correction, for the 2.5 GeV data set.

#### 4.2.3.11 Radiative Corrections

As mentioned in section 3.7.5, a systematic error of 0.17% was assigned to the radiative correction factor at all values of  $Q^2$ . The systematic error on  $G_M^n$  was calculated using Eqn 4.27 with:

$$\delta R = 0.0017R \quad (4.39)$$

The fractional systematic error on  $G_M^n$  due to systematic uncertainties in the radiative correction is shown in Fig 4.51 for the 4.2 GeV data, and in Fig 4.52 for the 2.5 GeV data.

#### 4.2.4 Combined systematic error

The combined systematic error for each of the 4 measurements (EC and SC neutrons at two different beam energies) was obtained by adding the applicable errors in quadrature. The results are shown in Fig 4.53, 4.54, 4.55, and 4.56. The systematic errors from the four individual measurements were combined into an averaged systematic error for comparison with the weighted average  $G_M^n$  plot. To determine a value of the average systematic error, the following quantity was calculated:

$$\tilde{x} = \frac{\sum_j \frac{x_j + \sigma_j^s}{\sigma_j^2}}{\sum_j \frac{1}{\sigma_j^2}} \quad (4.40)$$

where  $\sigma_j^s$  is the systematic error on the  $j^{\text{th}}$  histogram contributing in a given  $Q^2$  bin, and the other terms are as defined in Sec 4.1. The average systematic error in each

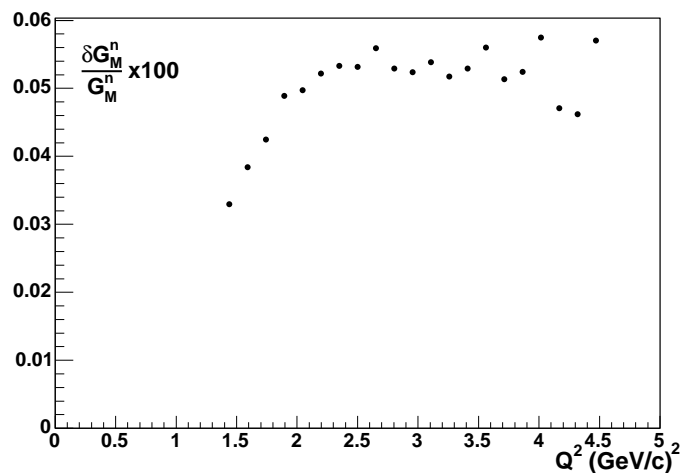


Figure 4.51: Estimated systematic error induced by uncertainties in the radiative correction, for the 4.2 GeV data set.

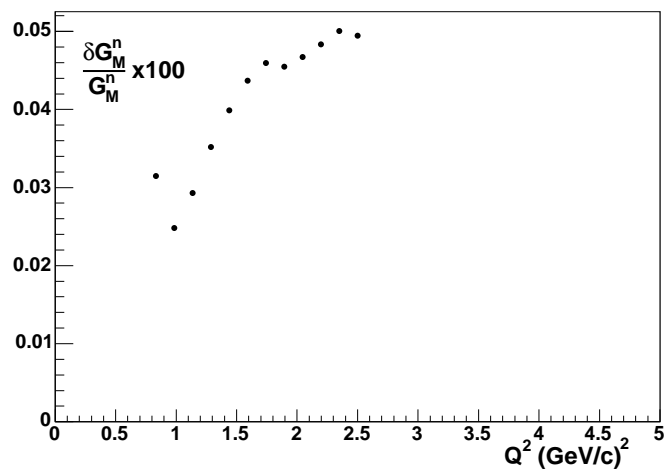


Figure 4.52: Estimated systematic error induced by uncertainties in the radiative correction, for the 2.5 GeV data set.

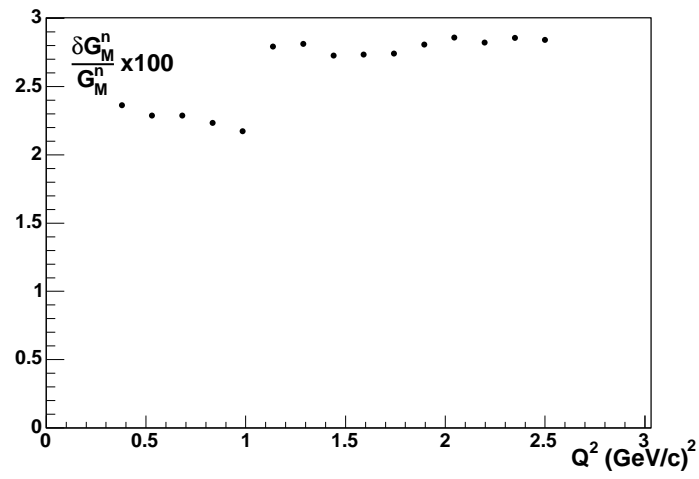


Figure 4.53: Combined fractional systematic error for the 2.5 GeV beam energy, with SC neutron detection.

$Q^2$  bin was then taken to be:

$$\overline{\sigma}_j^s = |\tilde{x} - \bar{x}| \quad (4.41)$$

The weighted average systematic error, binned in  $Q^2$  is shown in Fig 4.57.

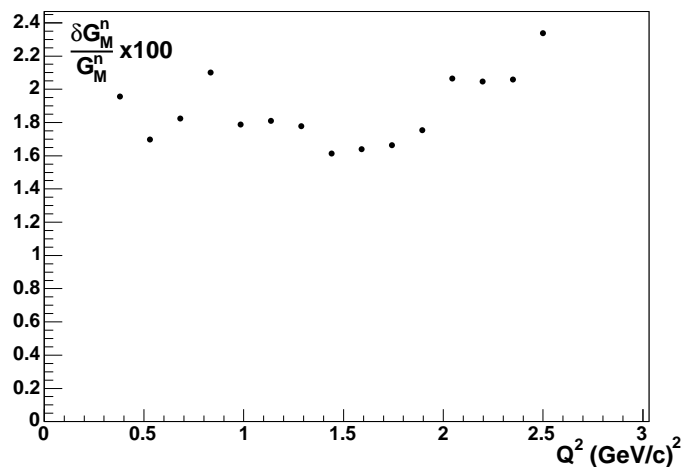


Figure 4.54: Combined fractional systematic error for the 2.5 GeV beam energy, with EC neutron detection.

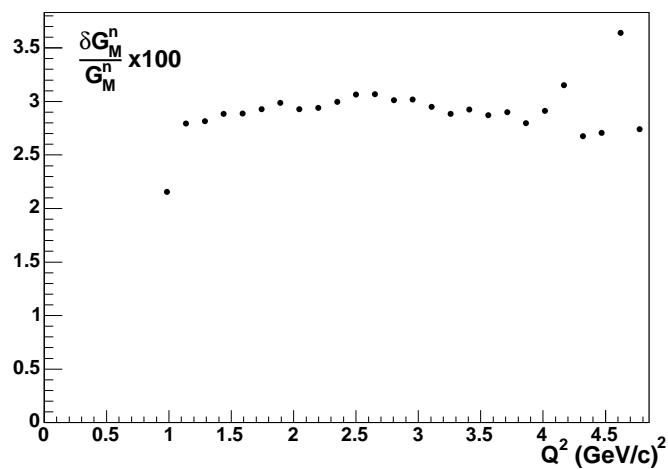


Figure 4.55: Combined fractional systematic error for the 4.2 GeV beam energy, with SC neutron detection.

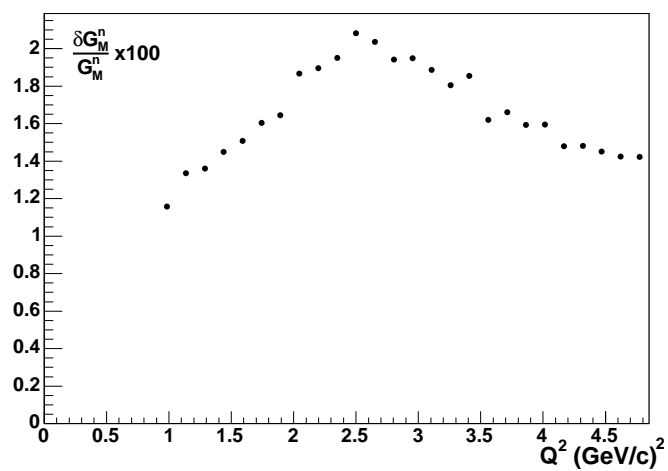


Figure 4.56: Combined fractional systematic error for the 4.2 GeV beam energy, with EC neutron detection.

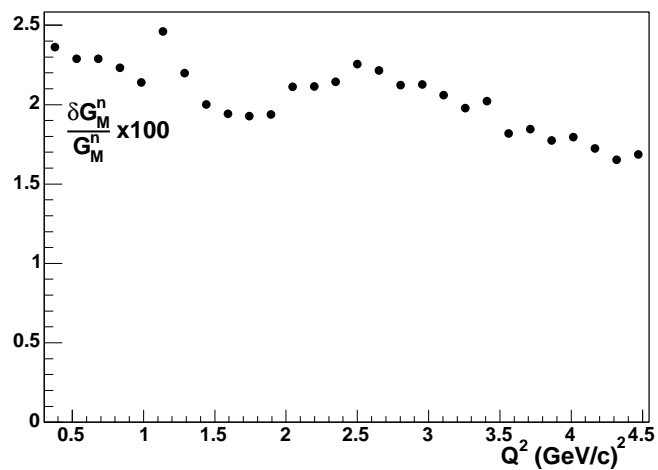


Figure 4.57: Weighted average fractional systematic error.

# Chapter 5

## Conclusions

The magnetic form factor of the neutron  $G_M^n$  has been extracted from the ratio of quasi-elastic e-n to e-p scattering from a deuterium target over a wide range of  $Q^2$  values. The use of the ratio technique resulted in the cancellation of many uncertainties. Neutrons were detected in two different detector systems (the time-of-flight detector and the forward calorimeter) at two different beam energies. This combination of multiple beam energies and multiple neutron detectors allowed four semi-independent measurements of  $G_M^n$  to be performed. The two neutron detectors are subject to completely different systematic errors, and the protons sample different regions of the drift chambers and time-of-flight detector at the two beam energies. The  $Q^2$  region covered by any of the four measurements overlaps a portion of the  $Q^2$  region covered by any of the other three measurements. The consistency of the measurements in the overlap regions gives confidence that systematic errors are under control.

### 5.1 Comparison to previous measurements

A comparison of the weighted average determination of  $G_M^n$  (scaled to the dipole parametrization) to previous measurements is shown in Figure 5.1. The weighted average systematic error is shown as an error band, and a line showing  $G_M^n = \mu_n G_D$  is drawn. A similar plot is shown in Fig 5.2. Fig 5.3 shows the statistical and systematic errors added in quadrature. The data is seen to be in agreement with previous measurements in the  $Q^2 > 1$  (GeV/c)<sup>2</sup> region. In the  $Q^2 < 1$  (GeV/c)<sup>2</sup> region, significant disagreement is seen with the Jourdan [57] measurement. The region of disagreement is the only  $Q^2$  region covered by a single measurement (SC neutrons at 2.5 GeV). The disagreement in this region provides a strong motivation to make further efforts to complete the analysis of the reversed-field portion of the e5 data, which was not performed as a part of this thesis. If successfully analyzed, the reversed field data will provide a second SC-based measurement, an EC-based measurement and possibly a Large-Angle Calorimeter based measurement of  $G_M^n$  in the low- $Q^2$  region.

The range of  $Q^2$  covered by this experiment, the number of points at which  $G_M^n$

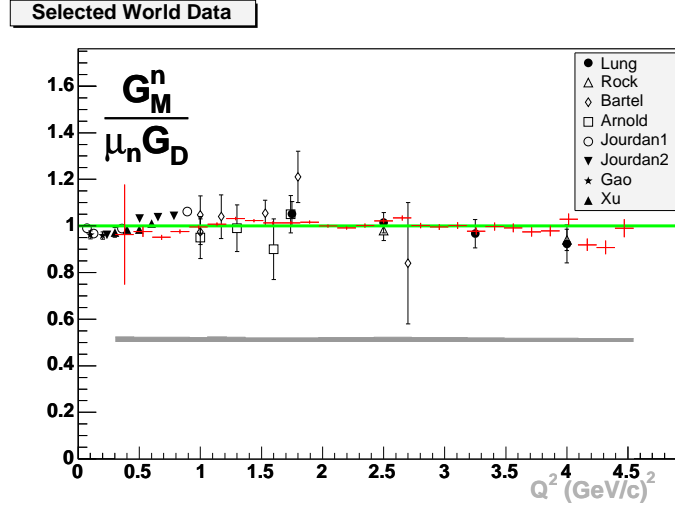


Figure 5.1: The weighted average value of  $G_M^n$ , scaled to the dipole parametrization. A selection of previous measurements is shown. The weighted average systematic error is shown as a grey band. The green line indicates  $G_M^n = \mu_n G_D$

was measured, and the precision with which it was measured represent a substantial improvement to the world data set. The standard dipole parametrization is seen to give a good representation of the data for  $Q^2 > 1$   $(\text{GeV}/c)^2$ , although the data may show  $G_M^n$  falling off faster than the dipole for  $Q^2 > 3.5$   $(\text{GeV}/c)^2$ . In the time elapsed since the e5 data set was taken, the maximum beam energy at Jefferson Lab has increased to 6 GeV. The e5 experiment used a proven technique, and the experiment could be repeated at the higher beam energy to extend the  $Q^2$  coverage up to  $Q^2 \approx 7$   $(\text{GeV}/c)^2$ . This would allow investigation of the possibility of deviations from the dipole at higher  $Q^2$ , and would extend our knowledge of  $G_M^n$  into a  $Q^2$  region where no reliable measurement currently exists.

### 5.1.1 Comparison to theoretical predictions and fits

A comparison between the weighted average value of  $G_M^n$  and the various theoretical predictions and fits discussed in Section 1.1.3 is shown in Fig 5.4. A close-up view is shown in Fig 5.5. The models that do the best, Lomon and Kelley, are the ones that are most tightly linked to previous data (the Kelley curve is really nothing more than a fit with a ratio of polynomials). This is not unexpected, as (at least in the  $Q^2 > 1$   $(\text{GeV}/c)^2$  region), the e5 data is consistent with previous world data. The Lomon results are seen to be superior to the Kelley fit. The IJL model appears to be ruled out, as its prediction of rapid growth with  $Q^2$  is entirely inconsistent with the data. This is surprising, given its success in the proton sector. The lattice prediction fails completely, never predicting a value less than  $\approx 35\%$  different from the data. Hopefully, the lattice results will improve in the future as computer power increases.

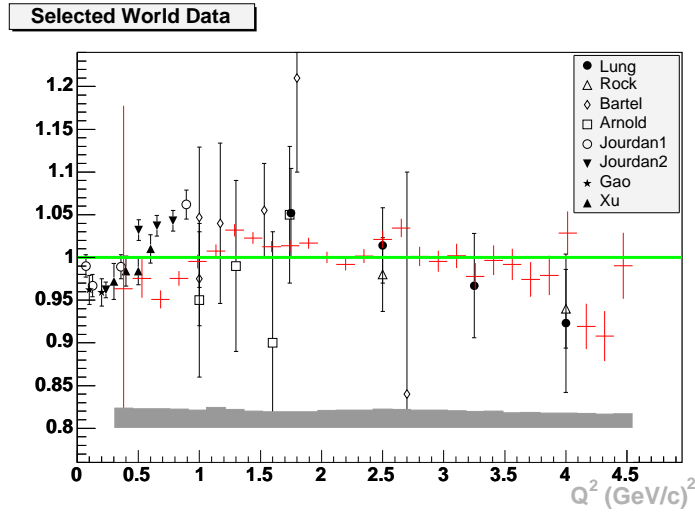


Figure 5.2: The weighted average value of  $G_M^n$ , scaled to the dipole parametrization. A selection of previous measurements is shown. The weighted average systematic error is shown as a grey band. The green line indicates  $G_M^n = \mu_n G_D$

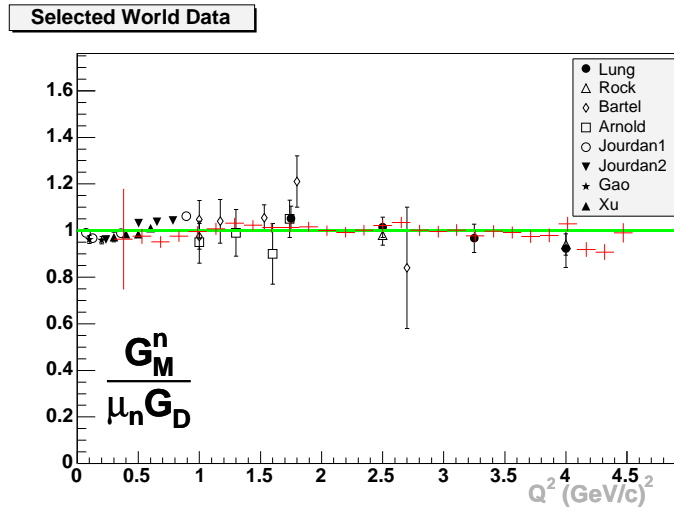


Figure 5.3: The weighted average value of  $G_M^n$ , scaled to the dipole parametrization. A selection of previous measurements is shown. The error bars on the data points are the quadrature sum of the statistical and systematic errors. The green line shows  $G_M^n = \mu_n G_D$

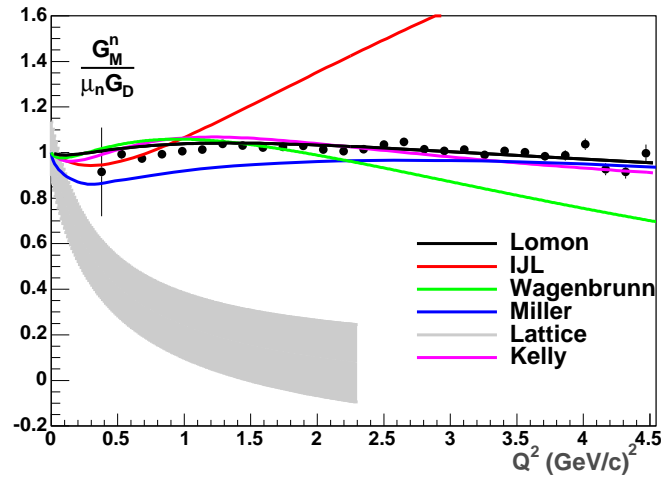


Figure 5.4: A comparison of the e5 data and the theoretical predictions discussed in Section 1.1.3. Only the statistical errors are shown.

The other two models do an adequate job in one  $Q^2$  region (low  $Q^2$  for Wagenbrunn, high  $Q^2$  for Miller), but are unable to reproduce the data over the full  $Q^2$  range. The Miller model is a hybrid which uses a pion cloud, implemented with a cloudy bag model and a relativistic constituent quark model. The pion cloud is important at low momentum transfer, while in the large momentum transfer region the prediction is dominated by a relativistic constituent quark model. The comparison with the data suggest the pion cloud portion of the model is not adequate, while the relativistic constituent quark portion performs well as  $Q^2$  becomes large.

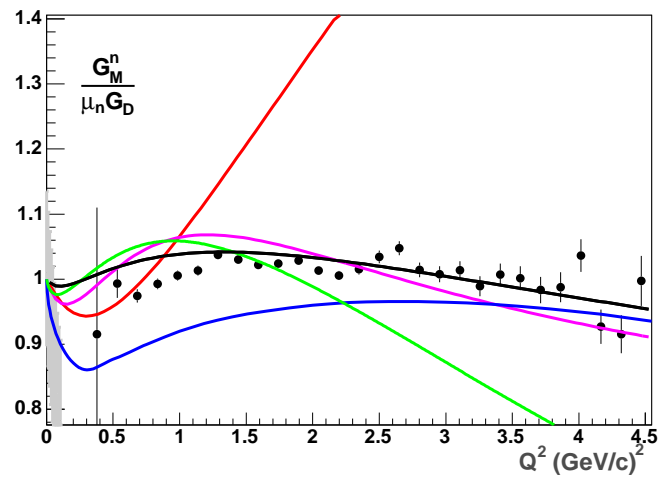


Figure 5.5: A comparison of the e5 data and the theoretical predictions discussed in Section 1.1.3. Only the statistical errors are shown. The colors have the meaning indicated in Fig 5.4.

# Bibliography

- [1] F.Halzen and A.Martin. *Quarks and Leptons*. J.Wiley, 1984.
- [2] F.Iachello, A.D.Jackson, and A.Lande. *Phys.Lett B*, 43B:191, 1973.
- [3] J.Bjorken and S.Drell. *Relativistic Quantum Mechanics*. McGraw Hill, 1965.
- [4] M.K.Jones et al. *Phys.Rev.Lett*, 84:1398, 2000.
- [5] O.Gayou et al. *Phys.Rev.Lett*, 88:092301, 2002.
- [6] M.Gari and W.Krumpelmann. *Z.Phys.A*, 322:689, 1985.
- [7] U. Kaulfuss and M. Gari. *Nucl.Phys.A*, 408, 1983.
- [8] S.Brodsky and S.Farrar. *Phys.Rev.D*, 11, 1975.
- [9] E.Lomon. *Phys.Rev.C*, 64, 2001.
- [10] E.Lomon. *nucl-th/0203081*.
- [11] P.Mergell, U.Meissner, and D.Dreschel. *Nucl.Phys.A*, 596, 1996.
- [12] G.Miller. *Phys. Rev. C*, 66, 2002.
- [13] V.B.Berestetskii and M.V.Terentev. *Sov.J.Nucl.Phys.*, 1977.
- [14] P. L. Chung and F. Coester. *Phys. Rev.*, D44:229–241, 1991.
- [15] R.F. Wagenbrunn *et al.*. *Eur. Phys. J. A.*, 18, 2002.
- [16] L. Ya. Glozman, W. Plessas, K. Varga, and R. F. Wagenbrunn. *Phys. Rev.*, D58:094030, 1998.
- [17] M.Gockeler et al. *hep-lat/0303019*.
- [18] J.D. Ashley et al. *Eur. Phys. J A*, 19, s01:9–14, 2004.
- [19] J.J.Kelly. *Phys. Rev. C*, 70:068202, 2004.
- [20] E.B.Hughes et al. *Phys. Rev.*, 146:973, 1965.

- [21] B.Grossetete et al. *Phys. Rev.*, 141:1435, 1966.
- [22] A.S. Esaulov et al. *Sov. J. Nucl. Phys.*, 45:258, 1987.
- [23] R. G. Arnold et al. *Phys. Rev. Lett.*, 61:806, 1988.
- [24] A.Lung et al. *Phys. Rev. Lett.*, 70:718, 1993.
- [25] P.Stein et al. *Phys. Rev. Lett.*, 16:592, 1966.
- [26] W.Bartel et al. *Nuc. Phys. B*, 58:429–475, 1973.
- [27] P. Markowitz et al. *Phys. Rev. C*, 48:R5, 1993.
- [28] K.M. Hanso et al. *Phys. Rev. D*, 8:753, 1973.
- [29] H. Anklin et al. *Phys. Lett.*, B336:313, 1994.
- [30] E.E.W. Bruins et al. *Phys. Rev. Lett.*, 75:21, 1995.
- [31] G. Kubon et al. *Phys. Lett.*, B524:26–32, 2002.
- [32] H. Gao. *nucl-ex/0301002v1*.
- [33] M.D. Mestayer et al. *NIM A*, 449:81, 2000.
- [34] E.S. Smith et al. *NIM A*, 432:265, 1999.
- [35] G.Adams et al. *NIM A*, 465:414, 2001.
- [36] M.Amarian et al. *NIM A*, 460:239, 2001.
- [37] J.W.C. McNabb. Ph.d. thesis. 2002.
- [38] E. J. Brash, A. Kozlov, S. Li, and G. M. Huber. *Phys. Rev.*, C65:051001, 2002.
- [39] Luke W. Mo and Yung-Su Tsai. *Rev. Mod. Phys.*, 41:205–235, 1969.
- [40] A. Afanasev, I. Akushevich, V. Burkert, and K. Joo. *Phys. Rev.*, D66:074004, 2002.
- [41] Jr. Adam, J., Franz Gross, Sabine Jeschonnek, Paul Ulmer, and J. W. Van Orden. *Phys. Rev.*, C66:044003, 2002.
- [42] J.Schwinger. *Phys.Rev.*, 76, 1949.
- [43] S.Jeschonnek. private communication.
- [44] S.Jeschonnek and T.Donnely. *Phys. Rev. C*, 57:2438–2452, 1998.

- [45] S.Jeschonnek and J.W. Van Orden. *Phys. Rev. C*, 62:044613, 2000.
- [46] S.Jeschonnek and T.Donnely. *Phys. Rev. C*, 59:2676–2668, 1998.
- [47] H.Arenhovel. private communication.
- [48] A.S.Raskin and T.W.Donnely. *Ann.Phys.*, 191:78, 1989.
- [49] T.W.Donnely and A.S.Raskin. *Ann. Phys.*, 169:247–351, 1986.
- [50] V.G.J.Stoks R.B.Wiringa and R.Sciavilla. *Phys. Rev. C*, 51:38, 1995.
- [51] W.Brooks. private communication.
- [52] J.Arrington. private communication.
- [53] P.Bosted. *Phys. Rev. C*, 51:409–411, 1995.
- [54] R.Schiavilla and I.Sick. *Phys. Rev. C*, 64:041002–1, 2001.
- [55] R.Bradford. private communication.
- [56] W.Brooks et al. E5 experiment proposal. 1994.
- [57] J. Jourdan. *Nucl. Phys.*, A721:395–400, 2003.

# Appendix A

## Measured $G_M^n$ values and errors

Table A.1: Measured values of  $\frac{G_M^n}{\mu_n G_D}$ , statistical and systematic errors for the 4.2 GeV beam energy with EC neutron detection. The  $Q^2$  values given are the central value of each  $Q^2$  bin.

$Q^2$	$\frac{G_M^n}{\mu_n G_D}$	Statistical	Systematic
1.43939	1.03303	0.0892285	0.0145
1.59091	1.02321	0.0174769	0.0150725
1.74242	1.02075	0.0123648	0.0160474
1.89394	1.03698	0.00955924	0.0164546
2.04545	0.997756	0.00892518	0.0186694
2.19697	0.999716	0.00936501	0.0189584
2.34848	1.00588	0.00992914	0.0194988
2.5	1.01303	0.0109049	0.0208164
2.65152	1.03408	0.0118468	0.0203572
2.80303	1.0024	0.0124425	0.0194208
2.95455	0.990675	0.0134671	0.0194922
3.10606	1.00237	0.0155773	0.0188635
3.25758	0.975636	0.0168241	0.0180567
3.40909	0.983286	0.0187109	0.0185434
3.56061	1.00733	0.0200905	0.0162037
3.71212	0.96238	0.0219672	0.0166032
3.86364	0.970364	0.0249725	0.0159274
4.01515	1.01692	0.0274167	0.0159431
4.16667	0.917071	0.0286722	0.0147973
4.31818	0.907847	0.031736	0.0148089
4.4697	0.994197	0.0428115	0.0145047

Table A.2: Measured values of  $\frac{G_M^n}{\mu_n G_D}$ , statistical and systematic errors for the 4.2 GeV beam energy with SC neutron detection. The  $Q^2$  values given are the central value of each  $Q^2$  bin.

$Q^2$	$\frac{G_M^n}{\mu_n G_D}$	Statistical	Systematic
0.984848	0.833335	0.260571	0.0215434
1.13636	1.01845	0.0673612	0.0279515
1.28788	1.01426	0.0316126	0.0281427
1.43939	1.07012	0.0195325	0.0288361
1.59091	1.04393	0.0190088	0.0288581
1.74242	1.04162	0.0196435	0.0292642
1.89394	1.03239	0.0195482	0.0298587
2.04545	1.04775	0.0200558	0.0292821
2.19697	1.003	0.0207324	0.0294041
2.34848	1.00066	0.0217728	0.0299643
2.5	1.06022	0.0238032	0.0306375
2.65152	1.03605	0.025793	0.0306766
2.80303	0.995402	0.0275382	0.0301151
2.95455	1.01906	0.0300813	0.030184
3.10606	0.999203	0.0351982	0.0294858
3.25758	0.990009	0.0386925	0.0288456
3.40909	1.06874	0.0433667	0.0292331
3.56061	0.909629	0.0462709	0.0287062
3.71212	1.04135	0.0522643	0.0289949
3.86364	1.02874	0.0593565	0.0279802
4.01515	1.09282	0.0646975	0.0291318
4.16667	0.932118	0.069162	0.031505
4.31818	0.908535	0.0774644	0.0267442
4.4697	0.973166	0.0891094	0.0270653

Table A.3: Measured values of  $\frac{G_M^n}{\mu_n G_D}$ , statistical and systematic errors for the 2.5 GeV beam energy with EC neutron detection. The  $Q^2$  values given are the central value of each  $Q^2$  bin.

$Q^2$	$\frac{G_M^n}{\mu_n G_D}$	Statistical	Systematic
0.984848	1.02905	0.0274909	0.0178769
1.13636	1.02591	0.0134874	0.0180966
1.28788	1.0371	0.0093458	0.0177686
1.43939	1.01105	0.00820353	0.0161245
1.59091	1.00178	0.00855422	0.0163843
1.74242	1.00653	0.00966249	0.0166409
1.89394	0.985969	0.0106488	0.0175305
2.04545	0.982432	0.012114	0.0206548
2.19697	0.976307	0.014556	0.0204765
2.34848	0.985776	0.0249617	0.0205911
2.5	1.02056	0.106045	0.0233788

Table A.4: Measured values of  $\frac{G_M^n}{\mu_n G_D}$ , statistical and systematic errors for the 2.5 GeV beam energy with SC neutron detection. The  $Q^2$  values given are the central value of each  $Q^2$  bin.

$Q^2$	$\frac{G_M^n}{\mu_n G_D}$	Statistical	Systematic
0.530303	0.975437	0.0225199	0.0228829
0.681818	0.950933	0.010491	0.0228798
0.833333	0.975324	0.0085539	0.0223268
0.984848	0.992182	0.00836544	0.0217311
1.13636	0.997284	0.00976334	0.0279341
1.28788	1.02565	0.012107	0.0281332
1.43939	1.03309	0.0143283	0.0272558
1.59091	1.01994	0.0163595	0.0273296
1.74242	0.998626	0.0185454	0.0274123
1.89394	1.01997	0.0203983	0.028081
2.04545	1.01589	0.0232673	0.0285848
2.19697	0.958902	0.0280185	0.0282168
2.34848	0.964886	0.0478034	0.0285554
2.5	1.01549	0.182697	0.0284096

Table A.5: Measured values of  $\frac{G_M^n}{\mu_n G_D}$ , statistical and systematic errors from the weighted average.

$Q^2$	$\frac{G_M^n}{\mu_n G_D}$	Statistical	Systematic
0.530303	0.975437	0.0225199	0.0228829
0.681818	0.950933	0.010491	0.0228798
0.833333	0.975324	0.0085539	0.0223268
0.984848	0.995306	0.00800311	0.0214045
1.13636	1.00728	0.00785473	0.0245978
1.28788	1.03186	0.0072034	0.0219763
1.43939	1.02284	0.00667009	0.02001
1.59091	1.01265	0.00653109	0.0194181
1.74242	1.0136	0.00662985	0.0192848
1.89394	1.01669	0.00635229	0.0193804
2.04545	1.00001	0.00649555	0.0211262
2.19697	0.991865	0.00712071	0.0211519
2.34848	1.0016	0.00836382	0.021443
2.5	1.02119	0.00985659	0.0225447
2.65152	1.03442	0.0107656	0.0221549
2.80303	1.00121	0.0113388	0.0212338
2.95455	0.995414	0.0122915	0.0212774
3.10606	1.00185	0.0142447	0.0206032
3.25758	0.977922	0.0154287	0.0197722
3.40909	0.996698	0.01718	0.020221
3.56061	0.991829	0.0184284	0.0181868
3.71212	0.974237	0.0202512	0.0184637
3.86364	0.979143	0.0230183	0.0177399
4.01515	1.02848	0.0252436	0.017951
4.16667	0.919278	0.0264864	0.0172476
4.31818	0.907946	0.029367	0.0165242
4.4697	0.990253	0.038589	0.0168603

# Appendix B

## EC neutron detection efficiency fits

### B.1 2.5 GeV beam energy

This section contains plots of the neutron detection efficiency measured on each of nine superpixels in each of six EC modules, as a function of neutron momentum for the 2.5 GeV dataset. Each plot is labelled by a pair of numbers  $a, b$  where  $a$  is the sector number of the EC modules and  $b$  is the superpixel number, as shown in Fig 3.13. Two curves are superimposed on each figure. The red curve shows the result of the maximum-likelihood fit performed on the whole-sector efficiency. The black curve shows the results of scaling the whole-sector efficiency to the superpixel measurements (see Eqn 3.31). Two numbers are indicated in black in each plot. The upper number is the value of  $\chi^2/ndf$  obtained from comparing the measured efficiency of each pixel to the sector fit. The lower black number is the value of  $\chi^2/ndf$  obtained from comparing the measured efficiency to the scaled fit. The blue number is the value of the scale factor, and the magenta number is the error on the scale factor.

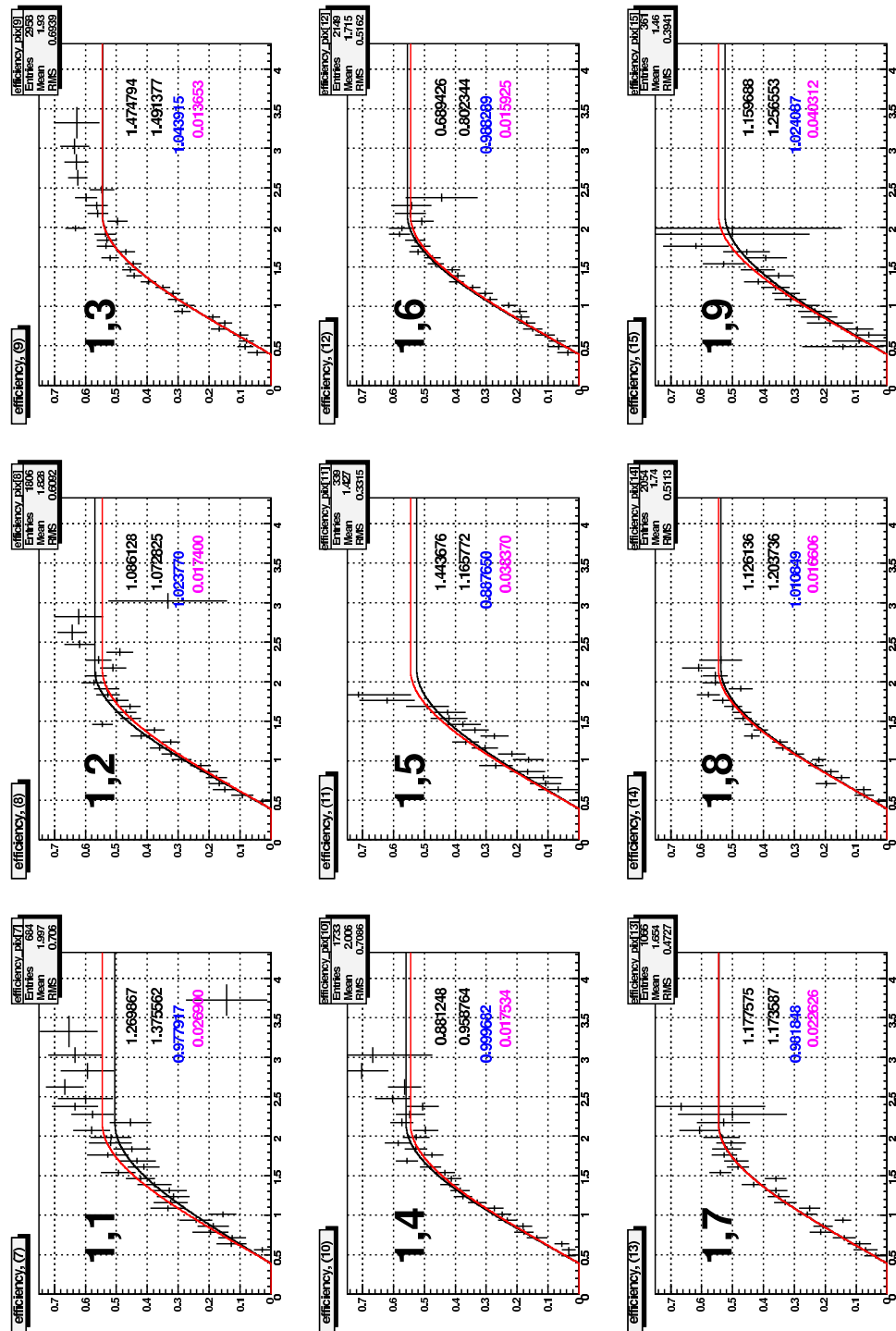


Figure B.1: Neutron detection efficiency by superpixel in sector 1, from the 2.5 GeV data. The red line shows the results of the fit to the entire sector. The black line shows the scaled sector fit.

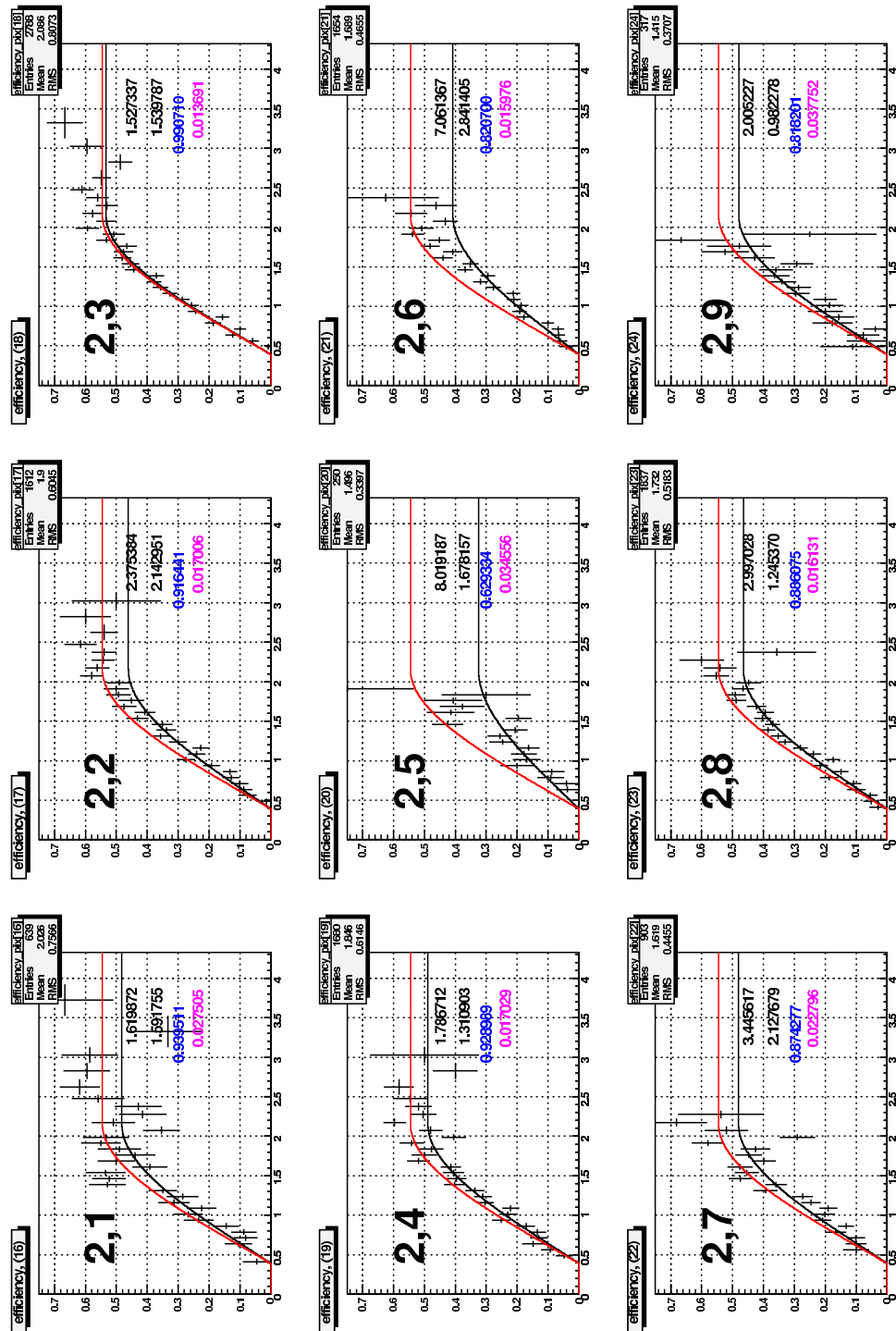


Figure B.2: Neutron detection efficiency by superpixel in sector 2, from the 2.5 GeV data. The red line shows the results of the fit to the entire sector. The black line shows the scaled sector fit.

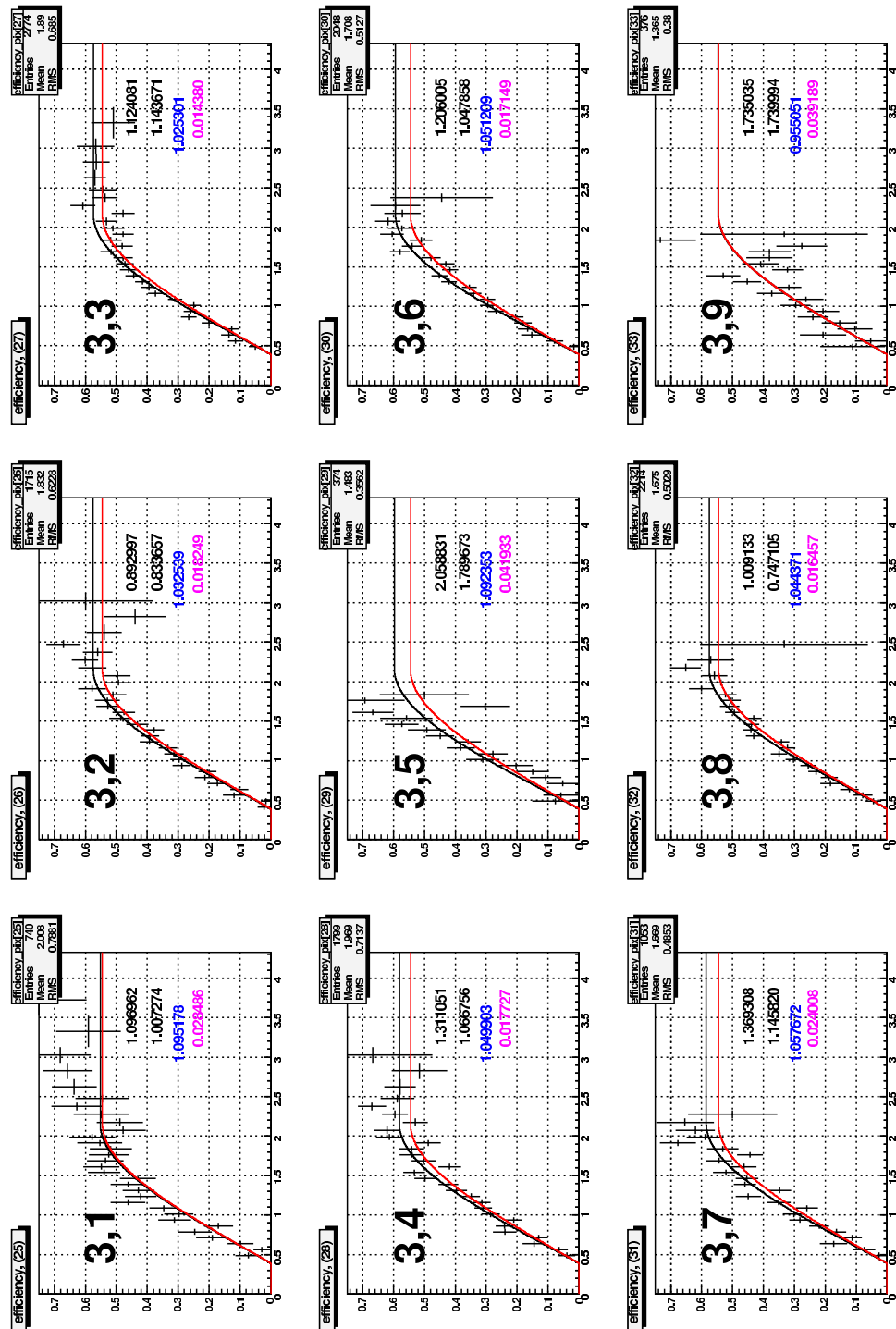


Figure B.3: Neutron detection efficiency by superpixel in sector 3, from the 2.5 GeV data. The red line shows the results of the fit to the entire sector. The black line shows the scaled sector fit.

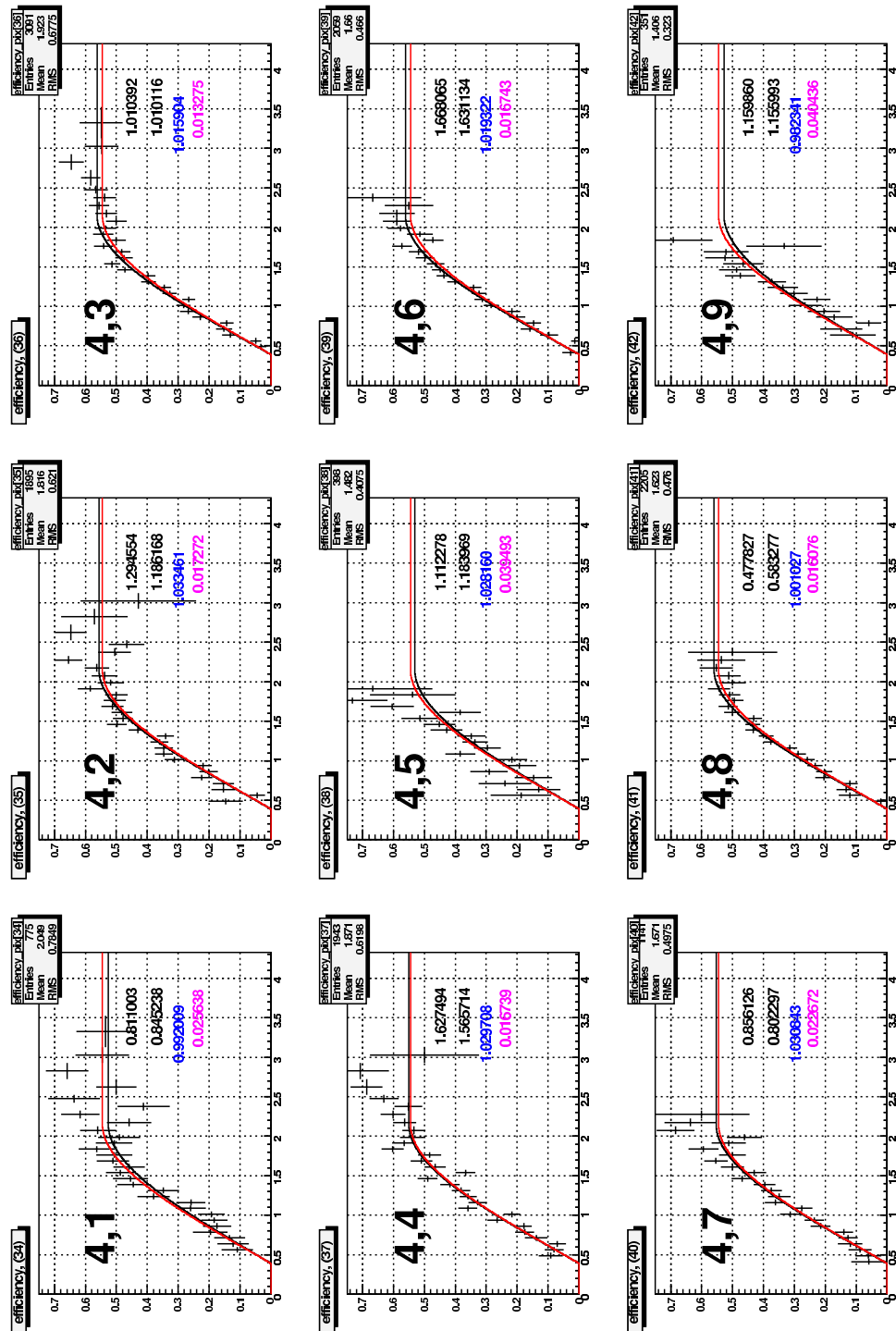


Figure B.4: Neutron detection efficiency by superpixel in sector 4, from the 2.5 GeV data. The red line shows the results of the fit to the entire sector. The black line shows the scaled sector fit.

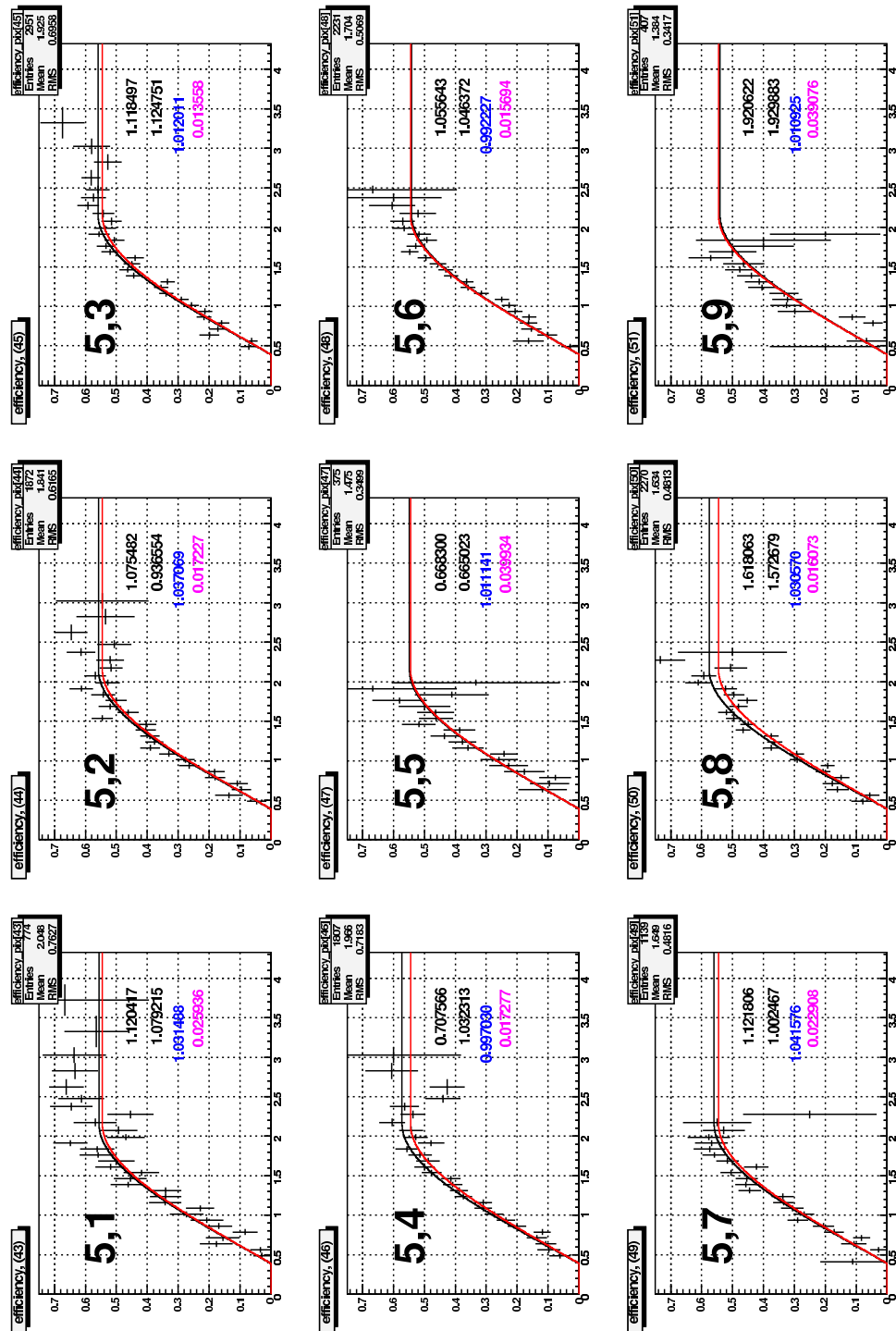


Figure B.5: Neutron detection efficiency by superpixel in sector 5, from the 2.5 GeV data. The red line shows the results of the fit to the entire sector. The black line shows the scaled sector fit.

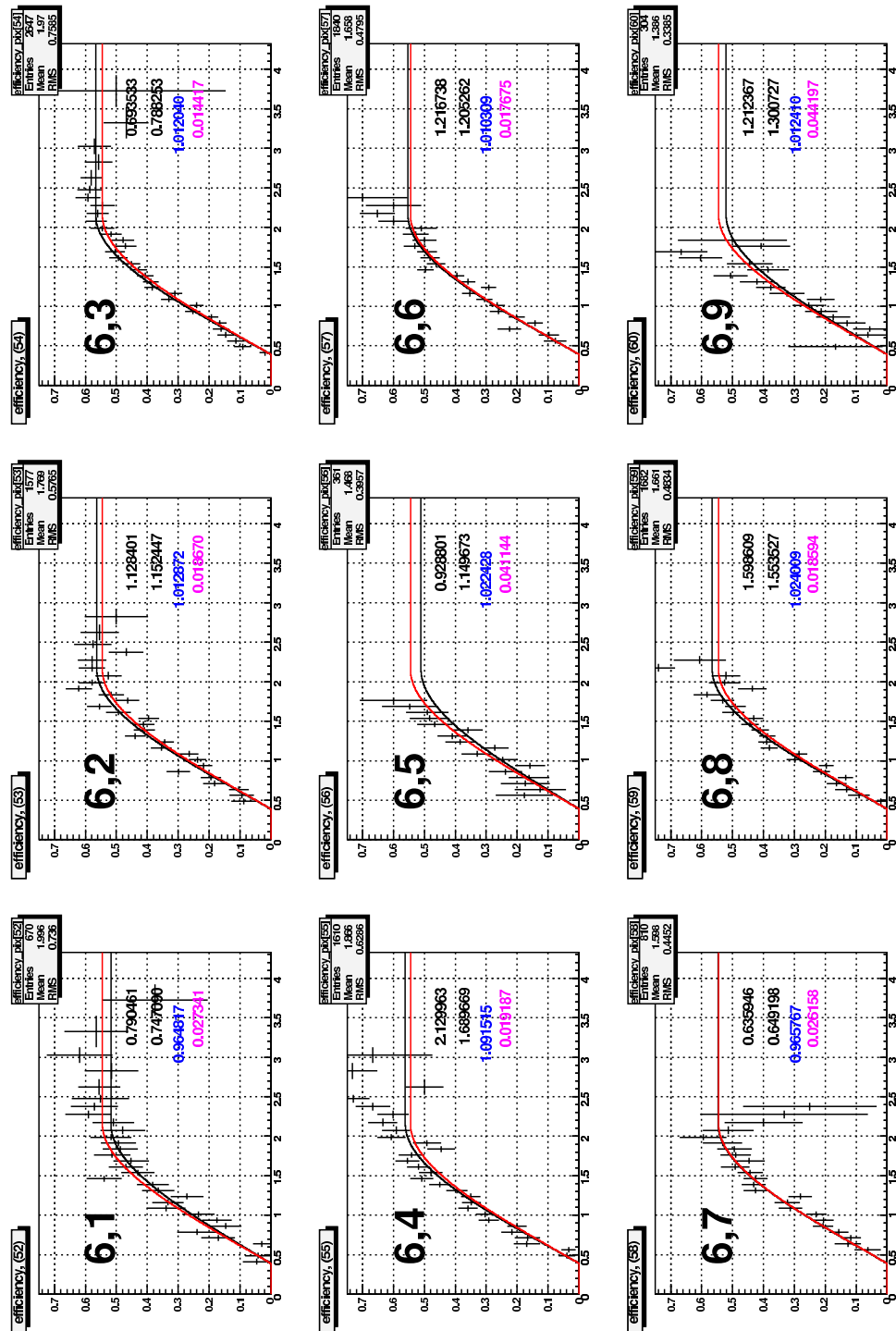


Figure B.6: Neutron detection efficiency by superpixel in sector 6, from the 2.5 GeV data. The red line shows the results of the fit to the entire sector. The black line shows the scaled sector fit.

## B.2 4.2 GeV beam energy

This section contains plots of the neutron detection efficiency measured on each of nine superpixels in each of six EC modules, as a function of neutron momentum for the 4.2 GeV dataset. Each plot is labelled by a pair of numbers  $a, b$  where  $a$  is the sector number of the EC modules and  $b$  is the superpixel number, as shown in Fig 3.13. Two curves are superimposed on each figure. The red curve shows the result of the maximum-likelihood fit performed on the whole-sector efficiency. The black curve shows the results of scaling the whole-sector efficiency to the superpixel measurements (see Eqn 3.31). Two numbers are indicated in black in each plot. The upper number is the value of  $\chi^2/ndf$  obtained from comparing the measured efficiency of each pixel to the sector fit. The lower black number is the value of  $\chi^2/ndf$  obtained from comparing the measured efficiency to the scaled fit. The blue number is the value of the scale factor, and the magenta number is the error on the scale factor.

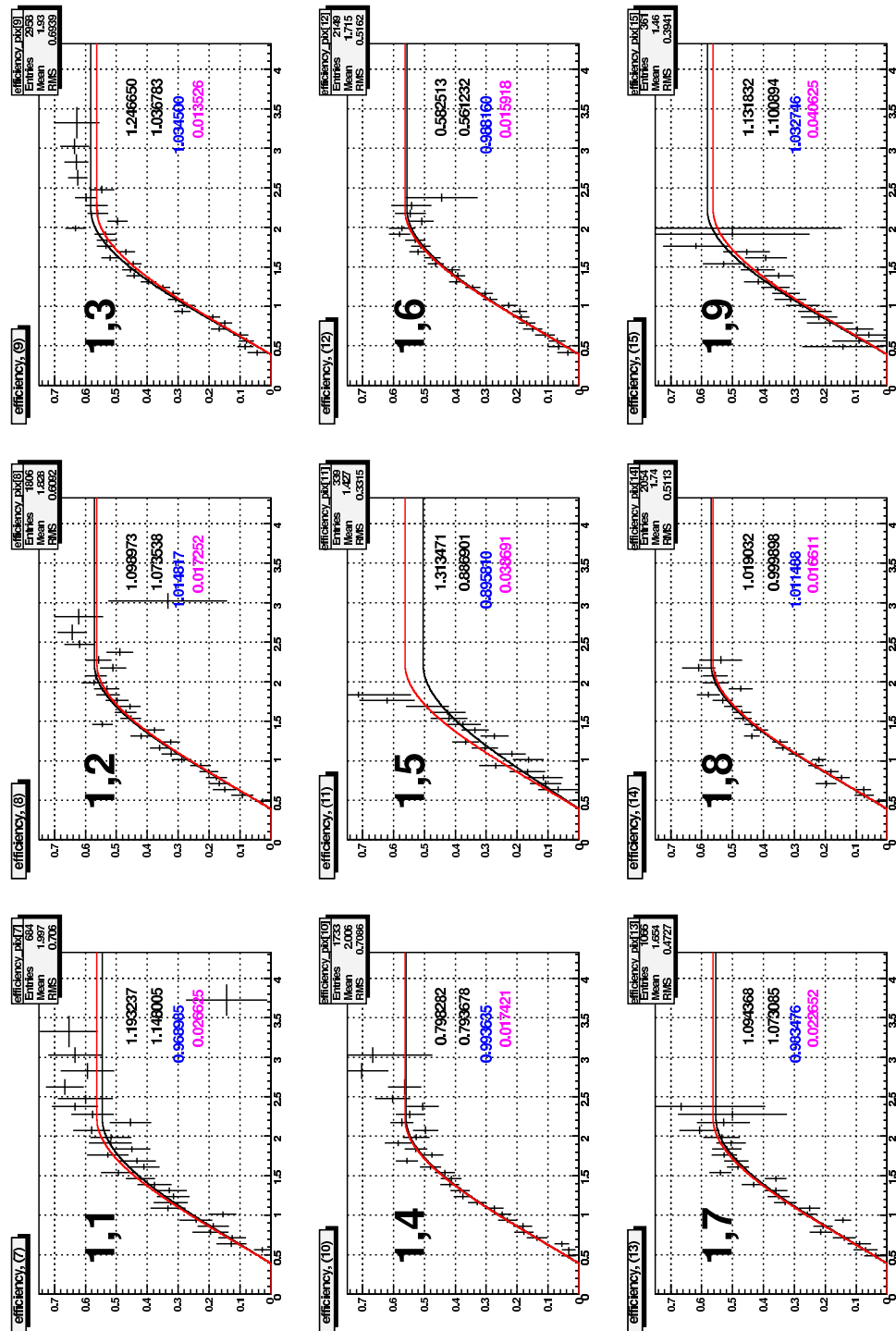


Figure B.7: Neutron detection efficiency by superpixel in sector 1, from the 4.2 GeV data. The red line shows the results of the fit to the entire sector. The black line shows the scaled sector fit.

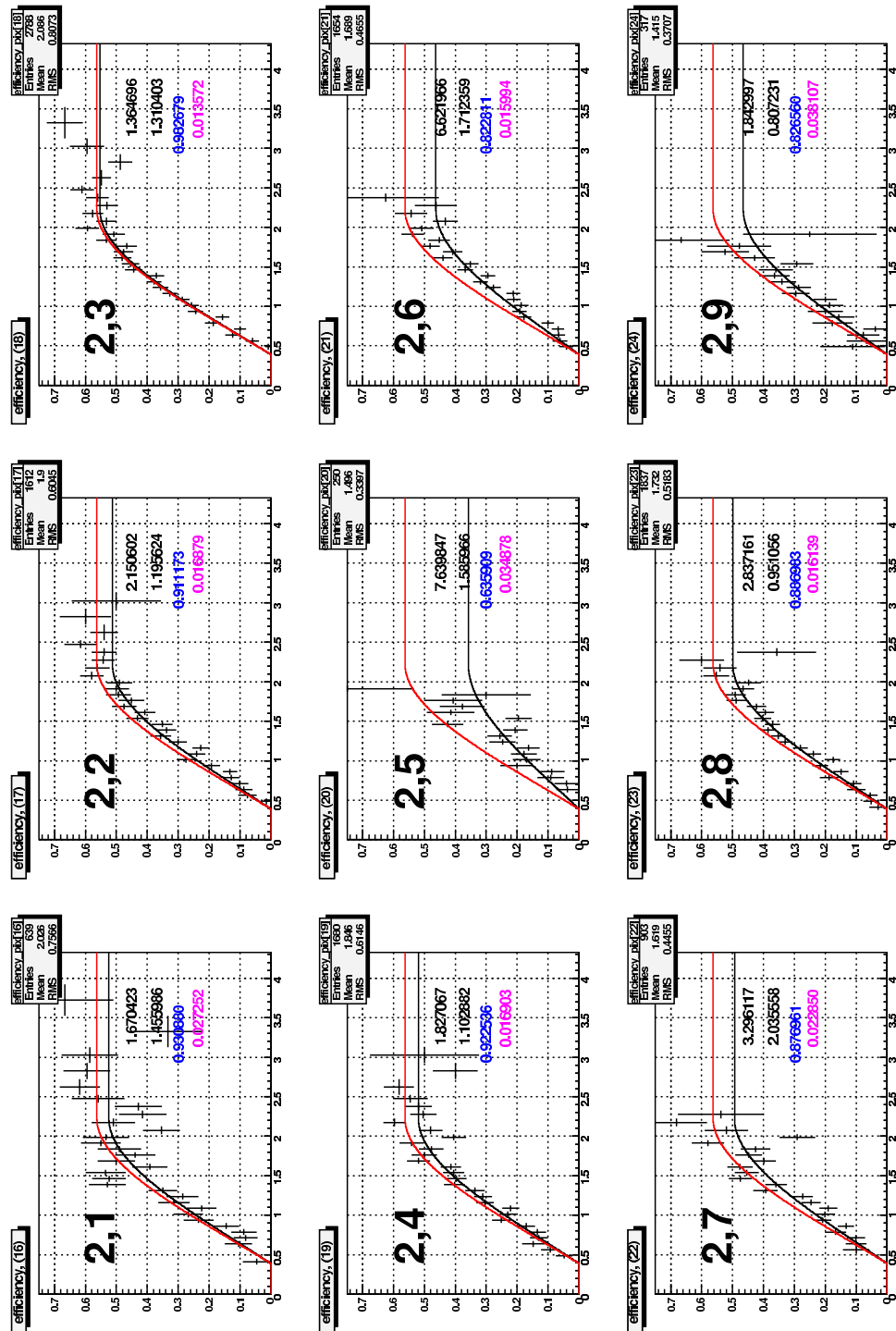


Figure B.8: Neutron detection efficiency by superpixel in sector 2, from the 4.2 GeV data. The red line shows the results of the fit to the entire sector. The black line shows the scaled sector fit.

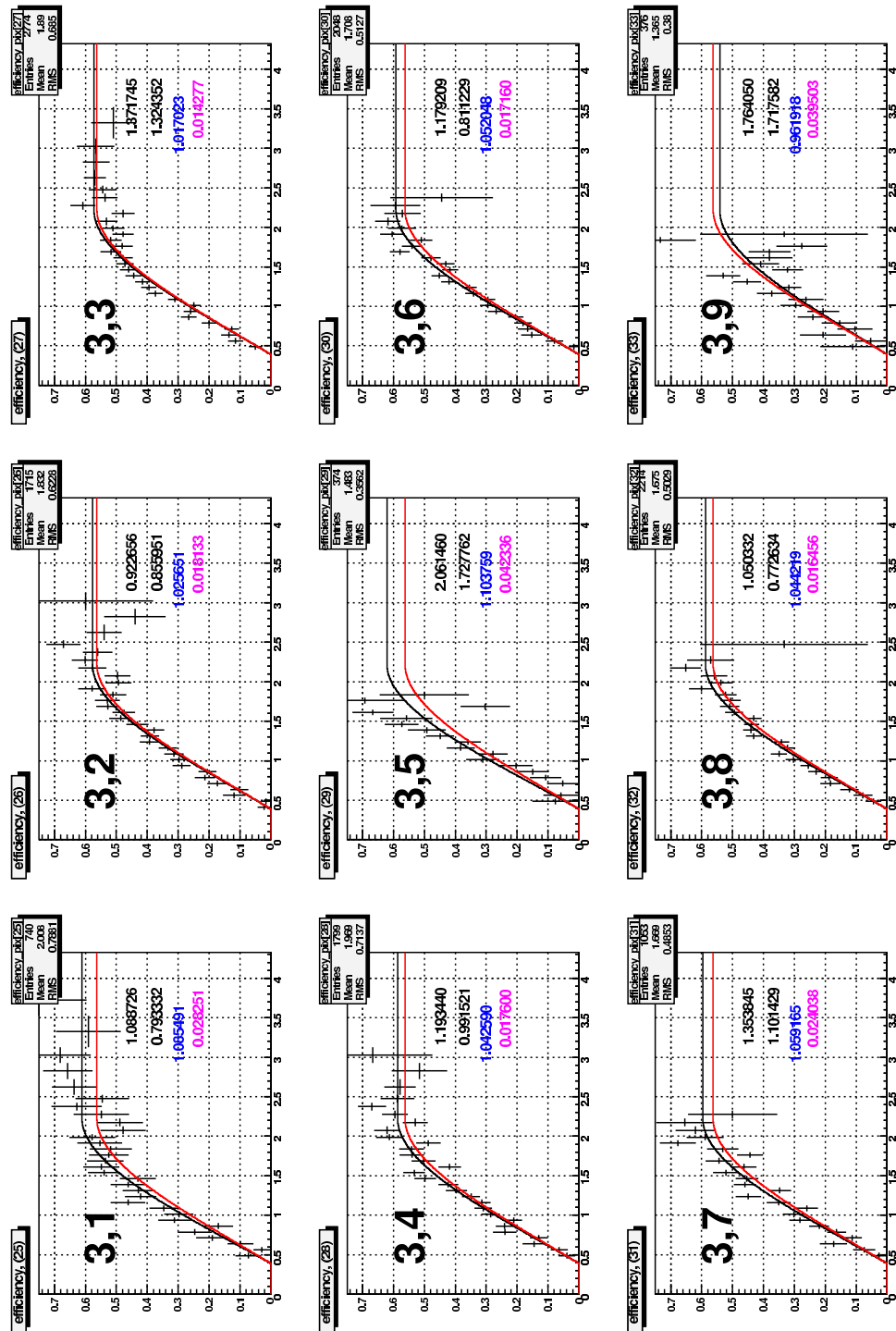


Figure B.9: Neutron detection efficiency by superpixel in sector 3, from the 4.2 GeV data. The red line shows the results of the fit to the entire sector. The black line shows the scaled sector fit.

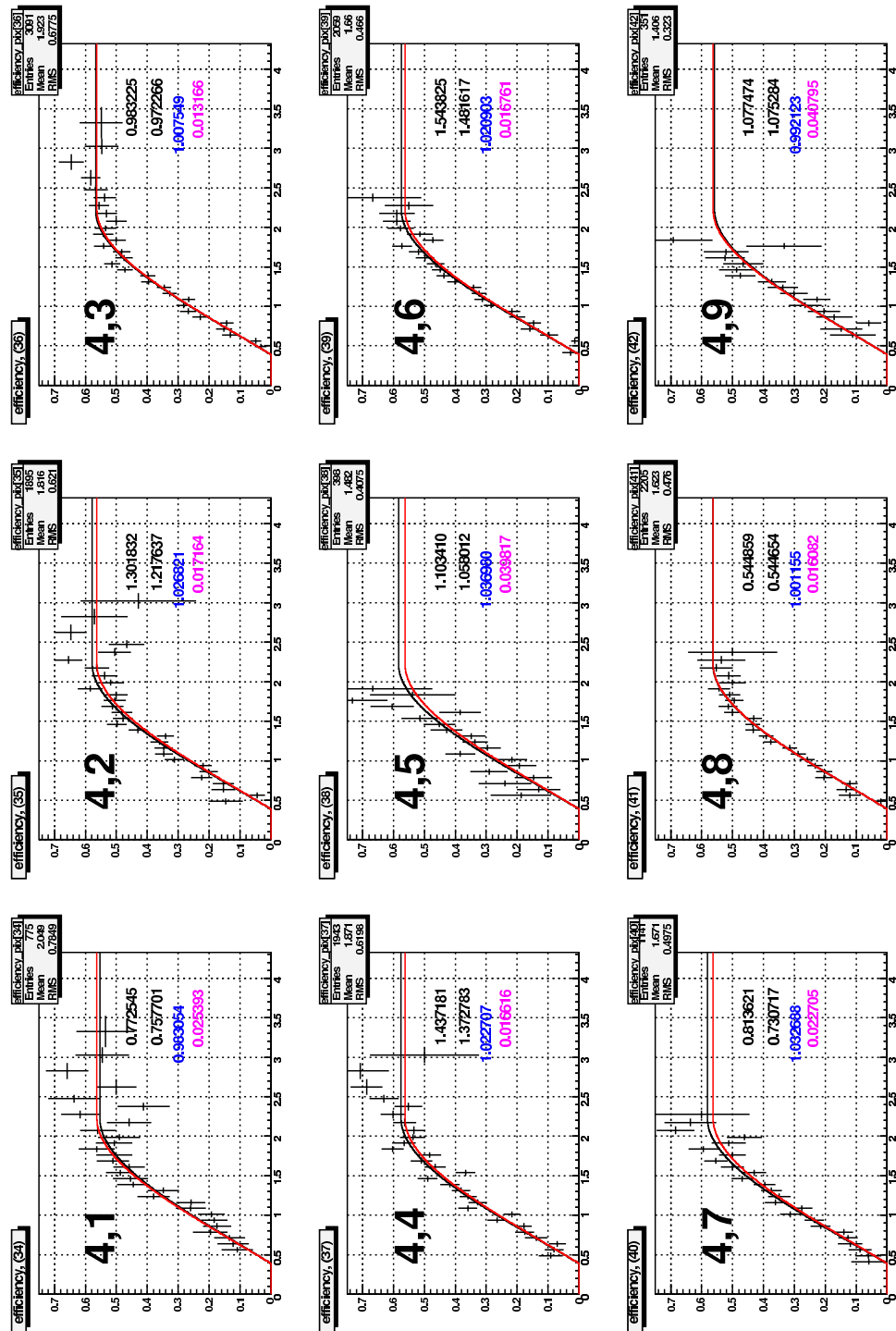


Figure B.10: Neutron detection efficiency by superpixel in sector 4, from the 4.2 GeV data. The red line shows the results of the fit to the entire sector. The black line shows the scaled sector fit.

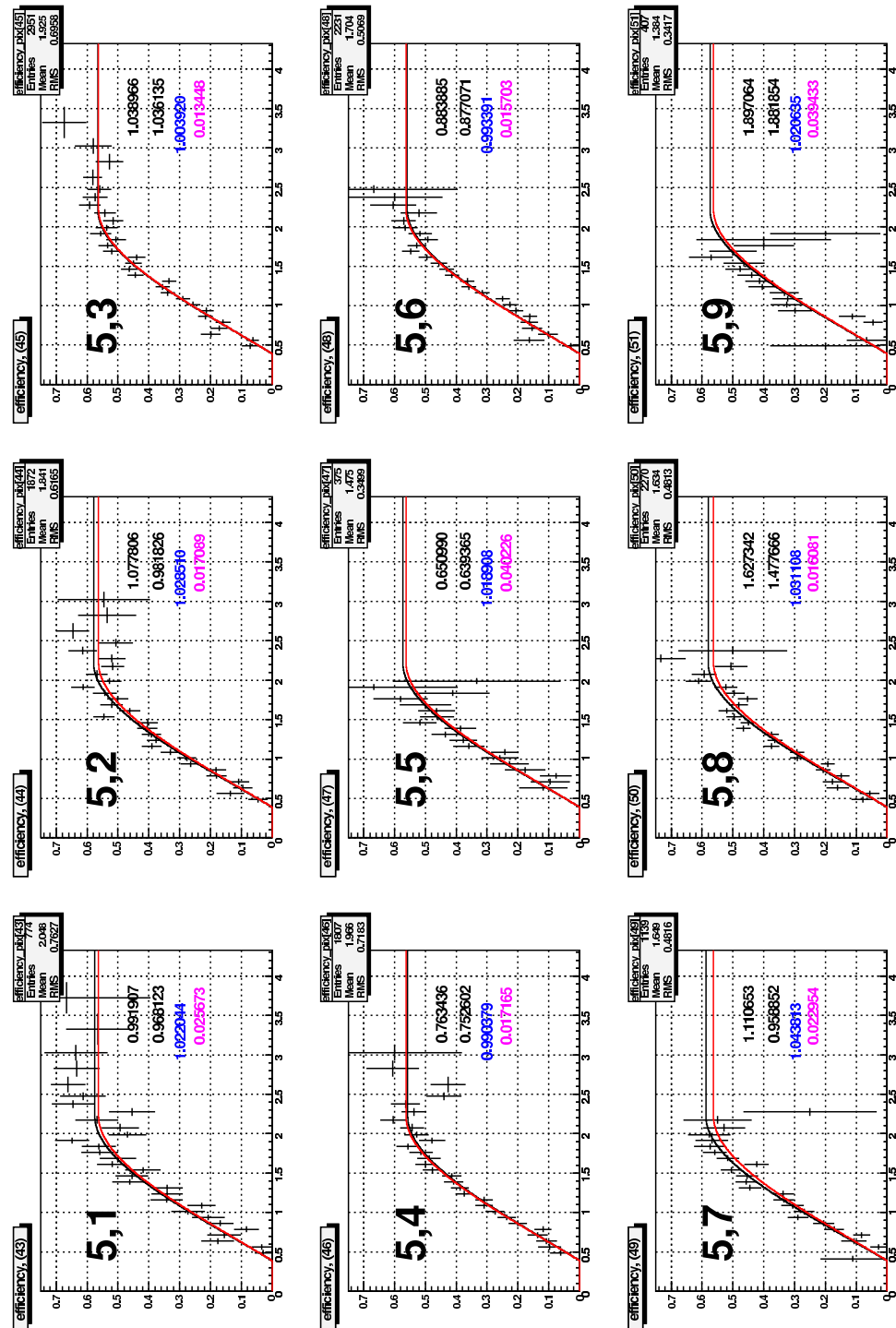


Figure B.11: Neutron detection efficiency by superpixel in sector 5, from the 4.2 GeV data. The red line shows the results of the fit to the entire sector. The black line shows the scaled sector fit.

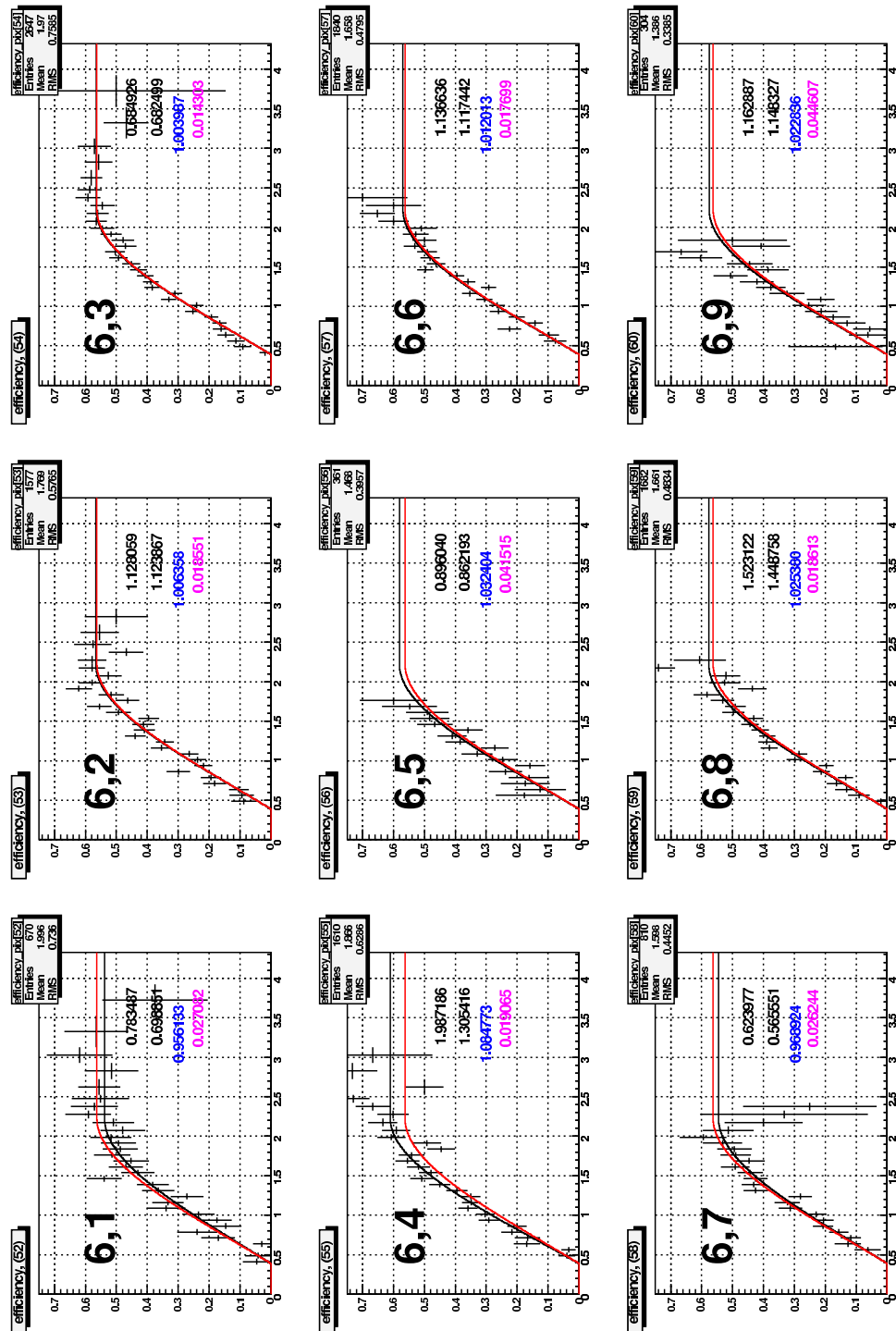


Figure B.12: Neutron detection efficiency by superpixel in sector 6, from the 4.2 GeV data. The red line shows the results of the fit to the entire sector. The black line shows the scaled sector fit.

# Appendix C

## SC neutron detection efficiency fits

### C.1 2.5 GeV beam energy

This section contains plots of the neutron detection efficiency measured on each of the paddles in each of the six sectors of the SC system, as a function of neutron momentum for the 2.5 GeV data set. Each plot is labelled by a pair of numbers  $a, b$ , where  $a$  is the sector number and  $b$  is the SC paddle number. Each plot shows a second pair of numbers. The upper number is the value of  $\chi^2/ndf$  for the comparison of the sector-based fit to the efficiency measured on the paddle. The lower number is the value of  $\chi^2/ndf$  for the comparison of the scaled, paddle-specific fit to the efficiency measured on the paddle. Two curves are superimposed on each figure. The blue number is the value of the scale factor, and the magenta number is the error on the scale factor. The red curve shows the result of the fit to the whole-sector efficiency. The black curve shows the results of scaling the whole-sector efficiency to the paddle measurements.

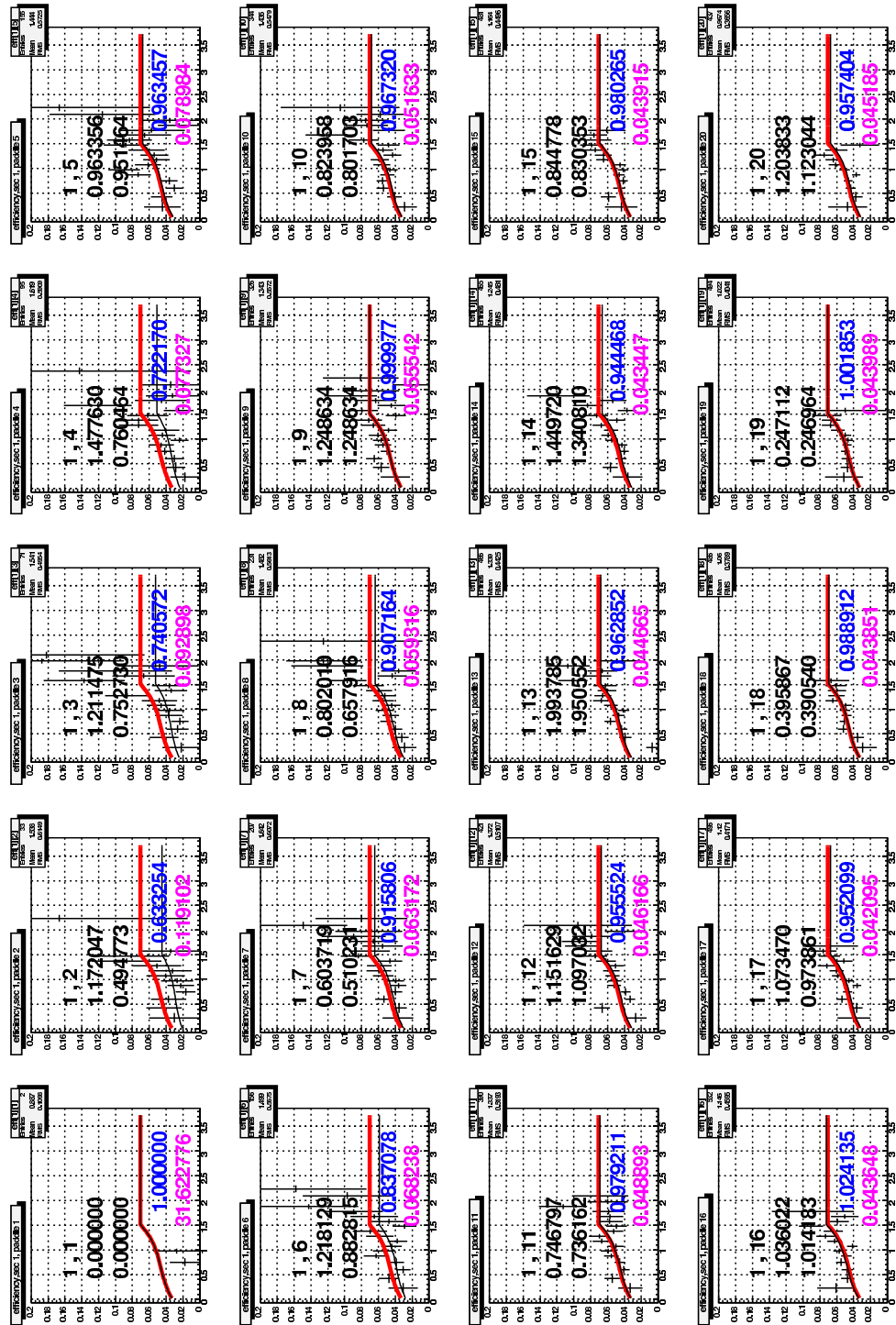


Figure C.1: Neutron detection efficiency by paddle in the SC, from the 2.5 GeV data. The red line shows the results of the fit to the entire sector. The black line shows the results of the scaled sector fits.

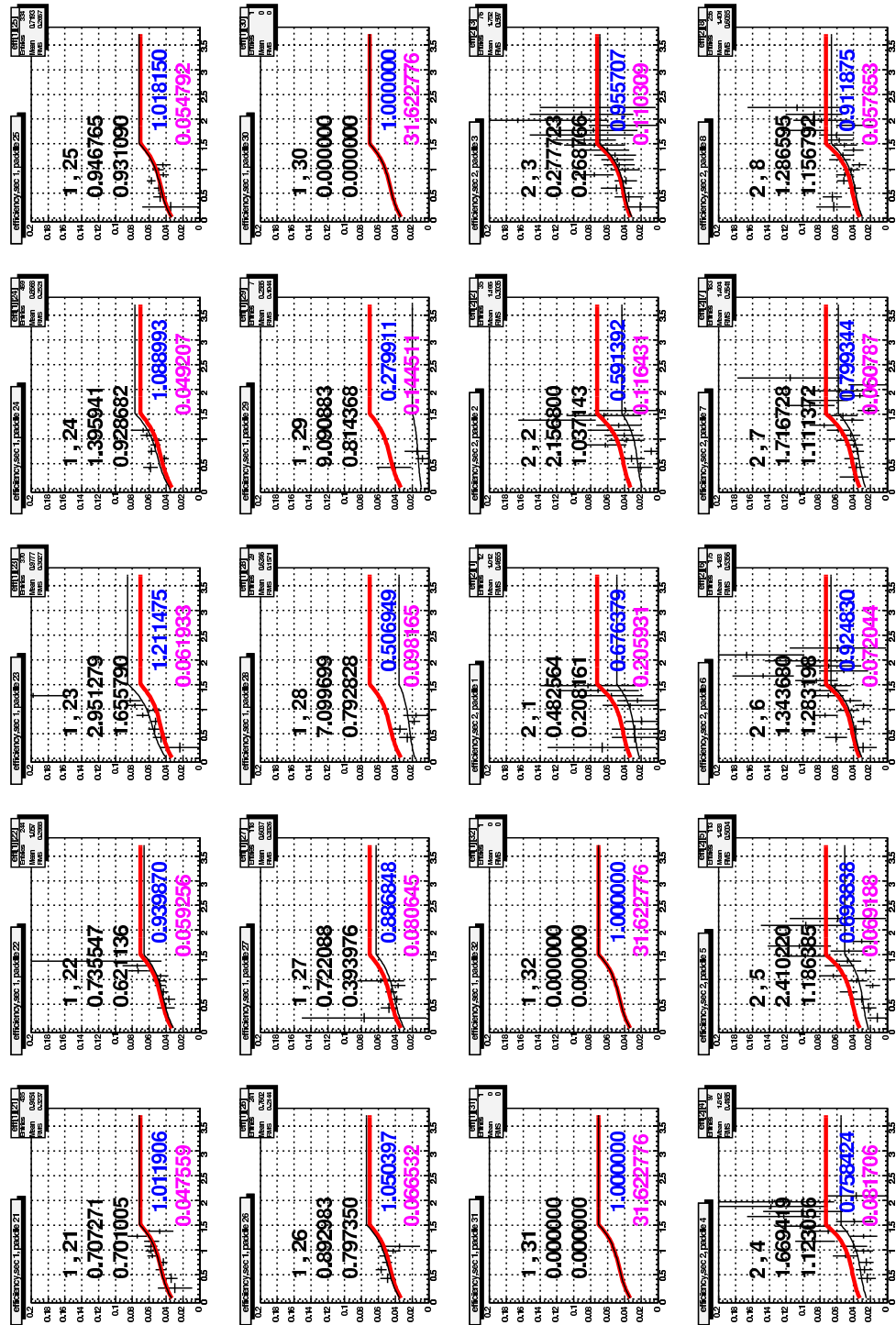


Figure C.2: Neutron detection efficiency by paddle in the SC, from the 2.5 GeV data. The red line shows the results of the fit to the entire sector. The black line shows the results of the scaled sector fits.

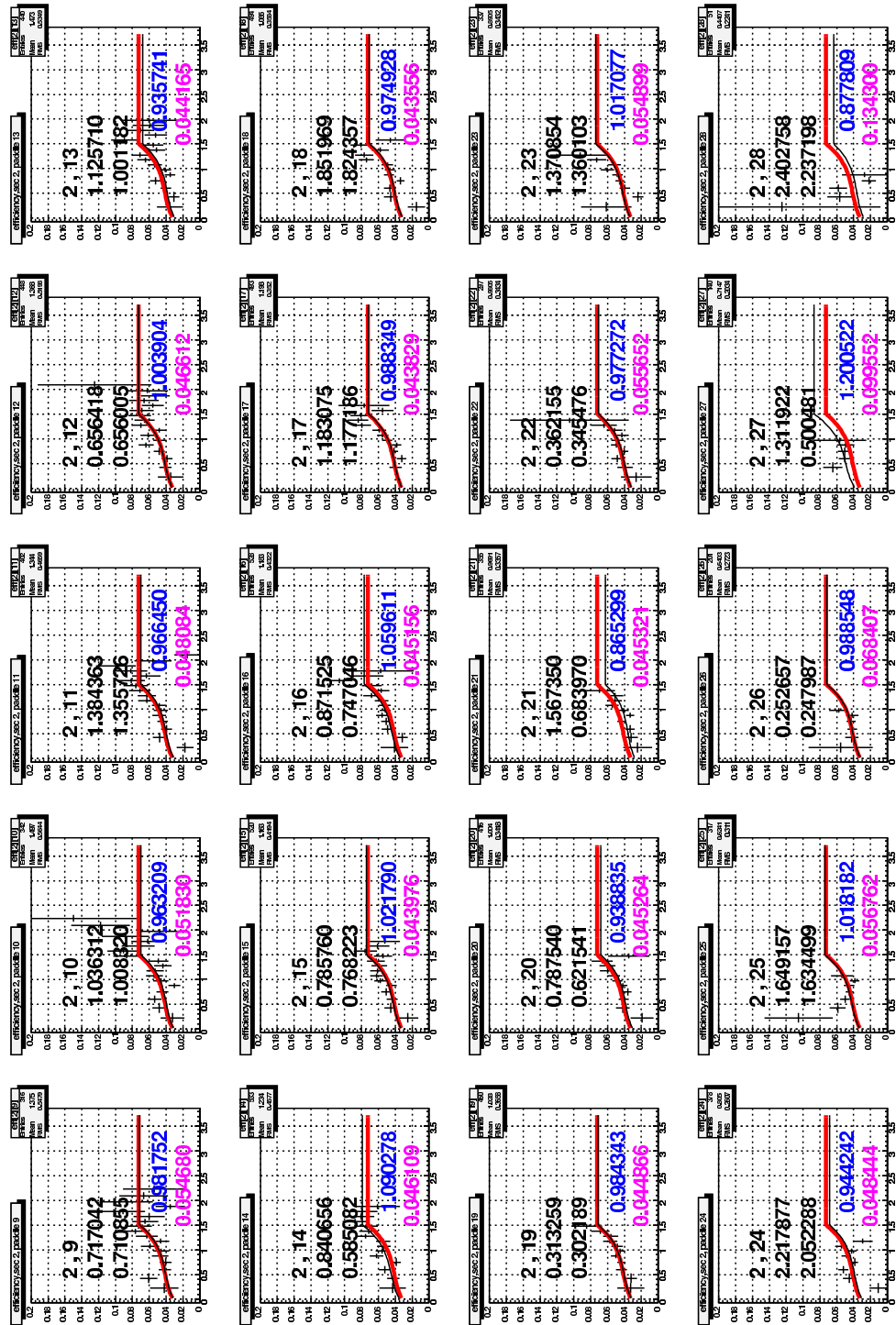


Figure C.3: Neutron detection efficiency by paddle in the SC, from the 2.5 GeV data. The red line shows the results of the fit to the entire sector. The black line shows the results of the scaled sector fits.

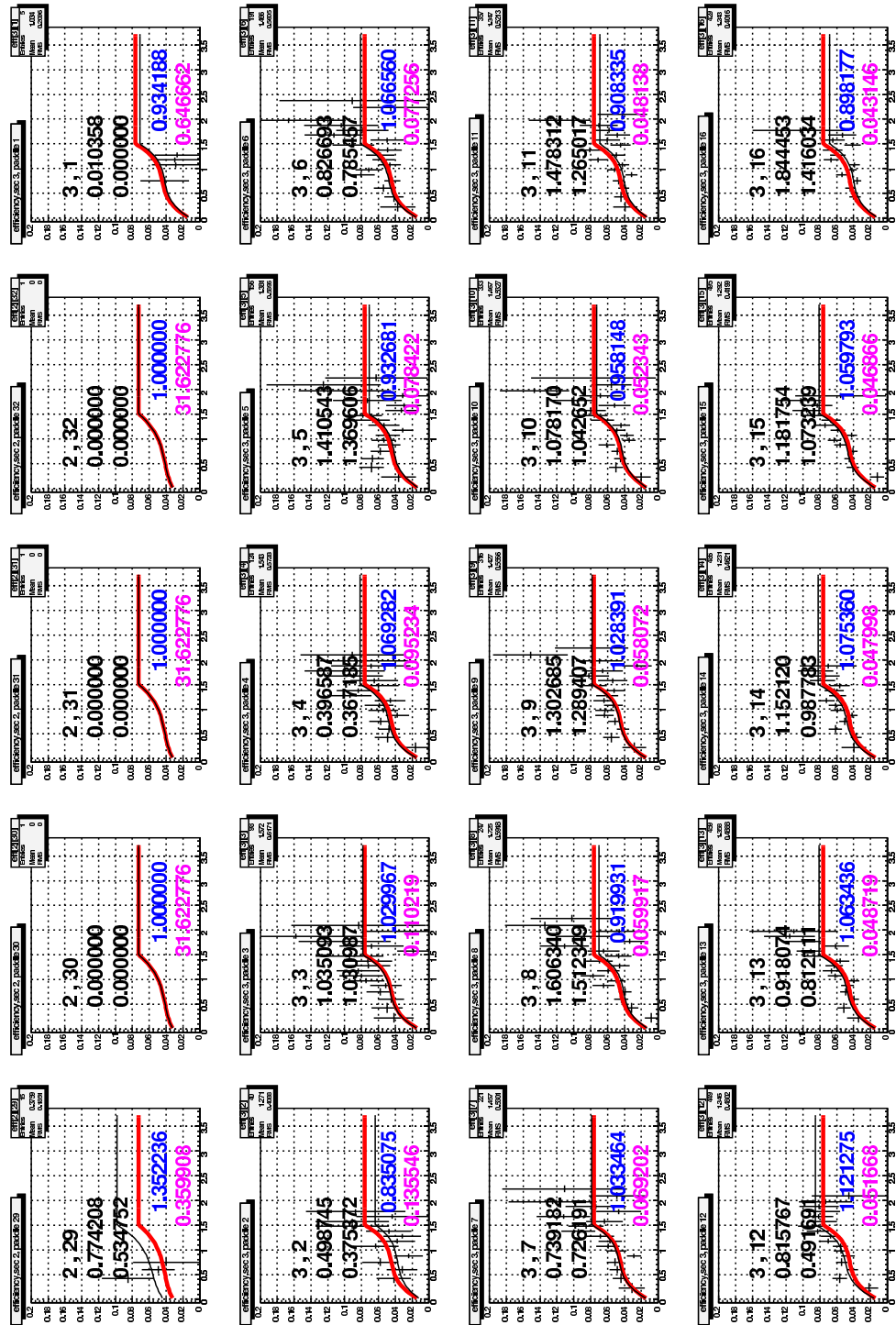


Figure C.4: Neutron detection efficiency by paddle in the SC, from the 2.5 GeV data. The red line shows the results of the fit to the entire sector. The black line shows the results of the scaled sector fits.

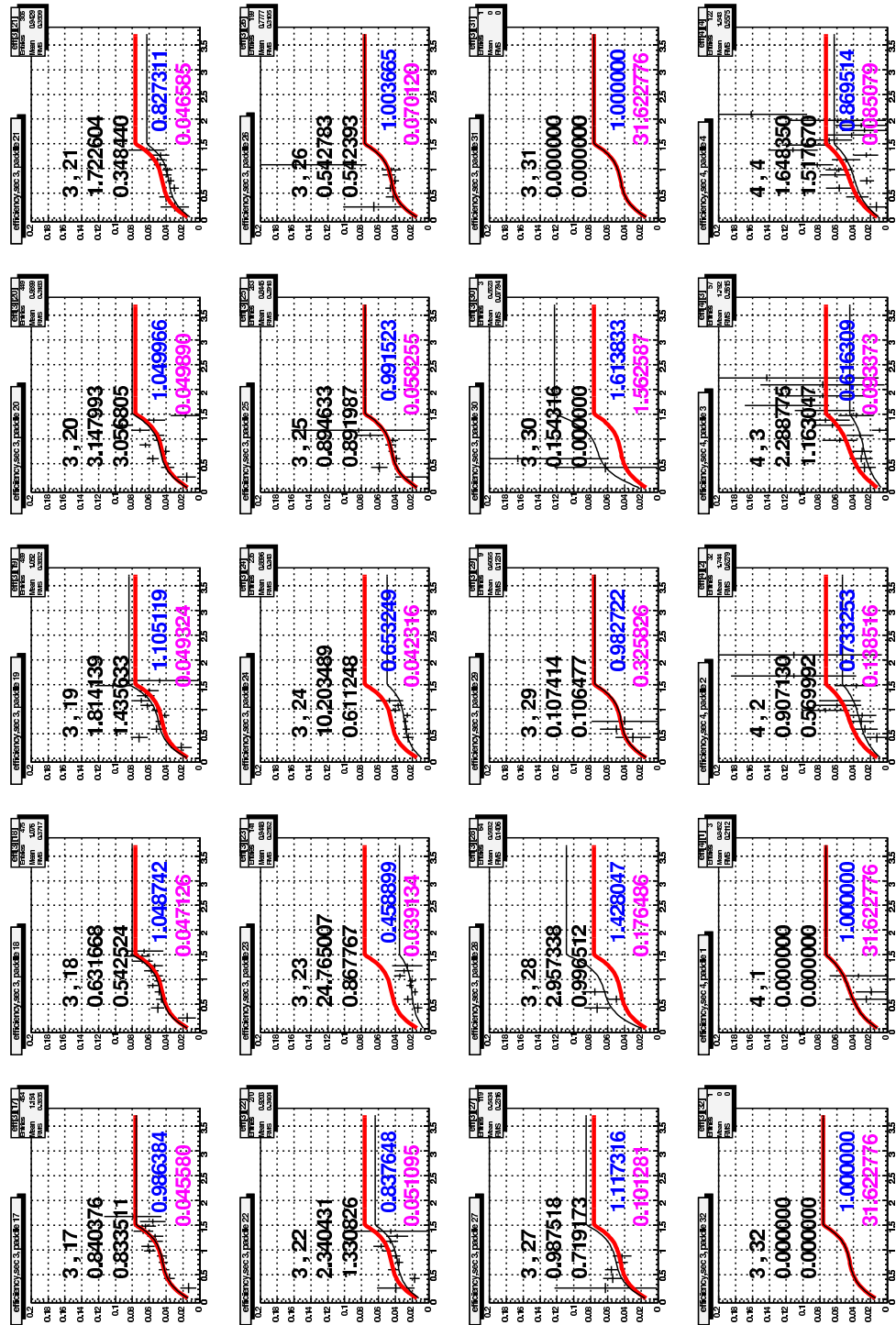


Figure C.5: Neutron detection efficiency by paddle in the SC, from the 2.5 GeV data. The red line shows the results of the fit to the entire sector. The black line shows the results of the scaled sector fits.

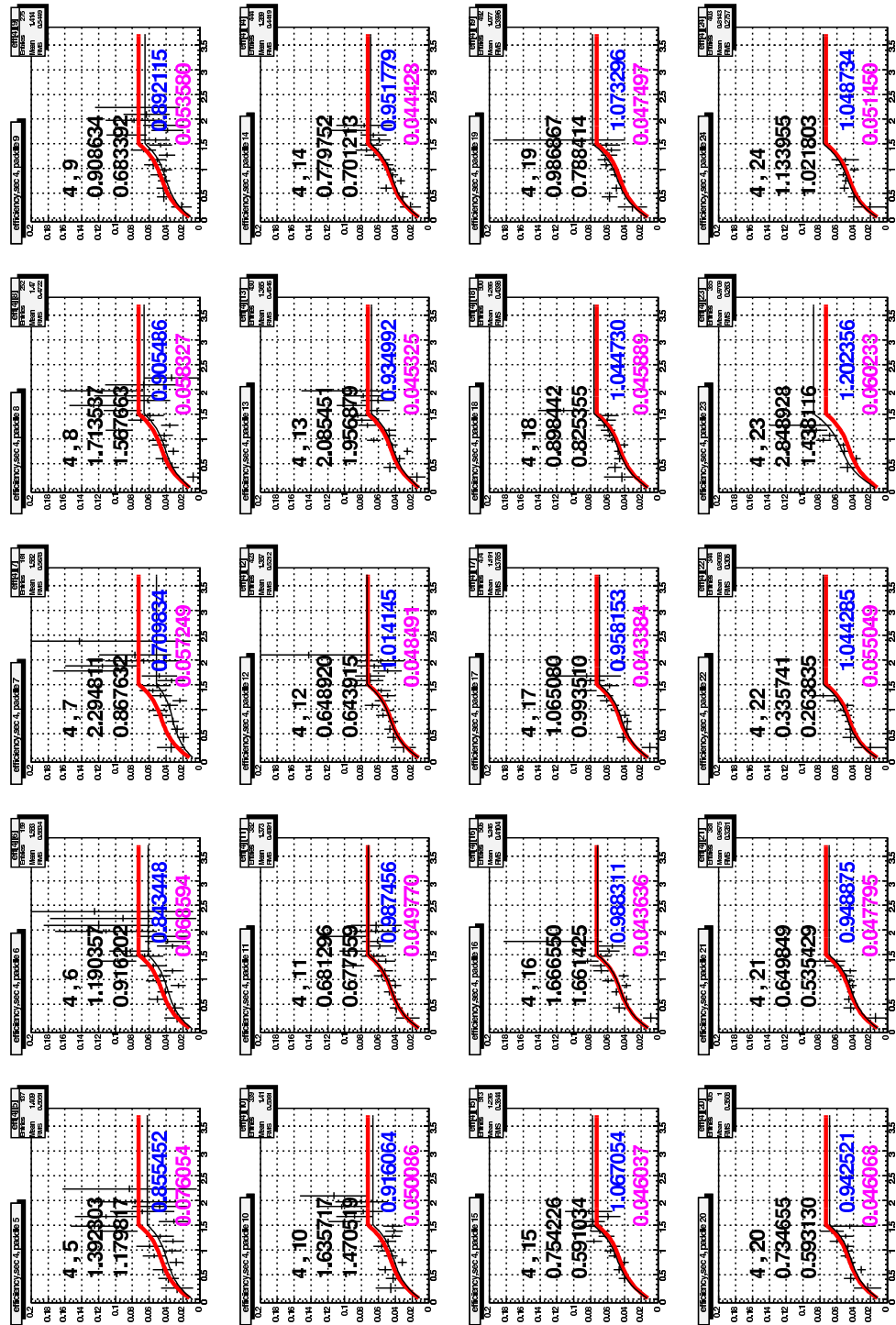


Figure C.6: Neutron detection efficiency by paddle in the SC, from the 2.5 GeV data. The red line shows the results of the fit to the entire sector. The black line shows the results of the scaled sector fits.

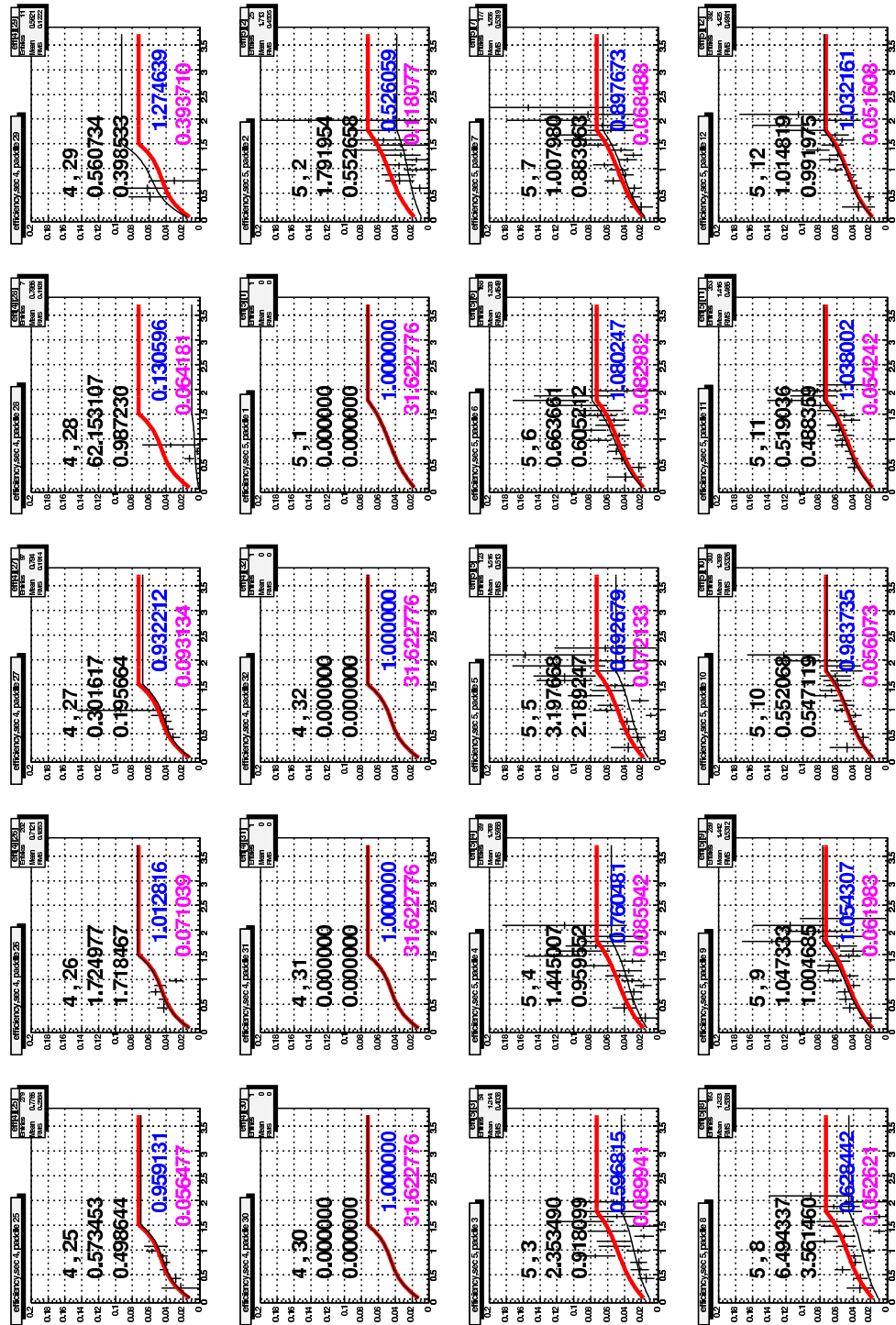


Figure C.7: Neutron detection efficiency by paddle in the SC, from the 2.5 GeV data. The red line shows the results of the fit to the entire sector. The black line shows the results of the scaled sector fits.

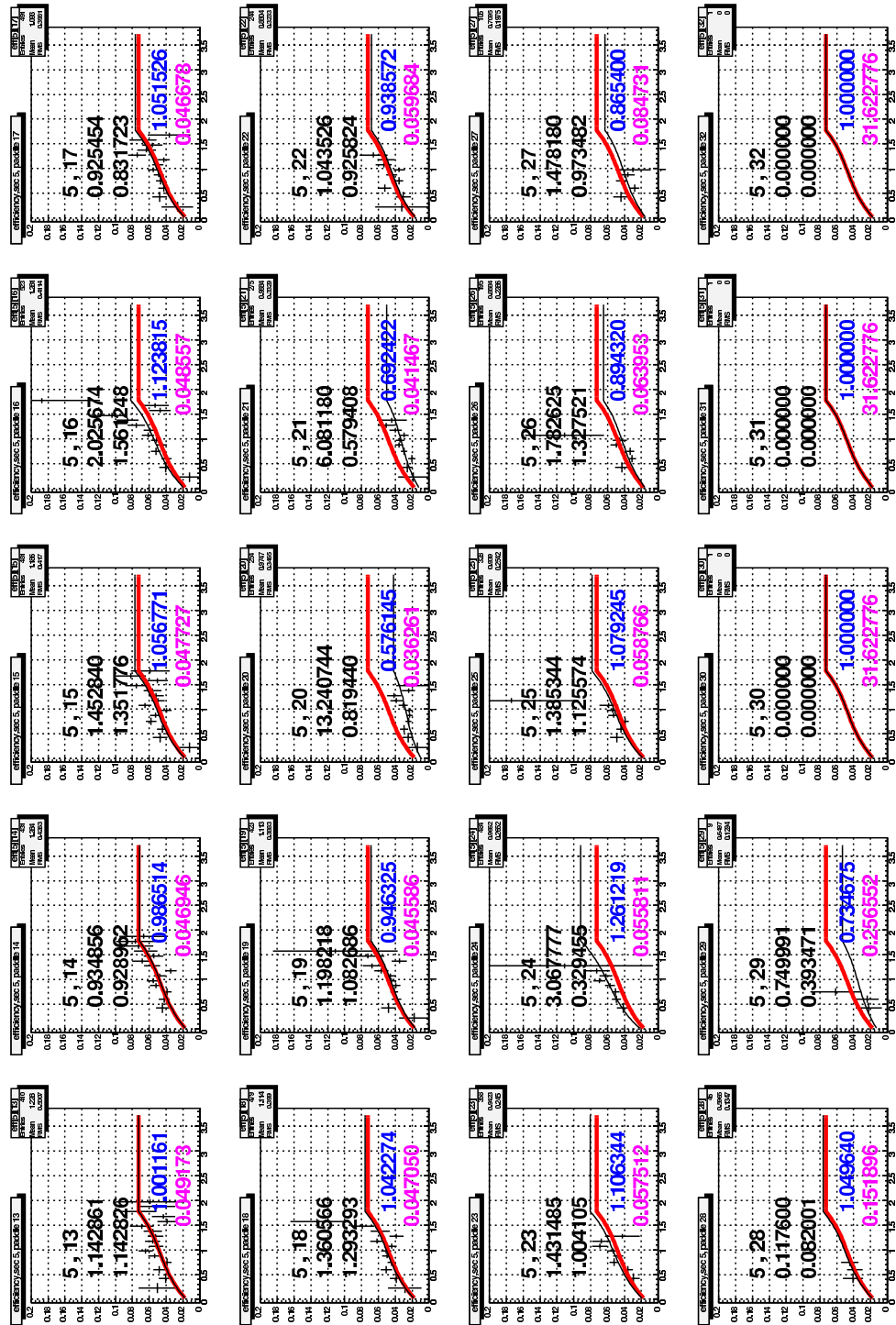


Figure C.8: Neutron detection efficiency by paddle in the SC, from the 2.5 GeV data. The red line shows the results of the fit to the entire sector. The black line shows the results of the scaled sector fits.

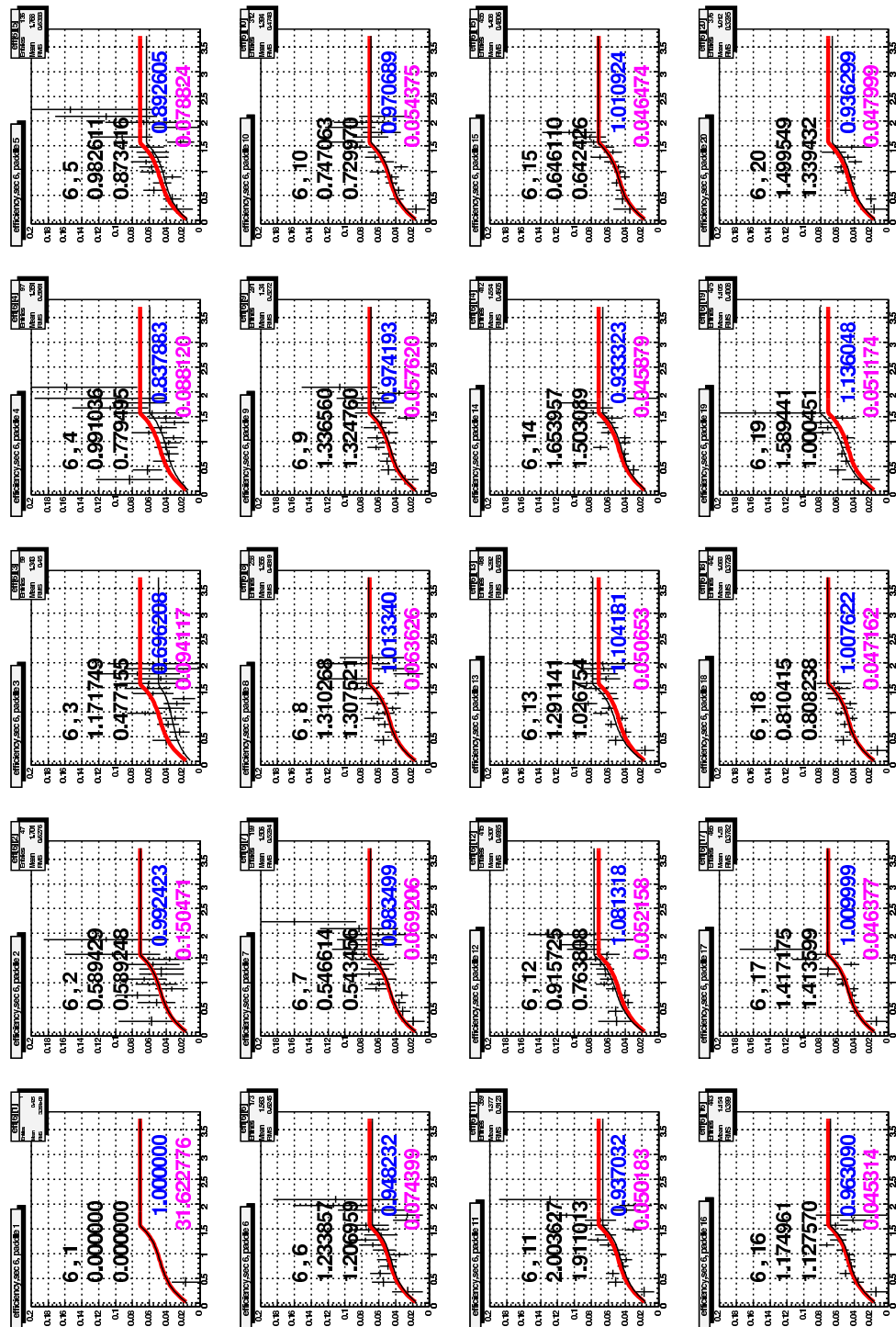


Figure C.9: Neutron detection efficiency by paddle in the SC, from the 2.5 GeV data. The red line shows the results of the fit to the entire sector. The black line shows the results of the scaled sector fits.

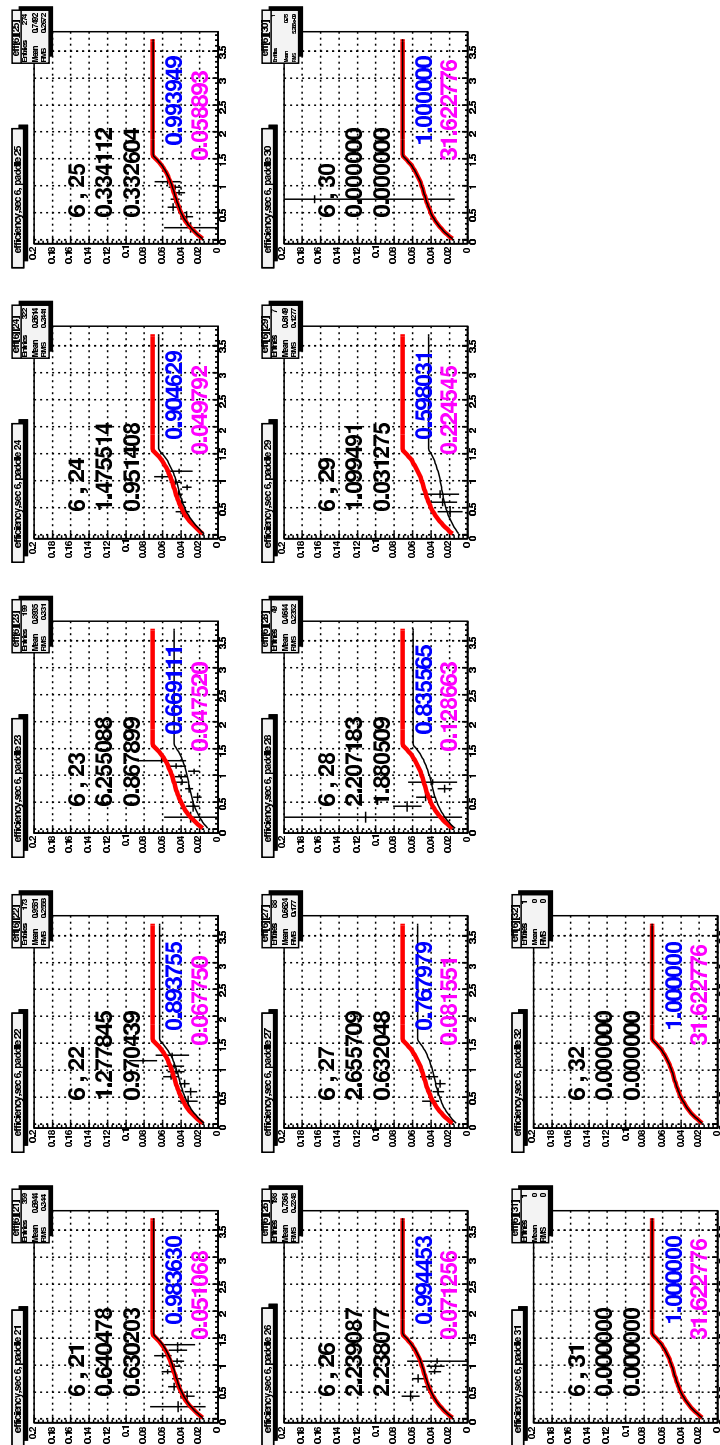


Figure C.10: Neutron detection efficiency by paddle in the SC, from the 2.5 GeV data. The red line shows the results of the fit to the entire sector. The black line shows the results of the scaled sector fits.

## C.2 4.2 GeV beam energy

This section contains plots of the neutron detection efficiency measured on each of the paddles in each of the six sectors of the SC system, as a function of neutron momentum for the 4.2 GeV data set. Each plot is labelled by a pair of numbers  $a, b$ , where  $a$  is the sector number and  $b$  is the SC paddle number. Each plot shows a second pair of numbers. The upper number is the value of  $\chi^2/ndf$  for the comparison of the sector-based fit to the efficiency measured on the paddle. The lower number is the value of  $\chi^2/ndf$  for the comparison of the scaled, paddle-specific fit to the efficiency measured on the paddle. The blue number is the value of the scale factor, and the magenta number is the error on the scale factor. Two curves are superimposed on each figure. The red curve shows the result of the fit to the whole-sector efficiency. The black curve shows the results of scaling the whole-sector efficiency to the paddle measurements.

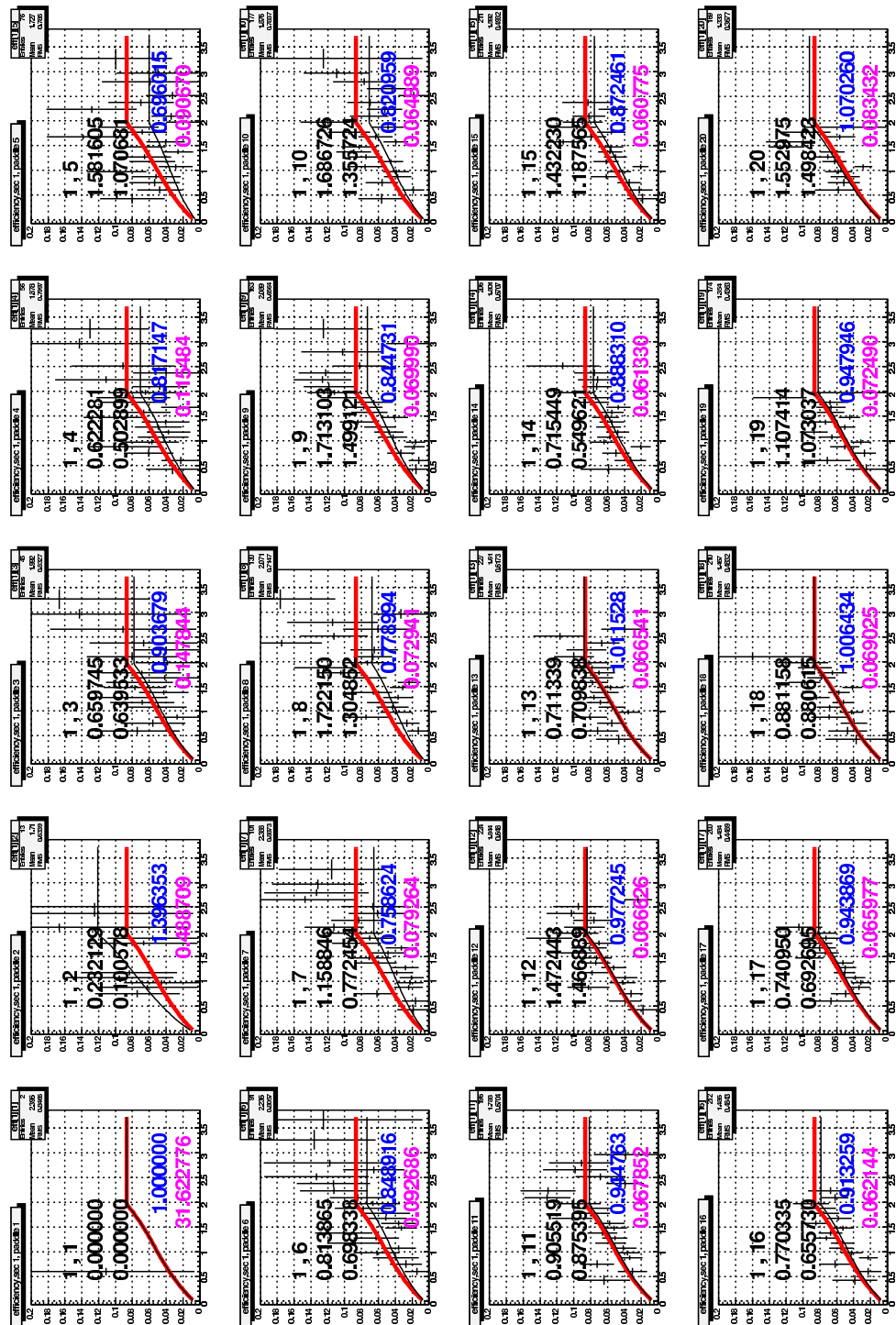


Figure C.11: Neutron detection efficiency by paddle in the SC, from the 4.2 GeV data. The red line shows the results of the fit to the entire sector. The black line shows the results of the scaled sector fits.

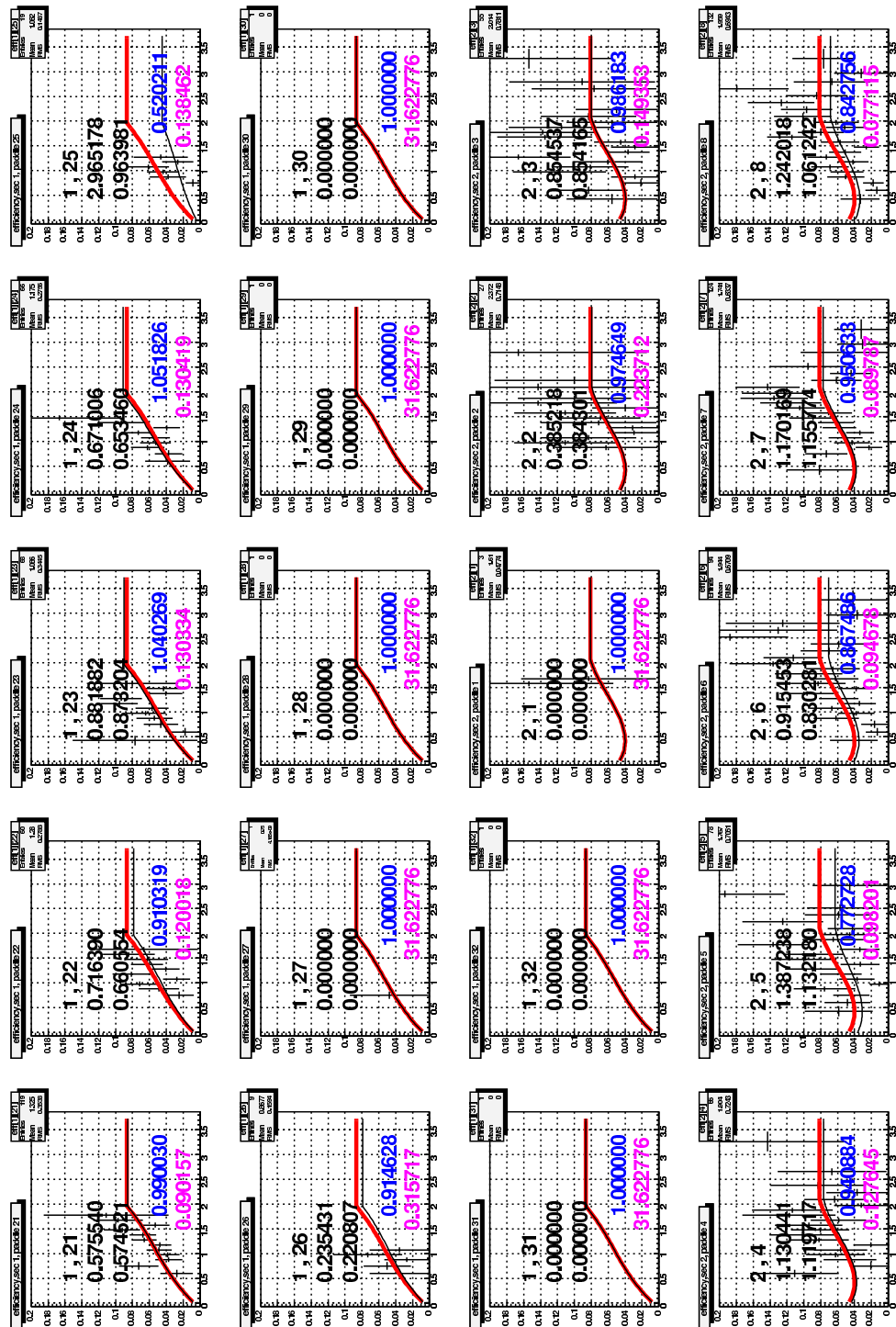


Figure C.12: Neutron detection efficiency by paddle in the SC, from the 4.2 GeV data. The red line shows the results of the fit to the entire sector. The black line shows the results of the scaled sector fits.

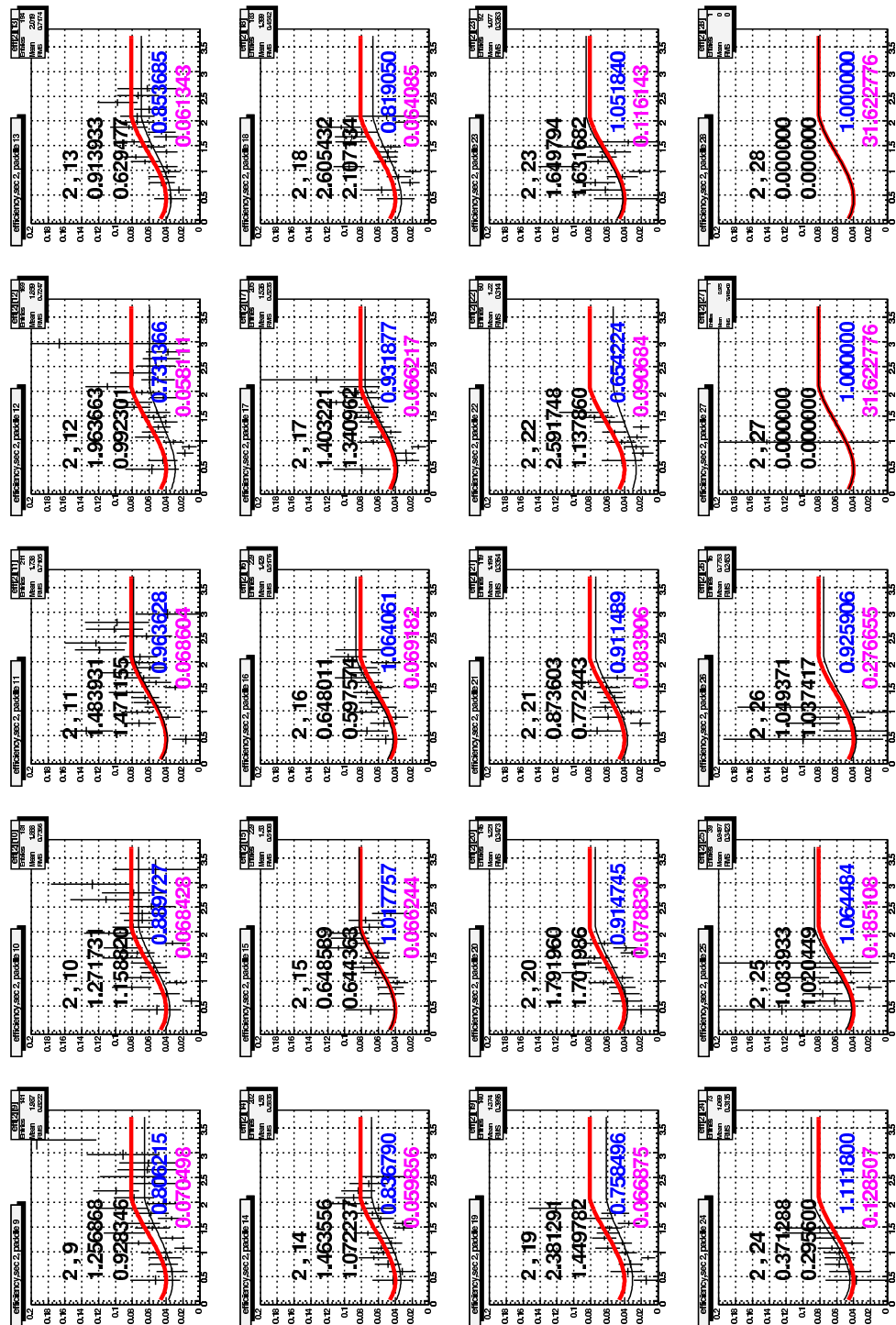


Figure C.13: Neutron detection efficiency by paddle in the SC, from the 4.2 GeV data. The red line shows the results of the fit to the entire sector. The black line shows the results of the scaled sector fits.

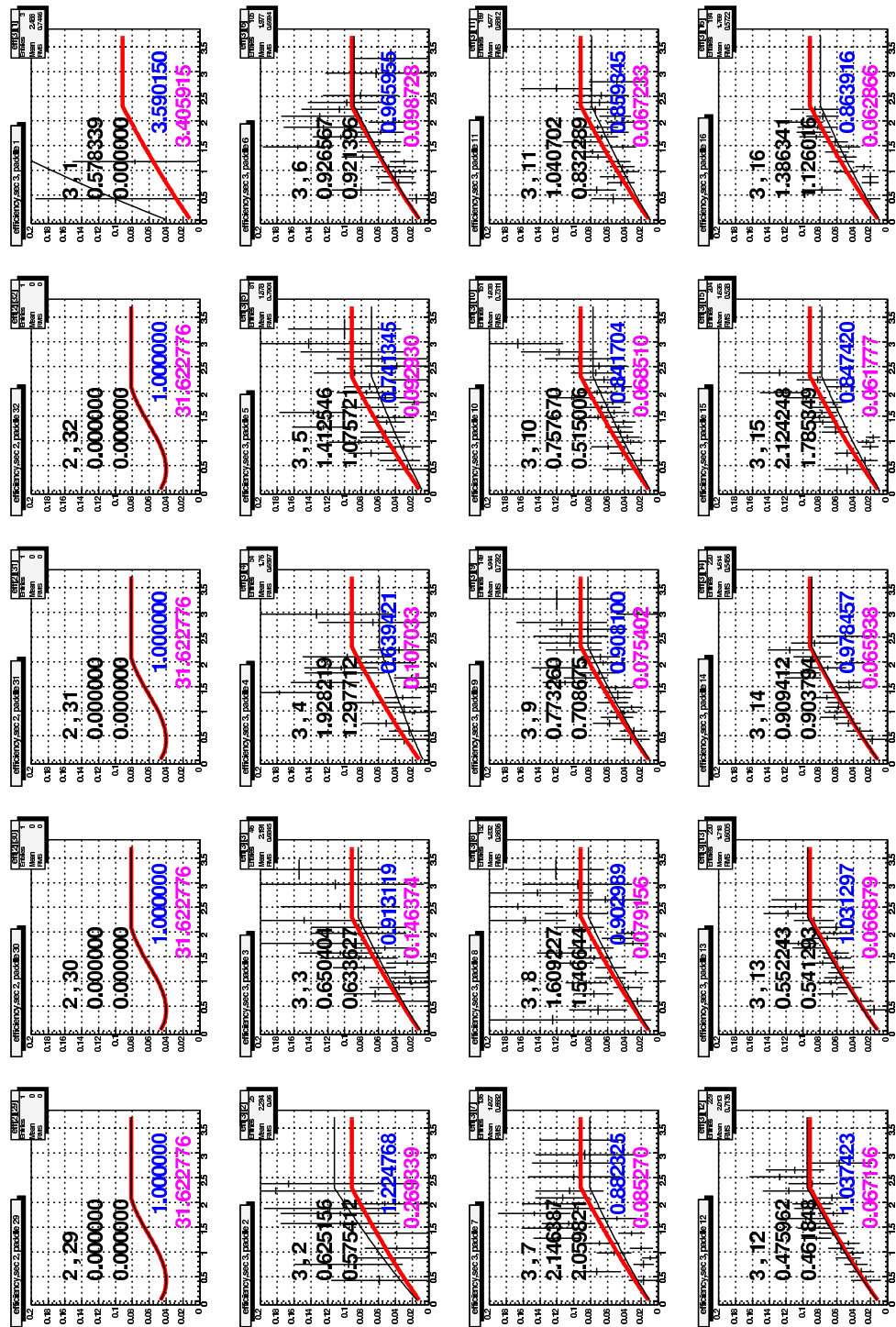


Figure C.14: Neutron detection efficiency by paddle in the SC, from the 4.2 GeV data. The red line shows the results of the fit to the entire sector. The black line shows the results of the scaled sector fits.

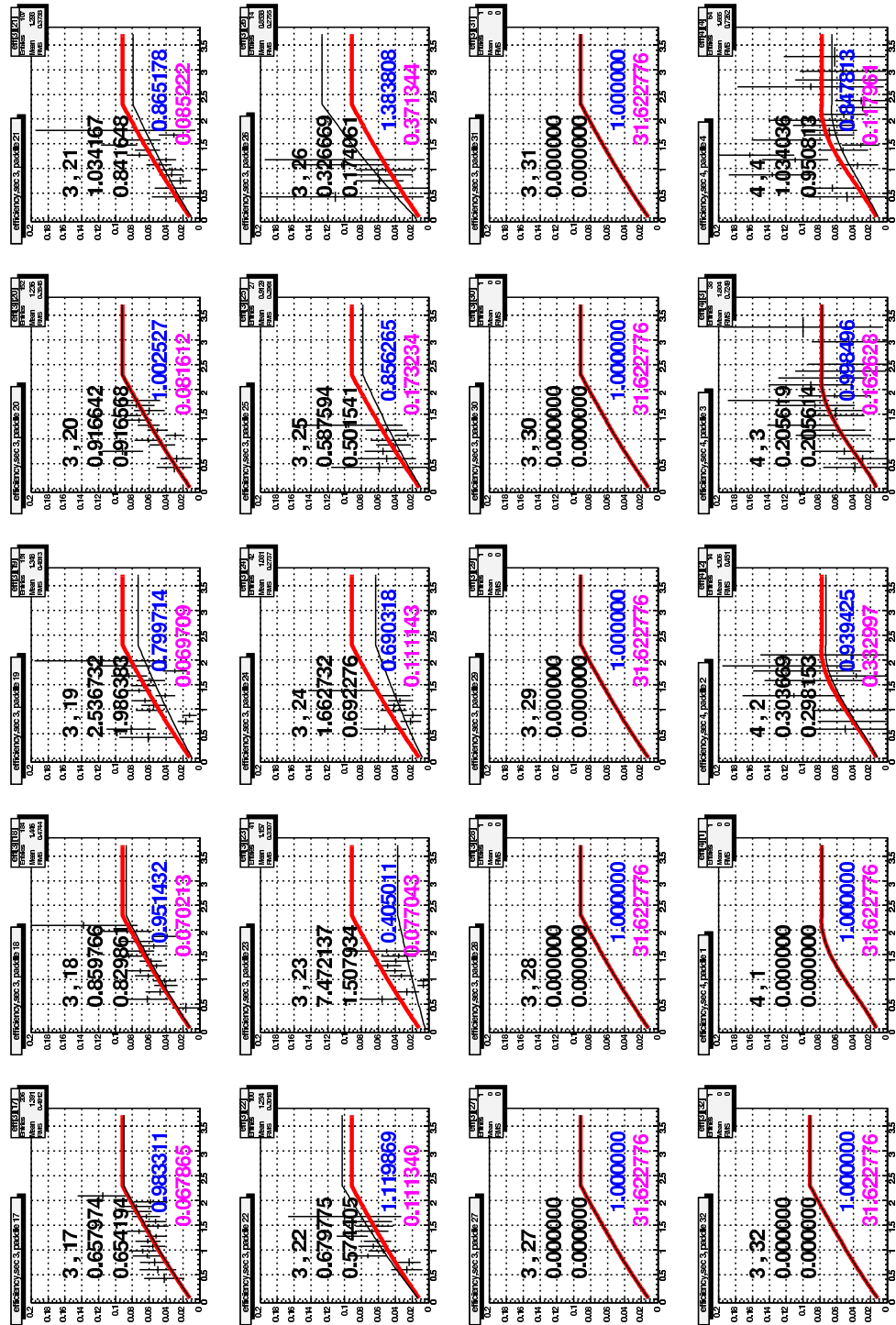


Figure C.15: Neutron detection efficiency by paddle in the SC, from the 4.2 GeV data. The red line shows the results of the fit to the entire sector. The black line shows the results of the scaled sector fits.

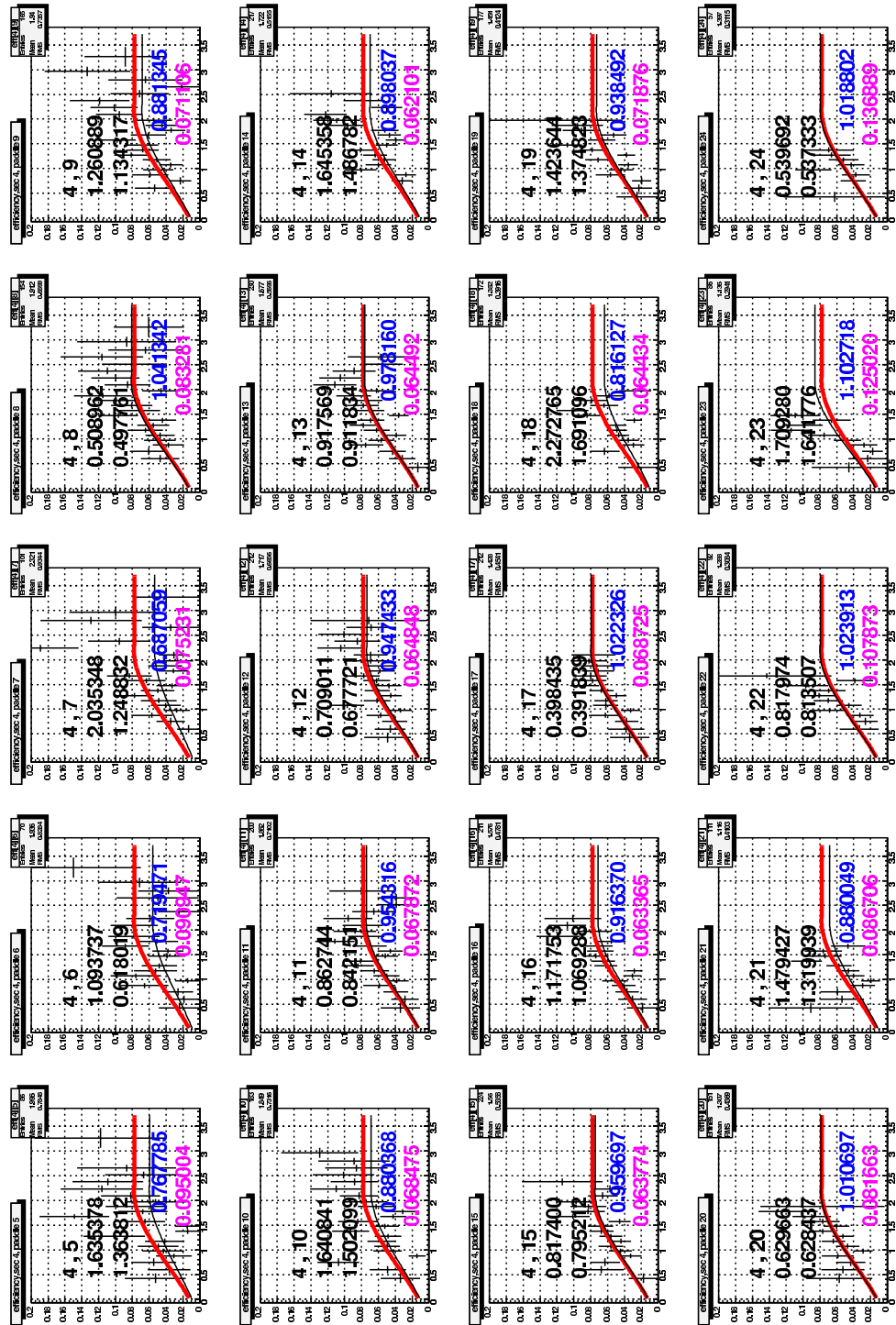


Figure C.16: Neutron detection efficiency by paddle in the SC, from the 4.2 GeV data. The red line shows the results of the fit to the entire sector. The black line shows the results of the scaled sector fits.

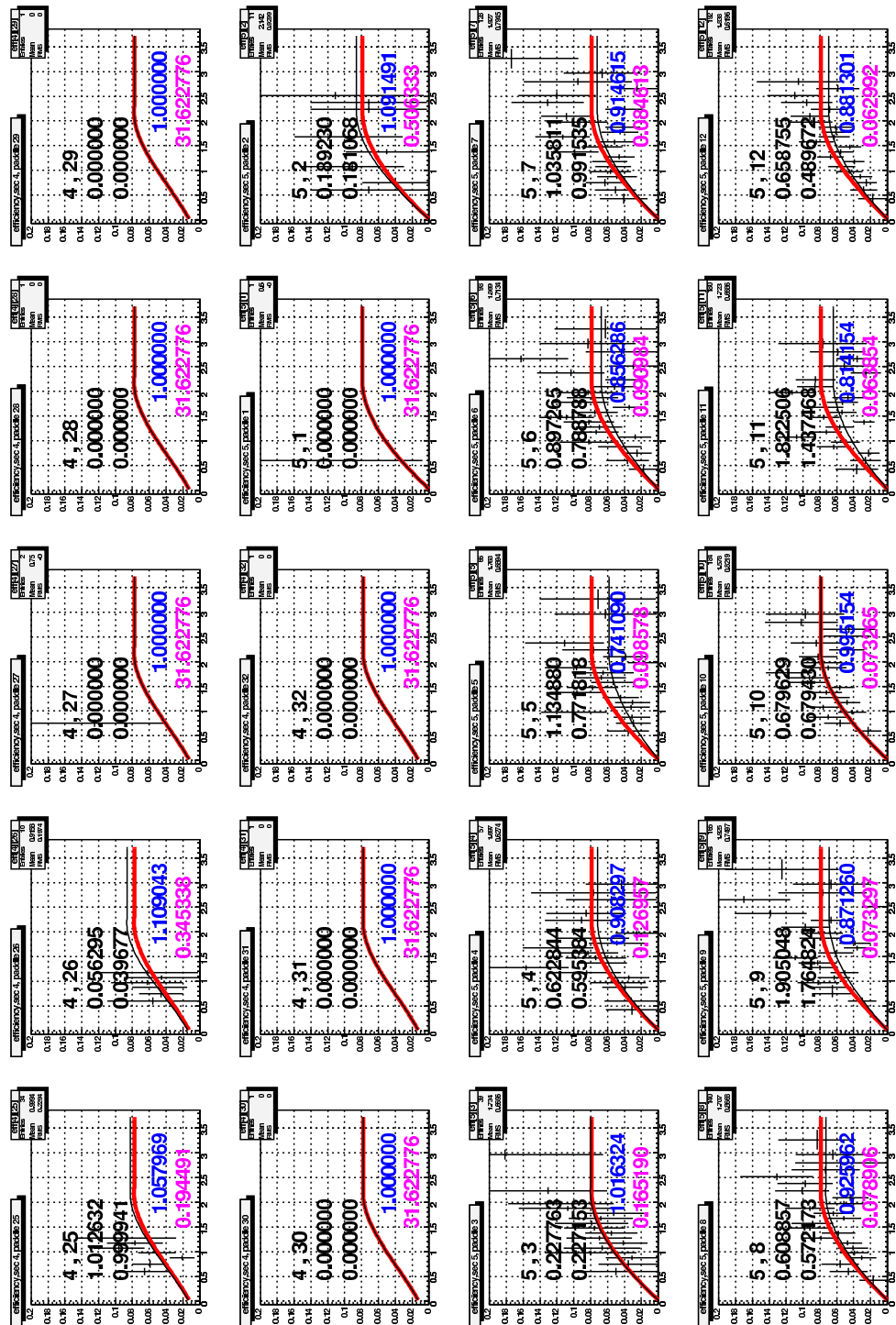


Figure C.17: Neutron detection efficiency by paddle in the SC, from the 4.2 GeV data. The red line shows the results of the fit to the entire sector. The black line shows the results of the scaled sector fits.

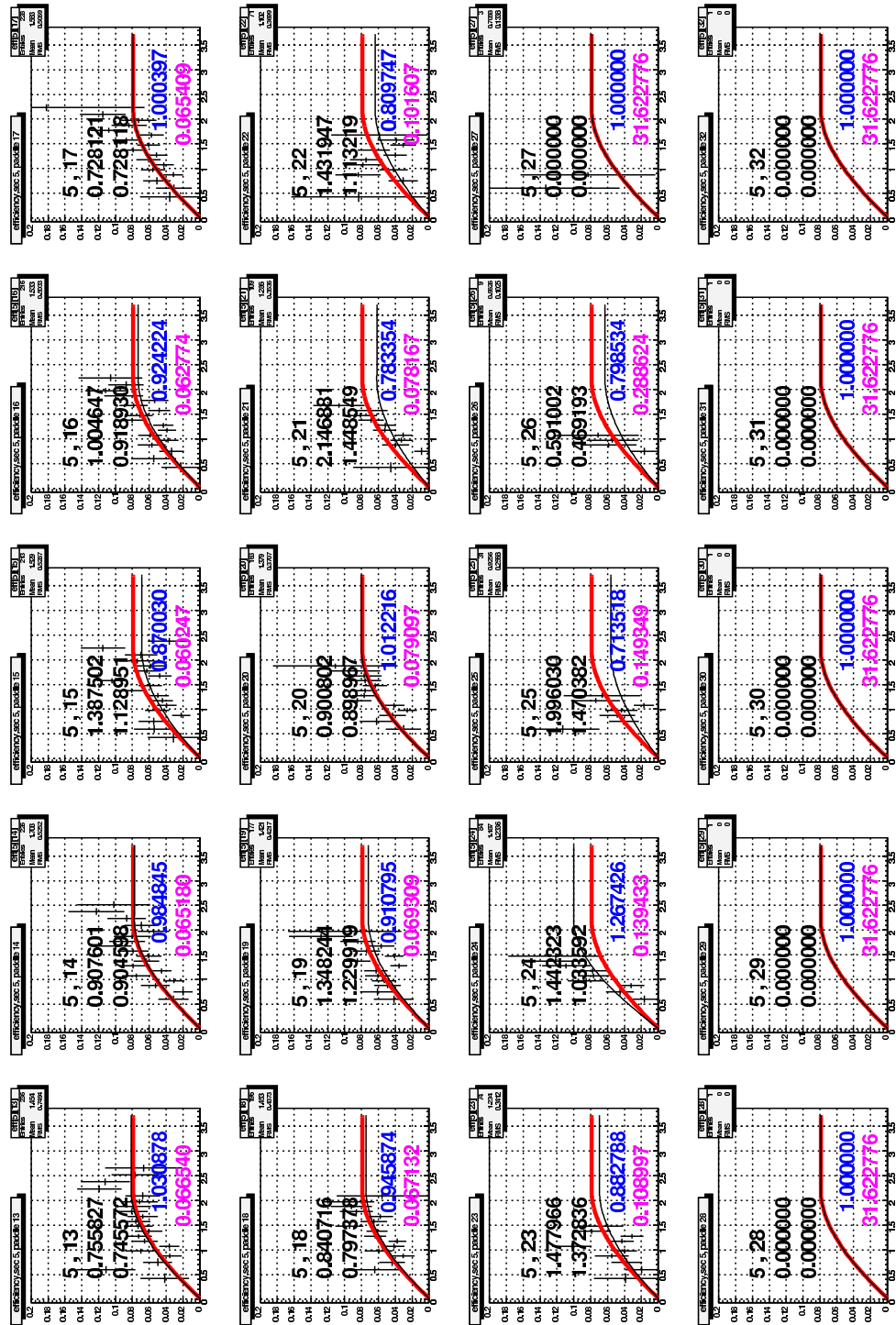


Figure C.18: Neutron detection efficiency by paddle in the SC, from the 4.2 GeV data. The red line shows the results of the fit to the entire sector. The black line shows the results of the scaled sector fits.

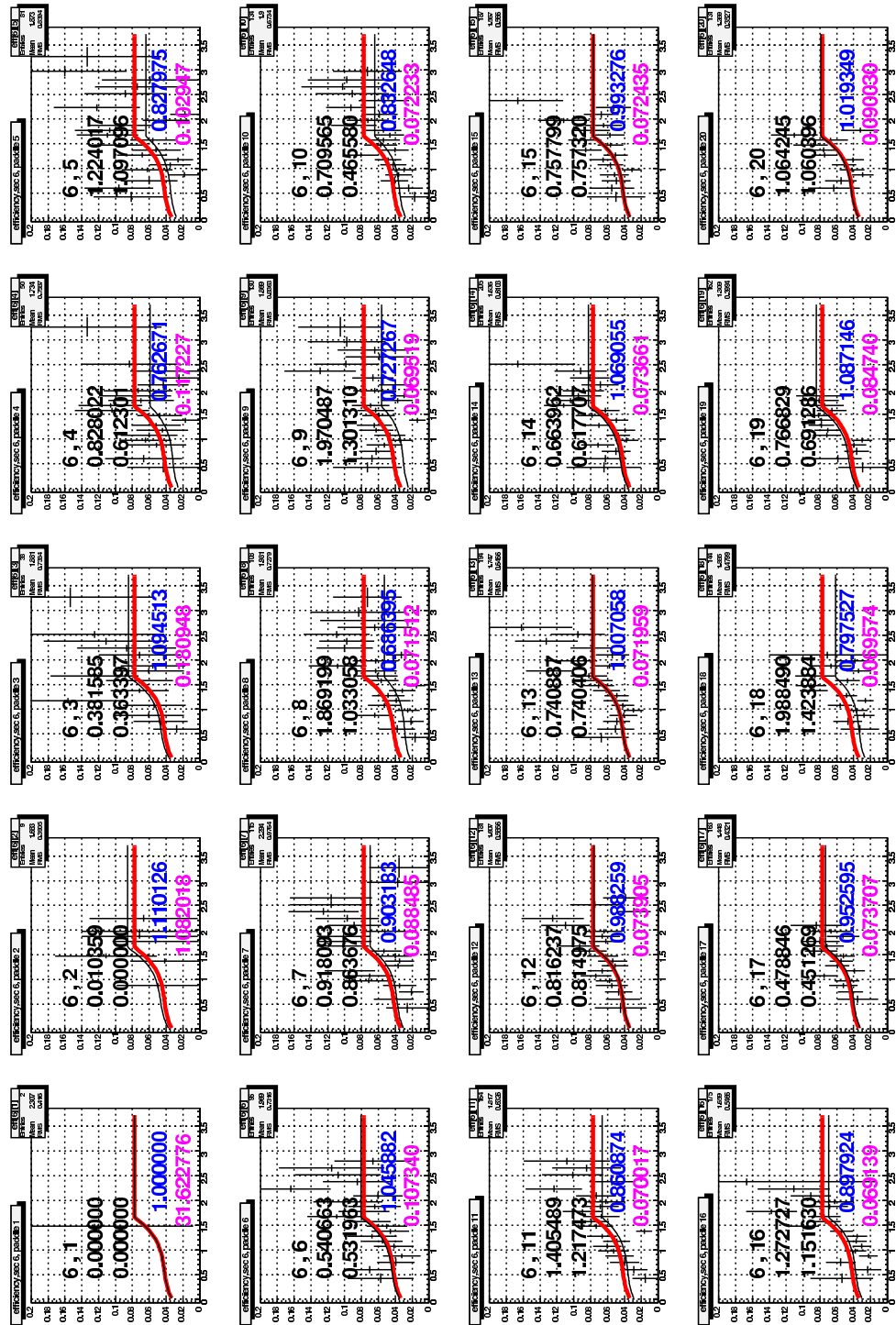


Figure C.19: Neutron detection efficiency by paddle in the SC, from the 4.2 GeV data. The red line shows the results of the fit to the entire sector. The black line shows the results of the scaled sector fits.

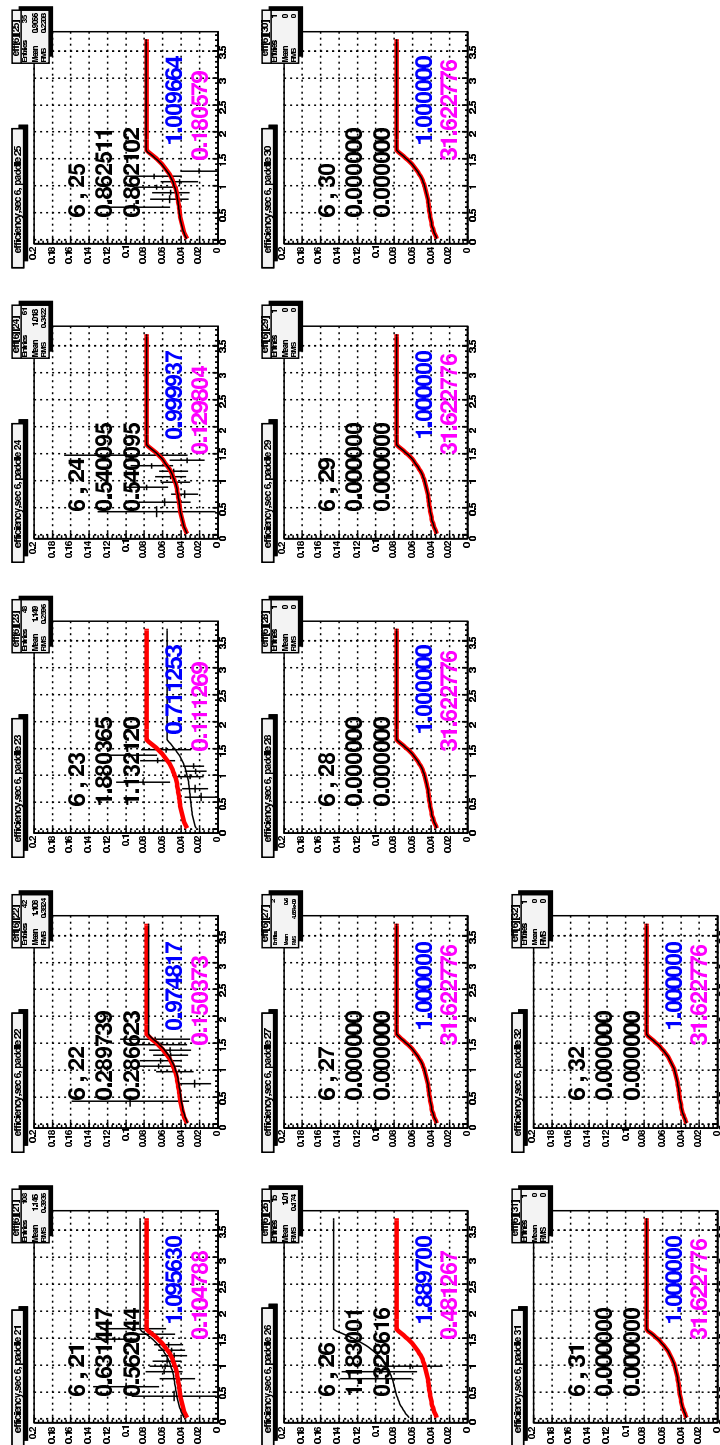


Figure C.20: Neutron detection efficiency by paddle in the SC, from the 4.2 GeV data. The red line shows the results of the fit to the entire sector. The black line shows the results of the scaled sector fits.

# Appendix D

## Kinematics of quasi-elastic scattering

There are two frames of interest for the analysis of quasi-elastic scattering: the lab frame, in which both the electron and the nucleon are moving, and the rest frame, in which the nucleon is stationary. Scattering in the rest frame is illustrated in Fig D.1.

In the rest frame, the particles have 4-momenta:

$$P_1 = E(1, \hat{P}_1) \quad (\text{D.1})$$

$$P_2 = (M_N, 0) \quad (\text{D.2})$$

$$P_3 = E'(1, \hat{P}_3) \quad (\text{D.3})$$

$$P_4 = (E'_N, \vec{P}_4) \quad (\text{D.4})$$

where  $P_1, P_3$  are the initial and final electron 4-momenta and  $P_2, P_4$  are the initial and final nucleon 4-momenta.

Scattering in the lab frame is illustrated in Fig D.2.

In the lab frame, the particles have 4-momenta:

$$P_1^* = E^*(1, \hat{P}_1^*) \quad (\text{D.5})$$

$$P_2^* = (E_N^*, \vec{p}_f) \quad (\text{D.6})$$

$$P_3^* = E^{*'}(1, \hat{P}_3^*) \quad (\text{D.7})$$

$$P_4^* = (E_N^{*'}, \vec{P}_4^*) \quad (\text{D.8})$$

where the \* denotes a lab frame quantity,  $p_f$  is the magnitude of the nucleon Fermi momentum,  $\theta_f$  is the angle between the direction of the Fermi momentum and the incident electron,  $E^*$  is the incident electron beam energy and  $E_N^* = \sqrt{M_N^2 + p_f^2}$ .

The relationship between the starred and unstarred quantities can be determined by considering invariant scalar products of 4-vectors. First,  $P_1 \cdot P_2$ :

$$\begin{aligned} P_1 \cdot P_2 &= P_1^* \cdot P_2^* \\ EM_N &= E^* E_N^* - E^* p_f \cos \theta_f \end{aligned}$$

which yields the relation between the incident electron energy in the rest frame and the incident electron energy in the lab frame:

$$E = \frac{E^*}{M_N} (E_N^* - p_f \cos \theta_f) \quad (\text{D.9})$$

Next, consider  $P_1 \cdot P_3$ :

$$\begin{aligned} P_1 \cdot P_3 &= P_1^* \cdot P_3^* \\ EE' - EE' \cos \theta_3 &= E^* E^{*'} - E^* E^{*' } \cos \theta_3^* \end{aligned}$$

which after rearrangement gives a relationship between the electron scattering angles in the two frames:

$$\frac{1 - \cos \theta_3}{1 - \cos \theta_3^*} = \frac{E^* E^{*' }}{EE'} \quad (\text{D.10})$$

Lastly, consider  $P_2 \cdot P_3$ :

$$\begin{aligned} P_2 \cdot P_3 &= P_2^* \cdot P_3^* \\ E' M_n &= E_N^* E^{*' } - E^{*' } p_f \cos(\theta_3^* - \theta_f) \end{aligned}$$

This yields a relationship between the scattered electron energies in the two frames:

$$E^{*' } = \frac{E' M_N}{E_N^* - p_f \cos(\theta_3^* - \theta_f)} \quad (\text{D.11})$$

Combining Eqns D.10 and D.11 gives:

$$\frac{1 - \cos \theta_3}{1 - \cos \theta_3^*} = \left( \frac{E^*}{EE'} \right) \left( \frac{E' M_N}{E_N^* - p_f \cos(\theta_3^* - \theta_f)} \right) \quad (\text{D.12})$$

which can be solved for  $\theta_3$ :

$$\theta_3 = \cos^{-1} \left\{ 1 - \left( \frac{M_N E^*}{E} \right) \left( \frac{1 - \cos \theta_3^*}{E_N^* - p_f \cos(\theta_3^* - \theta_f)} \right) \right\} \quad (\text{D.13})$$

This equation can be solved numerically to extract  $\theta_3^*$  given  $\theta_3$ .

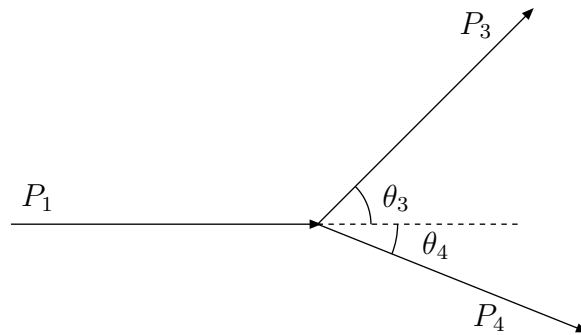


Figure D.1: Elastic scattering in the nucleon rest frame.

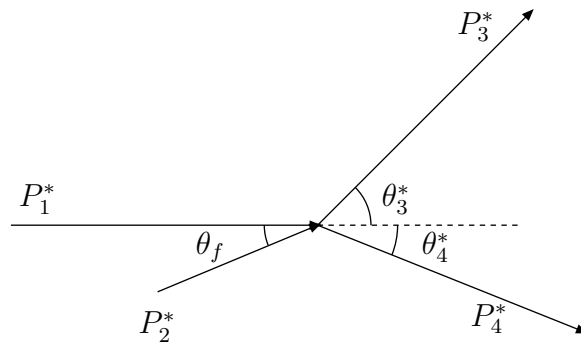


Figure D.2: Elastic scattering in the lab frame.